COMPUTATIONAL STUDY OF THE INTERNAL KINK MODE EVOLUTION AND ASSOCIATED MAGNETIC RECONNECTION PHENOMENA.

By

Vyacheslav S. Lukin

A DISSERTATION
PRESENTED TO THE FACULTY
OF PRINCETON UNIVERSITY
IN CANDIDACY FOR THE DEGREE
OF DOCTOR OF PHILOSOPHY

RECOMMENDED FOR ACCEPTANCE
BY THE DEPARTMENT OF
ASTROPHYSICAL SCIENCES
Adviser: Prof. Stephen C. Jardin

JANUARY, 2008

Abstract

Numerical study of plasma relaxation and self-organization in two-dimensional incompressible magnetohydrodynamic (MHD) systems is presented. A large semi-periodic tearing unstable reversed magnetic field configuration in flat Cartesian geometry and a driven tokamak-like kink-unstable screw pinch in helical geometry are considered. Special emphasis is made on the coupling between global and local scales by way of magnetic reconnection. The influence of the global system's size and geometry on the magnetic reconnection phenomenon and associated current sheet dynamics are evaluated in different collisionality regimes. Questions of plasmoid formation by way of current sheet break-up and onset of fast reconnection in a semi-collisional regime are investigated. Visco-resistive, electron and Hall MHD plasma fluid models are employed in the study. In helical geometry, application of Ohmic current drive to the periodic screw-pinch with large axial magnetic field and hollow resistivity profile are shown to result in "sawtooth-like" limit cycle behavior which is independent of the exact initial conditions. Incomplete reconnection sawteeth, maintaining the value of safety factor q in the central plasma region below unity throughout the cycle, are demonstrated for the first time in numerical simulations. Sensitivity of sawtooth characteristics to a number of plasma parameters is evaluated. The initial value problems described above are solved with an adaptive fully implicit parallel macroscopic modeling code SEL, which is capable of evolving a large range of extended MHD equations. The structure, key features, and thorough testing of the code are described in detail.

“Кому как, а мне нравится думать!”

М. Жванецкий

“A conclusion is the place where you got tired of thinking.”

Matz’s Maxim

Table of Contents

List of Tables

List of Figures

Acknowledgements

As this work is the formal culmination of my long climb up the academic education ladder, here, I would like to acknowledge all those who have made that climb possible, pulled and pushed me up along the way, and helped me to keep my sanity and the relative importance of it all in a greater perspective.

Of course, anything and everything that I have been able to accomplish is to a great degree due to the constant support and encouragement by my family, and particularly my parents – Sergey Lukin and Alla Lukina, who have always pointed me in the right direction and then done their best to let me choose my own path to get there.

I could never get to where I am today without the example and excitement for the scientific endeavor I have learned from my many teachers and mentors: Vladimir Ivanovich Zenkovich and Demyan Vladimirovich Sinkevich of the Lyceum of the Belarusion State University, Michael Brown and John Boccio of Swarthmore College, Bill Matthaeus of Bartol Research Institute at the University of Delaware, Nat Fisch and Steve Jardin of Princeton Plasma Physics Laboratory (PPPL) and Alan Glasser of Los Alamos National Laboratory. I am particularly thankful to Michael Brown and Bill Matthaeus, who introduced me to the field of plasma physics and its research community, as well as Alan Glasser and Steve Jardin, who have helped me to find my footing and make first strides in computational plasma physics.

During my graduate student career, I have been lucky to have shared an office with three of the brightest young analytical minds in plasma physics today: Ilya Dodin, Andrei Simakov and Nikolai Yampolsky. Their help and patience in our

many discussions on the mathematics of plasma physics cannot be overestimated. An immeasurable contribution to my knowledge and understanding of the topics discussed in this Dissertation has also been made by many of my colleagues – Luis Chacon, Chris Cothran, Nate Ferraro, Alexey Kuritsyn, Nuno Loureiro, Xianzhu Tang and many others, who have kept an open door and an open mind to welcome multiple discussions and debates on these subjects.

It would have been that much harder to get though my years at PPPL without the friendly attitude and bureaucratic expertise of Barbara Sarfaty, who is the one person that keeps the PPPL graduate program running one year to the next. A special "thank you" note also goes to Marg-anne Glasser, who always made me feel welcome in her home during my two-year tenure at and the subsequent visits to Los Alamos, New Mexico.

One does not always fully appreciate the importance of social life outside of the office as a graduate student. Yet, there are many friends who I have to thank for helping me to get through it. First of all, they are my wonderful Princeton housemates, Artem Smirnov and Ty Wilde. They, as well as Daria Babushok, Ilya and Jenya Dodin, Leonid Dorf, Vasya Dostoinov, Nastya Kolendo, Ira and Irina Lindsay, Sophia Moskalenko, Yuri Shubin, Pavel Smyshlyaev, Daria Solodkaia, Vita Verba, and Nikolai and Irina Yampolsky have spent many hours over tea and, sometimes, stronger beverages in conversations on a multitude of topics that have taken my mind off of work and kept me sane all these years. My fellow graduate students in Princeton University Program in Plasma Physics and many others have also made the experience much more than simply academic and I am grateful that I have had a chance to share it with them.

The computations presented in this Dissertation were performed at the National Energy Research Scientific Computing Center and a 92 processor cluster of the Plasma Theory Group, Los Alamos National Laboratory. This work was supported by appointment to the Fusion Energy Sciences Fellowship Program administered by Oak

Ridge Institute for Science and Education under a contract between the U.S. Department of Energy (DOE) and the Oak Ridge Associated Universities, under a National Science Foundation Graduate Research Fellowship, and by the DOE contracts DE-AC02-76-CHO3073 and DE-AC52-06NA25396.

Chapter 1

Introduction

In the last few decades, it has been increasingly recognized that "complexity" and the laws that govern the behavior of complex systems are no less fundamental than those which describe its elementary constituents and the ways in which the constituents interact. In fact, the idea of self-organization, the central concepts in the study of complexity, was first proposed by a cyberneticist, W. Ross Ashby[3], and the field has since consisted of an inter-disciplinary collection of contributions from a wide range of scientific fields – from mathematics, to biology and sociology[71, 103].

Starting with the work by Maxwell, Boltzmann and others in the mid-19th century, physicists began to study the complexity of the collective behavior of a large set of known particles interacting individually via a set of known forces. Statistical mechanics, kinetic theory of gases, solid state physics are all areas of the current physics research rooted in these early works. Likewise, the field of plasma physics concerns itself with describing the behavior of a large set of charged unbound particles (a plasma) interacting microscopically via electro-magnetic forces among themselves and, often, macroscopically with self-generated and externally imposed electric and magnetic fields.

Magnetized plasma is a prototypical complex system in the realm of physics, and self-organization is known to be a very important and often necessary component in the system's evolution (see Sato[130] and references therein). In this Dissertation, we numerically study a two-dimensional helical magnetohydrodynamic (MHD) system that manifestly exhibits self-organization dynamics; and, in detail, the physical process that allows it to take place – magnetic reconnection.

1.1 Magnetic reconnection

The phenomenon of magnetic reconnection, observed under many different conditions, is one of the key physical processes that allow coherent self-organization and relaxation on time-scales faster than the global dissipation time in magnetized plasmas.

What is magnetic reconnection? One could describe it as *local* reconfiguration and annihilation of magnetic field resulting in relaxation of the *global* topology of the magnetic configuration and transfer of the energy stored in the magnetic field into the kinetic and thermal energy of the plasma.

In the ideal MHD approximation of a magnetized plasma, Lorentz force perfectly binds both ions and electrons to magnetic field-lines by assuming the Larmor radii of particles' gyration around the field-lines to be infinitely small. Then, Faraday's law insures that the magnetic field-lines move together with the quasi-neutral plasma – i.e., magnetic field is "frozen" into the plasma fluid when collisional and inertial effects are ignored. As a result, ideal MHD allows no change in the topology of magnetic field immersed in plasma fluid and is therefore incapable of describing the process of magnetic reconnection.

In order to allow the magnetic field to reconnect, dissipative and other physical

processes that become important locally on spatial scales smaller than the system size have to be included in the plasma description. Depending on the magnitude of the ambient magnetic field, surrounding plasma temperature and density, various "non-ideal" effects can become the main mechanism for breaking the magnetic field lines. These include, but are not limited to – collisional resistivity, inertial separation of ion and electron fluids due to their mass density difference, anisotropy due to finite ion and electron Larmor radius effects, and combinations thereof.

Below, we briefly describe what is known to date about the magnetic reconnection phenomenon.

1.1.1 Observations of magnetic reconnection.

In nature, the phenomenon has been directly measured in the solar wind[118], the Earth's magnetotail[105] and magnetopause[54, 148]. There is much evidence that magnetic reconnection is responsible for the generation and evolution of solar flares[92, 101] and coronal mass ejections (CMEs)[91], while it has also been proposed as the mechanism for solar coronal heating[50]. And although presently there is much less astrophysical data available, magnetic reconnection processes have been conjectured to play an important role in heating of the interstellar, intergalactic and intracluster media, acceleration and relaxation of jets, and dynamics of accreting systems[58, 36].

In the laboratory environment, and particularly in toroidal magnetic fusion devices, magnetic reconnection has been identified as one of the most important mechanisms of energy redistribution and magnetic field relaxation[26, 131]. While it often has the destructive effect of ruining the magnetic confinement[59], it has also been proposed as a mechanism that is active in non-inductive coaxial helicity injection current drive[123]. Signatures of magnetic reconnection, such as the formation of a

finite amplitude current sheet which is spatially and temporally correlated with magnetic field reconfiguration and/or plasma heating has also been directly observed in a reversed-field pinch[41], field-reversed configurations(FRC)[38, 106, 140], spheromak interactions[27, 107], and reconnection-focused experiments[39, 48, 56, 158].

The plasma conditions under which reconnection is observed could not be more diverse. In the Earth's magnetotail and plasma sheet, plasma number density n is of order $.1cm^{-3}$, electron (T_e) and ion (T_i) temperatures are of order $100eV$ and $10^3 - 10^4eV$, respectively, magnetic field B outside of the reconnection region is about $10^{-4}G$, and the scale size of the system is about $10^4 - 10^5km$[49]. With these parameters, Debye length is $\lambda_D \approx .1 - 1km$, electron gyroradius is $\rho_e \approx 1 - 10km$, ion gyroradius and ion skin depth are $\rho_i \approx (c/\omega_{pi}) \approx 10^3km$, electron mean free path (mfp) is $\lambda_e \approx 10^{11}km$, and ion mfp is $\lambda_i \approx 10^{15}km$. Under such conditions, essentially no assumptions about the degree of plasma isotropization can be made. Furthermore, because the mfp for both electrons and ions is so much longer than the system size, no obvious mechanism for magnetic energy dissipation is available – magnetic reconnection under these conditions is called *collisionless* reconnection.

On the other hand, the environment of the solar corona, where the solar flares are observed, is distinctly different: $n \approx 10^9 - 10^{11}cm^{-3}$, $T_e \approx T_i \approx 100\ eV$, reconnecting magnetic field $B \approx 10^3G$ and the scale size $L \approx 10^5 - 10^6km$[104]. These give the ion and electron mfp of $\lambda_e \approx \lambda_i \approx 1 - 10km$, which is much less than the system size; and $\rho_e \ll \rho_i \ll (c/\omega_{pi}) \approx 1m$, which implies that while one still has to treat the ion and electron fluids separately (*i.e.* include the *two-fluid effects*), certain degree of plasma isotropization can be assumed. Yet another parameter regime is observed in the solar photosphere, where the solar flare and CME generation is presumed to take

place. There, plasma number density is about $10^{14} cm^{-3}$ and $T_i \approx T_e \approx 1eV$[104], which implies that $\lambda_e \approx \lambda_i \approx 10^{-2} - 10^{-1} cm$. Assuming the magnetic field strength of the emerging flux ropes to be about the same as in the corona, we observe that in the solar photosphere $\lambda_i \sim \rho_i < (c/\omega_{pi}) \ll L$, which implies that the plasma is *collisional* and a single-fluid resistive MHD description may suffice.

In a typical large tokamak plasma, such as the Joint European Torus (JET) tokamak, the system scale is approximately $1 - 5m$, plasma number density $n \approx 1 - 5 * 10^{14} cm^{-3}$, toroidal magnetic field $B \approx 10^4 - 10^5 G$ and plasma temperature varies from $T_e \approx T_i \approx 1 - 5\ keV$ in the tokamak core to near room temperature at the walls[89]. In the tokamak core region, these plasma parameters translate into $\rho_e \approx 2.5 * 10^{-3} cm$, $\rho_i \approx 0.1 cm$, $(c/\omega_{pi}) \approx 1.5 cm$, and $\lambda_e \approx \lambda_i \approx 500 m$, with rising collisionality and falling ion and electron mfp and Larmor radii towards the plasma edge. While strongly anisotropic and collisionless in the direction parallel to the dominant toroidal magnetic field, these parameters show that in the poloidal plane tokamak plasmas are very well bound to the magnetic field. Yet, since $(c/\omega_{pi}) \gg \rho_i \gg \rho_e$, local two-fluid effects should not be ignored and can play an important role in internal reconnection events of the tokamak core.

In addition, we note that unlike the plasmas of Earth's magnetosphere and solar corona and photosphere, magnetic field configuration of a tokamak, particularly an idealized tokamak, is a closed and periodic system. This, in itself, may have important consequences for the dynamics of magnetic reconnection, as we show in Chapter 4 below.

1.1.2 Phenomenology of magnetic reconnection.

Though magnetic reconnection is undoubtedly a three-dimensional (3D) phenomenon, to date, no agreed upon true 3D phenomenological description of magnetic reconnection exists in the community. Since in this work we investigate only two-dimensional (2D) systems, here we limit the discussion to that of 2D magnetic reconnection, as well.

Two phenomenological descriptions of 2D steady-state magnetic reconnection in the resistive MHD limit were proposed early on. One, by Sweet[141] and Parker[115], known as Sweet-Parker reconnection, describes evolution of a long and thin current layer, whose length is of the order of the system size and width is proportional to square root of resistivity. The other, by Petschek[116], proposed a localized reconnection region (Petschek proposed that such localization would be accomplished by slow shocks along the magnetic field separatrices) which would allow for faster plasma inflow and faster reconnection of magnetic field lines. The Sweet-Parker description of resistive reconnection has been confirmed by numerous numerical simulations (for example, see Uzdensky and Kulsrud[147]), however its predicted reconnection rate is too slow for that observed both in space[13] and in laboratory experiments[39, 158].

On the other hand, while there is no experimental or computational evidence of slow shocks emanating from the reconnection region, as proposed by Petschek[116], localization of the reconnection layer appears to be the key to the so-called "fast reconnection", which allows for release of magnetic energy in a period of time consistent with observations[90, 134]. Numerical simulations have confirmed that both of the mechanisms proposed to produce such localization – instability-induced locally enhanced resistivity[95] and two-fluid and/or kinetic effects[13] – lead to fast reconnection[25].

(Presence of ambient "guide" magnetic field appears to somewhat slow down but does not qualitatively change the character of two-fluid reconnection [73, 142].) There is also experimental evidence to support both models[148, 78, 124, 97].

However, despite numerous and primarily numerical publications on the subject, understanding of the fast reconnection phenomenon is still incomplete. In particular, a self-consistent description and understanding of the evolution of the laminar reconnection layer in the two-fluid regime is distinctly lacking. In this work, we attempt to advance the understanding of the fast reconnection phenomenon and its relevance to the self-organization dynamics observed in toroidal magnetic fusion devices.

1.2 Internal kink mode and sawtooth oscillations.

The m=1 internal kink mode has long been considered to be either the direct cause or at least a major component in the dynamics of the so-called sawtooth oscillations in tokamaks (see [67, 98, 149] and references therein). Beginning with linear growth rate calculations for the ideal[28, 129], resistive[37] and visco-resistive [5, 119] internal kink modes (from here on, unless stated otherwise, it will be assumed that m=n=1 mode is being considered), a large body of work exists on the subject.

There is consistent experimental evidence that the internal kink mode and/or some other $m = n = 1$ plasma activity play an important role in the onset of sawtooth oscillations[46, 47, 64, 111, 152]. Its primary manifestations in rotating tokamak plasmas are the appearance of the so-called pre-cursor oscillation in stationary diagnostics with a period corresponding to a single plasma rotation and measurements of perturbations localized to the $q = 1$ rational surface prior to the sawtooth temperature crash itself.

Multiple phenomenological theories with some support from analytical and numerical calculations have been proposed as to how the small m=n=1 island develops and/or couples to the rest of the plasma in such a way that the tokamak core confinement is rapidly lost and temperature crash can occur [7, 16, 17, 45, 46, 69, 79, 80, 85, 88, 120, 150, 159]. These are primarily based on the original complete resistive reconnection model by Kadomtsev[79], where the plasma core is assumed to reconnect out completely, thus leading to the loss of temperature confinement. The two main points of disagreement of the Kadomtsev theory with the experimental observations – loss of confinement on time-scales much faster than resistive Sweet-Parker reconnection and little change in the toroidal current profile relative to that expected from complete reconnection – are what all of the following theories have attempted to remedy. It has been shown that the former could possibly be recovered when the geometric and relevant collisionless effects are included in the analysis. However, with the notable exception of the work by Dubois *et. al.*[45, 46] where onset of kinematic plasma turbulence around an $m = n = 1$ island was proposed to be responsible for both loss of confinement and stabilization of the internal kink at small amplitude, none of the other theories have suggested a mechanism for preventing complete core reconnection in any appreciable fraction of the plasma parameter space in which sawtooth oscillations are observed.

A number of numerical simulations of the internal kink mode and sawtooth oscillations with various degrees of sophistication, physical models and simplifying assumptions have also been conducted in the attempts to understand the experimentally observed sawtooth dynamics [4, 5, 6, 18, 44, 112, 114, 127, 143, 145, 146, 160, 161].

These fall into two categories: (1) resistive and two-fluid simulations of a single internal kink reconnection event from a somewhat arbitrary ideally unstable initial condition; and (2) resistive long-term sawtooth simulations in 2D and 3D, including toroidal effects, anisotropic heat conduction, resistive plasma heating and temperature dependent Spitzer resistivity. Simulations in the first category have been able to demonstrate that fast reconnection might account for the observed sawtooth crash rates by including various two-fluid effects – Biskamp *et.al.*[14, 17], Aydemir[6], Rogers and Zakharov [127], Zhukov[160, 161] by including electron inertia and the Hall term $[(d_i/ne) * (J \times B - \nabla p_e)]$, and Aydemir[5], Rogers and Zakharov[127], and Zhukov[161] by including electron viscosity in place of the resistive dissipation. Furthermore, Biskamp and Sato[18] have shown that strong diamagnetic rotation can also stabilize the internal kink mode in the two-fluid regime resulting in partial reconnection of the plasma core. (The conditions for that to happen require large equilibrium density gradients within the $q = 1$ surface, which are not generally expected to be there.) However, simulations in the second category have consistently predicted complete Kadomtsev reconnection sawteeth with crash times too long relative to the experimental measurements [4, 44, 114, 143, 146]. There is also no computational confirmation of the Dubois kinematic theory[45, 46] described above.

Thus, no coherent conclusion on the role of the internal kink mode in the sawtooth cycle has been achieved to date. Two review papers by Migliuolo[98] and Hastie[67] and several of the latest publications[7, 18, 111, 161] summarize the extent of the present understanding of the internal kink mode dynamics and its role in the tokamak sawtooth oscillations.

In this work, we do not attempt to fully resolve the relationship between the

observed development of the internal kink mode and sawtooth oscillations. If the present state of understanding is to be a guide, such an attempt would require a full 3D toroidal simulation that allows for non-linear coupling between multiple helical modes and a possibility of kinetic extensions appropriate to highly collision-less plasmas that exist in the hot tokamak core, both of which are beyond the scope of this work. Instead, we attempt to characterize the evolution of the internal kink mode and investigate the possibility of sawtooth generation in 2D helical geometry (i.e. without 3D mode coupling) within a minimal model that allows for self-organization of a magnetized screw-pinch[51]. These studies are done both within the single-fluid visco-resistive and the two-fluid incompressible models, thus, for the first time, evaluating some of the effects of fast two-fluid reconnection on sawtooth dynamics.

1.3 Numerical methods.

The main numerical tool with which we achieve the above described goals is the new adaptive parallel spectral element macroscopic modeling code SEL[61]. SEL employs an adaptive implicit time-stepping and adaptive grid techniques with high order C^0 spectral element representation[70, 82] of the quantities being evolved in time. These allow for efficient and precise modeling of systems with disparate spatial and temporal scales, including those with dispersive waves which are characteristic of the two-fluid MHD systems.

The code is capable of following very sharp features of the solution in time by concentrating the grid where necessary using the harmonic grid generation techniques[93]. And the adaptive time-step used by the code is limited only by the non-linear dynamics of observable changes to the solution. The general flux-source formulation of

partial differential equations (PDEs) that can be solved by and the modular structure of the code also allow for a large variety of physical systems to be studied with SEL without any modifications to the core numerical scheme itself. We take extensive advantage of this feature for solving a number of different PDE systems in the simulations described below.

As shown in Chapter 2 below, SEL is non-dissipative and has been thoroughly tested both in linear and non-linear regimes.

1.4 Outline of the Dissertation.

We now briefly outline the content of this Dissertation.

In Chapter 2, we in detail describe the numerical techniques of and both linear and non-linear verification studies conducted with the SEL code. We conclude that its accuracy is more than adequate for the long time-integration of strongly non-linear single and two-fluid MHD simulations it is used for in the later chapters.

In Chapter 3, we qualitatively describe the structure of a reconnection region and then proceed to model a large scale semi-open tearing unstable magnetic field configuration in the visco-resistive, electron and two-fluid (Hall) MHD systems. Well known visco-resistive result – slow Sweet-Parker reconnection through a macroscopic system-size current layer – is reproduced. In electron MHD (EMHD), observed structure and scalings of characteristic quantities of a microscopic EMHD reconnection region are shown to agree with the derived qualitative estimates. Width of the electron current layer is shown to be determined by electron viscosity, *not* electron inertia, and observed electron current layer instability is derived and numerically confirmed to be due to the interaction of electron inertia and frozen-in magnetic field effects,

not Kelvin-Helmholtz instability of the sheared electron flow, as has been suggested previously[18].

In Hall MHD, in the semi-collisional regime, the reconnection region is shown to allow *three* different solutions: large aspect ratio system-size quasi-resistive reconnection region, localized X-point microscopic reconnection region, and an intermittent solution of a plasmoid formation unstable electron current layer embedded within a system-size reconnection region. The intermittent solution that we find to lie in between the quasi-resistive and X-point magnetic reconnection configurations is distinctly different than that recently reported in the literature[33]. Based on these and other reported two-fluid and collisionless particle simulation results, we propose an explanation for the numerically observed structure of a two-fluid reconnection region – 2-scale in the outflow direction and 4-scale in the inflow direction, and a general principle that determines the dynamics, the structure and the rate of magnetic reconnection in both collisional and collisionless systems.

In Chapter 4, we study an internal kink unstable helical screw-pinch system in an incompressible cylindrical tokamak approximation. Ideal and resistive linear and visco-resistive and Hall MHD non-linear simulations of the ideally unstable internal kink mode are shown to reproduce the known asymptotic analytical and previous numerical results. Over a longer time-integration period in driven systems with assumed hollow resistivity profile, sawtooth oscillations and relaxation of the magnetic field configuration is observed. Relying on similar results in simulations of reversed field pinches, clear evidence of self-organization of a tokamak-like magnetic field configuration is identified for the first time. Furthermore, for the first time, simulations of $m = 1$ sawteeth which exhibit incomplete reconnection of the plasma core and

maintain $q < 1$ throughout the cycle are demonstrated.

During both the ideally unstable internal kink and the following sawtooth oscillations, the coupling between the structure of the reconnection region and the global magnetic field configuration is emphasized and shown to play an important role in determining the observed reconnection rates. The results are well understood in the context of the visco-resistive and two-fluid magnetic reconnection simulations described in Chapter 3. In particular, during the sawtooth oscillations, presence of the Hall physics in shown to accelerate the non-linear development of the internal kink mode, while having little effect on the dynamics and time-scales observed during the remainder of a sawtooth cycle.

Finally, in Chapter 5, we conclude with a discussion of the results and future directions of the work described in this Dissertation.

Chapter 2

Numerical Tool

In this chapter we describe the framework of and some of the milestones achieved by the macroscopic modeling code SEL employed for all of the numerical simulations described in this Dissertation. The code has been co-developed by A.H. Glasser of Los Alamos National Laboratory and V.S. Lukin.

2.1 The SEL Framework

2.1.1 Generalized flux-source formulation.

Here, a generalization of the flux-source formulation[61] of a set of partial differential equations (PDEs) is presented. The flux-source form allows for solving a large family of initial and/or boundary value problems describable by appropriate systems of PDEs within the same SEL framework, while only a minimal effort is necessary to add any new system of PDEs to be solved by the code. The generalized formulation described below adds to this capability by allowing for the computation to proceed on a 2D logically rectangular computational domain of arbitrary shape and curvature, thus allowing for adaptive grid re-mapping and a wider variety of physical domain shapes.

Any system of coupled PDEs to be evolved in time by SEL has to be expressible

in the following general flux-source form as some M number of PDEs of M physical variables $\{U^i(\vec{x})\}_{i=1,M}$ (*e.g.* density, magnetic flux, etc.):

$$\left\{ \sum_{i=1,M} A^{ki} \frac{\partial U^i}{\partial t} + \nabla \cdot \vec{F}^k = S^k \right\}_{k=1,M} \tag{2.1.1}$$

$$\vec{F}^k = \vec{F}^k(t, \vec{x}, \{U^i\}_{i=1,M}, \{\nabla_{\vec{x}} U^i\}_{i=1,M})$$

$$S^k = S^k(t, \vec{x}, \{U^i\}_{i=1,M}, \{\nabla_{\vec{x}} U^i\}_{i=1,M}),$$

where $A^{ki} = A^{ki}(\vec{x})$, $\vec{F}^k$, and S^k are arbitrary functions of the given variables and $\vec{x} = (x, y)$ denotes a two-dimensional point vector in the physical metric space $\mathcal{X}$ in which PDEs are expressed. (Such as Cartesian, polar, or helical coordinate systems.) In order to show how this general form is discretized over any logically rectangular domain, we consider a single PDE of the form of Eq. (2.1.1) and therefore drop the superscript k. The extension to any M number of PDEs is straightforward.

In any curvilinear metric space Ξ, an equation of the form of Eq. (2.1.1) can be expressed as:

$$A \frac{\partial U}{\partial t} + \nabla \cdot \vec{F} = S \quad => \quad \mathcal{J} A \frac{\partial U}{\partial t} + \frac{\partial}{\partial \xi^i}(\mathcal{J} \vec{F} \cdot \nabla \xi^i) = \mathcal{J} S, \tag{2.1.2}$$

where $\{\xi^i\} = (\xi, \eta)$ are the coordinates of Ξ in which calculations are performed and $\mathcal{J}(\xi, \eta) \equiv (\hat{z} \cdot \nabla x \times \nabla y)(\hat{z} \cdot \nabla \xi \times \nabla \eta)^{-1}$ is the Jacobian of the transformation from $\mathcal{X}$ to Ξ. (Note, in the equation above and everywhere below we assume the usual Einstein summation convention.) For the time being, we assume that $x = x(\xi, \eta)$ and $y = y(\xi, \eta)$ are known – we come back to this point in Section 2.1.5.

In order to be able to evaluate Eq. (2.1.2), it is necessary to know the coordinate transformation $\nabla \xi^i = (\partial \xi^i / \partial x^j) \nabla x^j$:

$$\nabla \xi = \frac{\partial \xi}{\partial x} \nabla x + \frac{\partial \xi}{\partial y} \nabla y, \quad \nabla \eta = \frac{\partial \eta}{\partial x} \nabla x + \frac{\partial \eta}{\partial y} \nabla y,$$

where expressions $(\partial\xi^i/\partial x^j)$ have to be evaluated in Ξ. In order to do so, we note that

$$\mathcal{J} = \frac{\partial x}{\partial \xi}\frac{\partial y}{\partial \eta} - \frac{\partial x}{\partial \eta}\frac{\partial y}{\partial \xi} = \left[\frac{\partial \xi}{\partial x}\frac{\partial \eta}{\partial y} - \frac{\partial \xi}{\partial y}\frac{\partial \eta}{\partial x}\right]^{-1}.$$

As a demonstration, we find an expression for $(\partial\xi/\partial x)$ as a function of (ξ, η) and $\mathcal{J}$. From

$$\frac{\partial \eta}{\partial \eta} = 1 = \frac{\partial \eta}{\partial x}\frac{\partial x}{\partial \eta} + \frac{\partial \eta}{\partial y}\frac{\partial y}{\partial \eta},$$

we have:

$$\begin{aligned}\frac{\partial \xi}{\partial x} &= \frac{\partial \xi}{\partial x}\left(\frac{\partial \eta}{\partial x}\frac{\partial x}{\partial \eta} + \frac{\partial \eta}{\partial y}\frac{\partial y}{\partial \eta}\right) = \mathcal{J}^{-1}\frac{\partial y}{\partial \eta} + \frac{\partial \eta}{\partial x}\left(\frac{\partial \xi}{\partial x}\frac{\partial x}{\partial \eta} + \frac{\partial \xi}{\partial y}\frac{\partial y}{\partial \eta}\right) \\ &= \mathcal{J}^{-1}\frac{\partial y}{\partial \eta} + \frac{\partial \eta}{\partial x}\frac{\partial \xi}{\partial \eta} = \mathcal{J}^{-1}\frac{\partial y(\xi, \eta)}{\partial \eta}. \end{aligned} \tag{2.1.3}$$

Having the coordinate transformations at hand, the rest of the computations are done in the Ξ metric space. We call Ξ the logical space, as the computational domain in Ξ is a square $(\xi, \eta) \in ([0, 1] \times [0, 1])$ with grid distributed uniformly in ξ and η. A mappings $(\mathcal{M} : \Xi \to \mathcal{X})$ then allows the computational domain in the physical space to have an arbitrary shape and curvature of the grid, as long as its topology can be reproduced by identifying corresponding edges of a structured square grid.

2.1.2 Spatial discretization.

SEL's computational domains are spatially discretized using the method of spectral/(hp) elements[70, 82]. High order spectral element (or similarly finite element) representation combines the flexibility of an adaptable grid that can be shaped to fit any given physical domain and parallelization by domain decomposition with the exponential spatial convergence and low artificial wave dispersion of purely spectral codes. Its basic premise is to have a relatively coarse grid of cells (elements) with separate high order polynomial expansions within each cell. Thus, each basis function of

the overall expansion is identically zero in all but one or at most several neighboring cells. The exact set of basis functions and their coupling across the cell boundaries can vary. Among the codes presently employed or being developed in the extended MHD community, M3D-C1 code[76] uses a set of C^1-continuous finite elements which are constrained to be differentiable as well continuous across the cell boundaries, while NIMROD code[139] uses a set of C^0-continuous finite elements which only guarantee the continuity of the solution, but not of its gradients across the cell boundaries.

The set of basis functions presently implemented in SEL is the C^0-continuous set of spectral elements $\{\Lambda^i\}$ given by Jacobi polynomials[1] (See Figure 2.1), where all but the linear basis functions identically vanish at the cell boundaries. The linear basis functions are the only ones that provide the continuity of the solution and the coupling between the cells in each direction. Representation in ξ and η directions of the logical grid described above is done separately with the complete basis of 2D functions formed by the set of non-zero Cartesian products of two unidirectional basis functions $\alpha^k(\xi,\eta) = \Lambda^i(\xi)\Lambda^j(\eta)$. Any physical variable $U(t, x(\xi,\eta), y(\xi,\eta))$ is expanded in $\alpha^i(\xi,\eta)$ and time-dependent amplitudes $u_i(t)$:

$$
\begin{aligned}
U(t,\vec{x}) &= u_i(t)\alpha^i(\xi,\eta) \\
U_x(t,\vec{x}) &= u_i(t)\left[\frac{\partial\alpha^i}{\partial\xi}\frac{\partial\xi}{\partial x} + \frac{\partial\alpha^i}{\partial\eta}\frac{\partial\eta}{\partial x}\right] \\
U_y(t,\vec{x}) &= u_i(t)\left[\frac{\partial\alpha^i}{\partial\xi}\frac{\partial\xi}{\partial y} + \frac{\partial\alpha^i}{\partial\eta}\frac{\partial\eta}{\partial y}\right].
\end{aligned}
$$

We note that $x(\xi,\eta)$ and $y(\xi,\eta)$ can be represented similarly as:

$$
x(\xi,\eta) = x_i\alpha^i(\xi,\eta), \qquad \frac{\partial x}{\partial\xi} = x_i\frac{\partial\alpha^i}{\partial\xi} \qquad \frac{\partial x}{\partial\eta} = x_i\frac{\partial\alpha^i}{\partial\eta}, \qquad etc.
$$

Thus, if at some time t_0 during a simulation it becomes desirable to move the calculation from a grid in the physical space represented by a mapping ($\mathcal{M} : \Xi \to \mathcal{X}$) to

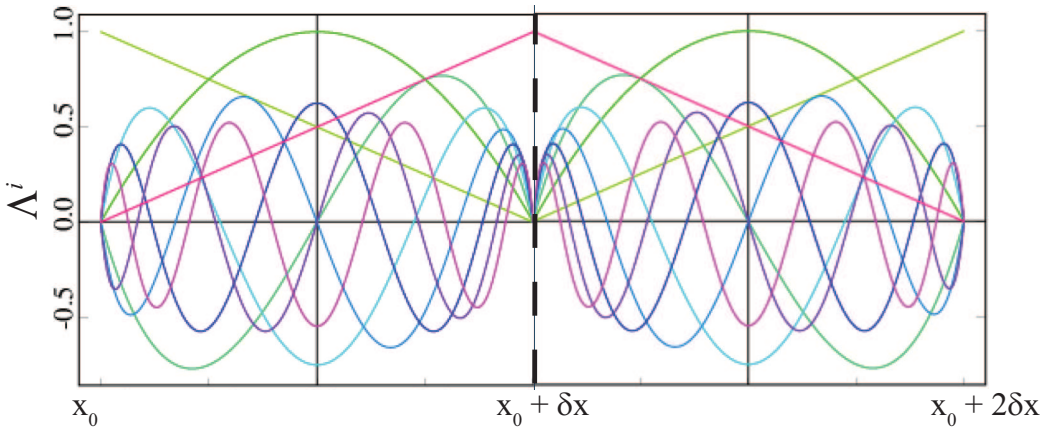

Figure 2.1: A one-dimensional illustration of spectral element basis functions Λ^i used in SEL. Shown are two neighboring cells with Jacobi polynomial $\{\Lambda^i\}_{i:0,n_p=8}$ basis functions in each cell: $\Lambda^0 = (1-\bar{x})/2$, $\Lambda^{n_p} = (1+\bar{x})/2$, and $\Lambda^i = (1-\bar{x}^2)P_i^{(1,1)}(\bar{x})$, for $i = 1, n_p - 1$. In these definitions, $\bar{x} \in [-1, 1]$ is renormalized from $x \in [x_0 + n\delta x, x_0 + (n+1)\delta x]$. Note that Λ^{n_p} from a cell on the left is joined with Λ^0 of the cell on the right to form a single basis function to insure continuity, while all other basis functions vanish at $x = x_0 + \delta x$.

a new grid represented by a new mapping ($\mathcal{M}' = \mathcal{L}\mathcal{M} : \Xi \to \mathcal{X}$), where $\mathcal{L}$ is some mapping ($\mathcal{L} : \Xi \to \Xi$); $U(t_0, x, y)$, $x(\xi, \eta)$, and $y(\xi, \eta)$ would all be remapped in the same manner.

Finally, Eq. (2.1.2) can be rewritten as:

$$\begin{aligned} \mathcal{J}A\frac{\partial U}{\partial t} &+ \frac{\partial}{\partial \xi}\left[(\vec{F}\cdot\nabla x)\mathcal{J}\frac{\partial \xi}{\partial x} + (\vec{F}\cdot\nabla y)\mathcal{J}\frac{\partial \xi}{\partial y}\right] \\ &+ \frac{\partial}{\partial \eta}\left[(\vec{F}\cdot\nabla x)\mathcal{J}\frac{\partial \eta}{\partial x} + (\vec{F}\cdot\nabla y)\mathcal{J}\frac{\partial \eta}{\partial y}\right] = \mathcal{J}S. \end{aligned} \tag{2.1.4}$$

Reformulating the equation in the weak form and defining $F_{x^i} \equiv \vec{F}\cdot\nabla x^i$, we have:

$$\begin{aligned} \left\{\mathbb{M}^{ji}\dot{u}_i \equiv (\alpha^j, \mathcal{J}A\alpha^i)\dot{u}_i = \int \mathcal{J}d\xi d\eta \left[S\alpha^j + F_x\left(\frac{\partial \xi}{\partial x}\frac{\partial \alpha^j}{\partial \xi} + \frac{\partial \eta}{\partial x}\frac{\partial \alpha^j}{\partial \eta}\right)\right.\right. \\ \left.\left. + F_y\left(\frac{\partial \xi}{\partial y}\frac{\partial \alpha^j}{\partial \xi} + \frac{\partial \eta}{\partial y}\frac{\partial \alpha^j}{\partial \eta}\right)\right] + boundary \equiv r^j\left(t, \{u_k\}_{k=1,N}\right)\right\}_{j=1,N}, \end{aligned} \tag{2.1.5}$$

where N is the size of the spectral element basis and therefore is the number of degrees of freedom in this time-dependent vector equation.[1]

With the derivation above, we have shown how the generalized flux-source formulation allows for advancing spatially discretized set of PDEs in an arbitrary logically rectangular domain, while the physical equations can be specified in an unrelated coordinate system most convenient for one's particular application. We note that fluxes F_x, F_y and sources S completely specify the physics of any given problem, coordinate transformation maps $x(\xi, \eta)$ and $y(\xi, \eta)$ specify its geometry, and with those as input, Eq. (2.1.5) contains all necessary information about SEL's spatial discretization to have the solution advanced in time. Such separation of physics, geometry and solution algorithm is the key to the structural organization of the SEL code.

2.1.3 Adaptive temporal advance algorithm.

The implicit temporal advance in SEL is generally accomplished by the Newton-Krylov iterative method[61]. However, like the rest of the code, the time-advance module of SEL is designed to be easily modifiable for any number of particular time-discretization schemes. The principle time-dependent equation to be solved is Eq. (2.1.5), which can be written as a vector equation:

$$\mathbb{M}\dot{\mathbf{u}} = \mathbf{r}(t, \mathbf{u}). \tag{2.1.6}$$

Presently, two well known algorithms are implemented to solve Eq. (2.1.6): the Θ-scheme, with an adjustable time-centering parameter θ; and a 2^{nd} order backward differencing formula (BDF2)[8]. Below, we briefly outline each of the time-discretization

[1] For a system of M PDEs on a logical grid with n_x and n_y cells in x- and y-directions, respectively, and polynomial basis expansion up to the n_p-th order, the total number of degrees of freedom is $N = M * n_x * n_y * n_p^2$.

schemes. We then describe the implementation of the Newton-Krylov iterative advance itself and the adaptive time-stepping algorithm.

Θ-scheme:

Equation (2.1.6) is discretized as:

$$\mathbb{M}\left(\frac{\mathbf{u}^{n+1}-\mathbf{u}^{n}}{h}\right)=\theta\mathbf{r}\left(t^{n+1},\mathbf{u}^{n+1}\right)+(1-\theta)\mathbf{r}\left(t^{n},\mathbf{u}^{n}\right), \tag{2.1.7}$$

where $h\equiv\delta t^{n+1}=t^{n+1}-t^{n}$ is the size of the $(n+1)$-st time-step. With $\theta=.5$, the Θ-scheme is known as the Crank-Nicholson method and is an implicit second order non-dissipative time-discretizetion method. Unless stated otherwise, all of the simulation results presented in this Dissertation were computed by advancing PDEs describing appropriate physical systems with the Crank-Nicholson method. However, with θ as a run-time input parameter, both $\theta=0$ explicit and $\theta=1$ first order dissipative implicit methods have been used for purposes of testing the code.

In order to solve Eq. (2.1.7) for $\mathbf{u}^{n+1}$ by Newton's iterations, an initial guess is set to $\mathbf{u}_0^{n+1}\equiv\mathbf{u}^{n}$, the change in the solution being sought is denoted by $\delta\mathbf{u}_i\equiv\mathbf{u}_{i+1}^{n+1}-\mathbf{u}_i^{n+1}$, the residual $\mathbf{R}$ is defined as

$$\mathbf{R}\left(\mathbf{u}_i^{n+1}\right)\equiv\mathbb{M}\delta\mathbf{u}_i-h\left[\theta\mathbf{r}\left(t^{n+1},\mathbf{u}_i^{n+1}\right)+(1-\theta)\mathbf{r}\left(t^{n},\mathbf{u}^{n}\right)\right]\rightarrow 0, \tag{2.1.8}$$

and the Jacobian of the iteration is defined as

$$\mathbb{J}^{ij}\equiv\mathbb{M}^{ij}-h\theta\left\{\frac{\partial r^{i}}{\partial u_j}\right\}_{t=t^{n+1},\mathbf{u}=\mathbf{u}^{n}}. \tag{2.1.9}$$

BDF2 scheme:

Equation (2.1.6) is discretized as:

$$\mathbb{M}\left(\frac{\mathbf{u}^{n+1}-a\mathbf{u}^{n}+b\mathbf{u}^{n-1}}{h}\right)=\mathbf{r}^{n+1}, \tag{2.1.10}$$

where

$$a \equiv \frac{\left(\delta t^n + \delta t^{n+1}\right)^2}{\delta t^n \left(\delta t^n + 2\delta t^{n+1}\right)},$$

$$b \equiv \frac{\left(\delta t^{n+1}\right)^2}{\delta t^n \left(\delta t^n + 2\delta t^{n+1}\right)},$$

$$h \equiv \frac{\delta t^{n+1}\left(\delta t^n + \delta t^{n+1}\right)}{\left(\delta t^n + 2\delta t^{n+1}\right)},$$

$\delta t^n = t^n - t^{n-1}$, and $\delta t^{n+1} = t^{n+1} - t^n$. Here, an initial guess is set to $\mathbf{u}_0^{n+1} \equiv a\mathbf{u}^n - b\mathbf{u}^{n-1}$, change in the solution is again $\delta\mathbf{u}_i \equiv \mathbf{u}_{i+1}^{n+1} - \mathbf{u}_i^{n+1}$, the residual is defined as

$$\mathbf{R}\left(\mathbf{u}_i^{n+1}\right) \equiv \mathbb{M}\delta\mathbf{u}_i - h\mathbf{r}\left(t^{n+1}, \mathbf{u}_i^{n+1}\right) \to 0, \tag{2.1.11}$$

and the Jacobian of the iteration is

$$\mathbb{J}^{ij} \equiv \mathbb{M}^{ij} - h\left\{\frac{\partial r^i}{\partial u_j}\right\}_{t=t^{n+1},\mathbf{u}=\mathbf{u}^n}. \tag{2.1.12}$$

Like Crank-Nicholson, BDF2 is also a second order time-discretization method. However, straightforward analysis of Equation (2.1.10) demonstrates that BDF2 damps high time-frequency modes of the solution, thus providing numerical dissipation in the algorithm. When using the BDF2 scheme, we resolve the issue of the first time-step by making the first time-step with the Θ-scheme, and then taking the initial condition and the first time-step as the $(n-1)$-st and the n-th values of $\mathbf{u}$, respectively. We also note that Eqs. (2.1.10)-(2.1.12) explicitly allow for $\delta t^{n+1} \neq \delta t^n$, which is necessary to have an adaptive time-stepping algorithm.

Using either of the time-discretization schemes described above, time advance is accomplished by iterating on:

$$\mathbf{R}_i + \mathbb{J}\delta\mathbf{u}_i = 0 \quad \to \quad \delta\mathbf{u}_i = -\mathbb{J}^{-1}\mathbf{R}_i \quad \to \quad \mathbf{u}_{i+1}^{n+1} = \mathbf{u}_i^{n+1} + \delta\mathbf{u}_i, (i \Rightarrow i+1) \tag{2.1.13}$$

until the condition $\mathfrak{N}(\mathbf{R}_i) \leq n_{tol}$ is satisfied, where $\mathfrak{N}$ is the $\mathbb{L}^2$ norm of $\mathbf{R}_i$ normalized to $\mathbf{R}_0$ and n_{tol} is a run-time input parameter determining the tolerance of the Newton iteration convergence. Once the Newton iteration has converged, the solution vector is advanced by setting $\mathbf{u}^{n+1} = \mathbf{u}_{i+1}^{n+1}$.

The above Newton iteration procedure includes a non-trivial step of solving the matrix $\mathbb{J}$, which is an $N \times N$ sparse matrix, where N is the total number of degrees of freedom. In fact, $\mathbb{J}$ describes the exact coupling between each of the degrees of freedom at time $t = t^n$. However, due to the C^0 nature of the basis functions employed in SEL (see discussion in Sec. 2.1.2), only "skeletons" representing the linear basis functions (linear in at least one direction) within each cell are coupled to each other across the cell boundaries. The so-called static condensation procedure[70, 82] allows to separate the skeletons from the interiors of the cells and use separate local solves for each of the cell's interiors[61]. By doing so, static condensation both greatly reduces the size of the global matrix to be solved and significantly improves the parallel efficiency of the code. We note that in order to enable the static condensation algorithm, the matrix $\{\partial r^i/\partial u_j\}$ involved in calculating $\mathbb{J}$ in both Eq. (2.1.9) and Eq. (2.1.12) has to be calculated explicitly by taking derivatives of Eq. (2.1.5) with respect to all degrees of freedom in the system. This is accomplished by specifying the analytical derivatives of the fluxes F_x, F_y and sources S with respect to the evolved physical variables U and their gradient components U_x and U_y. Though somewhat time-consuming both in coding and operation of SEL, this method allows for much greater accuracy of the time-advance algorithm.

The remaining global matrix is solved in parallel using the PETSc libraries[117] with the linear solvers available and appropriate for any given problem. Choice of

any particular solver, such as direct LU factorization or the Generalized Minimal Residual (GMRES) method is made at run-time and requires no modifications to the code. Local solves are accomplished with LAPACK routines.

We now return to Equation (2.1.13) and consider what happens if a time step δt^{n+1} taken in Eq. (2.1.7) for Θ-scheme or in Eq. (2.1.10) for BDF2 is either unnecessarily small, so that Newton iterations converge *too quickly*, or so large that *too many* iterations are necessary for convergence. Run time input parameters $newt_{max}$ and $newt_{min}$ define those limits for each particular simulation run. The automatic adaptivity of the time-step is accomplished by decreasing δt^{n+1} by some fraction $f_{decr} < 1$ and recalculating the Jacobian whenever Eq. (2.1.13) has not converged after $newt_{max}$ Newton iterations. Conversely, δt^{n+1} is set to $\delta t^{n+1} = f_{incr}\delta t^n$, $f_{incr} > 1$, whenever the Newton iterations of the previous time-step converged in less than $newt_{min}$ number of iterations. For iterative linear solvers such as GMRES, the number of GMRES iterations can be an additional factor in determining whether or not to increase/decrease the time step. As shown elsewhere in this Dissertation, this simple algorithm has proven to be very robust and useful in modeling systems that have both long periods of slow and/or linear evolution and bursts of activity with very short non-linear dynamical time-scales.

Additional performance gain has been achieved by re-evaluating the Jacobian $\mathbb{J}$ only during those time-steps when the number of Newton iterations it_N taken during the previous time-step was equal or greater than $newt_{max}$. However, if $newt_{max} > it_N \geq newt_{min}$, the Jacobian matrix used during the previous time-step is re-used

without being re-evaluated. While allowing for significant gain in performance, particularly during quasi-linear periods of evolution in any number of non-linear simulations, this technique does not lead to any deterioration in the accuracy of the computation.

2.1.4 Formulation of boundary conditions.

As indicated in Eq. (2.1.5), formulation of boundary conditions in SEL is integrated into the overall flux-source form. All quantities are advanced in time on the boundary and in the interior of the domain in a single time-step by solving the main system of PDEs in the interior together with a separate system of PDEs describing the boundary conditions on the boundary nodes.

Similarly to the flux-source form of interior PDEs (Eq. (2.1.1)), the most general form of the boundary PDEs is:

$$\left\{ A^{ik} \frac{\partial U^i}{\partial t} + B^{ik} \frac{\partial}{\partial t} \left(\hat{n} \cdot \nabla U^i \right) = S^k \right\}_{k=1,M} \tag{2.1.14}$$

$$S^k = S^k \left(t, \vec{x}, \{U^i\}_{i=1,M}, \{\nabla_{\vec{x}} U^i\}_{i=1,M}, \{\nabla_{\vec{x}\vec{x}} U^i\}_{i=1,M} \right),$$

where $A^{ik} = A^{ik}(\vec{x})$, $B^{ik} = B^{ik}(\vec{x})$, and S^k are arbitrary functions of the given variables and $\hat{n}$ denotes an outward unit vector normal to the boundary of the domain.

However, several special boundary condition options are also available. These are:

- **Periodic boundary condition:** whenever one or more of the physical variables evolved by the code are periodic in any one direction, their values on the right/top boundary are identified with the corresponding values on the left/bottom boundary, while the contribution of the interior PDEs (corresponding to those physical variables) to both boundaries is added together and evaluated in place of the boundary PDEs;

- **Polar "$r = 0$" boundary condition:** whenever the logically rectangular grid is wrapped into a circle in a manner identical to polar coordinates (ξ logical direction is quasi-radial and η-direction is quasi-angular periodic) with no interior boundary in the physical domain, one of the boundaries of the logical domain is shrunk into a point and no explicit boundary conditions can be specified there. For such logical boundary, similarly to the periodic boundary, all boundary nodes are identified with each other and the contribution of the interior PDEs on those nodes is added together and evaluated in place of the boundary PDEs;

- **"Natural" boundary condition:** whenever no explicit physical boundary condition exists for some physical variable, the interior PDE corresponding to that variable is taken to evaluate it at the boundary, as well. In such case, special care has to be taken to partially integrate the flux terms of Eq. (2.1.4) to account for the flux through the boundary of the domain being integrated over.

2.1.5 Adaptive grid generation and static rezoning algorithm.

There is a number of strategies and approaches that have been attempted to enable accurate and efficient grid adaptation for solving initial-value problems with multi-scale spatial behavior. These can be divided into two primary groups:

1. Adaptive mesh refinement (AMR), where parts of the grid with insufficient resolution are refined by effectively subdividing the existing grid cells[9, 10];

2. Dynamic Arbitrary-Lagrangian-Eulerian (ALE) techniques[72, 75, 83] and/or variational principle based harmonic grid generation[22, 23, 87], where an evolving mapping between some logical grid of a fixed size and the physical domain

provides the necessary adaptation by concentrating and rarefying the grid according to some prescribed rules or functionals.

Algorithms that combine the two approaches above are also beginning to be developed[2]. While each of the methods has its advantages and drawbacks in flexibility, accuracy and parallel efficiency, we have chosen to pursue a harmonic grid generation method which appears to be highly accurate, relatively flexible and does not in any way inhibit the parallel efficiency of the SEL code.

We have collaborated with Liseikin[93] in the development of such grid generation algorithm capable of finding an optimal mapping $\mathcal{M}$ between a logical domain Ξ and given physical domain $\mathcal{X}$ with an available directional spatial convergence error estimator $\mathbf{G}(x, y)$. Higher density of the grid in the physical domain results wherever maximum norm $||\mathbf{G}|| \equiv MAX(G^{\xi}, G^{\eta})$ is higher that its average magnitude and lower density wherever $||\mathbf{G}||$ is lower that its average magnitude over the full domain, with additional flexibility introduced by the directional properties of $\mathbf{G}$, as described below. Our approach has been developed in parallel and in consultation with Chacón and Lapenta[34].

Static rezoning

The mesh adaptation algorithm we employ is based upon having an initial mapping $[\mathcal{M} : \Xi \rightarrow \mathcal{X}, x^i(\xi^j)]$ from the logical domain to the physical domain of identical topology but arbitrary shape. Successive computational mesh transformations amount to an evolution of mappings, where the generation of each new mapping is triggered and determined by the spatial discretization error estimator $\mathbf{G}(x, y)$ of the spectral element representation on the logical domain with the existing mapping. (See Figure 2.2 for sample grids having been generated mid-way through highly non-linear

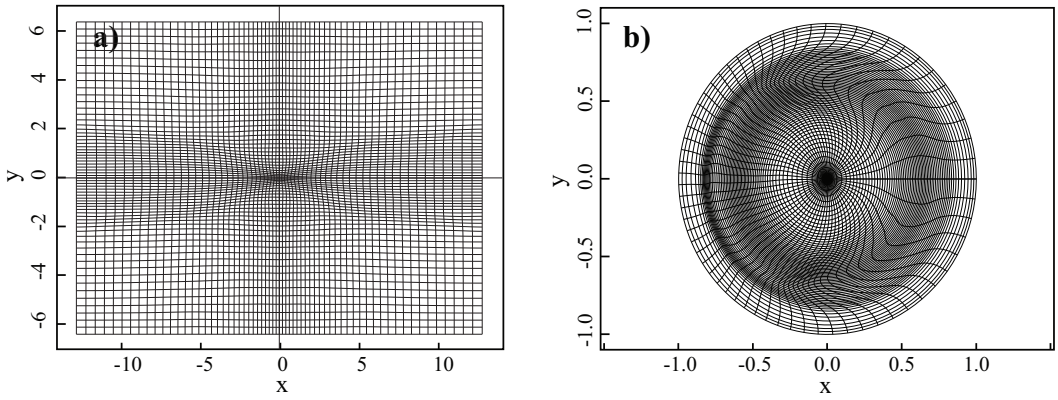

Figure 2.2: Examples of automatically generated 2D mappings from a structured rectangular logical domain (ξ, η) to physical domains of interest (x, y), where high density of the grid indicates regions of the physical domain where the solution required improved resolution.

simulations.) Unlike the ALE approach, where the computational grid is continuously evolved in time together with the physical variables[72], so far we have chosen the so-called static rezoning method, where the main computation is stopped whenever the measure of the overall spatial discretization error Δ_{max}, defined below, exceeds some pre-set limit D_{max}. Then, a new mapping is found, and the solutions are interpolated using the new mapping before the main computation proceeds. This choice has been motivated by the relative simplicity of the implementation and efficiency considerations, alike.[2]

The initial mapping $[\mathcal{M} : \Xi \rightarrow \mathcal{X}, x^i(\xi^j)]$, as well as all of the modified mappings

[2]For a system of M coupled PDEs in two spatial dimensions, introducing ALE grid adaptation means effectively increasing the size of the coupled system of PDEs to be solved for every time step to $M + 2$. For implicit time advance algorithms, that includes solving large sparse matrices as described in Section 2.1.3, where CPU time and memory required to find a solution scale with both the size and the degree of row-to-row coupling of the matrix. Therefore, for systems where necessary local spatial resolution requirements are expected to change slowly relative to the size of an implicit time-step, static regrid is preferable to ALE methods whenever computational and accuracy costs associated with interpolation are small relative to those of the time-advance itself.

$[\tilde{\mathcal{M}} : \tilde{\Xi} \rightarrow \mathcal{X}, x^i(\tilde{\xi}^l)]$ and intermediate interpolation mappings $[\mathcal{L} : \tilde{\Xi} \rightarrow \Xi, \xi^j(\tilde{\xi}^l)]$ are represented on the logical domain by the same basis set of high order spectral elements as the physical variables U. Furthermore, a new mapping is requested whenever spatial convergence error becomes significant, but before it begins to compromise the smoothness of the representation with the existing mapping. Thus, the mapping and interpolation procedures do not compromise the accuracy of the overall computation.

Mesh generation

Each new mapping is generated by solving a set of Beltrami Equations[93] on the whole computational domain:

$$\nabla \cdot \left(\frac{1}{\omega} \frac{\mathfrak{g}}{\sqrt{g}} \cdot \nabla \tilde{\xi}^l \right) = 0, \quad l = 1, 2 \tag{2.1.15}$$

where $\omega(\xi, \eta)$ is a weight function specifying the desired local density of the grid and $\left(\mathfrak{g}(\xi, \eta)/\sqrt{g}\right)$ is a $[2 \times 2]$ symmetric tensor

$$\mathfrak{g} = \begin{pmatrix} g^{11} & g^{12} \\ g^{21} & g^{22} \end{pmatrix}$$

normalized by its determinant g and designed to determine the shape and curvature of the desired grid in the physical space. (Solving Equation (2.1.15) is also equivalent to minimizing a variational

$$\tilde{\mathcal{L}} = \frac{1}{2} \int_{\Omega} \frac{1}{\omega\sqrt{g}} \mathfrak{g} : \nabla \tilde{\xi}^l \nabla \tilde{\xi}^l d\xi^1 d\xi^2,$$

with respect to $\tilde{\xi}^l(\xi^j)$, where integral is taken over the whole logical domain Ω.) We note that in a two-dimensional space any deformation of an infinitesimally small patch of space can be decomposed into three distinct operations: expansion/contraction, area preserving change in aspect ratio, and rotation. In Eqs. (2.1.15) above, $\omega(\xi, \eta)$ is

responsible for expansion/contraction of the grid at $[x(\xi,\eta), y(\xi,\eta)]$, ratio of eigenvalues of $\mathfrak{g}(\xi,\eta)$ is responsible for the elongation at $[x(\xi,\eta), y(\xi,\eta)]$, and the off-diagonal term $g^{12}(\xi,\eta) = g^{21}(\xi,\eta)$ is responsible for rotation of the grid at $[x(\xi,\eta), y(\xi,\eta)]$, relative to the corresponding grid deformations everywhere else in the domain. Since $x^i(\xi^j)$ is known, Eqs. (2.1.15) are formulated to be solved for $\tilde{\xi}^l(\xi^j)$ with the goal of finding an improved mapping $[\tilde{\mathcal{M}} : \tilde{\Xi} \rightarrow \mathcal{X}, x^j(\tilde{\xi}^l)]$. However, in order to find $[\tilde{\mathcal{M}} : \tilde{\Xi} \rightarrow \Xi \rightarrow \mathcal{X}]$, an inverse mapping $\xi^j(\tilde{\xi}^l)$ has to be known instead. It is found by expressing the divergence in Eqs. (2.1.15) in the new $\tilde{\xi}^l$ logical coordinates to derive the following system of two coupled PDEs to be solved for $\xi^j(\tilde{\xi}^l)$:

$$\frac{\partial}{\partial \tilde{\xi}^m}\left(\mathcal{J}\frac{1}{\omega}\frac{g^{ij}}{\sqrt{g}}\frac{\partial \tilde{\xi}^l}{\partial \xi^i}\frac{\partial \tilde{\xi}^m}{\partial \xi^j}\right) = 0, \quad l = 1,2 \tag{2.1.16}$$

where $\mathcal{J} \equiv Det[\partial \xi^j / \partial \tilde{\xi}^l]$ and the derivatives with respect to ξ^j are then inverted as shown in Eq. (2.1.3)[62].

We note that Equations (2.1.16) are already in the flux-source form described in Section 2.1.1 and can be solved by the core SEL algorithm for given functions $\omega(\xi,\eta)$ and $\mathfrak{g}(\xi,\eta)$, where ξ and η are treated as dependent variables.

Spatial convergence error estimator.

Functions $\omega(\xi,\eta)$ and $\mathfrak{g}(\xi,\eta)$ are computed from the directional spatial convergence error estimator $\mathbf{G}(x,y)$ by making direct use of the spectral element representation described above. Since well resolved spectral element representation of a quantity U over the grid has the property that the amplitudes u_m corresponding to high order basis function Λ^m should fall off exponentially with increasing degree of the basis function polynomial[82], monitoring the amplitudes corresponding to the highest order polynomials of a given basis set in each direction relative to the $\mathbb{L}^2$ norm of U,

provides a good measure of spatial convergence. (For U with spectral element representation $U(\xi,\eta) = u_{m,n}\Lambda^m(\xi)\Lambda^n(\eta)$, the $\mathbb{L}^2$ norm of U over a cell Ω_{ij} is defined as $|U|^{ij} \equiv \sqrt{\int_{\Omega_{ij}} U^2(\xi,\eta)d\xi d\eta}$.) Defining the contribution of the highest order polynomial basis function Λ^P in each logical direction as $\delta U_\xi(\xi,\eta) \equiv u_{P,n}\Lambda^P(\xi)\Lambda^n(\eta)$ and $\delta U_\eta(\xi,\eta) \equiv u_{m,P}\Lambda^m(\xi)\Lambda^P(\eta)$, the spatial discretization error of U over Ω_{ij} is defined in each separate direction as

$$\delta U_\xi^{ij} \equiv \frac{\sqrt{\int_{\Omega_{ij}} \delta U_\xi^2(\xi,\eta)d\xi d\eta}}{|U|^{ij}}$$

$$\delta U_\eta^{ij} \equiv \frac{\sqrt{\int_{\Omega_{ij}} \delta U_\eta^2(\xi,\eta)d\xi d\eta}}{|U|^{ij}}.$$

Maximum of the discretization error over all physical variables is taken in order to define two directional and a global spatial discretization error in each (i,j) cell: G_{ij}^ξ, G_{ij}^η, and $\delta_{ij} \equiv MAX(G_{ij}^\xi, G_{ij}^\eta)$. Finally, cell-by-cell step-function approximation $\tilde{\mathbf{G}}$ of the desired directional spatial convergence error estimator $\mathbf{G}$ is given by

$$\begin{aligned} ||\tilde{\mathbf{G}}||_{ij} &\equiv 1 + \alpha\left(\frac{\delta_{ij}}{\Delta_{max}}\right)^p, \\ \tilde{G}_{ij}^\xi &\equiv 1 + \alpha\left(\frac{G_{ij}^\xi}{\Delta_{max}}\right)^p, \\ \tilde{G}_{ij}^\eta &\equiv 1 + \alpha\left(\frac{G_{ij}^\eta}{\Delta_{max}}\right)^p, \end{aligned} \tag{2.1.17}$$

where $\Delta_{max} \equiv MAX(\delta_{ij})$ with maximum taken over all cells of the domain, and α and p are run-time input parameters to be adjusted to optimize adaptivity for each particular application[3]. A continuous and differentiable least squares bicubic spline fit $\mathfrak{F}$ of quantities calculated in Eqs. (2.1.17) is then used to generate C^1 smooth

[3] Common ranges for the grid adaptation input parameters are $\alpha \approx 0.5 - 1.0, p \approx 0.25 - 0.5$.

$\mathbf{G} \equiv \mathfrak{F}(\tilde{\mathbf{G}})$. Functions $\omega(\xi,\eta)$ and $\mathfrak{g}(\xi,\eta)$ necessary to solve the Beltrami harmonic grid generation system of Equations (2.1.16) are found as:

$$\omega = ||\mathbf{G}||_{ij}$$

$$g^{11} = G^{\eta}_{ij}$$

$$g^{22} = G^{\xi}_{ij}$$

$$g^{12} = g^{21} = 0.$$

Note that in the present formulation only two of the three local degrees of freedom afforded by Eq. (2.1.15) were put to use. Other formulations allowing for alignment of the grid lines with or perpendicular to magnetic field lines (see Brackbill[23] and Glasser *et.al.*[62]) or for any other desired properties of the computational grid relative to the solution U at the time of re-mapping make use of the full $\mathfrak{g}$ tensor.

2.2 Code Verification.

Following the development of a new code to be applied to some of the more challenging problems in computational plasma physics, such is SEL, we have considered it a priority to thoroughly verify and validate the accuracy, efficiency and robustness of its numerical techniques and the code as a whole. Below, we describe some of the linear and non-linear verification studies SEL has been subjected to.

2.2.1 Complex linear problems with known analytical solutions in reduced MHD.

There is a number of linear problems SEL has been applied to in order to test its accuracy and efficiency. Linear study of the ideal and resistive internal kink modes

is described in Section 4.2 of this Dissertation and is not reproduced here. There, it is shown that superior accuracy in reproducing both the ideal and resistive growth rates is achieved with the Crank-Nicholson time advance on a strongly non-uniform grid, thus proving the non-dissipative nature of the SEL formulation.

Resistive tearing mode in reduced MHD.

Another problem that has been considered is that of an incompressible resistive tearing mode in an infinite slab with perfectly conducting outer walls. The usual reduced resistive MHD equations

$$\frac{\partial \psi}{\partial t} + \mathbf{v} \cdot \nabla \psi = \eta \nabla^2 \psi$$

$$\frac{\partial \left(\nabla^2 \phi\right)}{\partial t} + \mathbf{v} \cdot \nabla \left(\nabla^2 \phi\right) = \mathbf{B} \cdot \nabla \left(\nabla^2 \psi\right) + \mu \nabla^4 \phi$$

with poloidal magnetic field $\mathbf{B} = \hat{z} \times \nabla \psi$ represented by flux function ψ, poloidal plasma flow $\mathbf{v} = \hat{z} \times \nabla \phi$ represented by stream function ϕ, resistivity η and viscosity μ have been solved in the $[x, y]$ plane.

Reversed magnetic field layer in the form of the Harris current sheet[66] $\psi_0 = \alpha \ln \left[\cosh(y/\alpha)\right]$ of width α and without plasma flow has been taken as the initial equilibrium on a computational domain with periodic boundary conditions in the $\hat{x}$-direction at $x = \pm L$ and perfectly conducting wall boundary conditions – $(\partial \psi / \partial t) = 0$, $\phi = 0$, and $\nabla^2 \phi = 0$ – in the $\hat{y}$-direction at $y = \pm a$. A perturbation of the form $\delta\psi = \epsilon \cos\left[k_x x\right] \exp\left[-(2y/\alpha)^2\right]$, with $\epsilon = 2 * 10^{-7}$ and $k_x \equiv \pi / L$ has been added to the equilibrium at $t = 0$ to initialize the tearing mode. Additionally, a current source term designed to support the Harris current sheet against resistive decay has been added to the equations above to exactly preserve the initial equilibrium and viscosity μ has been set to zero while studying the linear tearing mode problem.

In the limit of very small resistivity (*i.e.* width of the resistive layer much smaller than the width of the current layer), analytical growth rate γ of an incompressible resistive tearing mode $\psi_1(k_x, y)$ with wave number k_x in an infinitely long current layer described by some magnetic flux function $\psi_0(y)$ is given by a well known general dispersion relation[94]:

$$\Delta' = -\frac{\pi}{8}\gamma^{5/4}\tau_A^{1/2}\tau_R^{3/4}\frac{\Gamma\left(\frac{\hat{\lambda}^{3/2}-1}{4}\right)}{\Gamma\left(\frac{\hat{\lambda}^{3/2}+5}{4}\right)}, \tag{2.2.1}$$

where $\hat{\lambda} \equiv \gamma\tau_A^{2/3}\tau_R^{1/3}$, $\tau_A \equiv 1/(k_x\psi_0''|_{y=0})$ is the poloidal Alfvén time, $\tau_R \equiv (1/\eta)$ is the resistive time and Δ' is a characteristic parameter of the tearing mode theory[57] defined as

$$\Delta' \equiv \left|\frac{\partial(\ln\psi_1)}{\partial y}\right|_{y=0^-}^{y=0^+}$$

and found as the solution to the following equation:

$$\psi_0\left(\frac{\partial^2\psi_1}{\partial y^2} - k_x^2 * \psi_1\right) = \frac{\partial^2\psi_0}{\partial y^2} * \psi_1, \tag{2.2.2}$$

subject to appropriate boundary conditions on ψ_1 as $y \to \pm\infty$.

It can be shown[94], that for the Harris equilibrium $\psi_0(y)$ specified above and $\lim_{y\to\pm\infty}\psi_1 = 0$, the Δ' parameter is given by

$$\Delta'_\infty = \frac{2}{\alpha}\left(\frac{1}{\alpha k_x} - \alpha k_x\right)$$

However, in order to directly compare the results of the numerical simulations to the analytical growth rates given by Eq. (2.2.1), Eq. (2.2.2) has to be solved and appropriate expression for Δ' has to be found when $\psi_1(k_x, y)$ vanishes at $y = \pm a$, as prescribed by the specified above boundary conditions of the simulations. Fortunately,

an analytic expression for such Δ' also exists and is given by[4]:

$$\Delta'_a = \frac{2}{\alpha}\left(\frac{1}{\alpha k_x} - \alpha k_x\right)\frac{\alpha k_x - \tanh(a/\alpha)\tanh(ak_x)}{\alpha k_x \tanh(ak_x) - \tanh(a/\alpha)}.$$

The growth rates γ_c of the tearing modes for varying values of η, $L = \pi/k_x$, α and a obtained from the SEL simulations are summarized and compared to the analytically predicted values γ_a given by Eq. (2.2.1) in Table 2.1. Also given, are the corresponding growth rates γ_∞ obtained from Eq. (2.2.1) for the case of $a \to \infty$. Though SEL simulations were fully non-linear by design and it was only possible to extract the linear growth rate γ_c due to the smallness of the initial perturbation, remarkable agreement of better than 1% with the analytically predicted growth rate γ_a is evident for all simulation runs with $\eta = 1. * 10^{-6}$. However, for $\eta \geq 1. * 10^{-4}$, the computed growth rates are observed to be 5-10% lower than the analytically predicted ones. In light of the superior agreement for smaller η, the observed lower growth rates are attributed to the breakdown of the asymptotic approximation of the resistive width being much much smaller than α. We also note that for $L/a \gtrsim 2$, the stabilizing effect of the ideal wall at $y = \pm a$ is at least as strong as that of the finite width of the resistive layer and is well captured by the SEL results. We therefore conclude that SEL captures the growth rate of the resistive tearing mode as well (or better) as one could hope.

2.2.2 Formulation and linear wave tests in Extended MHD.

The following set of Extended MHD equations represents one of the most complex sets of coupled non-linear PDEs that has been coded into SEL to date.

$$\frac{\partial n}{\partial t} + \nabla \cdot (n\mathbf{v}_e) = 0 \tag{2.2.3}$$

[4]The analytic expression was found using the Mathematica 5.2 software package.

α	η	L	a	γ_c	γ_a	γ_∞
1.	$1.*10^{-6}$	12	6	$3.38*10^{-4}$	$3.38*10^{-4}$	$3.80*10^{-4}$
1.	$1.*10^{-6}$	16	6	$3.45*10^{-4}$	$3.47*10^{-4}$	$4.32*10^{-4}$
1.	$1.*10^{-6}$	24	6	$3.29*10^{-4}$	$3.32*10^{-4}$	$5.03*10^{-4}$
1.	$1.*10^{-6}$	32	6	$3.08*10^{-4}$	$3.09*10^{-4}$	$5.49*10^{-4}$
1.	$1.*10^{-6}$	32	12	$4.67*10^{-4}$	$4.66*10^{-4}$	$5.49*10^{-4}$
1.	$1.*10^{-6}$	32	18	$5.20*10^{-4}$	$5.23*10^{-4}$	$5.49*10^{-4}$
1.	$1.*10^{-6}$	32	24	$5.41*10^{-4}$	$5.41*10^{-4}$	$5.49*10^{-4}$
1.	$1.*10^{-6}$	128	24	$4.43*10^{-4}$	$4.45*10^{-4}$	$5.83*10^{-4}$
1.	$1.*10^{-4}$	4	5	$1.73*10^{-3}$	$1.92*10^{-3}$	$1.93*10^{-3}$
1.	$1.*10^{-4}$	12	5	$4.46*10^{-3}$	$4.62*10^{-3}$	$5.49*10^{-3}$
0.5	$1.*10^{-4}$	8/3	5	$9.19*10^{-3}$	$9.84*10^{-3}$	$9.84*10^{-3}$
0.5	$1.*10^{-4}$	4	5	$1.30*10^{-2}$	$1.36*10^{-2}$	$1.37*10^{-2}$
0.5	$1.*10^{-4}$	8	5	$1.61*10^{-2}$	$1.66*10^{-2}$	$1.71*10^{-2}$
0.25	$1.*10^{-4}$	8/3	5	$4.36*10^{-2}$	$4.55*10^{-2}$	$4.55*10^{-2}$
0.5	$2.5*10^{-4}$	8/3	5	$1.54*10^{-2}$	$1.69*10^{-2}$	$1.69*10^{-2}$
0.5	$2.5*10^{-4}$	4	5	$2.16*10^{-2}$	$2.30*10^{-2}$	$2.30*10^{-2}$
0.5	$2.5*10^{-4}$	8	5	$2.57*10^{-2}$	$2.65*10^{-2}$	$2.73*10^{-2}$
0.5	$2.5*10^{-4}$	12	5	$2.38*10^{-2}$	$2.47*10^{-2}$	$2.66*10^{-2}$
0.5	$2.5*10^{-4}$	18	5	$2.02*10^{-2}$	$2.12*10^{-2}$	$2.39*10^{-2}$
0.5	$2.5*10^{-4}$	24	5	$1.74*10^{-2}$	$1.85*10^{-2}$	$2.14*10^{-2}$

Table 2.1: Computed growth rates γ_c of the resistive tearing mode for varying values of the equilibrium current layer width α, resistivity η, half-wavelength of the mode L and half-width of the mode a obtained from the SEL simulations and compared to the analytically predicted values γ_a and γ_∞ for a mode of half-width a and infinite width, respectively.

$$\begin{aligned}\frac{\partial(n\mathbf{v}_i)}{\partial t} &+ \nabla\cdot\left(n\mathbf{v}_i\mathbf{v}_i+\Pi^i\right)=-\frac{1}{m_i}\nabla p_i+\frac{e}{m_i}\left(n\mathbf{E}+\frac{n\mathbf{v}_i\times\mathbf{B}}{c}\right)\\ &- en\frac{\mathbf{J}}{m_i\sigma}+\frac{.71n}{m_i}\left[\nabla\left(\frac{p_e}{n}\right)\cdot\hat{b}\right]\hat{b}\end{aligned}\tag{2.2.4}$$

$$\begin{aligned}\frac{\partial(n\mathbf{v}_e)}{\partial t} &+ \nabla\cdot\left(n\mathbf{v}_e\mathbf{v}_e+\Pi^e\right)=-\frac{1}{m_e}\nabla p_e-\frac{e}{m_e}\left(n\mathbf{E}+\frac{n\mathbf{v}_e\times\mathbf{B}}{c}\right)\\ &+ en\frac{\mathbf{J}}{m_e\sigma}-\frac{.71n}{m_e}\left[\nabla\left(\frac{p_e}{n}\right)\cdot\hat{b}\right]\hat{b}\end{aligned}\tag{2.2.5}$$

$$\begin{aligned}\frac{3}{2}\frac{\partial p_i}{\partial t} &+ \nabla\cdot\left\{\frac{3}{2}p_i\mathbf{v}_i-3.9\frac{p_i\tau_i}{m_i}\left[\nabla\left(\frac{p_i}{n}\right)\cdot\hat{b}\right]\hat{b}\right\}\\ &= -p_i\nabla\cdot\mathbf{v}_i-m_i\Pi^i:\nabla\mathbf{v}_i+\frac{3m_e}{m_i\tau_e}(p_e-p_i)\end{aligned}\tag{2.2.6}$$

$$\begin{aligned}\frac{3}{2}\frac{\partial p_e}{\partial t} &+ \nabla\cdot\left\{\frac{3}{2}p_e\mathbf{v}_e+p_e\left[\left(.71(\mathbf{v}_e-\mathbf{v}_i)-3.2\frac{\tau_e}{m_e}\nabla\left(\frac{p_e}{n}\right)\right)\cdot\hat{b}\right]\hat{b}\right\}\\ &= -p_e\nabla\cdot\mathbf{v_e}-m_e\Pi^e:\nabla\mathbf{v}_e+\frac{3m_e}{m_i\tau_e}(p_i-p_e)\\ &- \frac{en}{\sigma}\mathbf{J}\cdot(\mathbf{v}_e-\mathbf{v}_i)+.71n\left[(\mathbf{v}_e-\mathbf{v}_i)\cdot\hat{b}\right]\left[\nabla\left(\frac{p_e}{n}\right)\cdot\hat{b}\right]\end{aligned}\tag{2.2.7}$$

$$\nabla^2\phi=0\tag{2.2.8}$$

$$\nabla^2\mathbf{A}-\nabla(\nabla\cdot\mathbf{A})=\frac{4\pi ne}{c}(\mathbf{v}_e-\mathbf{v}_i)=-\frac{4\pi}{c}\mathbf{J}\tag{2.2.9}$$

$$\mathbf{E}=-\frac{1}{c}\frac{\partial\mathbf{A}}{\partial t}-\nabla\phi\tag{2.2.10}$$

$$\mathbf{B}=\nabla\times\mathbf{A},\quad \hat{b}\equiv\mathbf{B}/B\tag{2.2.11}$$

$$\Pi^i_\alpha=-.96\frac{p_i\tau_i}{m_i}\left(\nabla v_{i\alpha}+\frac{1}{3}\frac{\partial\mathbf{v}_i}{\partial x_\alpha}\right)\quad \Pi^e_\alpha=-.73\frac{p_e\tau_e}{m_e}\left(\nabla v_{e\alpha}+\frac{1}{3}\frac{\partial\mathbf{v}_e}{\partial x_\alpha}\right)$$

where plasma conductivity $\sigma\equiv 1.96ne^2\tau_e/m_e$, electron collision time $\tau_e\equiv 1.1311*10^{22}(p_e^{3/2}/n^{5/2})$sec and ion collision time $\tau_i\equiv 6.8544*10^{23}(p_i^{3/2}/n^{5/2})$sec. The above two-fluid set of equations includes, among other effect, electron inertia, parallel thermal force, anisotropic ion and electron heat conduction, parallel frictional heat flux,

and isotropic ion and electron pressure tensors with corresponding temperature and density dependent coefficients taken to be those derived by Braginskii(1965)[24]. (The Coulomb logarithm Λ is taken to be $\Lambda = 15$ in deriving the numerical values given above.)

Choice of gauge

The particular choice of a gauge made in deriving Eqs. (2.2.8-2.2.9) above, was assumed in order to be able to exclude from the system one of the dependent variables, namely ϕ, in solving problems where no external electric field is applied at the boundaries of the computational domain. Below, we show how Eqs. (2.2.8-2.2.9) are derived from the Maxwell equations and the definitions of $\mathbf{E}, \mathbf{B}$ in terms of $\mathbf{A}, \phi$ in Eqs. (2.2.10-2.2.11), given an appropriate choice of a gauge.

Assume the following form of Maxwell equations:

$$\nabla \cdot \mathbf{E} = 4\pi\rho \tag{2.2.12}$$

$$\nabla \cdot \mathbf{B} = 0 \tag{2.2.13}$$

$$\nabla \times \mathbf{E} = -\frac{1}{c}\frac{\partial \mathbf{B}}{\partial t} \tag{2.2.14}$$

$$\nabla \times \mathbf{B} = \frac{1}{c}\frac{\partial \mathbf{E}}{\partial t} + \frac{4\pi}{c}\mathbf{J} \tag{2.2.15}$$

In considering phenomena much slower than the speed of light, $(1/c)(\partial \mathbf{E}/\partial t)$ term in Eq. (2.2.15) can be ignored and Eq. (2.2.13) justifies the choice of $\mathbf{B} = \nabla \times \mathbf{A}$.[5] Using Eqs. (2.2.10-2.2.11), we can rewrite Eq. (2.2.12) and Eq. (2.2.15) as:

$$\nabla^2\phi + \frac{1}{c}\frac{\partial(\nabla \cdot \mathbf{A})}{\partial t} = -4\pi\rho$$

[5]Note that the approximation $(\partial \mathbf{E}/\partial t) \ll \mathbf{J}$ in Eq. (2.2.15) leads to the statement of plasma quasi-neutrality $\nabla \cdot \mathbf{J} \approx 0$, which implies that $(\partial\rho/\partial t) \approx 0$. Thus, in MHD, neither charge density nor electric field are explicitly advanced in time, but $\mathbf{E}$-field is calculated from the generalized Ohm's Law and "effective charge density" can then be computed from Eq. (2.2.12).

$$\nabla^2 \mathbf{A} - \nabla(\nabla \cdot \mathbf{A}) = -\frac{4\pi}{c}\mathbf{J}, \tag{2.2.16}$$

where we still have the freedom of transforming $\mathbf{A}$ and ϕ according to:

$$\mathbf{A} \rightarrow \mathbf{A}' = \mathbf{A} + \nabla\Lambda$$

$$\phi \rightarrow \phi' = \phi - \frac{1}{c}\frac{\partial \Lambda}{\partial t}$$

for arbitrary $\Lambda(t, \mathbf{x})$ without modifying $\mathbf{B}$ and $\mathbf{E}$.

We now note that by choosing Λ in such a way as to make $\nabla^2\phi' = 0$, Eqs. (2.2.16) can be rewritten as follows:

$$\begin{aligned}
\nabla^2\left(\phi - \frac{1}{c}\frac{\partial\Lambda}{\partial t}\right) &= \nabla^2\phi' = 0 = \\
&= -\frac{1}{c}\frac{\partial[\nabla\cdot(\mathbf{A}+\nabla\Lambda)]}{\partial t} - 4\pi\rho = -\frac{1}{c}\frac{\partial(\nabla\cdot\mathbf{A}')}{\partial t} - 4\pi\rho \\
&\nabla^2\mathbf{A}' - \nabla(\nabla\cdot\mathbf{A}') = -\frac{4\pi}{c}\mathbf{J}.
\end{aligned}$$

It is these $\mathbf{A}'$ and ϕ' that are the independent variables in Eqs. (2.2.3-2.2.11). Furthermore, we observe that the combination of Eqs. (2.2.4-2.2.5) provide the means to evaluate the "effective charge density" ρ in the plasma.

Energy Conservation

Below, we show that Eqs. (2.2.3-2.2.11) conserve total energy. We define total energy as:

$$\mathcal{E} \equiv \frac{m_i n v_i^2}{2} + \frac{m_e n v_e^2}{2} + \frac{3}{2}p_i + \frac{3}{2}p_e + \frac{B^2}{8\pi}$$

(Note that since $\hat{\mathbf{E}}$ and $\hat{\mathbf{B}}$ are both presumed to be order one and $(E_0/B_0) = (v_A/c) => (E^2/B^2) \approx (v_A/c)^2 \ll 1$, we ignore the $(E^2/8\pi)$ term in the definition of $\mathcal{E}$, which is also consistent with ignoring the displacement current in Eq. (2.2.15).)

From Eqs. (2.2.3-2.2.5), the change in kinetic energy $\mathcal{E}_K \equiv (m_i n v_i^2 + m_e n v_e^2)/2$ is:

$$\begin{aligned}\frac{\partial \mathcal{E}_K}{\partial t} &= -\nabla \cdot \left(\frac{m_i n v_i^2}{2} \mathbf{v}_i + \frac{m_e n v_e^2}{2} \mathbf{v}_e \right) - m_i \mathbf{v}_i \cdot (\nabla \cdot \Pi^i) - m_e \mathbf{v}_e \cdot (\nabla \cdot \Pi^e) \\ &- \mathbf{v}_i \cdot \nabla p_i - \mathbf{v}_e \cdot \nabla p_e - \frac{J^2}{\sigma} + \mathbf{E} \cdot \mathbf{J} + .71 n [\nabla T_e \cdot \hat{b}][(\mathbf{v}_i - \mathbf{v}_e) \cdot \hat{b}].\end{aligned}$$

From Eqs. (2.2.6-2.2.7), the change in thermal energy $\mathcal{E}_T \equiv 3(p_i + p_e)/2$ is:

$$\begin{aligned}\frac{\partial \mathcal{E}_T}{\partial t} &= -\nabla \cdot \left[\frac{3}{2}(p_i \mathbf{v}_i + p_e \mathbf{v}_e) - 3.9 \frac{p_i \tau_i}{m_i} \left(\nabla T_i \cdot \hat{b} \right) \hat{b} - 3.2 \frac{p_e \tau_e}{m_e} \left(\nabla T_e \cdot \hat{b} \right) \hat{b} \right] \\ &- p_i \nabla \cdot \mathbf{v}_i - p_e \nabla \cdot \mathbf{v}_e - m_i \Pi^i : \nabla \mathbf{v}_i - m_e \Pi^e : \nabla \mathbf{v}_e \\ &+ \frac{J^2}{\sigma} + .71 T_e \hat{b} \cdot \nabla [n(\mathbf{v}_i - \mathbf{v}_e) \cdot \hat{b}].\end{aligned}$$

And from Eqs. (2.2.10-2.2.11), the change in magnetic energy $\mathcal{E}_M \equiv B^2/8\pi$ is:

$$\frac{\partial \mathcal{E}_M}{\partial t} = -\frac{c}{4\pi} \mathbf{B} \cdot \nabla \times \mathbf{E}.$$

Finally, putting them all together, we have:

$$\begin{aligned}\frac{\partial \mathcal{E}}{\partial t} &+ \nabla \cdot \left\{ \frac{m_i n v_i^2}{2} \mathbf{v}_i + \frac{m_e n v_e^2}{2} \mathbf{v}_e + \frac{5}{2}(p_i \mathbf{v}_i + p_e \mathbf{v}_e) \right. \\ &+ m_i \mathbf{v}_i \cdot \Pi^i + m_e \mathbf{v}_e \cdot \Pi^e + \frac{c}{4\pi} \mathbf{E} \times \mathbf{B} + .71 p_e \hat{b} \left[(\mathbf{v}_e - \mathbf{v}_i) \cdot \hat{b} \right] \\ &- \left. 3.9 \frac{p_i \tau_i}{m_i} \left(\nabla T_i \cdot \hat{b} \right) \hat{b} - 3.2 \frac{p_e \tau_e}{m_e} \left(\nabla T_e \cdot \hat{b} \right) \hat{b} \right\} = 0,\end{aligned}$$

where

$$\mathcal{F}_K \equiv \frac{m_i n v_i^2}{2} \mathbf{v}_i + \frac{m_e n v_e^2}{2} \mathbf{v}_e,$$

$$\mathcal{F}_T \equiv \frac{5}{2}(p_i \mathbf{v}_i + p_e \mathbf{v}_e),$$

$$\mathcal{F}_M \equiv \frac{c}{4\pi} \mathbf{E} \times \mathbf{B},$$

$$\mathcal{F}_{FH} \equiv m_i \mathbf{v}_i \cdot \Pi^i + m_e \mathbf{v}_e \cdot \Pi^e,$$

$$\mathcal{F}_{HC} \equiv .71 p_e \hat{b} \left[(\mathbf{v}_e - \mathbf{v}_i) \cdot \hat{b} \right] - 3.9 \frac{p_i \tau_i}{m_i} \left(\nabla T_i \cdot \hat{b} \right) \hat{b} - 3.2 \frac{p_e \tau_e}{m_e} \left(\nabla T_e \cdot \hat{b} \right) \hat{b}$$

are kinetic, thermal, electro-magnetic, frictional heat and parallel heat conduction fluxes, respectively.

Normalization and flux-source form

The system of Eqs. (2.2.3-2.2.11) can be normalized by setting $\nabla = (1/L_0)\hat{\nabla}$, $\partial/\partial t = (1/\tau_A)\partial/\partial\hat{t}$, $\mathbf{v}_\alpha = v_A\hat{\mathbf{v}}_\alpha$, where $v_A = L_0/\tau_A$, $n = \bar{n}\hat{n}$, $\mathbf{B} = \bar{B}\hat{\mathbf{B}}$, where $\bar{B} = v_A\sqrt{4\pi m_i\bar{n}}$, $\mathbf{A} = \bar{B}L_0\hat{\mathbf{A}}$, $\mathbf{E} = (\bar{B}v_A/c)\hat{\mathbf{E}}$, $\phi = (\bar{B}v_AL_0/c)\hat{\phi}$, and $p_\alpha = m_i\bar{n}v_A^2\hat{p_\alpha}$.

Dropping hats for normalized quantities, substituting for $\mathbf{E}$ and $\mathbf{B}$ from Eqs. (2.2.10-2.2.11), combining Eq. (2.2.4) and Eq. (2.2.5), and defining $\epsilon \equiv m_e/m_i$, $d_i \equiv (c/\omega_{pi})/L_0 = (cm_i/eL_0\sqrt{4\pi m_i\bar{n}})$, $\kappa_e \equiv \epsilon\tau_A/\tau_e = (2.226 * 10^{10}\bar{n}\tau_A^4/L_0^3)(n^{5/2}/p_e^{3/2})$, and $\kappa_i \equiv \tau_A/\tau_i = (6.7444 * 10^{11}\bar{n}\tau_A^4/L_0^3)(n^{5/2}/p_i^{3/2})$, the normalized Eqs. (2.2.3-2.2.11) are equivalent to:

$$\frac{\partial n}{\partial t} + \nabla\cdot(n\mathbf{v}_e) = 0 \tag{2.2.17}$$

$$\begin{aligned}\frac{\partial(\epsilon n v_{e\alpha} + n v_{i\alpha})}{\partial t} &+ \nabla\cdot\left[(p_i+p_e)\,\hat{\alpha} + n\mathbf{v}_i\frac{n v_{i\alpha}}{n} + \epsilon n\mathbf{v}_e\frac{n v_{e\alpha}}{n} + \Pi^i + \Pi^e\right] \\ &= \frac{n\mathbf{v}_i - n\mathbf{v}_e}{d_i}\cdot\left(\frac{\partial\mathbf{A}}{\partial x_\alpha} - \nabla A_\alpha\right)\end{aligned} \tag{2.2.18}$$

$$\begin{aligned}\frac{\partial(\epsilon n v_{e\alpha} - nA_\alpha/d_i)}{\partial t} &+ \nabla\cdot\left[p_e\hat{\alpha} + \epsilon n\mathbf{v}_e\frac{n v_{e\alpha}}{n} - \frac{1}{d_i}n\mathbf{v}_eA_\alpha + \Pi^e\right] \\ &= \frac{n}{d_i}\frac{\partial\phi}{\partial x_\alpha} - \frac{n\mathbf{v}_e}{d_i}\cdot\frac{\partial\mathbf{A}}{\partial x_\alpha} + \frac{\kappa_e}{1.96}(n v_{i\alpha} - n v_{e\alpha}) \\ &- .71\left[\left(\nabla p_e - \frac{p_e}{n}\nabla n\right)\cdot\hat{b}\right]b_\alpha\end{aligned} \tag{2.2.19}$$

$$\begin{aligned}\frac{3}{2}\frac{\partial p_i}{\partial t} &+ \nabla\cdot\left\{\frac{5}{2}\frac{p_i}{n}n\mathbf{v}_i - \frac{3.9}{\kappa_i}\frac{p_i}{n}\left[\left(\nabla p_i - \frac{p_i}{n}\nabla n\right)\cdot\hat{b}\right]\hat{b}\right\} \\ &= \frac{n\mathbf{v}_i}{n}\cdot\nabla p_i - \frac{1}{n}\Pi^i_\alpha\cdot\left[\nabla(n v_{i\alpha}) - \frac{n v_{i\alpha}}{n}\nabla n\right] + 3\kappa_e(p_e - p_i)\end{aligned} \tag{2.2.20}$$

$$\begin{aligned}\frac{3}{2}\frac{\partial p_e}{\partial t} &+ \nabla\cdot\left\{\frac{5}{2}\frac{p_e}{n}n\mathbf{v}_e - \frac{3.2}{\kappa_e}\frac{p_e}{n}\left[\left(\nabla p_e - \frac{p_e}{n}\nabla n\right)\cdot\hat{b}\right]\hat{b} + .71\frac{p_e}{n}\left[(n\mathbf{v}_e - n\mathbf{v}_i)\cdot\hat{b}\right]\hat{b}\right\} \\ &= \frac{n\mathbf{v}_e}{n}\cdot\nabla p_e + 3\kappa_e(p_i - p_e) - \frac{1}{n}\Pi^e_\alpha\cdot\left[\nabla(n v_{e\alpha}) - \frac{n v_{e\alpha}}{n}\nabla n\right] \\ &+ \frac{\kappa_e}{1.96}\frac{|n\mathbf{v}_e - n\mathbf{v}_i|^2}{n} + \frac{.71}{n}\left[(n\mathbf{v}_e - n\mathbf{v}_i)\cdot\hat{b}\right]\left[\left(\nabla p_e - \frac{p_e}{n}\nabla n\right)\cdot\hat{b}\right]\end{aligned} \tag{2.2.21}$$

$$\nabla^2\phi = 0 \tag{2.2.22}$$

$$\nabla\cdot[\nabla A_\alpha - (\nabla\cdot\mathbf{A})\hat{\alpha}] = \frac{nv_{e\alpha} - nv_{i\alpha}}{d_i}, \tag{2.2.23}$$

where

$$b_\alpha = \epsilon_{\alpha\beta\gamma}\frac{\partial A_\gamma}{\partial x_\beta}\Big/\sqrt{\frac{\partial A_l}{\partial x_m}\frac{\partial A_l}{\partial x_m} - \frac{\partial A_l}{\partial x_m}\frac{\partial A_m}{\partial x_l}}$$

$$\Pi^i_\alpha = -.96\frac{p_i}{n\kappa_i}\left[\nabla(nv_{i\alpha}) - \frac{nv_{i\alpha}}{n}\nabla n + \frac{1}{3}\frac{\partial(n\mathbf{v}_i)}{\partial x_\alpha} - \frac{1}{3}\frac{n\mathbf{v}_i}{n}\frac{\partial n}{\partial x_\alpha}\right]$$

$$\Pi^e_\alpha = -.73\frac{\epsilon p_e}{n\kappa_e}\left[\nabla(nv_{e\alpha}) - \frac{nv_{e\alpha}}{n}\nabla n + \frac{1}{3}\frac{\partial(n\mathbf{v}_e)}{\partial x_\alpha} - \frac{1}{3}\frac{n\mathbf{v}_e}{n}\frac{\partial n}{\partial x_\alpha}\right].$$

In the particular two-fluid extended MHD formulation described in this Section, Equations (2.2.17-2.2.23) represent thirteen equations advanced by SEL in time in order to evolve the following thirteen primary variables: plasma density n, three components of ion momentum $nv_{i\alpha}$, three components of electron momentum $nv_{e\alpha}$, ion pressure p_i, electron pressure p_e, electrostatic potential ϕ, and three components of the vector potential A_α. As presented, the equations are already in the flux-source form required by the code and are therefore coded-in exactly as shown above.

Linearization

In order to conduct linear wave tests of the SEL implementation of Eqs. (2.2.17-2.2.23), the dispersion relation and eigenmodes of the system in a uniform magnetized medium have been found. Eqs. (2.2.17-2.2.23) have been linearized assuming equilibrium of the form: $\mathbf{B}_0 = B_0\hat{x}$ (*i.e.* $\mathbf{A}_0 = A_0 y\hat{z}$), $n_0 > 0$, $p_{i0} = p_{e0} = p_0 > 0$, $\mathbf{v}_{i0} = \mathbf{v}_{e0} = 0$, $\phi = 0$; and the perturbation is of the form: $u_1 = \tilde{u} * exp[i(k_\parallel x + k_\perp y - \Omega t)]$.

Figure 2.3 shows real and imaginary parts of three branches of the dispersion relation derived from linearized Eqs. (2.2.17-2.2.23) for $\bar{n} = 5 * 10^{13}\ cm^{-3}, L_0 = 10\ cm, \tau_A = 4 * 10^{-8}\ sec, n_0 = 1$, and $p_0 = 10^{-4}$, for which the real part ω of

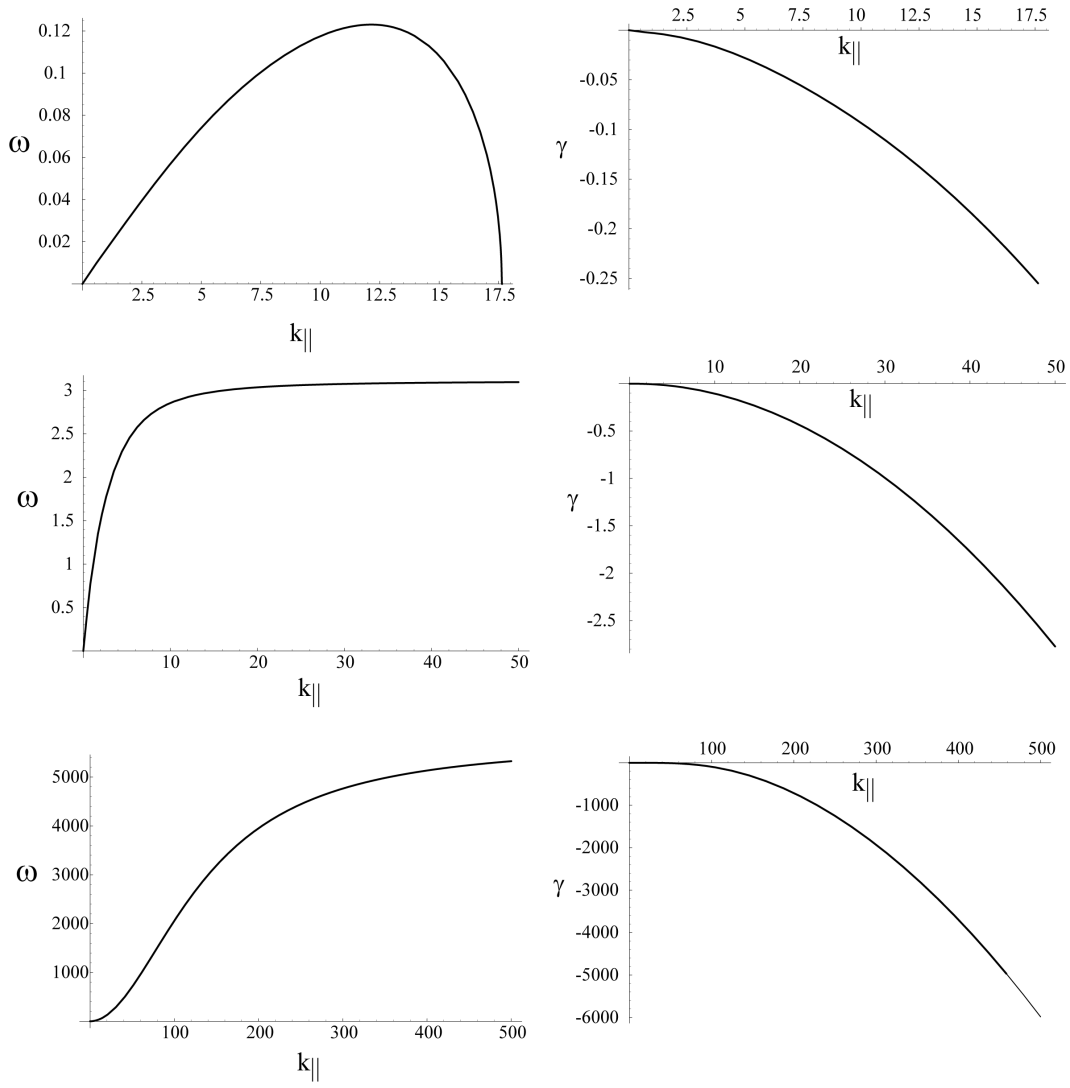

Figure 2.3: Real and imaginary parts of three branches of the dispersion relation derived from linearized Eqs. (2.2.17-2.2.23) for the following parameters: $\bar{n} = 5 * 10^{13}\ cm^{-3}, L_0 = 10\ cm, \tau_A = 4 * 10^{-8}\ sec, n_0 = 1, p_0 = 10^{-4}, B_0 = 1, k_\perp = 1$. Note, the three branches shown are the ones for which the real part ω of $\Omega = \omega + i\gamma$ is positive.

$\Omega = \omega + i\gamma$ is positive. Several things should be noted in Figure 2.3. It is easily observed that for all three waves damping (γ) relatively quickly becomes as large (or larger) as the real part of Ω. However, upon inspecting the dispersion relation with all of the dissipation coefficients "turned off", one can quickly identify the three panels shown in all four figures as the slow magnetosonic (sound) wave, the modified shear Alfven wave and the modified fast magnetosonic (compressional Alfven) waves, from top to bottom, respectively. (Since plasma beta $\beta \equiv 2 * p_0/B_0^2$ is taken to be much smaller than unity, the names given for the waves in parenthesis are in the limit of $\beta \to 0$.)

The "modified" in the names above refers to the dispersion relation modifications due to the two-fluid effects. In particular, the modified shear Alfven wave is observed to asymptote to some ω_{M1} as $k_\parallel \to \infty$, which is explained by the fact that in the two-fluid regime the shear Alfven wave is supported mostly by the motion of ions (not electrons), whose inertia does not allow them to develop ω higher than some ω_{M1}. Similarly, in the two-fluid regime, the compressional Alfven wave is observed to transform into the Whistler wave where $\omega \sim k_\parallel^2$ for $k_\parallel \leq 50$ and also asymptotes to some $\omega_{M2} \gg \omega_{M1}$ as $k_\parallel > \infty$. It is interesting to note that $\omega_{M2}/\omega_{M1} \approx m_i/m_e$, which confirms that the upper limit on the frequency of Whistler waves is set by the effects of electron inertia.[6]

Implementation and Quasi-Linear Test Results

When the system of linearized Eqs. (2.2.17-2.2.23) is solved for Ω in terms of $k_\parallel$, $k_\perp$, B_0, n_0, p_0 and given normalization quantities $L_0, v_A, \bar{n}$, eight non-zero roots are

[6] See the dispersion relation, Eq. 3.3.2, and follow up comments in the investigation of the electron MHD system in Section 3.3 below.

found.[7] Of these, for moderate parameter values, six roots form three pairs of waves with both real and imaginary non-zero parts $\Omega_{1,\ldots,6} = \pm\omega_{1,2,3} - i\gamma_{1,2,3}$ The other two roots have purely negative imaginary roots $\Omega_{7,8} = -i\gamma_{4,5}$ and represent purely decaying perturbations.

In order to test SEL, for each Ω_i, corresponding set of complex eigenmodes is found and coded up as an initial condition with the perturbation amplitude of 10^{-3}. It is important to note that since the full non-linear system of equations is used to compute these linear waves in the code, in order to test the total energy conservation, both the equilibrium and the perturbation must be evolved together as a single quantity for plasma density and pressures, while the uniform equilibrium magnetic field can be added to the Eqs. (2.2.17-2.2.23) and is therefore not a part of the evolved set of variables. The waves are set up in a doubly periodic box $[0, L_x] \times [0, L_y]$, where $L_x = 2\pi/k_{\|}$ and $L_y = 2\pi/k_{\perp}$ on a 6×6 spectral element grid with the 5th order polynomial expansion in each grid cell. Each computation is performed for 20 full wave periods with a fixed time-step $\delta t = (2\pi/\omega)/50$, that is with 50 time-steps per period for a total of 1000 time steps.

The following set of plasma parameters has been chosen for these linear wave tests: $\bar{n} = 5 * 10^{13}\ cm^{-3}, L_0 = 10\ cm, \tau_A = 4 * 10^{-8}\ sec$. The resulting dimensionless parameters are: $d_i = .322$, $\kappa_i = 8.633 * 10^{-8}(n_0^{5/2}/p_0^{3/2})$, $\kappa_e = 2.849 * 10^{-9}(n_0^{5/2}/p_0^{3/2})$. The results of the SEL runs are summarized in Table 2.2, where all of the presented data was produced with $B_0 = 1$, $n_0 = 1$ and $p_0 = 10^{-4}$. Here, only the results for linear modes with non-zero real and imaginary parts of Ω are given. In examining the data shown in Table 2.2, it should be noted that for both sets of parameters, the

[7] The system of equations has no analytical solution and is solved numerically using Mathematica 5 software package.

$k_\parallel$	$k_\perp$	$\Omega = \omega - i\gamma$	$\delta x/L_x$	γ_c	$\delta\mathcal{E}/\mathcal{E}$	it_N	it_K
.1	1	$1.75 * 10^{-3} - i6.51 * 10^{-4}$	$2.21 * 10^{-4}$	$6.17 * 10^{-4}$	$2.5 * 10^{-9}$	1-2	1
		$9.99 * 10^{-2} - i6.46 * 10^{-4}$	$1.31 * 10^{-3}$	$6.37 * 10^{-4}$	$7.0 * 10^{-8}$	2	1
		$1.01 - i8.32 * 10^{-4}$	$1.60 * 10^{-3}$	$8.28 * 10^{-4}$	$3.9 * 10^{-7}$	2-3	1
.1	.1	$1.81 * 10^{-3} - i8.77 * 10^{-5}$	$1.24 * 10^{-3}$	$8.59 * 10^{-5}$	$1.6 * 10^{-9}$	1-2	1
		$9.99 * 10^{-2} - i1.28 * 10^{-5}$	$1.31 * 10^{-3}$	$1.26 * 10^{-5}$	$2.8 * 10^{-9}$	2	1
		$1.42 * 10^{-1} - i1.46 * 10^{-5}$	$1.28 * 10^{-3}$	$1.44 * 10^{-5}$	$4.2 * 10^{-9}$	2	1

Table 2.2: Results from non-linear propagation of eigenmodes of the system of PDEs given by Eqs. (2.2.17-2.2.23) and linearized in uniform magnetized medium. Here, $\delta x/L_x$ is a measure of the phase-shift of a wave over 50 time steps (one analytically calculated wave period); γ_c is the wave damping rate calculated from the magnetic energy decay rate; $\delta\mathcal{E}/\mathcal{E}$ is a ratio of the variation of the total energy to the total energy (minus $B_0^2/2$, where B_0 is not a part of the evolved set of variables); it_N is the number of Newton iterations per time step; and it_K is the number of Krylov iterations per Newton iteration.

first mode has both the slowest real frequency and the greatest γ/ω ratio. In fact, in both cases the ratio is big enough, so that the mode begins to decay non-linearly within the first couple wave periods. Therefore, for those runs, the damping rate was measured at the very beginning of a run.

In all cases, the conservation of total energy is shown to be remarkably good, with energy variation $\delta\mathcal{E}$ being less than $1/10^6$ of total energy and less than 1% of the maximum individual energy variation. With a single calculation of the system's Jacobian required to take all 1000 time-steps and a very low number of both Newton and Krylov iterations per time-step, it is clear that the semi-analytically calculated eigenmodes of the linearized system of Eqs. (2.2.17-2.2.23) are, in fact, also those of the numerical system coded up in SEL. The phase shift $\delta x/L_x$ of the numerically advanced wave is shown to be $\approx 0.1\%$ of the period and numerical damping rate to be within better than 2.5% in all cases except when $\gamma/\omega \sim 1$.

nx	ny	np	δt	it_N	it_K	N_J	Run time (sec)
12	12	5	4.09176e-2	2-3	4-5	1	$6.102 * 10^2$
12	12	5	8.18352e-2	3-4	4-5	1	$6.556 * 10^2$
12	12	5	1.6367e-1	3-4	5	1	$7.286 * 10^2$
12	12	5	3.2734e-1	3-6	5-6	6	$1.144 * 10^3$
12	12	5	6.5468e-1	4-8	5-7	13	$1.665 * 10^3$

Table 2.3: Results from a test of the SEL's implicit Newton-Krylov time-advance algorithm. Linear combination of the system's eigenmodes is propagated for 100 time-steps. [nx,ny,np] is the size of the logical grid; δt is the time step used; it_N and it_K are the number of Newton iterations per time step and Krylov iterations per Newton iteration, respectively; N_J is the number of Jacobian calculations during the run; Run time – total clock-time used by the run, including the start-up and IO.

Thus, we again conclude that the accuracy of the SEL code is more than satisfactory even while advancing a set of equations as complex as Eqs. (2.2.17-2.2.23).

Nonlinear Newton-Krylov Solver Testing

Tests of the efficiency of the implicit Newton-Krylov solver used in SEL have been conducted by means of running the following initial configuration with the Θ-scheme with $\theta = .6$ (see Eq. (2.1.7)), while scanning through several different fixed computational time steps.

The initial configuration consists of the equilibrium quantities: $\bar{n} = 5 * 10^{13}\ cm^{-3}$, $L_0 = 10\ cm$, $\tau_A = 4 * 10^{-8}\ sec$, $n_0 = 1$, $p_0 = 10^{-4}$, $B_0 = 1$, and a perturbation, which is the sum of all three $\omega > 0$ modes computed for that equilibrium with $k_\perp = k_\parallel = 1$ and the perturbation amplitude of $4 * 10^{-2}$ for each of the modes. (That is, the initial condition is $u_{init} = u_{equil} + \epsilon * u_1 + \epsilon * u_2 + \epsilon * u_3$, where $\epsilon = 4 * 10^{-2}$.) All simulations were conducted on 36 processors in a doubly periodic box $[0, 2L_x] \times [0, 2L_y]$, where $L_x = 2\pi/k_\parallel$ and $L_y = 2\pi/k_\perp$, and were run for 100 fixed time steps, independent of the size of the time step.

Table 2.3 presents the results of these scans. There, $\delta t = 4.09176 * 10^{-2}$ used in the top row, is $1/100^{th}$ of the period of the fastest linear wave calculated to exist in the given equilibrium. The Newton iterative solver is considered to have converged when every component of the normalized residual is more than 10^4th times smaller than its value before the first iteration (or is less than 10^{-10}). Similarly, the Krylov solver is considered to have converged when every component of the matrix-vector equation agrees to within 10^{-10} of its initial value. Note that for this initial condition, which includes equal magnitudes of all three waves present in the system, once the time-step becomes appreciable in comparison to the period of the fastest of the waves, that wave is numerically damped within first few time-steps. That is exactly what should be expected of an implicit Θ-scheme with $\theta > 1/2$. The code then proceeds to propagate the remaining wave(s) in a semi-linear fashion.

The benefits of the implicit time-stepping are apparent when comparing the total run times to the sizes of the time-step δt taken. While each next line of Table 2.3 shows a run with its time-step doubled, the total run-time is shown to increase by only $\approx 10 - 45\%$, with the greatest increase coming from the necessity to frequently recalculate the Jacobian matrix due to the increased size of the time-steps.

2.2.3 Study of accuracy and efficiency of the static rezoning algorithm.

We have systematically evaluated the benefits and potential drawbacks of the static rezoning algorithm described in Section 2.1.5 using the reduced MHD systems of equations and somewhat modified tearing mode problem set-up described in Section 2.2.1. In particular, the initial equilibrium has been modified to include reversed flow profile

given by $\phi_0 = M\psi_0 = M\alpha \ln[\cosh(y/\alpha)]$, where M is the Mach number of the equilibrium flow. The following initial condition and plasma parameters were considered: resistivity $\eta = 10^{-4}$, viscosity $\mu = 10^{-4}$, half-period of the perturbed tearing mode $L = 2$, width of the equilibrium current and flow shearing layers $\alpha = .2$, half-distance between the two perfectly conducting walls bounding the current layer $a = .5$, magnitude of the initial perturbation $\epsilon = 10^{-4}$, and Mach number of the equilibrium flow $M = .5$. This problem set-up was also considered by Glasser *et. al.*[61] for initial linear and non-linear testing of the SEL code on a fixed uniform grid.

Several runs of the code with and without adaptive grid capability and with different sizes of the logical grid have been completed. Each time, the code was run with the same pre-fixed time-step size and the same number of time-steps. The final state of the simulations is one of non-linear saturation of the tearing mode with a single large magnetic island occupying most of the domain. Figure 2.4 shows zoomed-in contour plots of the final state of vorticity $\omega = \nabla^2\phi$ and plasma current $j = \nabla^2\psi$ from three different simulation runs. Panels (a,b) show the final state of a simulation conducted on a fixed, uniformly distributed (in physical space) grid of size $[n_\xi, n_\eta, n_p] = [6, 16, 12]$, where n_ξ, n_η, and n_p are number of cells in ξ-direction, number of cells in η-direction, and polynomial order of each cell in each direction of the logical grid, respectively. It is apparent that the uniform grid of the given size does not adequately resolve either the X-point or separatrices around it, as numerical noise is easily observed in the panels (a,b) of Figure 2.4. Panels (c,d) show the final state of a run completed on a smaller logical grid with $[n_\xi, n_\eta, n_p] = [6, 16, 10]$, but with the adaptive grid feature turned on. The initial logical-to-physical grid mapping used in this second run was also uniform. It is easily observed that none of the numerical

noise present in panels (a,b) is there when grid adaptivity is turned on. Panels (e,f) demonstrate the final state of a run completed on a yet smaller logical grid with $[n_\xi, n_\eta, n_p] = [6, 16, 8]$ and the grid adaptivity turned on. Though marginally noisier than panels (c,d), the final state achieved on this smallest adaptive grid is still much cleaner than the one calculated on a fixed uniform grid of more than twice its size.[8]

Time evolution of the measure of the spatial discretization error Δ_{max} defined in Section 2.1.5 is shown in Figure 2.5 for several simulation runs with varied polynomial order n_p but the same number of cells $[n_\xi, n_\eta] = [6, 16]$ of the logical grid. It is shown that the simulation run with fixed uniform grid and $n_p = 12$ has steadily increasing Δ_{max} with the final value significantly exceeding that of the simulations with grid adaptivity enabled. On the other hand, the simulations with adaptive grid and lower n_p value are shown to have significant decreases in Δ_{max} each time the maximum allowed spatial discretization error $D_{max} \approx 1. * 10^{-3} - 1.5 * 10^{-3}$ is reached and a new mapping between the logical and physical spaces is generated.

The code's overall performance improvement due to grid adaptivity has been quantitatively evaluated by defining efficacy ε of the algorithm as $\varepsilon \equiv 1/(\text{cpu time} * \Delta_{max})$, with Δ_{max} taken to be that of the final state. Table 2.4 presents the results for all five simulation runs shown in Figure 2.5. Due to the varied size of the logical grid used in these simulations, a different number of processors was used for different runs. (More processors were used for larger problem sizes.) However, the number of processors for each simulation run was chosen such that the amount of memory used per processor was kept approximately constant at $\approx 40 - 50\%$ of the memory available

[8] Since each cell is expanded in n_p polynomials in each direction, increase from $n_p = 8$ to $n_p = 12$ constitutes an increase of the total number of degrees of freedom in 2.25 times. Furthermore, due to the exponential spatial convergence of the spectral element representation, an actual increase in resolution that comes from increasing n_p is presumed to be significantly greater than that.

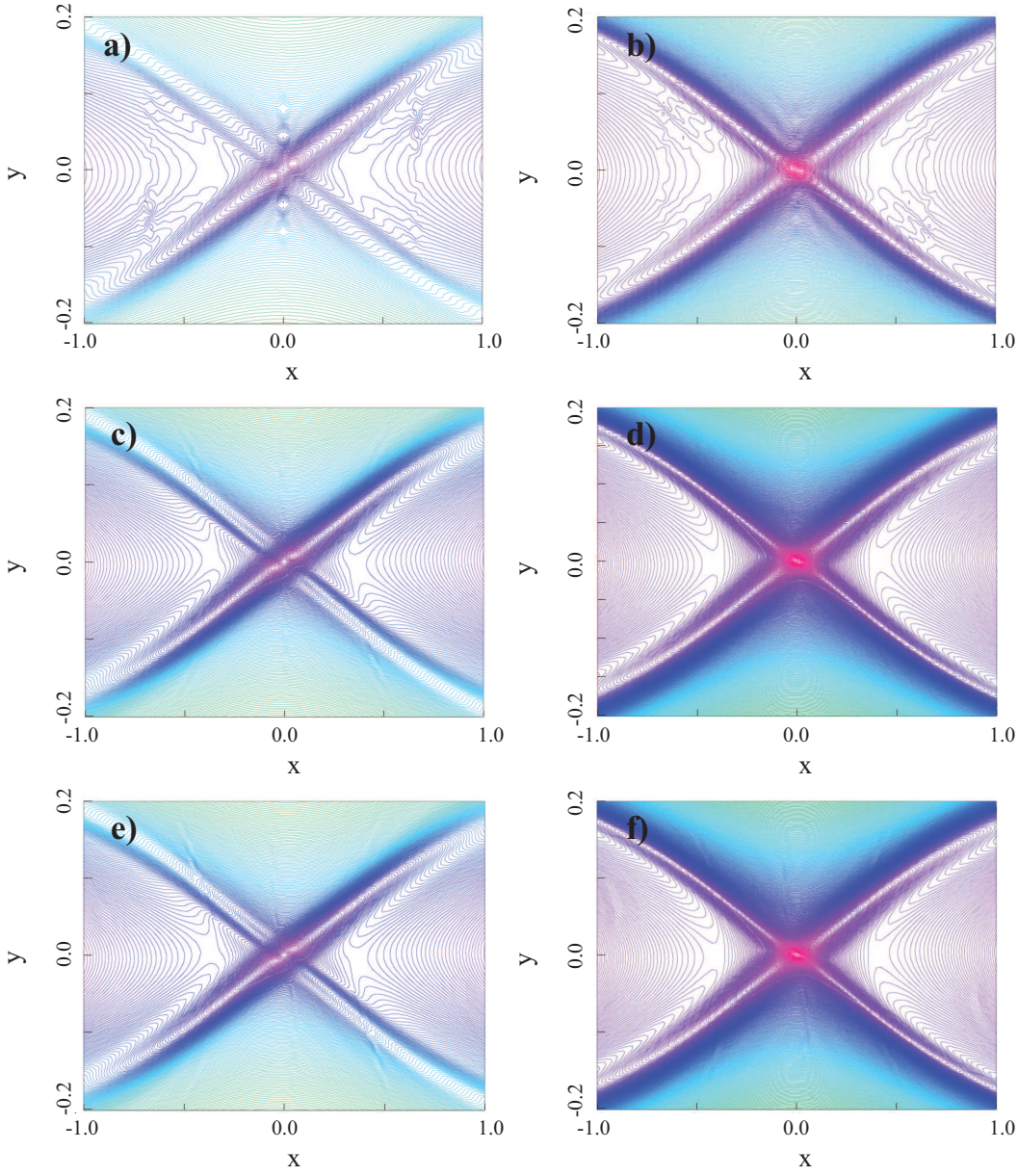

Figure 2.4: Zoomed-in contour plots of the final state of vorticity $\omega = \nabla^2\phi$ (panels a,c,f) and plasma current $j = \nabla^2\psi$ (panels b,d,e) from three simulation runs conducted on logical grids of different size and with/without grid adaptivity are shown. Final state on a fixed, uniform grid with $[n_\xi, n_\eta, n_p] = [6, 16, 12]$ is shown in panels (a,b); final state on adaptive grid with $[n_\xi, n_\eta, n_p] = [6, 16, 10]$ is shown in panels (c,d); and final state on adaptive grid with $[n_\xi, n_\eta, n_p] = [6, 16, 8]$ is shown in panels (e,f).

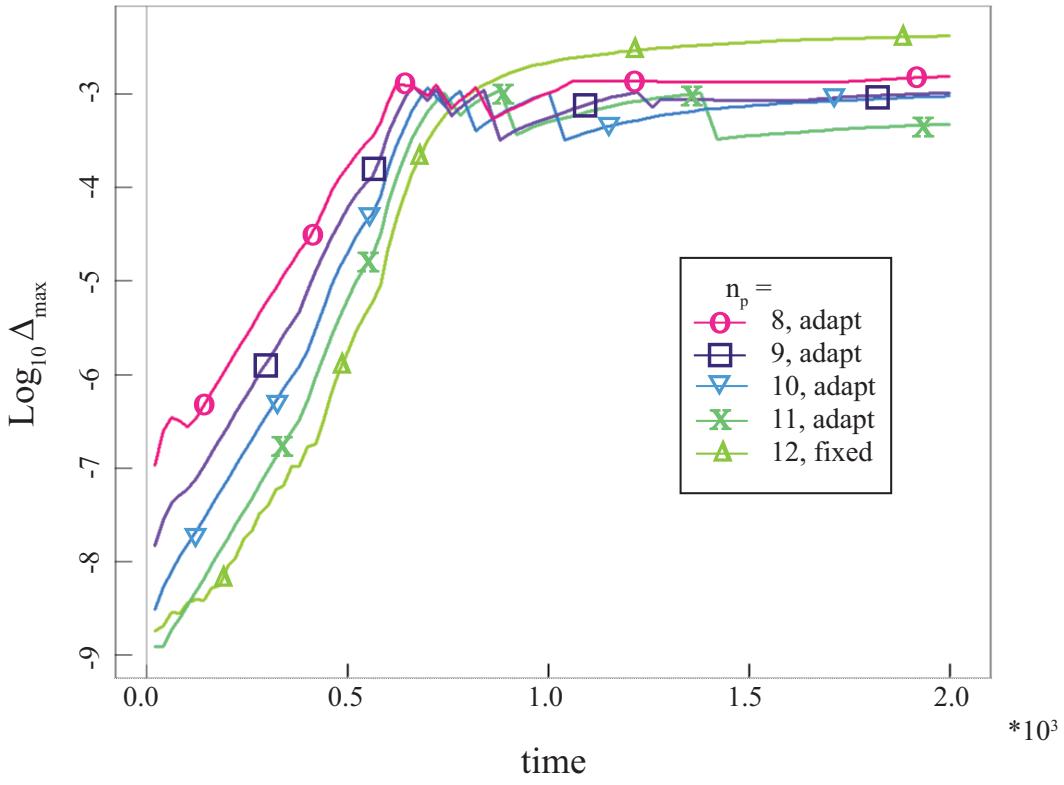

Figure 2.5: Time evolution of the measure of the spatial discretization error Δ_{max} from several simulation runs of non-linear tearing mode is shown. All simulations were conducted on logical grids with the same number of cells $[n_\xi, n_\eta] = [6, 16]$ but varied polynomial order n_p. For the simulations with adaptive grid, the maximum allowed spatial discretization error was $D_{max} \approx 1. * 10^{-3} - 1.5 * 10^{-3}$.

n_p	cpu time	Δ_{max}	efficacy ε	# of regrids	% of cpu time for adaptivity
12	$8.784 * 10^4$ sec	$4.11 * 10^{-3}$	$2.77 * 10^{-3}$	fixed grid	0
11	$8.774 * 10^4$ sec	$4.69 * 10^{-4}$	$2.43 * 10^{-2}$	3	7.4%
10	$3.544 * 10^4$ sec	$9.26 * 10^{-4}$	$3.04 * 10^{-2}$	3	7.8%
9	$2.490 * 10^4$ sec	$1.01 * 10^{-3}$	$3.97 * 10^{-2}$	4	11.3%
8	$1.696 * 10^4$ sec	$1.53 * 10^{-3}$	$3.85 * 10^{-2}$	5	14.7%

Table 2.4: Quantitative evaluation of the performance of the adaptive re-gridding algorithm on the non-linear tearing mode problem run from linear phase through non-linear evolution to saturation.

per processor. Examining Table 2.4, it is apparent that the grid adaptivity not only improves the spatial resolution and therefore the precision of the computation, but can also decrease the amount of memory and time taken up by any given simulation. It should be noted that for any given problem, there exists a minimum size of the required logical grid. Furthermore, when such minimum size is approached, the overhead due to increasing frequency of grid re-mappings can overtake the benefits of the present adaptive grid algorithm.[9]

2.2.4 Verification of SEL against other non-linear numerical simulations.

We have completed a number of non-linear studies in order to verify the accuracy of SEL over long periods of time-integration both with and without making use of adaptive temporal and spatial algorithms available in the code. These include both detailed reproductions of numerical results that have been published prior to the application of SEL to these problems and simultaneous collaborative numerical studies

[9] We also point out that the overhead due to grid adaptivity becomes smaller and smaller as a fraction of total run-time, as the complexity of the physical equations and number of dependent variables M increases.

conducted for the sole purpose of cross-code verification. The physical phenomenon of choice for the SEL verification studies has been magnetic reconnection. Besides the obvious motivation of interest in the physical phenomenon itself (particularly so by V.S. Lukin), magnetic reconnection was chosen as a test problem because it can provide arbitrarily challenging conditions for numerical codes both in terms of spatial and temporal scales involved in a single non-linear computation.

Verification against existing published results.

Making use of the flexible flux-source form of PDEs that can be evolved by SEL, the code has been tested with several different physical models. In collaboration with L. Chacón of LANL, reduced visco-resistive set of MHD equations (see Section 2.2.1) was used to simulate the problem of magnetic island coalescence in order to reproduce and cross-verify results subsequently published by Knoll and Chacón[86]. The SEL simulations were conducted using the full adaptive re-gridding and time-stepping capabilities and the results matched in detail those shown in Ref. [86].

By adding electron inertia effects to the reduced visco-resistive MHD (see Ref. [110] for analysis and justification of such physical model), the numerical results on collisionless reconnection in a regime dominated by electron inertia effects by Ottaviani and Porcelli [109, 110] have also been reproduced. These doubly periodic simulations of non-linear evolution of a tearing mode were conducted on a fixed but strongly non-uniform grid and with a fixed time-step size. Plasma parameters and magnetic equilibrium identical to those used by Ottaviani and Porcelli [109] were also used in the SEL simulations, however the precise form and magnitude of the perturbation was not known and therefore the time of the onset of non-linear regime could not be verified. Sample contour plots of modified poloidal magnetic flux $F \equiv (1 - d_e^2 \nabla^2)\psi$,

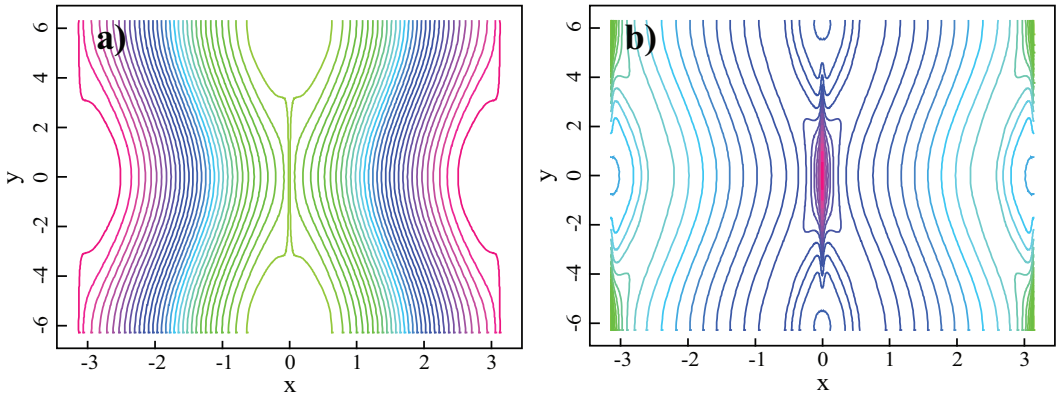

Figure 2.6: Sample contour plots of (a) modified poloidal magnetic flux $F \equiv (1 - d_e^2\nabla^2)\psi$ and (b) plasma current $J = \nabla^2\psi$ from a doubly periodic simulation of nonlinear collisionless reconnection ($\mu = \eta = 0$, $d_e = .25$) reproducing simulation results by Ottaviani and Porcelli [109, 110]. The quantities are shown at $t = 170$.

where d_e is the electron skin depth $d_e^2 \equiv (m_e/n_0e^2)$ and $\mathbf{B} = \hat{z} \times \nabla\psi$, and plasma current $J = \nabla^2\psi$ for a simulation with $\mu = \eta = 0$ and $d_e = .25$ are shown in Figure 2.6 and can be qualitatively compared with those of Figure 3 of Ottaviani and Porcelli [109].

The model has been further extended by adding the effects of parallel electron compressibility (and, correspondingly, perpendicular ion compressibility) in order to verify SEL against the simulation results by Cafaro *et.al.*[29]. In this model, the evolution equations are

$$\begin{aligned} \mathbf{E} + \frac{1}{c}\mathbf{v} \times \mathbf{B} &= \eta\mathbf{J} - \frac{1}{n_0 e}\nabla p_e + \frac{m_e}{n_0 e^2}\frac{d\mathbf{J}}{dt} \\ m_i n_0 \left[\frac{\partial \mathbf{v}}{\partial t} + (\mathbf{v} \cdot \nabla)\mathbf{v}\right] &= \frac{1}{c}\mathbf{J} \times \mathbf{B} - \nabla p_i + \mu\nabla^2\mathbf{v}, \end{aligned}$$

where plasma is assumed to be incompressible with density n_0 constant and uniform and plasma flow velocity represented as $\mathbf{v} \equiv \hat{z} \times \nabla\phi$ with some stream function ϕ. Using the total momentum equation and the quasi-neutrality condition ($\nabla \cdot \mathbf{J} = 0$),

it can be shown that in an appropriate limit of large out-of-plane magnetic field and non-negligible plasma pressure, the term $(1/n_0 e)\nabla p_e$ in the Ohm's Law can be approximated to first order by $\rho_s^2 \hat{z} \cdot \nabla\omega \times \nabla\psi$, where the so-called ion sound radius ρ_s is defined as $\rho_s^2 \equiv (T_e/m_i\omega_{ci}^2)$, vorticity $\omega \equiv \hat{z} \cdot \nabla \times \mathbf{v} = \nabla^2\phi$, and ψ is the poloidal magnetic flux. Then, by taking the $\hat{z}$-projection of curl of the first (total momentum) equation and normalizing the equations appropriately, the following set of equations results:

$$\begin{aligned} \frac{\partial F}{\partial t} + [\phi, F] &= \rho_s^2[\omega, \psi] + \eta\nabla^2\psi \\ \frac{\partial \omega}{\partial t} + [\phi, \omega] &= \frac{1}{d_e^2}[\psi, F] + \mu\nabla^2\omega, \end{aligned}$$

where $[A, B] \equiv \hat{z} \cdot \nabla A \times \nabla B$ and $F \equiv (1 - d_e^2\nabla^2)\psi$.

It is well known[53, 94] that the inclusion of finite electron compressibility effects into a reduced MHD system, as in the equations above, introduces a new scale (ρ_s) and modifies the dispersion relation in such a way as to bring in dispersive kinetic Alfvén waves into the system. As discussed elsewhere in this Dissertation, these effects serve to dramatically increase reconnection rate by shortening the current sheet and opening up the outflow part of a reconnection region.

Figure 2.7 shows sample contour plots of modified poloidal magnetic flux F and plasma current J from a doubly periodic simulation of non-linear evolution of a tearing mode qualitatively reproducing the result of Cafaro, *et.al.*[29]. (Compare to Figure 1 of Ref. [29]). These results were obtained on a fixed but strongly non-uniform grid, with a constant time-step size, and plasma parameters of $\mu = \eta = 10^{-4}$, $d_e = .25$ and $\rho_s = .75$.

Since the initial condition for simulations with and without the electron compressibility effects described above are identical, it is worth comparing the corresponding

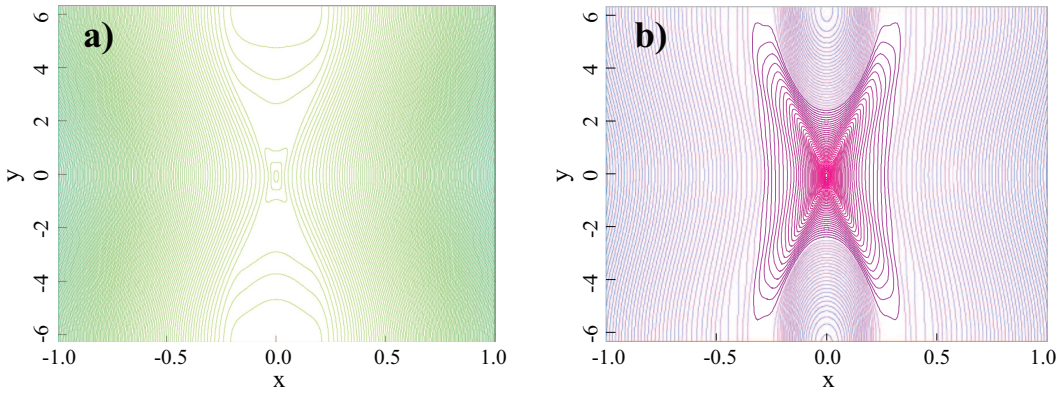

Figure 2.7: Sample contour plots of (a) modified poloidal magnetic flux F and (b) plasma current J from a doubly periodic simulation of non-linear semi-collisional reconnection ($\mu = \eta = 10^{-4}$, $d_e = .25$, $\rho_s = .75$), qualitatively reproducing simulation results by Cafaro, *et. al.* [29]. The quantities are shown at $t = 31.2$ and only the central part of the full domain in the x-direction is included.

panels of Figure 2.6 and Figure 2.7. It is apparent that, as expected, in the simulation with $\rho_s \neq 0$ the current sheet is significantly shortened and the reconnection region is transformed from an elongated Y-shape layer to an open X-point like configuration.

Further verification of the SEL code has been conducted with the reduced four-field model[40, 52, 53]. Under the assumption of incompressibility and constant and uniform density, the following set of equations in the flux-source form has been implemented in SEL:

$$\frac{\partial \psi}{\partial t} + \nabla \cdot [\psi \hat{z} \times \nabla \phi_i - \eta \nabla \psi - d_i \mu_e \nabla W_e] = d_i \hat{z} \cdot \nabla \psi \times \nabla Z$$

$$\frac{\partial Z}{\partial t} + \nabla \cdot [Z \hat{z} \times \nabla \phi_i - W_e \hat{z} \times \nabla \psi - \eta \nabla Z + d_i \mu_e \nabla \omega_e] = 0$$

$$\frac{\partial \omega_i}{\partial t} + \nabla \cdot \left[\omega_i \hat{z} \times \nabla \phi_i - \frac{1}{d_i}(W_i - W_e) \hat{z} \times \nabla \psi - \nabla(\mu_i \omega_i + \mu_e \omega_e) \right] = 0$$

$$\frac{\partial W_i}{\partial t} + \nabla \cdot [W_i \hat{z} \times \nabla \phi_i - \nabla(\mu_i W_i + \mu_e W_e)] = \hat{z} \cdot \nabla \psi \times \nabla Z$$

$$\nabla \cdot (d_i \nabla \psi) = W_i - W_e, \quad \omega_i = \nabla \cdot (\nabla \phi_i), \quad \omega_e = \nabla \cdot (d_i \nabla Z + \nabla \phi_i),$$

where $\mathbf{B} = \hat{z} \times \nabla\psi + \hat{z}Z$, $\mathbf{v}_i = \hat{z} \times \nabla\phi_i + \hat{z}W_i$, $\mathbf{v}_e = \mathbf{v}_i - d_i\mathbf{J}$, $d_i \equiv (c/\omega_{pi})/L_0$ is the ion skin depth normalized to the unit length L_0, and η, μ_i, μ_e are resistivity, ion viscosity and electron viscosity, respectively. We note that the four-field equations above include separate ion and electron flow velocities, thus providing a two-fluid plasma description. As a result, another dispersive (Whistler) wave enters the dispersion relation of the four-field model in a uniform magnetized medium.

Two different published results were reproduced with the SEL code using this model. Doubly periodic domain with fixed and uniform computational grid and fixed time-step was used to verify SEL against numerical simulation results of magnetic merging by Craig, *et. al.*[40] (not shown). A more challenging numerical problem of forced magnetic reconnection driven by boundary perturbations, the so-called Taylor problem, was considered by Fitzpatrick[52]. Some of the results obtained by Fitzpatrick[52] were quantitatively and in detail reproduced using SEL (see Figure 2.8) on a fixed non-uniform grid and making effective use of the adaptive time-advance algorithm.

Dedicated cross-code verification studies.

A series of numerical simulations has been performed with the SEL code as a part of the joint cross-code verification effort by several initial-value macroscopic modeling codes (including M3D-C1[76], NIMROD[139], JFNK-FD[125]). The so-called GEM reconnection challenge[13], initially defined to study non-linear evolution of the tearing mode in different collisionality regimes, has been taken as a standard 2D problem set-up for extended MHD code verification.

This problem has been addressed within both compressible resistive and Hall MHD models. Within a single-fluid approximation, the following system of energy

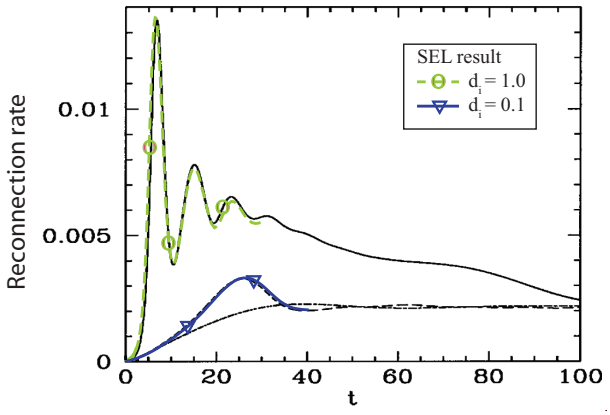

Figure 2.8: Time trace of the reconnection rate from two SEL simulations overlaid on top of the results obtained by Fitzpatrick (adapted from Fig. 1 of Ref.[52]) in simulations of forced magnetic reconnection driven by boundary perturbations. The model, initial, and boundary conditions of SEL simulations exactly reproduce those of Fitzpatrick[52]. Dissipation parameters for both SEL runs are: $\eta = 10^{-4}$, $\mu_i = 10^{-8}$, and $\mu_e = 10^{-10}$.

conserving compressible visco-resistive MHD equations has been evolved:

$$\frac{\partial \rho}{\partial t} + \nabla \cdot (\rho \mathbf{v}) = 0$$

$$\frac{\partial \rho v_\alpha}{\partial t} + \nabla \cdot \left[\rho \mathbf{v} v_\alpha + \left(p + \frac{B^2}{2} \right) \hat{\alpha} - \mathbf{B} B_\alpha - \mu \left(\nabla v_\alpha + \frac{\partial \mathbf{v}}{\partial \alpha} \right) \right] = 0, \quad \alpha \in \{x, y\}$$

$$\frac{1}{\gamma - 1} \frac{\partial p}{\partial t} + \nabla \cdot \left(\frac{\gamma}{\gamma - 1} p \mathbf{v} - \kappa \nabla T \right) = \mathbf{v} \cdot \nabla p + \eta J^2 + \mu (\nabla \mathbf{v} + \nabla \mathbf{v}^T) : \nabla \mathbf{v}$$

$$\frac{\partial \psi}{\partial t} - \nabla \cdot [\eta \nabla \psi] = -\hat{z} \cdot \mathbf{v} \times \mathbf{B},$$

where resistivity η, plasma viscosity μ, and isotropic heat conductivity κ are normalized diffusion coefficients, $p = \rho T$, $\mathbf{B} = \hat{z} \times \nabla \psi$, $J = \nabla^2 \psi$, $\mathbf{v} = v_x \hat{x} + v_y \hat{y}$, and out-of-plane $\hat{z}$-components of magnetic field and plasma flow are assumed to be zero at $t = 0$ and therefore decouple from the above system of equations. Adiabatic equation of state with $\gamma = 5/3$ has been assumed. Harris current sheet equilibrium[66]

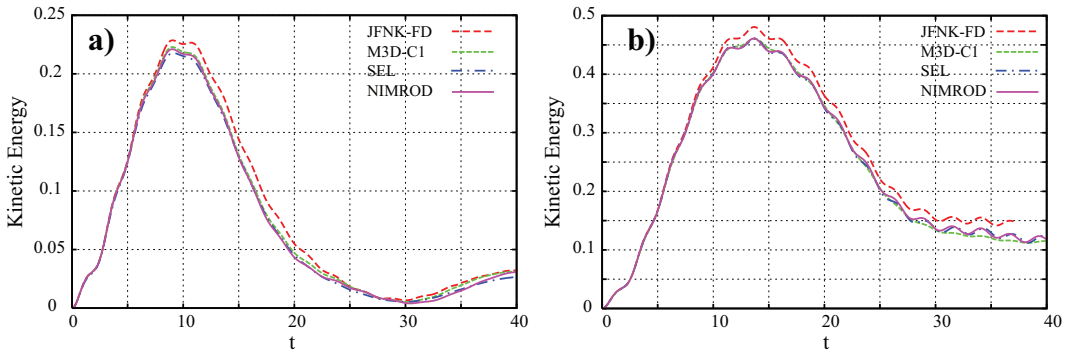

Figure 2.9: Time traces of the kinetic energy from four different codes JFNK-FD[125], M3D-C1[76], SEL[61], NIMROD[139] solving identical GEM reconnection problems [13] within visco-resistive MHD for two values of normalized viscosity (a) $\mu = 5 * 10^{-2}$ and (b) $\mu = 5 * 10^{-4}$. All other normalized equilibrium and plasma parameters have been taken as: $L_x = 25.6$, $L_y = 12.8$, $\lambda = .5$, $p_b = .2$, $\eta = 5 * 10^{-3}$ and $\kappa = 2 * 10^{-2}$.

defined by $\psi_0 = -\lambda \ln[\cosh(y/\lambda)]$, $p_0 = 1/2 \cosh^2(y/\lambda) + p_b$ of width λ, background pressure p_b, uniform temperature $T_0 = 1/2$, and additional large magnetic field perturbation $\delta\psi = 0.1 \cos(2\pi x/L_x) \cos(\pi y/Ly)$ have been taken as the initial condition on a rectangular domain $(x, y) \in [-L_x/2, L_x/2] \times [-L_y/2, L_y/2]$ with perfectly conducting, perfect slip, zero temperature gradient walls on $\hat{y}$-boundaries and periodic b.c. in the $\hat{x}$-direction.

Using the symmetry of the problem, SEL simulations have been conducted on a quarter domain $(x, y) \in [0, L_x/2] \times [0, L_y/2]$ using the full temporal and spatial adaptive capability of the code. Figure 2.9 shows the time-traces of total kinetic energy integrated over the full domain for four different MHD codes solving the identical problem outlined above for two different values of normalized viscosity $\mu = 5 * 10^{-2}$ (panel a) and $\mu = 5 * 10^{-4}$ (panel b), with all other normalized equilibrium and plasma parameters taken to be: $L_x = 25.6$, $L_y = 12.8$, $\lambda = .5$, $p_b = .2$, $\eta = 5 * 10^{-3}$ and $\kappa = 2 * 10^{-2}$. Remarkable agreement among all four codes, with only the JFNK-

FD code showing small deviation of $< 5\%$ from the other three results, is apparent in comparing a global quantity, such as the total kinetic energy in the system. No detailed comparison of any local measurables, such as a local reconnection rate, has been performed. It is worth noting that the boundary conditions and visco-resistive MHD equations employed in solving this problem imply conservation of total energy in the system. The total energy maintained by the SEL code through $t = 50$ for the case of $\mu = 5 * 10^{-2}$ is $E_{total} = 219.4407 \pm 0.0006$ and for the case of $\mu = 5 * 10^{-4}$ is $E_{total} = 219.4402 \pm 0.0012$.

The Hall MHD model used in the cross-code verification study extends the resistive Ohm's Law to include some of the two-fluid terms, thus coupling the evolution of out-of-plane components of magnetic field and plasma flow to the visco-resistive MHD model given above and introducing dispersive waves into the system. The following system of PDEs has been implemented in the SEL code:

$$\frac{\partial \rho}{\partial t} + \nabla \cdot (\rho \mathbf{v}_i) = 0$$

$$\begin{aligned} \frac{\partial \rho v_{i\alpha}}{\partial t} &+ \nabla \cdot \left[\rho \mathbf{v}_i v_{i\alpha} + \left(p + \frac{B^2}{2} \right) \hat{\alpha} - \mathbf{B} B_\alpha - \mu_i \left(\nabla v_{i\alpha} + \frac{\partial \mathbf{v}_i}{\partial \alpha} \right) \right. \\ &- \left. \mu_e \nabla v_{ez} \left(\hat{z} \cdot \hat{\alpha} \right) \right] = 0, \quad \alpha \in \{x, y, z\} \end{aligned}$$

$$\begin{aligned} \frac{1}{\gamma - 1} \frac{\partial p}{\partial t} &+ \nabla \cdot \left(\frac{\gamma}{\gamma - 1} p \mathbf{v}_i - \kappa \nabla T \right) = \mathbf{v}_i \cdot \nabla p + \eta |\mathbf{J}|^2 \\ &+ \mu_i (\nabla \mathbf{v}_i + \nabla \mathbf{v}_i^T) : \nabla \mathbf{v}_i + \mu_e |\nabla v_{ez}|^2 \end{aligned}$$

$$\frac{\partial \psi}{\partial t} - \nabla \cdot \left[\eta \nabla \psi + d_i \mu_e \frac{\nabla v_{ez}}{\rho} \right] = -\hat{z} \cdot \left(\mathbf{v}_i \times \mathbf{B} - d_i \frac{\mathbf{J} \times \mathbf{B}}{\rho} \right) + d_i \mu_e \frac{\nabla v_{ez} \cdot \nabla \rho}{\rho^2}$$

$$\frac{\partial B_z}{\partial t} + \nabla \cdot \left[\mathbf{v}_i B_z - \mathbf{B} v_{ez} + d_i \beta_e \hat{z} \times \frac{\nabla p}{\rho} - \eta \nabla B_z \right] = d_i B_z \hat{z} \cdot \frac{\nabla B_z \times \nabla \rho}{\rho^2},$$

where resistivity η, ion viscosity μ_i, electron viscosity μ_e and isotropic heat conductivity κ are normalized diffusion coefficients, $p = p_i + p_e = \rho T$, $\mathbf{B} = \hat{z} \times \nabla\psi + \hat{z}B_z$, $\mathbf{J} = \nabla \times \mathbf{B} = \rho(\mathbf{v}_i - \mathbf{v}_e)/d_i$, $d_i \equiv (c/\omega_{pi})/L_0$ is the normalized ion skin depth, and β_e is fixed and uniform electron-to-ion plasma pressure ratio $\beta_e \equiv (p_e/p_i)$. Once again, adiabatic equation of state with $\gamma = 5/3$ has been assumed.

The computational domain, initial and boundary conditions for the Hall MHD cross-code verification study have been chosen the same as those of the visco-resistive MHD simulations described above. We note, however, that the explicit presence of the out-of-plane components of magnetic field, ion and electron flow velocities requires additional specifications in both initial and boundary conditions. In particular, we have set $B_{z0} = 0$, all of the plasma current at $t = 0$ has been assumed to be carried by electrons $\mathbf{J}_0 = -\rho\mathbf{v}_{e0}/d_i$, and zero flow boundary condition on the electron out-of-plane flow has been assumed at the walls. We further note that the latter assumption, together with the form of the electron viscosity given in the equations above, leads to the possibility of energy transport in and out of the domain by the electron viscous forces.

Figure 2.10 presents some of the results from the simulations of the GEM reconnection challenge with the Hall MHD model described above and produced within the scope of the cross-code verification study. Panel (a) shows time traces of the kinetic energy (K.E.) from the SEL, NIMROD and M3D-C1 codes run with the following normalized equilibrium and plasma parameters: $L_x = 25.6$, $L_y = 12.8$, $\lambda = .5$, $p_b = .2$, $\beta_e = 1/6$, $d_i = 1.$, $\eta = 5 * 10^{-3}$, $\mu_i = 5 * 10^{-2}$ and $\kappa = 2 * 10^{-2}$. The Hall MHD model equations advanced by the three codes are identical except for implementations of the electron viscosity terms (formulated as hyper-resistivity in M3D-C1 and altogether

absent in NIMROD) and introduction of small artificial density diffusion in NIMROD and M3D-C1 codes. These differences in the models are presumed to be responsible for the small but significant variations in the time-traces shown in panel (a) of Figure 2.10. Panel (b) shows the sensitivity of the SEL-produced K.E. trace to the exact magnitude of normalized electron viscosity $\mu_e = [2. * 10^{-5}, 1. * 10^{-5}, 5. * 10^{-6}]$ and the trace of total energy in the system for $\mu_e = 10^{-5}$. Observed variation in the K.E. traces appears to be consistent with the variation between the three codes demonstarted in panel (a).[10]

Panels (c) and (d) of Figure 2.10 show the contour plot of out-of-plane electron momentum, which carries most of the plasma current, and a representation of the grid density, respectively, from a simulation run with $\mu_e = 10^{-5}$ at $t = 29.125$, which corresponds to the peak of K.E. in the system. Very localized spike of the electron current at the X-point and sharp separatrices propagating outward are characteristic of Hall reconnection and are apparent in panel (c). In the SEL code simulations, these are smoothly resolved by making extensive use of the adaptive grid re-mappings, with panel (d) of Fig. 2.10 showing a representation of the grid on which the electron current of panel (c) has been computed. This particular SEL simulation was conducted on a logical grid of size $[n_\xi, n_\eta, n_p] = [40, 40, 8]$ representing the full simulation domain shown in Figure 2.10 and made a total of 18 re-mappings in the course of the whole simulation run, which consisted of 419 time-steps with time-step size varying between $\delta t = 0.0625 \rightarrow 0.25$.

[10] As shown elsewhere in this Dissertation, electron viscosity (or hyper-resistivity) has to be included in any Hall MHD model that is used to simulate a physical system where magnetic reconnection takes place and attempts to spatially resolve the reconnection region. In the absence of such terms, as in the results obtained with the NIMROD code, numerical diffusion facilitated by lack of spatial resolution effectively replaces the local electron viscosity effects.

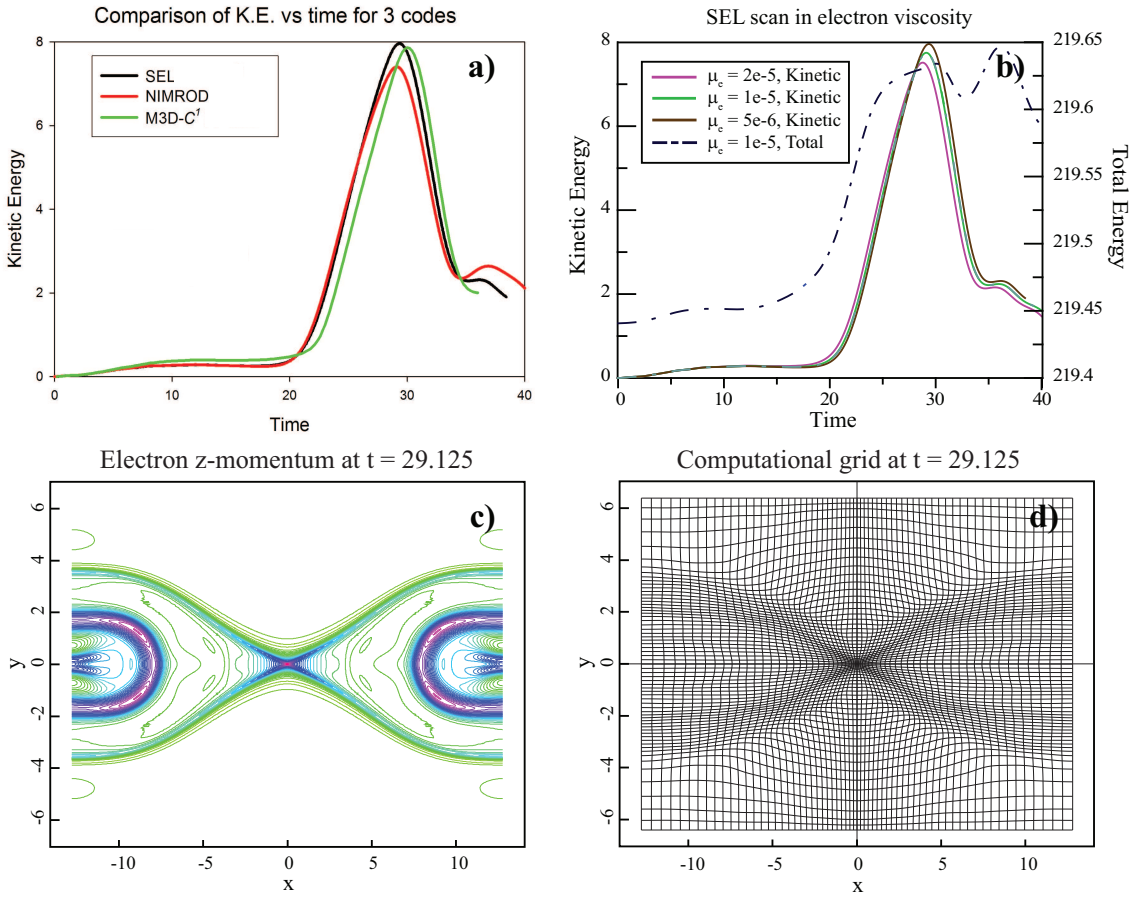

Figure 2.10: Panel (a) shows time traces of the kinetic energy (K.E.) from three different codes SEL[61], NIMROD[139], M3D-C1[76], solving GEM reconnection problems[13] within the Hall MHD model. The problem set-up and Hall MHD models are identical across the three codes, except for implementations of the electron viscosity terms and presence of artificial density diffusion in some of the codes. Panel (b) presents K.E. traces from three SEL runs with varied values of electron viscosity and the trace of total energy in the system from one of the runs. Panels (c) and (d) show the contour plot of out-of-plane electron momentum and a representation of the grid density, respectively, at the time corresponding to peaking of K.E. in the system for a simulation run with $\mu_e = 10^{-5}$. In all simulations presented, all normalized equilibrium and plasma parameters, aside from μ_e, have been taken as: $L_x = 25.6$, $L_y = 12.8$, $\lambda = .5$, $p_b = .2$, $\beta_e = 1/6$, $d_i = 1.$, $\eta = 5 * 10^{-3}$, $\mu_i = 5 * 10^{-2}$ and $\kappa = 2 * 10^{-2}$.

We now conclude the description the SEL code's verification studies having demonstrated its accuracy, efficiency and robustness on multiple challenging linear and nonlinear problems using a range of plasma fluid models from the simplest reduced to extended two-fluid MHD. This allows us to rely on the SEL code in the studies of various physical phenomena we indulge in in the following Sections of this Dissertation.

Chapter 3

Magnetic Reconnection

In this chapter, dedicated simulations of two-dimensional magnetic reconnection (MR) using several MHD models of varying collisionality and complexity are described. Some of the outstanding and unsettled questions of relevance to evolution of an internal kink mode, as well as many other fusion, space and solar physics phenomena are addressed below.

3.1 Fundamentals of magnetic reconnection by way of current layers.

The Sweet-Parker[115, 141] theory of two-dimensional incompressible resistive MR provides the fundamental framework for describing MR by way of current layers. We now outline the basic elements of the theory, as well as how it can be extended to describe MR in a greater and more complex set of plasma models.

Figure 3.1 provides a schematic of a symmetric two-dimensional reconnection region (RR) with a current layer of length L and width δ. By definition, $L > \delta$. Correspondingly, plasma flows into RR from top and bottom with velocity v_{in} carrying magnetic field of magnitude B_{in} and flows out to the left and right with velocity

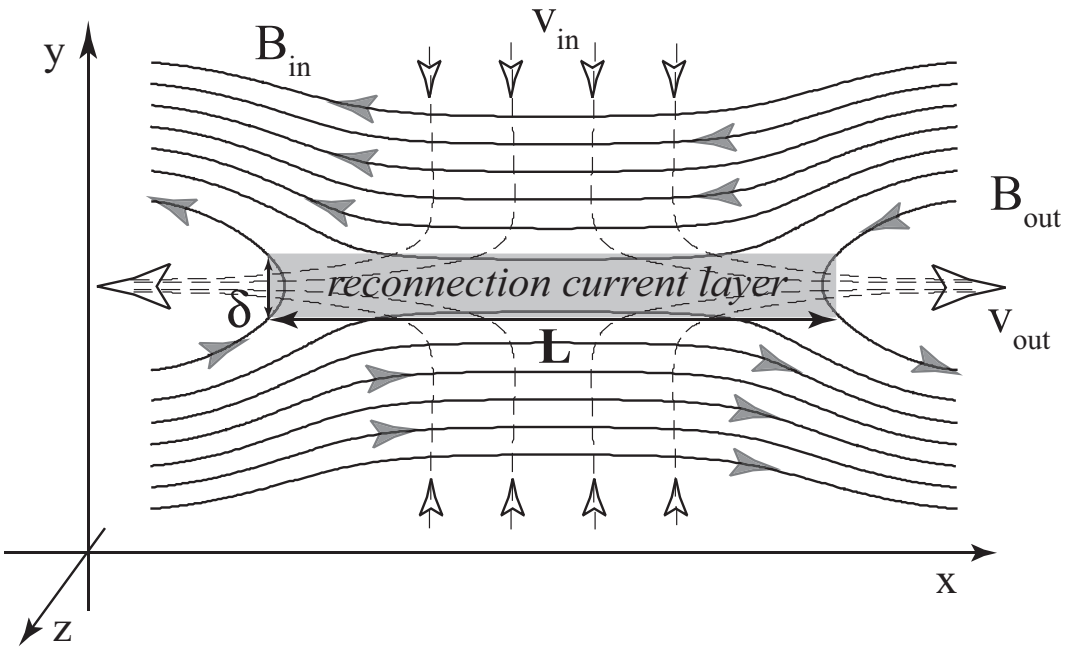

Figure 3.1: Schematic of an up-down and left-right symmetric two-dimensional reconnection region.

v_{out} carrying away reconnected magnetic field of magnitude B_{out}. Horizontal axis is the x-axis, vertical axis is the y-axis, and z-axis points out of the page. Such orientation of a reconnection region is used throughout this Chapter. We also define ion and electron Alfvén velocities $v_A^i \equiv (B_0/\sqrt{4\pi m_i n_0})$ and $v_A^e \equiv (B_0/\sqrt{4\pi m_e n_0})$, respectively, based on the magnitude of global magnetic fields $B_0 \sim B_{in}$ and some average plasma number density n_0. Here and below in this Chapter, all quantities are normalized using B_0, n_0 and some unit of length l_0.

3.1.1 Resistive MHD

In a single-fluid model, such as resistive MHD, the plasma velocity corresponds to the only velocity of a conducting fluid. Then, in the upstream region outside of the current layer, out-of-plane electric field is given by $E_z = \hat{z} \cdot (-\mathbf{v} \times \mathbf{B}) = v_{in} B_{in}$. In steady-state, $(\partial \mathbf{B}/\partial t) = -\nabla \times \mathbf{E} = 0$, and therefore E_z must be uniform over the RR. Thus, the so-called reconnection electric field is given by $E_R = v_{in} B_{in} = v_{out} B_{out}$. At the center of RR, the X-point, all in-plane plasma flows go to zero due to symmetry and therefore E_R must be supported by "non-ideal" (*i.e.* non-$\mathbf{v} \times \mathbf{B}$) effects. In resistive MHD, the only non-ideal term in the Ohm's Law is $\eta \mathbf{J}$, where η is appropriately normalized plasma resistivity, so that at the X-point $E_R = \eta J_z$.

No plasma accumulation within the current layer is possible in the steady-state. (In fact, in many of the simulations described below, plasma has been assumed to be incompressible.) Therefore, from mass conservation, $v_{in} L = v_{out} \delta$. It follows that $B_{in} \delta = B_{out} L$. Similarly, energy conservation, or, equivalently, integrating the in-plane components of the momentum equation along the inflow and outflow directions, provides another relation between the inflow and outflow quantities in the RR.

The Sweet-Parker theory effectively assumes that L is of the order of the system

size by presuming δ to be microscopic and in-plane plasma velocities outside of the current layer to be small relative to v_A^i[90]. Then, $L \gg \delta$, $J_z = 2B_{in}/\delta$, and $v_{out} = B_{in}$ follows from energy conservation under the assumption that plasma density and pressure are approximately constant outside of the current layer and viscous effects can be neglected.[1] W. Park, *et.al.*[113] have extended the Sweet-Parker model by including the viscous effects in the momentum equation whenever kinematic viscosity μ is comparable to η. In that case, energy conservation relation gives $v_{out} = B_{in}(1 + \mu/\eta)^{-1/2}$. Using this visco-resistive relationship between B_{in} and v_{out}, the following identities are also implied:

$$\delta = \eta^{1/2}(1+\mu/\eta)^{1/4}\sqrt{\frac{2L}{B_{in}}} \tag{3.1.1}$$

$$v_{in} = B_{out}(1+\mu/\eta)^{-1/2} = \eta^{1/2}(1+\mu/\eta)^{-1/4}\sqrt{\frac{2B_{in}}{L}} \tag{3.1.2}$$

$$E_R = (1+\mu/\eta)^{-1/4}\left(\frac{2\eta}{L}\right)^{1/2} B_{in}^{3/2}, \tag{3.1.3}$$

where we have expressed all other quantities in terms of plasma resistivity, kinematic viscosity, inflow magnetic field and current layer length. The reconnection electric field E_R is often also referred to as the reconnection rate, which we denote by R_{rec}, and the Sweet-Parker reconnection rate is denoted by $R_{rec}^{SP} \sim \eta^{1/2}$, whenever $(\mu/\eta) \ll 1$ and B_{in} and L are both of order unity.

We emphasize that in the Sweet-Parker model L and B_{in} have been assumed to be determined by the global magnetic field configuration, while the steady-state condition was only necessary to enforce approximate uniformity of the out-of-plane electric

[1] The Sweet-Parker theory assumes that peaked plasma pressure inside the current layer is responsible for deceleration of plasma inflow and following acceleration of plasma outflow. However, it is evident from considering an incompressible plasma model that plasma pressure cannot play an important role in determining the current layer structure and it is magnetic field line tension that accelerates plasma out of the current layer.

field and non-accumulation of plasma and energy in the current layer. Therefore, whenever global magnetic field structure around a RR evolves slowly enough to be able to approximate the evolution as a sequence of Sweet-Parker steady-states, resistive reconnection may continue to be described by the Sweet-Parker model even while R_{rec} may significantly change due to changes in L, B_{in}, or both.

Below, we consider how the length of a resistive reconnection layer becomes of the order of the system size. However, we now note that an incompressible resistive MHD system has no other characteristic length scales except for width of a resistive diffusion layer and global scales given by the magnetic configuration. Thus, it is reasonable to assume that the length of a current layer has to be either on the scale of reconnecting magnetic structures or proportional to some power of the resistive diffusion width $L \propto l_\eta^p$, where $0 < p < 1$ and $\delta \sim l_\eta$. And since in ideal MHD a local X-configuration of magnetic field not supported by a global structure is intrinsically unstable to collapse[35], L can only be of order δ when the reconnection process itself can support local X-configuration against the collapse. (For example, sufficiently high resistivity allows for faster reconnection and stronger inflows, which may allow the magnetic field convected into RR to reconnect fast enough to avoid current layer elongation.)

3.1.2 Electron MHD

Another single-fluid MHD model that can be analyzed using the Sweet-Parker methodology is the electron MHD (EMHD) model, where ions are considered to be immobile neutralizing background and only electrons have non-zero velocity field $\mathbf{v}_e$. The model

is described by a single normalized vector equation:

$$\mathbf{E} - d_e^2 \left(\frac{\partial \mathbf{J}}{\partial t} + \mathbf{v}_e \cdot \nabla \mathbf{J} \right) = d_i \mathbf{J} \times \mathbf{B} - d_i \nabla p_e + \eta \mathbf{J} - d_i^2 \nu \nabla^2 \mathbf{J}, \tag{3.1.4}$$

where $d_i \equiv (c/\omega_{pi})/l_0 = \frac{c}{e}\sqrt{\frac{m_i}{4\pi}}\frac{1}{l_0\sqrt{n_0}}$, $d_e^2 \equiv d_i^2(m_e/m_i)$, $\eta \equiv \tilde{\eta}c^2\sqrt{\frac{m_i}{4\pi}}\frac{\sqrt{n_0}}{l_0 B_0}$, $\nu \equiv \tilde{\mu_e}\sqrt{\frac{4\pi}{m_i}}\frac{1}{l_0 B_0\sqrt{n_0}}$ and $\{\tilde{\eta}, \tilde{\mu_e}\}$ are physical values for resistivity and kinematic electron viscosity. Note that $\mathbf{J} = \nabla \times \mathbf{B} = -\mathbf{v}_e/d_i$, $(\partial \mathbf{B}/\partial t) = -\nabla \times \mathbf{E}$ and an evolution equation for p_e is not necessary, as p_e evolution decouples from that for the magnetic field, as is shown in Section 3.3 below.

Unlike resistive MHD, the EMHD system described by Eq. (3.1.4) contains multiple spatial scales. Those are resistive diffusion scale l_η, electron viscous diffusion scale l_ν, and electron inertial scale d_e. (Eq. (3.1.4) can be re-normalized to eliminate the ion inertial scale d_i, as ions have been assumed to be immobile.) Any one or a combination of those scales can play a role in determining both the width δ and the length L of a reconnection layer. In the following analysis, we assume that the effects of both resistivity and electron inertia are negligible in comparison to the electron viscosity, thus setting $\eta = d_e = 0$.[2] Also note that since ions are assumed to be stationary, electron flows into and out of the current layer constitute plasma currents carried by the same electrons that carry the reconnection current in the out-of-plane direction. Such current pattern is correlated with a quadrupolar out-of-plane magnetic field structure that is inherent in EMHD magnetic reconnection[96]. We denote the magnitude of this quadrupolar B-field generated around the corners of the reconnection current layer by B_q. (See Figure 3.2.)

Doing the Sweet-Parker-like analysis of an EMHD RR, the assumption of steady-state once again gives: $E_R = v_{in}B_{in} = v_{out}B_{out}$ and $v_{in}L = v_{out}\delta$. And it again follows

[2]Note that by setting $d_e = 0$ all electron inertial effects are neglected, electrons are assumed to carry no kinetic energy, and arbitrarily high electron velocities are allowed.

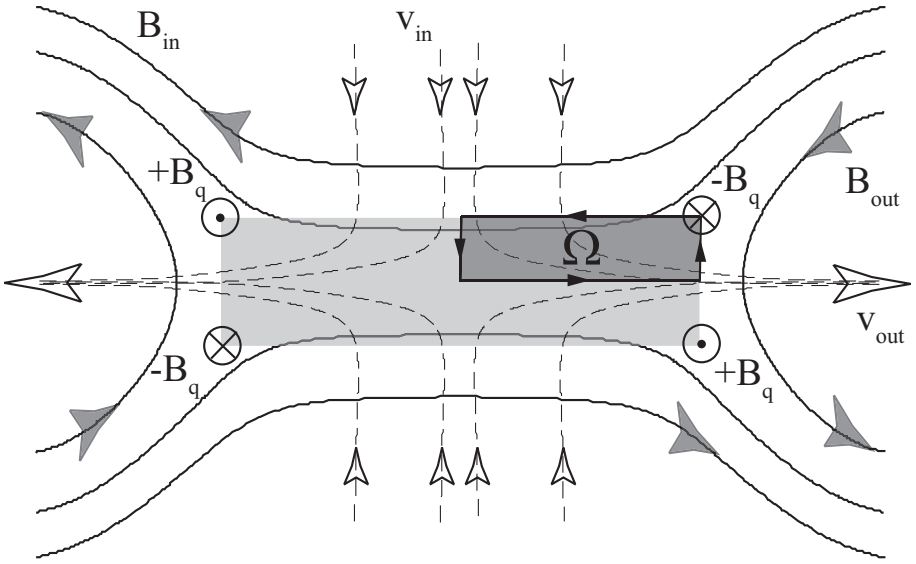

Figure 3.2: Schematic of a single scale reconnection region in electron MHD. Inflow and outflow velocities are those of an electron fluid carrying B-field through the current layer.

that $B_{out} = B_{in}(\delta/L)$. We now assume that δ/L is sufficiently smaller than unity to ignore terms of order $(\delta/L)^2$ and higher. Then, at the X-point, $E_R = d_i^2 \nu B_{in}/\delta^3$. The only relation still missing is that obtained from the momentum equation in resistive MHD. In the case of EMHD, it is replaced by a similar relation derived from $\int_\Omega \nabla \times \mathbf{E} = 0 = \int_{\partial\Omega} \mathbf{E} \cdot dl$, where Ω is a quarter of the current layer bounded by an outside boundary and midplanes of the current layer, as shown in Figure 3.2. Integrating along such closed path, we have:

$$\frac{B_{in}^2}{2} = \nu \frac{L}{\delta^2} v_{out},$$

where the magnetic field line tension force accelerating plasma out of the current layer is now balanced by the in-plane electron viscous force. (In computing the line integral, total contribution from $d_i \nabla p_e$ is exactly zero. Ignoring terms of order $(\delta/L)^2$

and higher, $d_i\mathbf{J}\times\mathbf{B}$ term gives two equal contributions from the path segments interior to the RR, and $d_i^2\nu\nabla^2\mathbf{J}$ term gives two equal contributions from the two horizontal segments of the path.) From the relations above, the following scalings are derived:

$$\delta = \left(\sqrt{2}d_i\nu\frac{L}{B_{in}}\right)^{1/3} \tag{3.1.5}$$

$$v_{in} = \frac{d_i}{\sqrt{2}}\frac{B_{in}}{L} \tag{3.1.6}$$

$$v_{out} = B_{in}\left(\frac{d_i^2}{4\nu}\frac{B_{in}}{L}\right)^{1/3} \tag{3.1.7}$$

$$B_{out} = \left[\sqrt{2}d_i\nu\left(\frac{B_{in}}{L}\right)^2\right]^{1/3} \tag{3.1.8}$$

$$R_{rec}^{\nu} = E_R = \frac{d_i}{\sqrt{2}}\frac{B_{in}^2}{L}. \tag{3.1.9}$$

We observe that in this case the resulting reconnection rate has no explicit dependence on electron viscosity ν, which breaks the magnetic field frozen-in condition within the current layer, while v_{out} is inversely proportional to $L^{1/3}$. Assuming an infinite reservoir of magnetic energy available to be released through reconnection, it is reasonable to expect that for given ν, magnetic field line tension accelerates the plasma outflow to the maximum allowable velocity by shortening the current layer. Thus, a localized RR with strongly enhanced reconnection rate results.

Various factors might come into play in restricting either the maximum allowable velocity or the minimum allowable current layer length. An obvious one is the initial assumption of $(\delta/L) < 1$. Applying that to Eq. (3.1.5) gives a restriction on L of the form $L^2 > (\sqrt{2}d_i\nu/B_{in})$. We also note that to the same order in (δ/L) as above, $v_{out} = d_i(2B_q/\delta)$, which implies that $B_q = (B_{in}/2\sqrt{2})$. Another consideration is that in the case of such localized current layer, B_{in} itself is no longer uniquely determined

by the magnitude of the global magnetic field convected towards RR, but is only some fraction of that. Instead, both the reconnection rate and the structure of RR are in large part determined by the physics of the current layer.

In the above derivation, both plasma resistivity and electron inertia were neglected. However, the same analysis can be done by setting $\nu = 0$ and allowing for non-zero plasma resistivity. In that case, it is easy to show that:

$$\delta = \frac{\eta}{\sqrt{2}d_i}\frac{L}{B_{in}},$$

$$v_{out} = \frac{4d_i^2}{\eta}\frac{B_{in}^2}{L},$$

and

$$R_{rec}^{\eta} = 2\sqrt{2}d_i\frac{B_{in}^2}{L}.$$

Note that reconnection rate is again independent on the mechanism that breaks the frozen-in condition and outflow velocity can be increased by making the current layer shorter. However (δ/L) is now independent of L, which suggests that the current layer can contract proportionally and without bound, making the current layer singular. That is, in fact, what is observed in numerical simulations of MR where electron dynamics plays an important role and no electron viscosity-like term is included[109, 127].

Finally, when $d_e > 0$ but both resistivity and kinematic electron viscosity are neglected, no steady-state reconnection is possible[29]. That trivially follows from the fact that in such collisionless model only the time-dependent $d_e^2(\partial\mathbf{J}/\partial t)$ term in Eq. (3.1.4) remains non-zero and can balance the out-of-plane electric field at the X-point. Thus, this system also tends towards a singular current layer.

Based on the above reasoning, one could argue that inclusion of both resistivity

and electron inertia might be sufficient to allow for EMHD steady-state reconnection through a current layer of finite size: resistivity would act to balance the reconnection E-field at the X-point, while electron inertia would limit the outflow velocity. However, as has been shown by numerical simulations where no electron viscosity-like term is included[109, 127], such RR acquires a two-scale structure where electron fluid decouples from magnetic field on the electron inertial scale, while the current layer itself contracts to sub-d_e scales and towards a singularity. Thus, while no straightforward Sweet-Parker-like arguments can be made for the full multi-scale systems, it is apparent that kinematic electron viscosity is necessary to enable steady-state MR in the EMHD regime.[3]

3.1.3 Two-fluid MHD

We now consider MR in a two-fluid plasma model, where both electron and ion fluids have non-zero velocity fields, yet they decouple on some scale which is greater than the current layer width δ. In 2D systems with no or weak overall out-of-plane magnetic "guide"-field B_{guide}, such scale is the ion inertial scale d_i, where ions decouple from the magnetic field due to inertia while electrons continue to $\mathbf{E}\times\mathbf{B}$-drift together with the B-field[96, 128]. And in systems where the global magnetic field is fully three-dimensional or in the presence of significant guide-field $B_{guide}/B_{in} \gtrsim 1$, the relevant decoupling scale is generally assumed to be the so-called ion sound radius $\rho_s \equiv c_s/\omega_{ci}$, where c_s is the speed of sound, ω_{ci} is the ion cyclotron frequency and decoupling is due to a combination of compressibility and finite ion Larmor radius effects[6, 29, 128].

[3] It has been shown in recent kinetic simulations of MR by Karimabadi *et al.*[81] that divergence of the effective electron pressure tensor plays the key role in determining the structure of and balancing the reconnection electric field in the current diffusion layer. However crude, the kinematic viscosity term $d_i\nu\nabla^2\mathbf{v}_e$ in Eq. (3.1.4) is what models the full electron pressure tensor term $\nabla\cdot\Pi^e$ in the EMHD approximation.

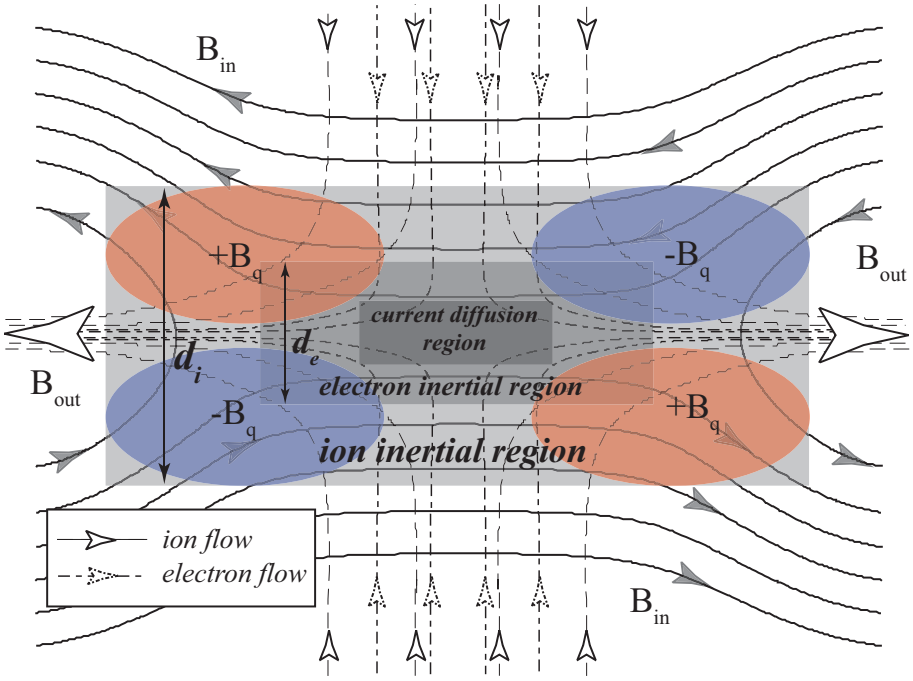

Figure 3.3: Schematic of a two-fluid multi-scale reconnection region with no magnetic guide field. Current diffusion region has been assumed to be sub-d_e scale.

Figure 3.3 shows a schematic of a two-fluid multi-scale RR with $B_{guide} = 0$. Observe that within the ion inertial region, ion flow follows a global convection pattern independently of how and where current diffusion takes place. Accordingly, B-field evolution within the ion inertial region is independent of $\mathbf{v}_i$ and therefore can be described by the EMHD model.

Note that, as discussed above, in EMHD the width of the current diffusion region is determined by the electron viscous scale l_ν. Thus, whenever $l_\nu > d_e$, no separate electron inertial region exists. Similarly, whenever the resistive scale l_η is greater than the ion inertial scale d_i (or ion sound radius ρ_s), the current diffusion region consumes the ion inertial region and reconnection proceeds in the resistive MHD manner. The transition between the two-fluid and resistive MR has recently been numerically investigated by Cassak *et. al.*[32, 33] and is described further in Section 3.4 below.

3.2 Visco-resistive magnetic reconnection in large systems.

Magnetic reconnection in visco-resistive MHD systems has been extensively studied and is generally well understood[113, 15, 147, 90, 94]. In the simulations described below, we are interested in following the development of a reconnection layer from a small localized perturbation in a large semi-periodic system. We then compare and contrast these results with similar simulations using EMHD and two-fluid MHD models.

3.2.1 Definition of the problem.

SEL simulations of a resistive tearing mode within a Harris current sheet[66] were described in Section 2.2.1 above and showed remarkable agreement of the computed

linear growth rates with the analytical calculations. Here, we focus on the strongly non-linear regime of resistive current layer (also referred to as the current diffusion layer) reconnection.

In order to simplify the model, an assumption of incompressibility has been made. It can be justified by either presence of large magnetic guide field $B_{guide} \gg B_0$ or large plasma $\beta \equiv (p/B^2)$, where p is the plasma pressure.[4] It has also been shown[25] that compressibility effects do not play an important role in the evolution of a resistive current layer.

As in Section 2.2.1, poloidal B-field is represented by a flux function ψ, $\mathbf{B} = \hat{z} \times \nabla\psi + \hat{z}B_z$, and poloidal flow by a stream function ϕ, $\mathbf{v} = \hat{z} \times \nabla\phi + \hat{z}v_z$. Plasma density is taken to be initially uniform and remains so due to the assumption of incompressibility. Then, the momentum equation and the Ohm's Law are sufficient to specify evolution of the plasma:

$$\frac{\partial \mathbf{v}}{\partial t} = -\mathbf{v} \cdot \nabla\mathbf{v} + \mathbf{J} \times \mathbf{B} - \nabla p + \mu\nabla^2\mathbf{v} \tag{3.2.1}$$

$$\mathbf{E} = -\mathbf{v} \times \mathbf{B} + \eta\mathbf{J}, \tag{3.2.2}$$

where η and μ are plasma resistivity and kinematic viscosity. Using $\hat{z} \cdot \nabla\times$ operator on Eq. (3.2.1) and $\hat{z}\cdot$ operator on Eq. (3.2.2), plasma pressure and $\hat{z}$-components of magnetic and flow fields are eliminated from the problem and the system is reduced to:

$$\begin{aligned} \frac{\partial\left(\nabla^2\phi\right)}{\partial t} &+ \nabla \cdot \left[(\nabla^2\phi)\hat{z} \times \nabla\phi - (\nabla^2\psi)\hat{z} \times \nabla\psi - \mu\nabla(\nabla^2\phi))\right] = 0 \\ \frac{\partial\psi}{\partial t} &+ \nabla \cdot (\psi\hat{z} \times \nabla\phi) = \eta\nabla^2\psi. \end{aligned} \tag{3.2.3}$$

[4]Strictly speaking, the second condition for incompressibility requires plasma flows to be much slower than the sound velocity, c_s. However, since it was shown in Section 3.1.1 that in a visco-resistive RR outflow velocity is of the order of the ion Alfvén velocity, $v_{out} \sim v_A^i$, it has to be true that $\beta = (c_s/v_A^i)^2 \gg 1$.

The reduced visco-resistive MHD equations, Eqs. (3.2.3), are solved in a rectangular box $(x, y) \in [-L_x, L_x] \times [-L_y, L_y]$. Periodic boundary conditions (BC) are used in the outflow $\hat{x}$-direction, while "open" boundary is assumed in the inflow $\hat{y}$-direction in order to reduce the effects of the domain boundary on the reconnection layer. Here, we define "open" boundary to have zero tangential flow, zero vorticity and constant and uniform tangential component of magnetic field. Thus, on the y-boundary, $\hat{y} \cdot \nabla\phi = 0$, $\nabla^2\phi = 0$, and $\hat{y} \cdot \nabla\psi = const$ are the enforced BC. Simulations are initialized with a Harris equilibrium[66] with an additional small and localized perturbation: $\psi_0 = \lambda \ln[\cosh(y/\lambda)] + \delta\psi$, $\delta\psi = \epsilon \exp[-x^2/(2\lambda)^2] \exp[-y^2/(\lambda/2)^2])$, where λ is the half-width of the Harris equilibrium and ϵ is the magnitude of the perturbation. Note that the perturbation is localized within the equilibrium current sheet.

In order to model the expected development of a macroscopic resistive current layer from a local perturbation in a large system, the following simulation parameters are chosen: $\lambda = .5$, $L_x = 48$, $L_y = 6$, $\epsilon = 10^{-4}$ and $\eta = \mu = 10^{-4}$, where width of the initial Harris equilibrium are taken as the effective unit length. Making use of the symmetries of the initial conditions and those inherent in Eqs. (3.2.3), simulations are conducted only in the top-right quarter domain and appropriate symmetry BC are applied.

Though here we are not interested in either linear or early non-linear development of the tearing instability, it is important to comment on the reason for choosing a localized perturbation rather than one that spans the whole domain, as is commonly done. (In numerical modeling of spontaneous MR, it is common to initialize simulations with a macroscopic tearing-unstable current layer in a periodic domain of length

L_x and a perturbation $\delta\psi \propto \cos(2\pi x/L_x)$, which spans the whole domain along the initial current layer[13, 94].) As discussed in Section 2.2.1, linear growth rate γ of a tearing mode with a wave number k_x in a Harris current sheet of width λ depends on the quantity λk_x. For given λ and η, the function $\gamma(k_x)$, solution to Eq. (2.2.1), is positive for $\lambda k_x < 1$ and has a maximum at some wave number $0 < k_{max} < 1/\lambda$ [37, 94]. Therefore, whenever a simulation is initialized with an unstable monochromatic perturbation, only the tearing mode of that wavelength grows to become non-linear and form a reconnection current layer whose initial length is correlated with the wavelength of the perturbation. However, if the initial perturbation is sufficiently small and contains all wave numbers allowed in the simulation box, it is the tearing mode with k_x closest to k_{max} which determines the initial length of the reconnection current layer independently of the shape of the perturbation. We have chosen the perturbation to be a localized Gaussian and L_x sufficiently large such that $2\pi/k_{max} < 2L_x$, in order to allow the system to "forget" about the shape of the perturbation when it forms the reconnection current layer.

3.2.2 Simulation results.

We now study the results of such large scale resistive MR simulation. Following the linear development phase, a thin and relatively short ($L \sim \pi/k_{max}$) current layer is established at $t \approx 400$ (not shown). Panels (a) and (b) of Figure 3.4 show time-traces of R_{rec} and reconnection layer dimensions as that initial current layer rapidly extends in the outflow direction with its length L becoming a large fraction of the domain size. Two measures of the reconnection layer length are presented: half-length of the current diffusion layer $L_J/2$, calculated as half-length at half-max of $J_z = \nabla^2\psi$, and half-length of the plasma outflow layer $L_v/2$, calculated as the distance from

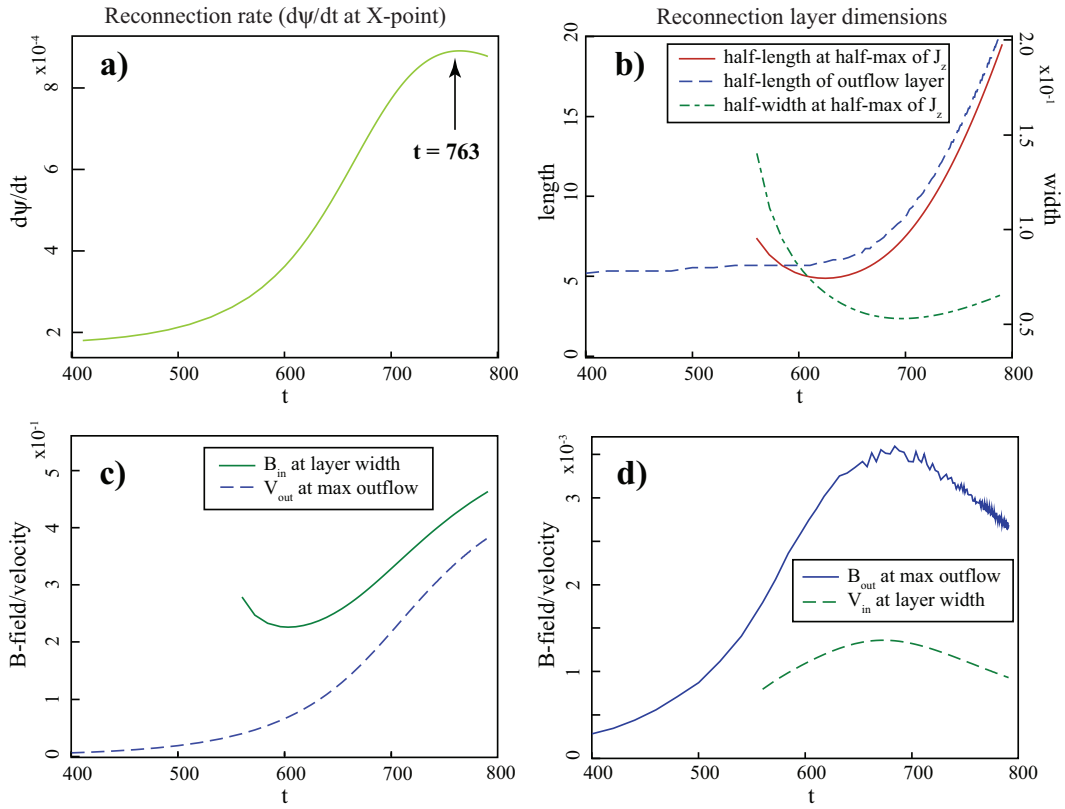

Figure 3.4: Time-traces of several characteristic reconnection current layer quantities during the non-linear phase of a visco-resistive incompressible MHD simulation of MR in a large semi-open domain. Shown are (a) reconnection rate at the X-point; (b) reconnection layer dimensions; (c) B_{in} and v_{out}; and (d) B_{out} and v_{in}.

the X-point to the point of maximum v_{out}; yet no characteristic scale could be easily identified in the plasma inflow velocity profile and the only reconnection layer width diagnostic is the half-width of the current diffusion layer $\delta_J/2$, calculated as half-width at half-max of J_z. Note that until $t \approx 600 - 650$, remnants of the initial Harris current sheet dominate the diagnostic of the current diffusion layer dimensions and neither L_J nor δ_J are meaningful. However, once the reconnection current becomes sufficiently strong, it is apparent that the current diffusion layer and plasma flow scales coincide, as expected in visco-resistive MHD reconnection.

The rate of current layer elongation after $t = 650$ can be inferred from panel (b) of Fig. 3.4 and is ≈ 0.15, or about 40% of the ion Alfvén velocity based on the inflow magnetic field B_{in} and nearly 50% of the plasma outflow velocity v_{out}, shown in panel (c) of Fig. 3.4.[5] It is clear that such dynamic reconnection layer cannot be treated as if it was in steady-state. Nevertheless, we attempt to compare the simulation results with the modified visco-resistive Sweet-Parker model described in Section 3.1.1. We first observe that despite the current layer elongation, the reconnection rate increases until $t = 763$ due to the simultaneous increase of B_{in} from $\approx$ 20% to $\approx$ 40% of the B-field supplied at the inflow boundary of the domain. However, since B_{in} is ultimately bounded by $B(y = L_y) = 1$, as the current layer continues to extend, the reconnection rate begins to drop in accordance with Eq. (3.1.3). Similarly, the width of the current layer begins to increase and the inflow velocity and outflow magnetic fields, shown in panel (d) of Figure 3.4, begin to drop in accordance with Eqs. (3.1.1-3.1.2). Taking a ratio (B_{in}/v_{out}) during the layer expansion, we also note that it is

[5] Both B_{in} in panel (c) and v_{in} in panel (d) of Figure 3.4 are evaluated at $y = \delta_J/2$. As discussed above, δ_J is only meaningful after $t \lessapprox 600 - 650$, and therefore little value should be put into the magnitudes of B_{in} and v_{in} shown for $t < 600$.

generally consistent with the visco-resistive relation derived by W. Park, *et.al.*[113], which for $(\mu/\eta) = 1$ gives $(B_{in}/v_{out}) = \sqrt{2}$. Yet, we observe $(B_{out}/v_{in}) \approx 3$, while the modified Sweet-Parker model, Eq. (3.1.2), predicts $(B_{out}/v_{in}) \approx \sqrt{2}$. That is the only significant discrepancy with the modified Sweet-Parker model and can be attributed to the time-dependent nature of the elongating current layer.

Panels (a-c) of Figure 3.5 show profiles of the reconnected magnetic field B_y, reconnection current J_z, and plasma outflow velocity v_x along the $y = 0$ axis at four different times. As the current layer extends, accumulation of the reconnected field just outside of the current layer is apparent. Such accumulation easily accounts for the discrepancy with the Sweet-Parker model described above. The profiles of J_z show how the current layer itself grows and elongates in time. Note that the small dips in current density observed at the ends of the current layer are the remnants of the Syrovatsky singularities[144] largely removed by the effect of kinematic viscosity. Similarly, the rounded-off shape of the current profiles is due to the viscous force counter-acting the magnetic tension forces pulling the plasma out of the reconnection layer. The outflow velocity itself is observed to increase linearly from the X-point to the point of maximum outflow, followed by a sudden drop-off whenever magnetic back-pressure becomes significant. It is remarkable that even in the regime of non-negligible kinematic viscosity, the forces within the current layer self-balance in a way to provide constant plasma acceleration along the layer.

Contour plots of the magnetic flux ψ, plasma current J_z, and plasma stream function ϕ over the full computational domain at $t = 781$ are presented in panels (d-f) of Figure 3.5. At this time the back pressure of the reconnected B-field, which is not being convected away from the RR sufficiently fast, is beginning to influence

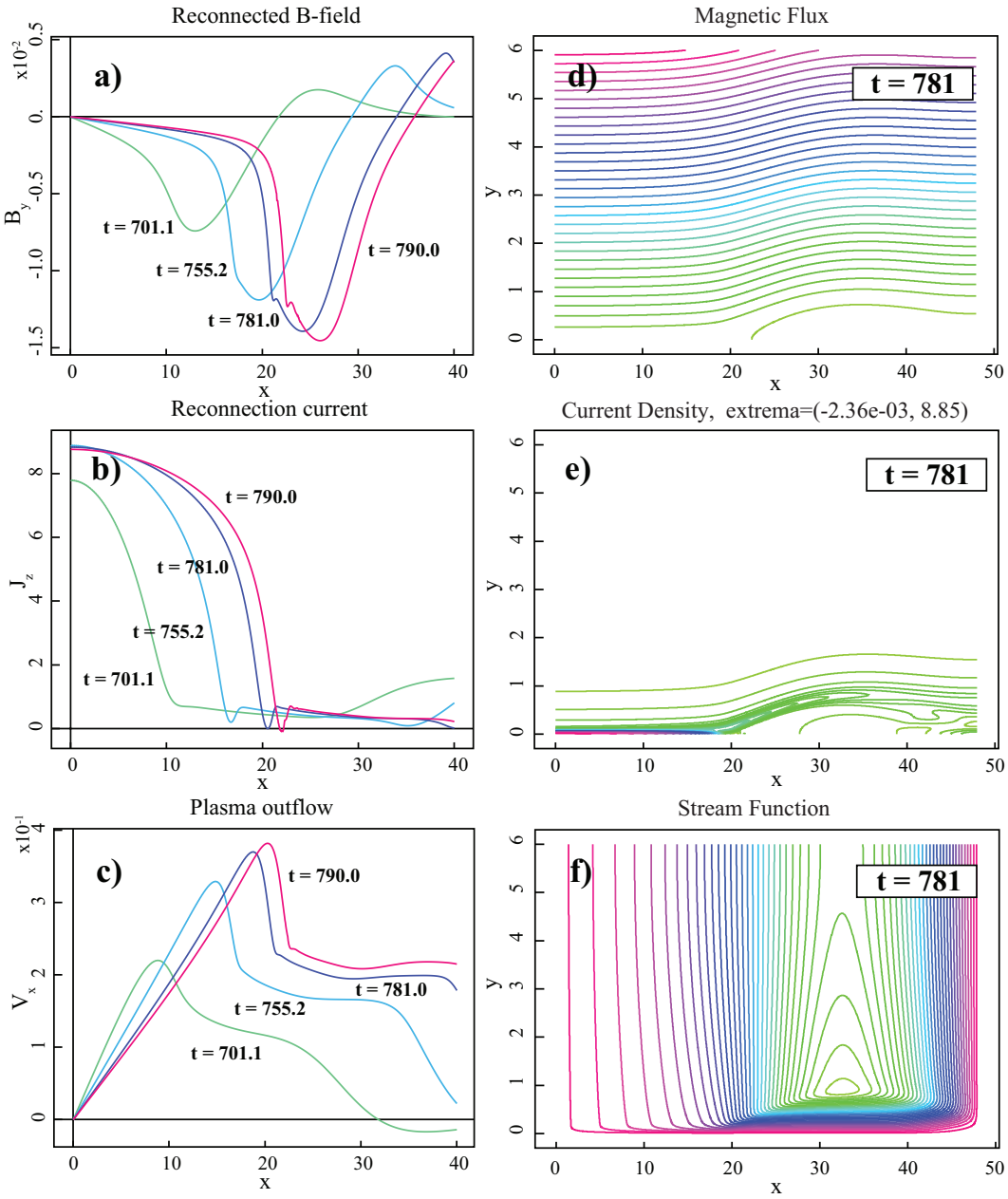

Figure 3.5: Panels (a-c) show profiles of B_y, J_z, and v_x, respectively, along the $y = 0$ axis through the reconnection layer at four different times before and after the peak reconnection rate has been achieved. Panels (d-f) show contour plots of ψ, J_z, and ϕ, respectively, late in the simulation at $t = 781$.

the dynamics of the current layer. Panels (d) and (e) demonstrate exactly why that happens: a pair of merging magnetic islands are formed in the outflows of the current layer and begin to obstruct further outward motion of magnetic field lines. (One of the islands can be seen in the figure, while the other is located symmetrically on the left hand side of the current layer. Due to the domain periodicity, the two islands interact and eventually merge.)

Particular attention should be paid to the self-established flow pattern into and out of the domain through the current layer, shown in panel (f) of Figure 3.5. Since no flow velocity is explicitly specified on the top "open" boundary of the domain, the flow pattern that does form is due solely to the properties of visco-resistive MHD and the drive supplied by the tension of reconnecting magnetic field lines. We observe that none of the flow that goes through the current layer recirculated within the domain, but instead chooses to leave the system completely. Thus, the flow accelerated by the reconnection has little influence on further evolution of the RR.

The large system simulation results described above have also been verified by varying the size of the simulation domain $[L_x, L_y]$ with no other changes to either initial conditions or plasma parameters of the simulation. Little quantitative and no qualitative difference in the simulation results was observed in increasing L_y from 6 to 8, or decreasing L_x from 48 to 36. In fact, the former had almost no effect on the simulation at all. And the latter naturally resulted in earlier onset of the boundary effects with no other discernable differences in the results. We again point out that here the periodic boundary only begins to affect the reconnection rate and current layer dynamics when the current layer becomes $\approx 1/2$ of the system's period.

3.3 Magnetic reconnection in electron MHD.

We now turn from visco-resistive MHD to the electron MHD model and conduct a set of numerical simulations which are equivalent to that described in Section 3.2 above.

3.3.1 Description of the model.

The electron MHD plasma fluid model is completely described by the Equation (3.1.4). As has already been emphasized in Section 3.1.2, electron MHD is a single-fluid model where ions are assumed to be stationary and magnetic field is coupled only to the electron fluid. It is also intrinsically an incompressible model, as

$$\mathbf{v}_e = -d_i \mathbf{J} \Rightarrow \nabla \cdot \mathbf{v}_e = -d_i \nabla \cdot \mathbf{J} = 0.$$

The key difference between the reduced visco-resistive MHD and electron MHD is that in electron MHD plasma flows also carry charge and therefore current, thus self-generating magnetic fields around any plasma flow channel.

As in reduced MHD, we employ the condition of incompressibility to eliminate pressure from Eq. (3.1.4) by reproducing the transformations applied to Eqs. (3.2.1-3.2.2). Resulting system of two coupled PDEs has the following form:

$$\begin{aligned} \frac{\partial}{\partial t}(B_z - d_e^2 \nabla^2 B_z) &+ d_i \nabla \cdot \left[(\nabla^2 \psi)\hat{z} \times \nabla \psi - d_e^2 (\nabla^2 B_z)\hat{z} \times \nabla B_z + d_i \nu \nabla (\nabla^2 B_z) \right] \\ &= \eta \nabla^2 B_z \qquad (3.3.1) \\ \frac{\partial}{\partial t}(\psi - d_e^2 \nabla^2 \psi) &+ d_i \nabla \cdot \left[(\psi - d_e^2 \nabla^2 \psi)\hat{z} \times \nabla B_z + d_i \nu \nabla (\nabla^2 \psi) \right] = \eta \nabla^2 \psi, \end{aligned}$$

where the out-of-plane magnetic field B_z now acts as the poloidal electron flow stream function.

Studying Eqs. (3.3.1), we observe that the ion inertial length d_i can be eliminated from the system by renormalizing time $t \to t/d_i$ and absorbing factors of d_i into the

dissipation coefficients. Therefore, while the reconnection rate should vary linearly with d_i in accordance with the Sweet-Parker-like estimate in Eq. (3.1.9), evolution of the system described by Eqs. (3.3.1) is otherwise independent of d_i, which is only to be expected in a system where ions have been assumed to be stationary.

Dispersion relation in uniform B-field.

It is useful to derive the dispersion relation for the system described by Eqs. (3.3.1) in a uniform magnetic field background. Let the background B-field be given by $\mathbf{B}_0 = \bar{B}\hat{y}$, so that the only non-zero equilibrium quantity in Eqs. (3.3.1) is $\nabla\psi_0 = \bar{B}\hat{x}$. Assuming a perturbation of the form $\xi = \tilde{\xi}\exp\left[i(k_x x + k_y y - \omega t)\right]$, the following dispersion relation is easily derived:

$$\omega = \frac{\pm d_i \bar{B} k k_y - i(\eta k^2 + d_i^2 \nu k^4)}{1 + d_e^2 k^2}, \tag{3.3.2}$$

where $k^2 \equiv k_x^2 + k_y^2$ and the only wave present in the system is the dispersive Whistler wave with phase velocity $\omega/k \sim k_y$. Also observe that whenever $d_i(\mathbf{k}\cdot\mathbf{B}_0) \gg \eta k$, resistivity does not significantly damp the wave, and even in the limit of $d_e k \gg 1$ electron inertia only limits the real frequency to $(d_i/d_e)(\mathbf{k}\cdot\mathbf{B}_0/d_e k)$ without introducing any explicit damping. Thus, in the limit of high $k_{\parallel} \equiv (\mathbf{k}\cdot\mathbf{B}/|\mathbf{B}|)$, plasma resistivity plays little role and the only damping is provided by the electron viscosity term, which is consistent with the qualitative analysis of the reconnection layer in Section 3.1.2 and previous numerical studies referenced therein. In the following numerical simulations, plasma resistivity has been neglected by setting $\eta = 0$.

Linear properties of EMHD in non-uniform B-field.

Some of the behavior of an EMHD system in non-uniform magnetic field can also be studied analytically. Here, we are interested in finding potentially unstable modes of

such a system and therefore discard all of the dissipative effects, $\eta = \nu = 0$, in order to simplify the analysis. Let the background magnetic field have no curvature and be non-uniform in the direction perpendicular to itself, $\mathbf{B}_0 = \bar{B}_y(x)\hat{y} + \bar{B}_z(x)\hat{z}$ and consider a perturbation of the form $\xi = \tilde{\xi}(x)\exp[i(k_y y - \omega t)]$.

First, let the gradient scales of interest be much larger than the electron inertial length – $\nabla_x, k_y \ll 1/d_e$. Then, Eqs. (3.3.1) are reduced to:

$$\begin{aligned} \omega\tilde{b}_z &+ d_i k_y \left[\bar{B}_y''\tilde{\psi} - \bar{B}_y\left(\partial_x^2 - k_y^2\right)\tilde{\psi}\right] = 0 \\ \omega\tilde{\psi} &+ d_i k_y \left(\bar{B}_y\tilde{b}_z - \bar{B}_z'\tilde{\psi}\right) = 0, \end{aligned}$$

where $F' \equiv \partial_x F$. Assuming $\bar{B}_y(x) > 0$ and substituting for $\tilde{b}_z$ in terms of $\tilde{\psi}$, these can be further simplified to yield:

$$\left[\frac{\bar{B}_y''}{\bar{B}_y} + \left(\frac{\bar{B}_z'}{2\bar{B}_y}\right)^2 - \left(\partial_x^2 - k_y^2\right)\right]\tilde{\psi} = \left(\frac{\omega}{d_i k_y \bar{B}_y} - \frac{\bar{B}_z'}{2\bar{B}_y}\right)^2\tilde{\psi}. \tag{3.3.3}$$

From the form of Eq. (3.3.3), it is apparent that for given $\bar{B}_z(x)$, whenever $(\bar{B}_y''/\bar{B}_y)$ is sufficiently large and negative in some interval in x, a localized instability will result. It is also clear that presence of a non-uniform guide-field $\bar{B}_z$ acts to stabilize the instability, while uniform $\bar{B}_z$ of arbitrary magnitude does not have any effect on the system. We further observe that $\bar{B}_y''$ is a gradient of an out-of-plane current density and $(\bar{B}_y''/\bar{B}_y)$ is always negative on the inflow sides of a reconnection current layer, where $\bar{B}_y$ are the reconnecting B-field components. Figure 3.6 shows a schematic of how such an instability develops in a system with no magnetic guide-field.

In the absence of guide-field gradients, $\bar{B}_z' = 0$, and assuming that $\tilde{\psi}(x) \neq 0$, a substitution of the form $f \equiv (\tilde{\psi}'/\tilde{\psi})\bar{B}_y{}^2 - \bar{B}_y{}'\bar{B}_y$ reduces Eq. (3.3.3) to a first order non-linear ordinary differential equation:

$$f' + \frac{f^2}{\bar{B}_y^2} = k_y^2\bar{B}_y^2 - \Omega^2, \tag{3.3.4}$$

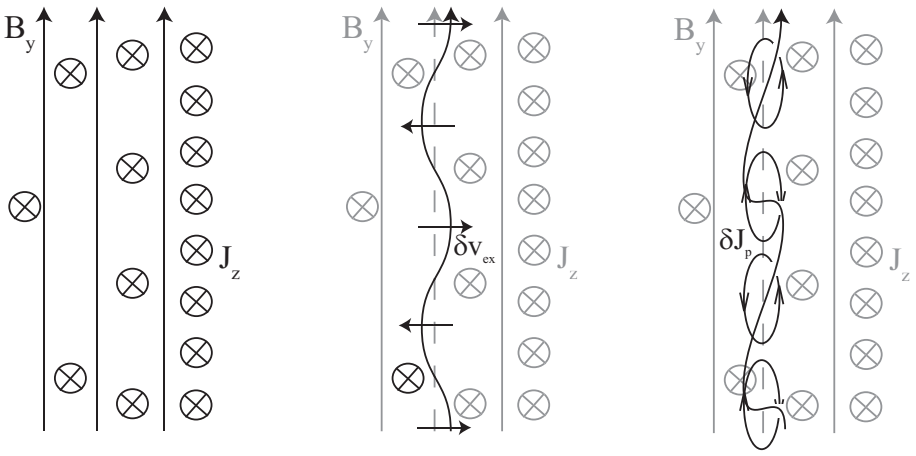

Figure 3.6: Schematic of how a large scale instability with $\nabla_x, k_y \ll 1/d_e$ can develop in an electron MHD system with background out-of-plane current density gradient. A perturbed in-plane magnetic field line is swept by the sheared out-of-plane electron flow, which generates oscillating out-of-plane magnetic fields. Resulting in-plane plasma currents reinforce the perturbation whenever $(\bar{J}_z'/\bar{B}_y) < 0$.

where $\Omega \equiv \omega/(d_i k_y)$. For a given profile of $\bar{B}_y(x) > 0$, Eq. (3.3.4) can be solved numerically and possibly analytically in some special cases. However, in the present work, we do not pursue this line of inquiry any further.

When gradient scales of the background, perturbation, or both are sufficiently small for the electron inertia to begin playing a role, intuitive treatment of the full linearized form of Eqs. (3.3.1) in non-uniform background B-field becomes prohibitive. In the limit of zero background guide-field gradients and no dissipation, linearized Eqs. (3.3.1) are:

$$\begin{aligned} \omega\left[1-d_e^2\left(\partial_x^2-k_y^2\right)\right]\tilde{b}_z &+ d_i k_y\left[\bar{B}_y''-\bar{B}_y\left(\partial_x^2-k_y^2\right)\right]\tilde{\psi}=0 \\ \omega\left[1-d_e^2\left(\partial_x^2-k_y^2\right)\right]\tilde{\psi} &+ d_i k_y\left(\bar{B}_y-d_e^2\bar{B}_y''\right)\tilde{b}_z=0. \end{aligned}$$

We now assume that the perturbation is localized in x such that $\tilde{\xi}(x) \gg d_e^2\left(\partial_x^2-k_y^2\right)\tilde{\xi}(x)$. (Note that this does not necessarily imply the length scale of the perturbation to be

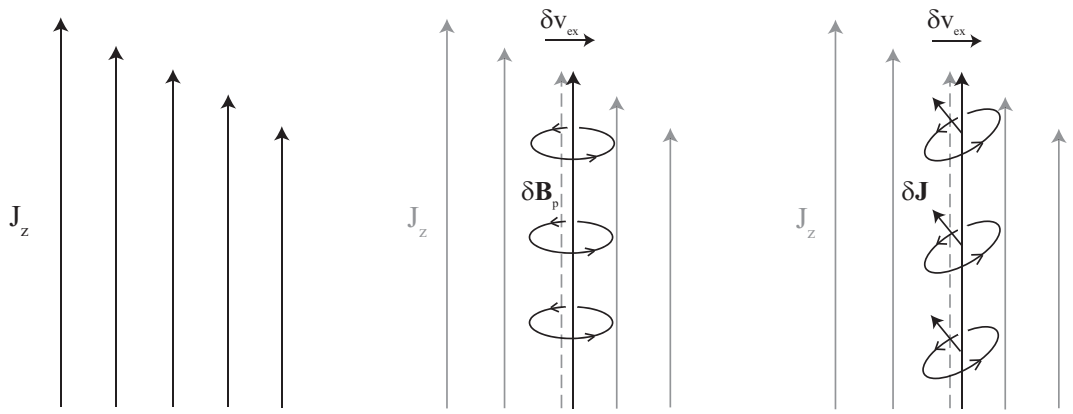

Figure 3.7: Schematic of how a localized instability can develop in an electron MHD system with strong current gradients in weak magnetic field. A localized electron flow perturbation in the direction of the current gradient displaces some of the background current due to the effect of electron inertia, resulting in a perturbation in the poloidal B-field. The same sheared background electron current then differentially rotates the perturbation and generates poloidal plasma currents which reinforce the initial perturbation.

much larger than the electron inertial scale.) Then, for $\bar{B}_y(x) \neq 0$, we have the following dispersion relation:

$$\left(\frac{\omega}{d_i k_y \bar{B}_y}\right)^2 \tilde{\psi} = \left(1 - d_e^2 \frac{\bar{B}_y''}{\bar{B}_y}\right) \left[\frac{\bar{B}_y''}{\bar{B}_y} - \left(\partial_x^2 - k_y^2\right)\right] \tilde{\psi}. \tag{3.3.5}$$

If $1 \gg d_e^2(\bar{B}_y''/\bar{B}_y)$, Eq. (3.3.5) is reduced to Eq. (3.3.3). Therefore, we consider a background profile of $\bar{B}_y$ such that $1 \lesssim d_e^2(\bar{B}_y''/\bar{B}_y)$. From the assumption above, it follows that $(\bar{B}_y''/\bar{B}_y)\tilde{\psi} \gg \left(\partial_x^2 - k_y^2\right)\tilde{\psi}$ and Eq. (3.3.5) can be further reduced to yield:

$$\left(\frac{\omega}{d_i k_y}\right)^2 = \bar{B}_y'' \left(\bar{B}_y - d_e^2 \bar{B}_y''\right). \tag{3.3.6}$$

From Eq. (3.3.6) we observe that whenever $d_e^2 \bar{B}_y''(x) > \bar{B}_y(x)$ for some region in x, a localized non-propagating instability with $\tilde{\xi}(x) \gg d_e^2 \left(\partial_x^2 - k_y^2\right)\tilde{\xi}(x)$ may grow. Figure 3.7 shows a schematic of how such localized instability can be generated.

Qualitative nonlinear analysis of an inertia-less EMHD RR.

An analytic description for the collapse mechanism of an EMHD current layer with electron inertia effects neglected has recently been offered by Shaikhislamov[133]. Though, as we explain below, the derivation given by Shaikhislamov does not include some of the important effects present in a reconnecting EMHD system, here we follow the general spirit of the derivation.

We again begin by neglecting the effects of electron inertia and resistivity and taking the zero magnetic guide-field limit. Then, Eq. (3.1.4) that describes the full EMHD system is reduced to:

$$\mathbf{E} = d_i \mathbf{J} \times \mathbf{B} - d_i \nabla p_e - d_i^2 \nu \nabla^2 \mathbf{J}.$$

The key observation made by Shaikhislamov[133] is that application of the $\nabla \times \nabla \times$ operator to the above vector equation produces an equation for the time-dependence of the plasma current density $\mathbf{J}$:

$$\left(\frac{\partial}{\partial t} + d_i^2 \nu \nabla^4 \right) \mathbf{J} = d_i \nabla \times \left[(\mathbf{J} \cdot \nabla) \mathbf{B} - (\mathbf{B} \cdot \nabla) \mathbf{J} \right]. \tag{3.3.7}$$

Following Shaikhislamov[133], we also consider two projections of Eq. (3.3.7) – in the out-of-plane $\hat{z}$-direction and plasma outflow $\hat{x}$-direction – along the outflow symmetry axis (x-axis) of the reconnection layer:

$$\left(\frac{\partial}{\partial t} + d_i^2 \nu \nabla^4 \right) J_z = 2 J_z \frac{\partial v_{ex}}{\partial x} - v_{ex} \frac{\partial J_z}{\partial x} - B_y \frac{\partial^2 v_{ex}}{\partial y^2} \tag{3.3.8}$$

$$\left(\frac{\partial}{\partial t} + d_i^2 \nu \nabla^4 \right) v_{ex} = d_i^2 \left(B_y \frac{\partial^2 J_z}{\partial y^2} + \frac{\partial B_x}{\partial y} \frac{\partial J_z}{\partial x} \right), \tag{3.3.9}$$

where we recall that $\mathbf{v}_e = -d_i \mathbf{J}$ and several terms have been dropped due to symmetry considerations. It is now easy to show from Sweet-Parker-like considerations presented

in Section 3.1.2, that in a sufficiently elongated current layer every term on the right hand side (RHS) of Eq. (3.3.8), as well as Eq. (3.3.9), is of the same order in δ/L. It is this fact that in our view renders further simplification of the system of Eqs. (3.3.8)-(3.3.9) impossible.

However, here we pursue the method further and apply two more projections of Eq. (3.3.7) – in the out-of-plane $\hat{z}$-direction and plasma inflow $\hat{y}$-direction – along the inflow symmetry axis (y-axis) of the reconnection layer:

$$\left(\frac{\partial}{\partial t} + d_i^2 \nu \nabla^4\right) J_z = -2J_z \frac{\partial v_{ey}}{\partial y} - v_{ey} \frac{\partial J_z}{\partial y} + B_x \frac{\partial^2 v_{ey}}{\partial y^2} \tag{3.3.10}$$

$$\left(\frac{\partial}{\partial t} + d_i^2 \nu \nabla^4\right) v_{ey} = -d_i^2 \left(B_x \frac{\partial^2 J_z}{\partial x^2} + \frac{\partial B_y}{\partial y} \frac{\partial J_z}{\partial y}\right), \tag{3.3.11}$$

where all terms on the RHS of each equation are again of the same order in δ/L.

Though it might be possible to solve the system of Eqs. (3.3.8)-(3.3.11) in time by applying appropriate approximations in the limit of $\delta/L \ll 1$, we do not attempt to do it here. Instead, we simply analyze each of the RHS terms for each of the equations to determine whether it acts to locally increase or decrease reconnection current and electron inflow/outflow velocity in time within the reconnection current layer. While no definitive conclusion can be made about the overall sign of the RHS for Eq. (3.3.8) and Eq. (3.3.10), it is easy to show that both RHS terms of Eq. (3.3.9) act to locally increase the electron outflow and both RHS terms of Eq. (3.3.11) act to locally increase the electron inflow velocity within the electron current layer. Thus, even in the fully non-linear regime, any EMHD current layer should be expected to collapse by locally self-generating both inflow and outflow through the RR.

Numerical problem set-up.

In all of the simulations described below, $d_i = 2.0$ has been chosen. Under the assumption of hydrogen plasma, it follows that $d_e = 4.667 * 10^{-2}$.

To be able to compare reduced MHD and EMHD results, the EMHD simulations are conducted in the same semi-open, semi-periodic rectangular domain as those described in Section 3.2.1. On the open boundary, equivalent BC are applied to the electron stream function B_z as those applied to the plasma stream function ϕ. Simulations are also initialized with the identical Harris current sheet of half-width $\lambda = .5$ and a localized perturbation of magnitude $\epsilon = 10^{-4}$ as in Section 3.2.1. Note that $\lambda = d_i/4 \approx 10 d_e$, *i.e.* gradient scale of the initial condition is a fraction of the scale on which ions can be legitimately assumed to be stationary in a two-fluid model, yet much greater than the electron inertial scale.

We now describe a number of EMHD simulations where sensitivity of the solution to the size of the computational domain $[L_x, L_y]$ and kinematic electron viscosity ν is investigated.

3.3.2 Viscosity dominated simulation results.

Whenever kinematic electron viscosity is sufficiently large, the viscous diffusion scale l_ν becomes greater than the electron inertial scale d_e and dominates the structure of the RR.

Figure 3.8 shows snap-shots of magnetic flux, reconnection current and electron flow stream function over a full computational domain, panels (a-b), and directly around the current later, panels (c-d) from simulations with $\nu = 4 * 10^{-5}$ after an electron MHD reconnection region has fully developed. It is immediately clear that

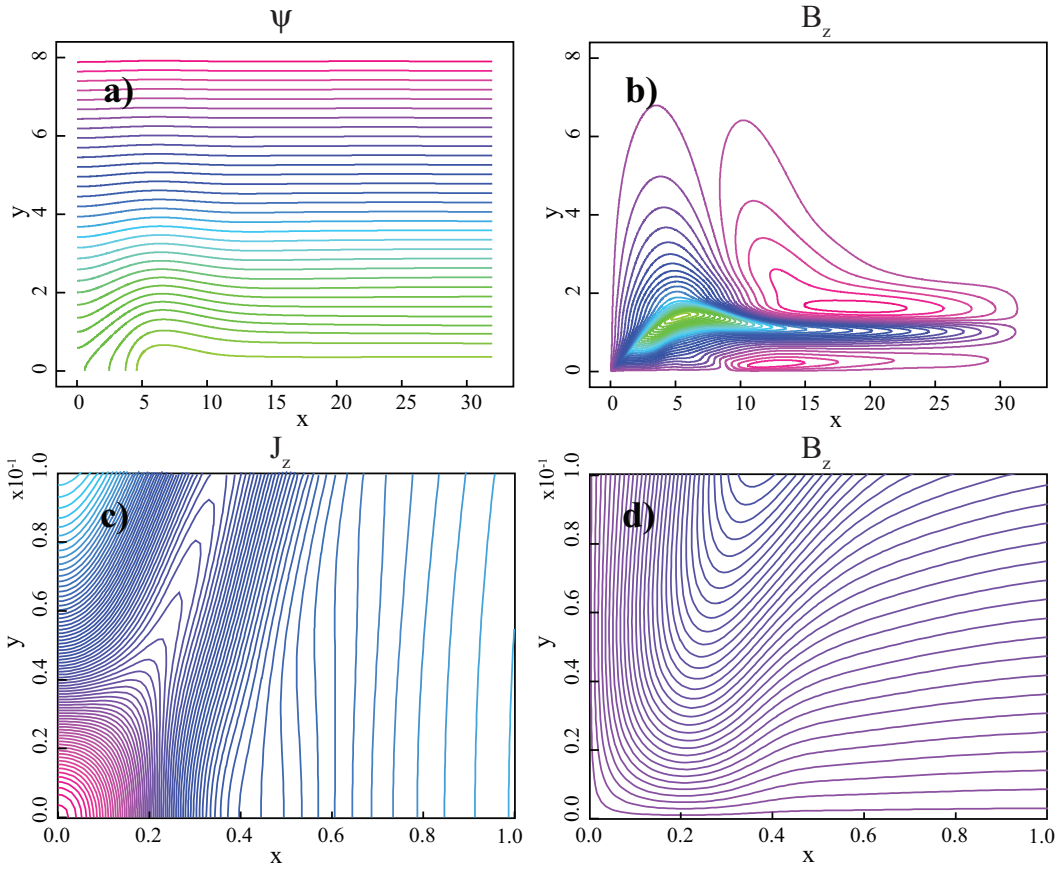

Figure 3.8: Snap-shots of (a) magnetic flux ψ and (b) out-of-plane B-field B_z over a full computational domain; and (c) out-of-plane current J_z and (d) B_z around the current layer from simulations with $\nu = 4 * 10^{-5}$ after an electron MHD reconnection region has fully developed.

unlike resistive MHD, the EMHD RR remains localized near the X-point. Also unlike the resistive MHD plasma flow, the in-plane electron flow chooses to stay entirely within the computational domain recirculating the outflow from the RR back into the RR. Despite the localization, panel (c) of Fig. 3.8 shows that the EMHD reconnection current layer remains elongated with $\delta/L \approx 5$. For the chosen value of electron viscosity, the half-width of the current layer $\delta/2$ is observed to approximately equal the electron inertial scale $d_e = 4.667 * 10^{-2}$, which suggests that for $\nu \gtrsim 4 * 10^{-5}$, $l_\nu > d_e$ and vice versa. Finally, rotation of the electron flow through the RR is shown to be localized within the current layer.

Time evolution of the viscous EMHD reconnection region for various domain sizes and values of kinematic electron viscosity is described in Figure 3.9. Panel (a) shows the time evolution of the reconnection rate $d\psi/dt$ at the X-point for four different simulation domain sizes with $\nu = 4 * 10^{-5}$. Unlike analogous resistive MHD results shown in Fig. 3.4 above, in EMHD we observe a short initial quasi-linear development of the tearing instability followed by an explosive onset of fast reconnection with peak reconnection rates orders of magnitude higher than those achieved in resistive MHD. It is apparent from the data that the dynamics of that transition to fast reconnection is independent of the system size when the domain sizes considered are sufficiently large. However, the long-term behavior of the system does appear to be sensitive to the system length. (The width variation between $L_y = 6$ and $L_y = 8$ has virtually no effect on the system. That is to be expected since, as shown in Figure 3.8, in-plane electron flow chooses to circulate close to the initial Harris current layer.) Panel (b) of Figure 3.9 shows time evolution of $d\psi/dt$ for a domain size of $[L_x, L_y] = [48, 8]$ and a range of kinematic electron viscosity values $\nu \in [4*10^{-5}, 4*10^{-4}]$. Here, we observe

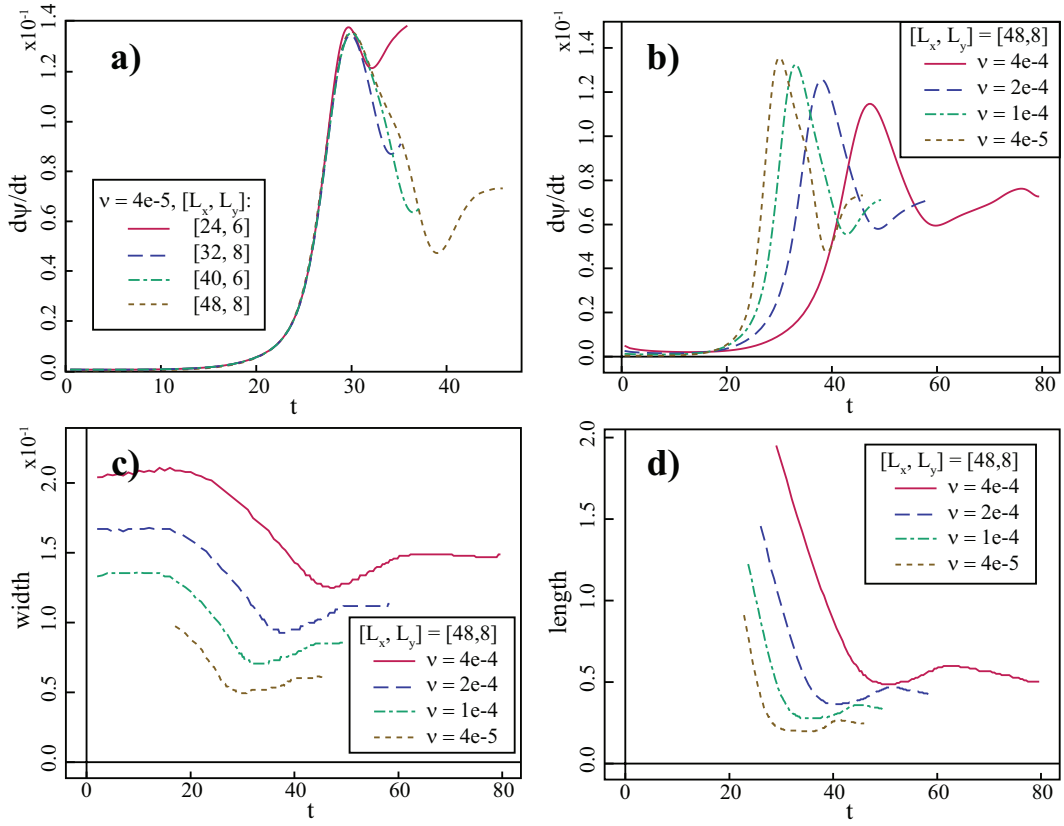

Figure 3.9: Time-traces of the EMHD reconnection rate and RR dimensions for different domain sizes and magnitudes of kinematic electron viscosity. Panel (a) shows the variation in reconnection rate time evolution $d\psi/dt$ at the X-point with domain size for $\nu = 4 * 10^{-5}$; and panels (b,c,d) the variation in time-evolution of $d\psi/dt$, RR half-width and RR half-length with ν for a given domain size, respectively. Half-width and half-length of the RR are determined by tracking the location of the peak in in-plane electron flow inflow and outflow velocities, respectively.

that the rate of the onset and peak magnitude of fast reconnection can be sensitive to electron viscosity, while the long term evolution appears to settle to a ν-independent reconnection rate.

Panels (c) and (d) of Figure 3.9 show the time-evolution of half-width and half-length of the RR based on the poloidal electron inflow and outflow profiles, respectively. (Note that in the electron viscosity dominated regime, these correspond well with the reconnection current layer dimensions.) The collapse of the RR from that developed during the initial linear and early non-linear tearing mode evolution to a much shorter one following the onset of fast reconnection is apparent. After the collapse, little temporal variation in RR dimensions is observed. Unlike the ever expanding RR in resistive MHD, viscous EMHD RR width δ and length L appear to stabilize at $d_e < \delta/2 < L/2 < d_i$ and are smaller for lower values of ν.

Leaving aside the time-asymptotic behavior of the system, Figure 3.10 shows how the reconnection rate at the X-point (panel (a)), half-width of the RR (panel (b)), outflow electron velocity (panel (c)), and inflow magnetic field (panel (d)) scale with ν at the time when peak reconnection rate is achieved. In order to separate any possible effects of electron inertia, which are discussed below, several simulation runs with $d_e = 0$ have also been conducted and the data from those runs is shown, as well. It is apparent that for sufficiently small values of ν, maximum reconnection rate becomes independent of ν. Yet, other characteristic RR quantities display prominent power law dependencies on the magnitude of viscous electron dissipation. In particular, whenever electron inertia has no effect on the system, $\delta \propto \nu^{2/5}$, $v_{out} \propto \nu^{-1/5}$, and $B_{in} \propto \nu^{1/5}$. Observe that these are consistent with the Sweet-Parker-like analysis of an EMHD RR in Section 3.1.2 above and give a scaling of $\delta/L \propto \nu^0$ for the RR aspect

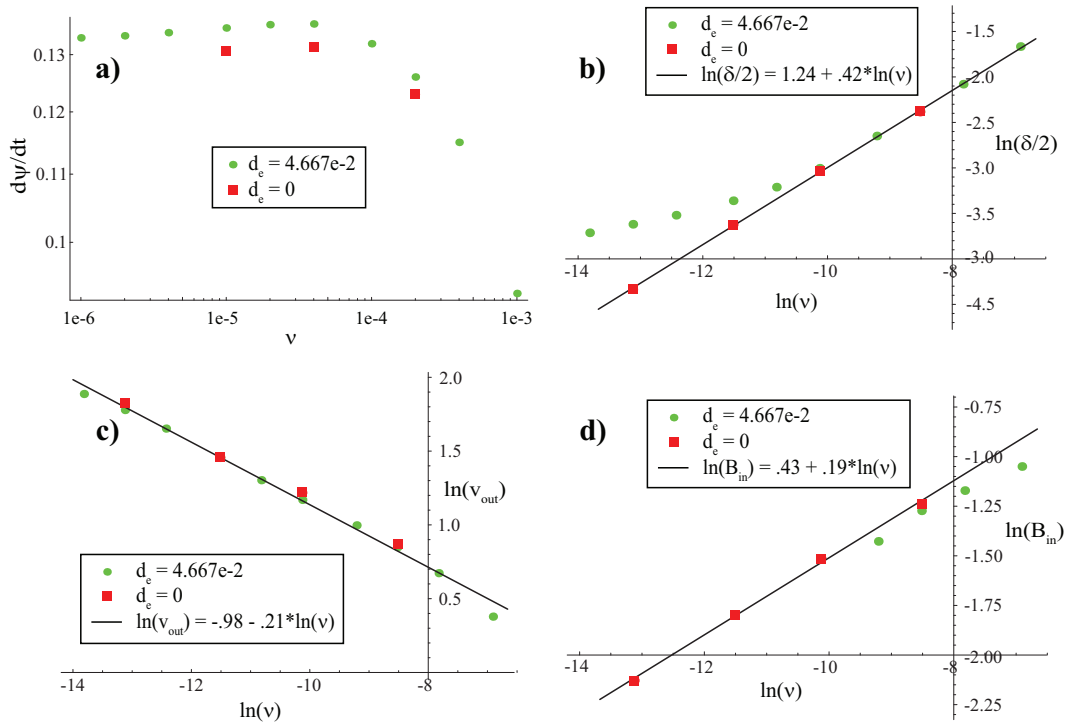

Figure 3.10: Scaling with kinematic electron viscosity ν of (a) peak reconnection rate at X-point; (b) half-width of RR – $\delta/2$; (c) outflow velocity – v_{out}; and (d) inflow magnetic field – B_{in}. Quantities in panels (b-d) are evaluated at the time of peak reconnection rate and at the location of peak inflow/outflow velocity. All simulations have been conducted in a domain of size $[L_x, L_y] = [48, 8]$.

ratio.

3.3.3 Two scale EMHD reconnection.

We now focus on the simulation results where electron viscosity is sufficiently small to allow the RR half-width $\delta/2$ to become smaller than d_e. Panel (b) of Fig. 3.10 clearly demonstrates that the viscous scaling applicable to the width of the reconnection inflow region becomes invalid for $\delta/2 < d_e$, suggesting that a new RR structure develops when $l_\nu \lesssim d_e$. However, we note that the v_{out} scaling shown in panel (c) of Fig. 3.10 does not appear to depend on the presence of the electron inertia for the range of kinematic electron viscosities considered here. Similarly, the peak reconnection rate shows little influence of electron inertia on the rate of magnetic flux passing through the RR with and without the electron inertia effects present in the system.

Figure 3.11 shows the time evolution and the two-scale structure of the RR from a simulation with $\nu = 10^{-6}$. During the onset of fast reconnection, the peak plasma inflow velocity is observed to greatly increase and the inflow layer is forced to widen due to the effects of electron inertia. At the same time, the reconnection current channel is observed to peak and become narrower, thus separating the boundary of the electron inflow layer from the current diffusion region. Profiles of the electron inflow velocity and reconnection current across the RR downstream of the X-point, at $x = 0.15$, show particularly dramatic scale separation: $\sim d_e$ wide inflow layer and a much narrower sub-d_e current channel embedded in another wider and weaker current layer associated with the electron inflow layer. Thus, it is clear that in EMHD, for sufficiently small magnitude of ν, the d_e scale determines the width of the inflow layer, while kinematic electron viscosity determines the width of the reconnection current layer.

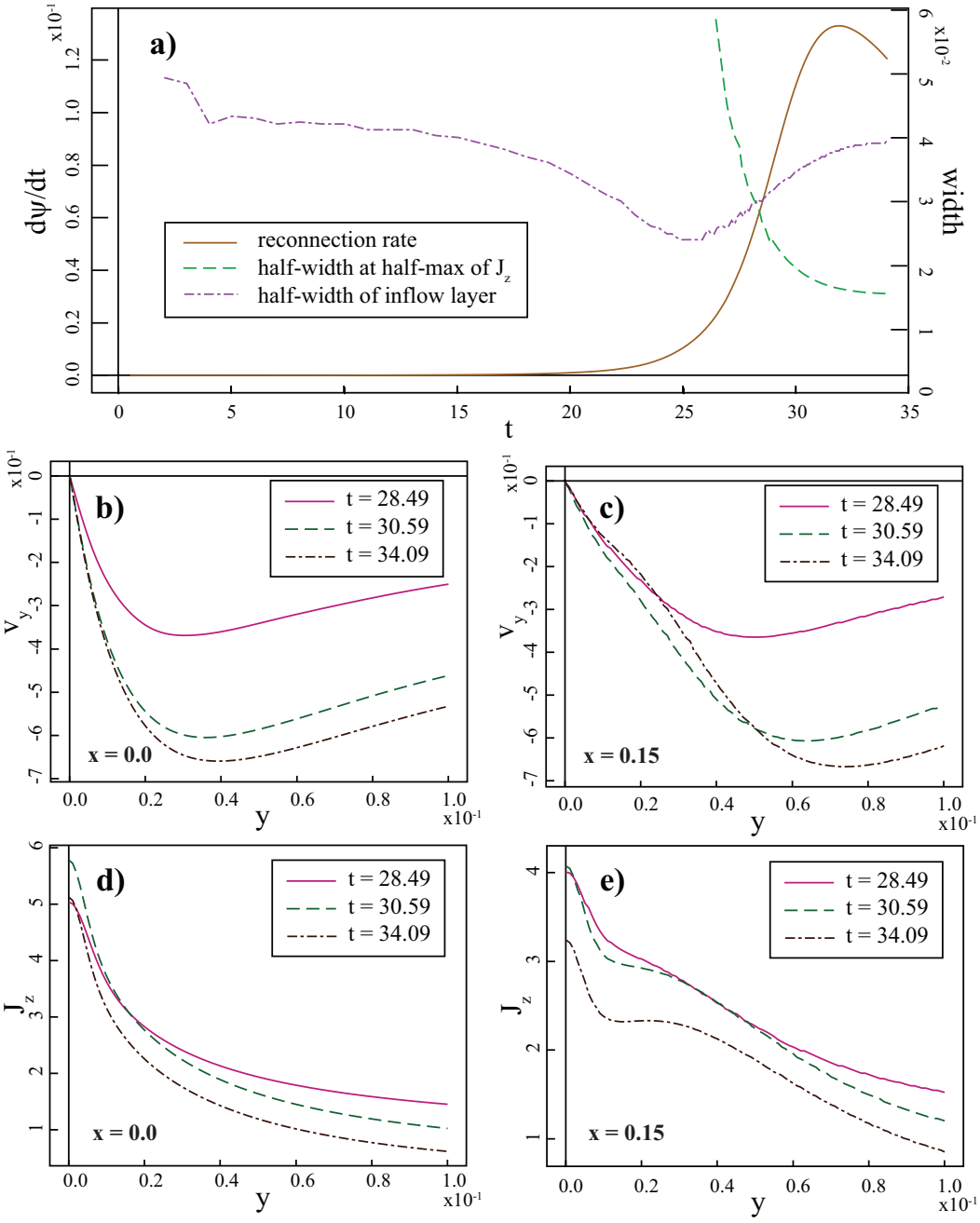

Figure 3.11: Results of a simulation with $\nu = 10^{-6}$. Time evolution of the reconnection rate and two measures of the RR width are shown in panel (a). Panels (b,c) show profiles of inflow electron velocity and (d,e) of reconnection current across the RR at two locations along the layer, $x = 0.0$ and $x = 0.15$, at three different times during the evolution. The simulation has been conducted in a domain of size $[L_x, L_y] = [48, 8]$.

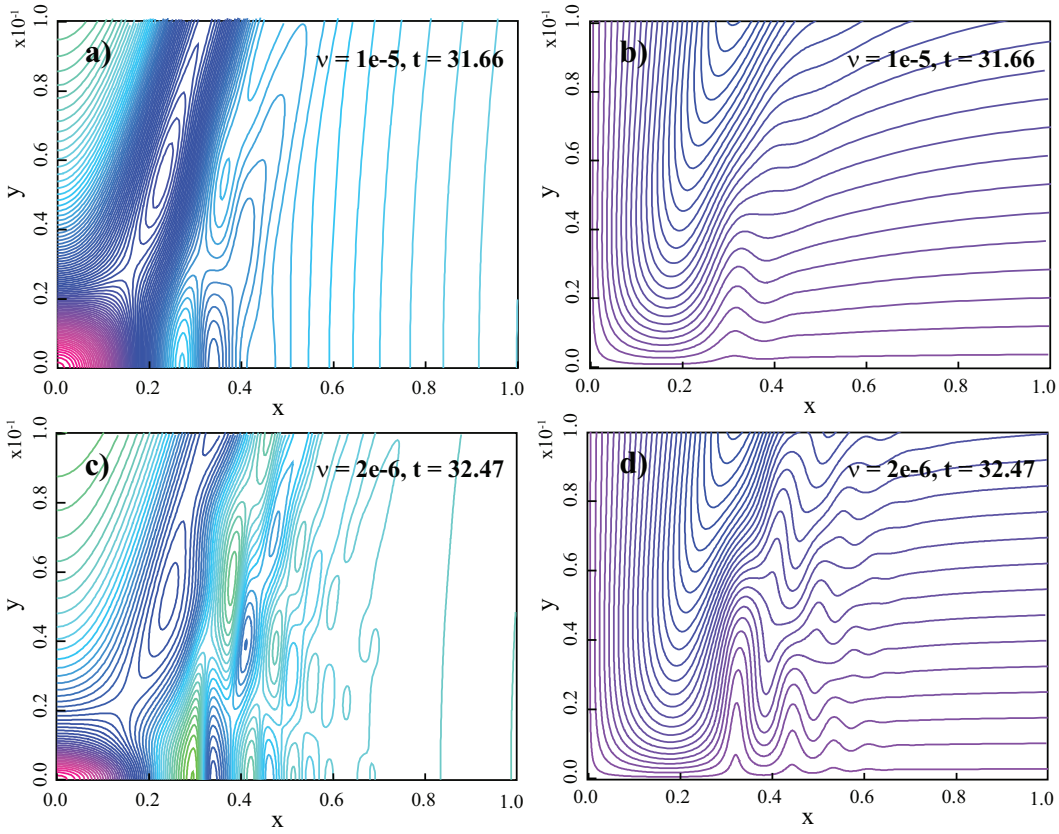

Figure 3.12: Contour plots of J_z, panels (a,c), and B_z, panels (b,d), around the RR after onset of fast reconnection from two simulation runs with $\nu = 10^{-5}$, panels (a,b), and $\nu = 2 * 10^{-6}$, panels (c,d). Both simulations have been conducted in a domain of size $[L_x, L_y] = [40, 6]$.

Contours of J_z and B_z around the RR following the onset of fast reconnection are shown in Figure 3.12 from two simulation runs with $\nu = 10^{-5}$, panels (a,b) and $\nu = 2{*}10^{-6}$, panels (c,d), both of which have $l_\nu < d_e$. These can be compared to panels (c,d) of Fig. 3.8 above, where at $\nu = 4 * 10^{-5}$ electron viscous and inertial scales are about equal. Here, again, continued narrowing of the current layer with decreasing ν is apparent. But even more importantly, an instability in the outflow region of the RR can now be observed. Absent when $l_\nu \geq d_e$, more and more of the instability vortices appear as the diffusion due to kinematic electron viscosity is decreased. The observed vortices grow on the outflow side of the current layer gradient, are non-propagating, and decay as the reconnection current gradient decreases. These are not signatures of any kind of turbulence or numerical spatial resolution problems. Instead, we believe this instability to be the one identified in Section 3.3.1 as a localized instability which can grow on a current gradient in weak magnetic fields due to interaction of electron inertial and ideal electron MHD effects.

Very similar signature of a d_e-scale instability has been previously observed in two-dimensional EMHD simulations of merging magnetic flux bundles by Biskamp *et. al.*[19]. (See Fig. 4 of [19].) However, there, the instability mechanism was described as a Kelvin-Helmholtz instability attributable purely to the shear in the fluid flow and responsible for generating turbulence.

3.3.4 Discussion and conclusions from the EMHD study.

While the simulation data presented in Figures 3.8-3.12 is not sufficient to determine the true long-term behavior of a reconnecting electron MHD system, these results provide several important clues to understanding the dynamic evolution of the system. We believe that the super-d_e scale instability described in Section 3.3.1 above serves

as the trigger for the onset of the RR collapse. In the absence of any magnetic guide-field, current layer formed by the weakly non-linear tearing mode provides sufficient current density gradient to destabilize the mode. As shown in Figure 3.6, development of the instability leads to faster electron inflow and greater compression of the reconnecting magnetic field lines. This, in turn, generates even stronger current gradients, which is what accounts for the explosive character of the fast reconnection onset. The qualitative non-linear analysis presented in Section 3.3.1 also supports that conclusion.

Saturation of the current layer collapse and maximum achievable reconnection rate appears to be ultimately due to the geometric effect of having to bend the inflowing magnetic field lines in order to accomplish reconnection through a microscopic current diffusion layer; while tension of the reconnected field lines forces the plasma outflow to accelerate to the maximum velocity allowable by the electron viscous forces and therefore maximally reduce the current layer length. The main evidence for such a conclusion comes from the Sweet-Parker-like arguments presented in Section 3.1.2 and observed independence of both the maximum reconnection rate and the current layer aspect ratio from the magnitude of electron viscosity.

Following saturation of the collapse, observed reduction in the reconnection rate is attributable to the relaxation of the reconnecting X-point configuration and resulting decrease in the magnitude of the inflowing B-field. Such relaxation continues until the effect of the periodic boundary in the outflow direction comes into play. Then, the formation of large electron flow vortices on the system-length scale leads to the feedback of electron outflows accelerated by the reconnection back into the RR inflow, thus forcing the reconnection rate to stay higher than it would in a completely open

EMHD system.

Most of these conclusions remain valid when the scale of the current diffusion region becomes smaller than the electron inertial scale and the RR exhibits a two-scale structure. While plasma inflow is slowed down by the inertial effects, tension in the reconnected field lines continues to accelerate plasma out of the current diffusion layer up to the maximum velocity allowed by the viscous effects. It has to be noted that for sufficiently small electron viscosity, the maximum outflow velocity has to be limited by the electron Alfvèn speed and not the viscous effects. This follows both from simple energy conservation considerations as well as the scalings presented in Fig. 3.10. Though for such small kinematic electron viscosities the structure of the EMHD reconnection current layer begins to resemble that of resistive MHD – with diffusion controlling the width of the current layer and inertia controlling the maximum outflow velocity – several important differences remain. In particular, upstream of the current layer the magnetic field is not frozen into the plasma fluid and poloidal flow through the current layer itself carries poloidal plasma current. While this parameter regime is outside the scope of the present work, detailed numerical studies of the electron diffusion region in such absolutely collisionless regime have recently been conducted by Daughton *et. al.*[42, 81] with a fully kinetic code.

Finally, clear signature of a localized non-propagating d_e-scale instability on the outflow slope of the reconnection current layer, where magnetic field is weak, and its distinct absence on the inflow side of the current layer or outside of the region of strong current gradients – justify the analytic arguments made in Section 3.3.1. This also provides additional support for our argument that it is the current gradient driven instability that triggers onset of fast reconnection, as described above.

3.4 Magnetic reconnection in a two-fluid system.

Having considered both visco-resistive and electron single fluid MHD models, we now study MR in a two-fluid system represented by the Hall MHD model. The main goal of this study is to understand how a tearing-unstable two-fluid ion-electron plasma system, where the ion-electron scale separation is much smaller than either the dimensions of the domain or the gradient scale of the initial condition, evolves in time.

3.4.1 Hall MHD model.

Several code verification calculations with two different Hall MHD models have already been described in the Section 2.2.4. In general, a normalized two-fluid system of equations with axial symmetry is given by:

$$\frac{\partial \rho}{\partial t} + \nabla \cdot (\rho \mathbf{v}_i) = 0$$

$$\frac{\partial (\rho \mathbf{v}_i)}{\partial t} + \nabla \cdot \left[\rho \mathbf{v}_i \mathbf{v}_i + \left(p + \frac{B^2}{2} \right) \mathbb{I} - \mathbf{B}\mathbf{B} + \Pi^i + \Pi^e \right] = 0$$

$$\frac{1}{\gamma_i - 1} \frac{\partial p_i}{\partial t} + \nabla \cdot \left(\frac{\gamma_i}{\gamma_i - 1} p_i \mathbf{v}_i - \mathbf{q}_i \right) = \mathbf{v}_i \cdot \nabla p_i - \Pi^i : \nabla \mathbf{v}_i + Q_i$$

$$\frac{1}{\gamma_e - 1} \frac{\partial p_e}{\partial t} + \nabla \cdot \left(\frac{\gamma_e}{\gamma_e - 1} p_e \mathbf{v}_e - \mathbf{q}_e \right) = \mathbf{v}_e \cdot \nabla p_e - \Pi^e : \nabla \mathbf{v}_e + Q_e$$

$$\frac{\partial \psi}{\partial t} + \frac{d_i}{\rho} \left[\hat{z} \cdot (\nabla \cdot \Pi^e - \mathbf{R}) \right] = -\hat{z} \cdot \mathbf{v}_e \times \mathbf{B}$$

$$\frac{\partial B_z}{\partial t} + \nabla \cdot \left[\mathbf{v}_i B_z - \mathbf{B} v_{ez} + \frac{d_i}{\rho} \hat{z} \times (\nabla p_e + \nabla \cdot \Pi^e - \mathbf{R}) \right] = d_i B_z \hat{z} \cdot \frac{\nabla B_z \times \nabla \rho}{\rho^2},$$

where electron inertia terms have been neglected, $\gamma_{i/e}$, $\mathbf{q}_{i/e}$, $Q_{i/e}$, $\Pi^{i/e}$ are ion/electron adiabatic constant, heat flux, heating, and stress tensor terms, $\mathbf{R}$ is the electron to ion momentum transfer term, $p = p_i + p_e$, $\mathbf{B} = \hat{z} \times \nabla \psi + \hat{z} B_z$, $d_i \nabla \times \mathbf{B} = \rho(\mathbf{v}_i - \mathbf{v}_e)$,

and $d_i \equiv (c/\omega_{pi})/L_0$ is the normalized ion skin depth. In Hall MHD, in order to simplify the system, it is common to evolve only a single pressure[53, 73] by assuming either a very fast heat exchange and equilibration mechanism or one of the species to be much colder than the other. In doing so, we let $p_e = \alpha p$, where $0 \leq \alpha \leq 1$.

A dispersion relation for the Hall MHD system of equations can be derived in uniform magnetic field with normalized uniform background density $\rho_0 = 1$ and total pressure p_0, by neglecting all of the non-ideal terms in the equations above: $\Pi^i = \Pi^e = Q_i = Q_e = \mathbf{q}_i = \mathbf{q}_e = \mathbf{R} = 0$. Let the perturbation wave vector $\mathbf{k}$ define the x-direction, $\xi = \tilde{\xi} e^{i(kx-\omega t)}$, and the background magnetic field $\mathbf{B}_0$ lie in the $[x, z]$-plane and be normalized in such a way that $\mathbf{k} \cdot \mathbf{B}/k = 1$, *i.e.* $B_0 = 1\hat{x} + \bar{b}_z \hat{z}$. Then, assuming the pressure to be convected by the ion fluid, the following dispersion relation results:

$$\Omega^6 - \Omega^4 \left(\bar{b}_z^2 + \beta + 2 + d_i^2 k^2\right) + \Omega^2 \left[1 + \bar{b}_z^2 + \beta(2 + d_i^2 k^2)\right] - \beta = 0, \tag{3.4.1}$$

where $\Omega \equiv \omega/k$ and $\beta \equiv \gamma_i p_0$. Note that here β is normalized to the poloidal magnetic field and $\bar{b}_z$ is a measure of the strength of the magnetic guide-field relative to the poloidal magnetic field.

It is apparent that the Eq. (3.4.1) has three pairs of roots. One of them, in the limit of $d_i \to 0$, is the slow magnetosonic wave, which for $d_i \approx 1$ is found to have phase velocity Ω_s go to zero for $k \to \infty$. We now consider how the other two pairs of waves – the shear Alfven Ω_{sh} and the fast magnetosonic Ω_f in the limit of $d_i \to 0$ – depend on β and $\bar{b}_z$ when $d_i \approx 1$.

Using the Mathematica 5 software package to solve and plot solutions of Eq. (3.4.1) for $\Omega(k)$ with multiple combinations of values for β and $\bar{b}_z$, we find the following:

- **Fast Compressional Wave:**

Whistler-like dispersion relation: $\Omega_f^2(k) \approx 1 + \bar{b}_z^2 + \beta + d_i^2 k^2$;

- **Shear Alfven wave:**

  $\beta \leq 1$: $\Omega_{sh}^2(k)$ monotonically decreases from $\Omega_{sh}^2(0) = 1$ with $\lim_{d_i k \to \infty} \Omega_{sh}^2(k) = \beta$;

  $\beta > 1$: $\Omega_{sh}^2(k) \approx 1 + \frac{\beta - 1}{\beta + \bar{b}_z^2} d_i^2 k^2$, for $d_i^2 k^2 \lesssim \beta$ with $\lim_{d_i k \to \infty} \Omega_{sh}^2(k) = \beta$.

These results can also be reproduced analytically by solving the general dispersion relation Eq. (3.4.1) with the appropriate orderings for β, $\bar{b}_z$, and $d_i k$.

Note that the Whistler wave originates from the fast compressional wave and for large enough value of $d_i k$, as compared to 1, β and $\bar{b}_z$, we have $\Omega_f \approx d_i k$. We again point out that, as considered by Rogers *et.al.*[128] and in Section 3.3.1 above, inclusion of electron inertia in the evolution equations cuts off the growth of $\Omega_f(k)$ to some constant value for sufficiently high k, $\lim_{d_i k \to \infty} \Omega_f(k) = \Omega_f^\infty$.

The so-called kinetic Alfvén wave is observed to originate from the shear Alfvén wave for $\beta > 1$. The dispersive characteristic $\Omega_{sh} \propto k$ associated with the kinetic Alfven wave in the reduced models[53, 68], in the full compressible model is only a transitional behavior.[6] In the limit of $d_i^2 k^2 \geq MAX\left(\bar{b}_z^2, \beta\right)$, the modified shear Alfven wave always approaches $\lim_{d_i k \to \infty} \Omega_{sh}^2(k) = \beta$.

In the MR simulations described below, we assume all flows to be subsonic (and therefore $\beta \gg 1$) in order to simplify the model by making use of the incompressibility condition $\nabla \cdot \mathbf{v}_i = \nabla \cdot \mathbf{v}_e = 0$. We again conduct the simulations on a quarter domain and consider MR without a guide field – set $\bar{b}_z = 0$. Note that in this limit, $\Omega_{sh}^2 \approx d_i^2 k^2$ for $1 < d_i^2 k^2 < \beta$ and $\Omega_k^2 \approx d_i^2 k^2$ for $d_i^2 k^2 > \beta$, thus preserving the dispersive nature

[6] As noted by Rogers *et.al.*[128] and Fitzpatrick[53], the reduced two-fluid model, which is derived under the assumption of large guide field $\bar{b}_z \gg \beta$[68], is only valid for $\beta \gg 1$.

of a two-fluid system for a wide range of k magnitudes. Plasma density ρ is assumed to be uniform at $t = 0$ and therefore remains constant and uniform due to the incompressibility and continuity conditions. The simplest form of kinematic viscosity is assumed for both ion and electron stress tensors: $\Pi^i = \mu\nabla\mathbf{v}_i$ and $\Pi^e = \nu\nabla\mathbf{v}_e$, where μ and ν are the ion and electron kinematic viscosity coefficients, respectively. The electron to ion momentum transfer is given by the usual isotropic resistive term $\mathbf{R} = \eta(\rho^2/d_i)\mathbf{J}$ and plasma pressure is again decoupled from the rest of the system by applying the $\hat{z}\cdot\nabla\times$-operator to the momentum equation.

The resulting set of incompressible Hall MHD equations evolved by the SEL code in this study has already been presented in Section **??** and is given here for completeness:

$$\frac{\partial\psi}{\partial t} + \nabla\cdot[\psi\hat{z}\times\nabla\phi_i - \eta\nabla\psi - d_i\nu\nabla W_e] = d_i\hat{z}\cdot\nabla\psi\times\nabla B_z$$

$$\frac{\partial B_z}{\partial t} + \nabla\cdot[B_z\hat{z}\times\nabla\phi_i - W_e\hat{z}\times\nabla\psi - \eta\nabla B_z + d_i\nu\nabla\omega_e] = 0$$

$$\frac{\partial\omega_i}{\partial t} + \nabla\cdot\left[\omega_i\hat{z}\times\nabla\phi_i - \frac{1}{d_i}(W_i - W_e)\hat{z}\times\nabla\psi - \nabla(\mu\omega_i + \nu\omega_e)\right] = 0$$

$$\frac{\partial W_i}{\partial t} + \nabla\cdot[W_i\hat{z}\times\nabla\phi_i - \nabla(\mu W_i + \nu W_e)] = \hat{z}\cdot\nabla\psi\times\nabla B_z$$

$$\nabla\cdot(d_i\nabla\psi) = W_i - W_e, \quad \omega_i = \nabla\cdot(\nabla\phi_i), \quad \omega_e = \nabla\cdot(d_i\nabla B_z + \nabla\phi_i)\,,$$

where $\mathbf{B} = \hat{z}\times\nabla\psi + \hat{z}B_z$, $\mathbf{v}_i = \hat{z}\times\nabla\phi_i + \hat{z}W_i$ and $\mathbf{v}_e = \mathbf{v}_i - d_i\mathbf{J}$.

The initial and boundary conditions employed in the Hall MHD simulations are set to enable direct comparison with the visco-resistive and electron MHD simulation results described above. The semi-open boundary conditions enforce periodicity in the $\hat{x}$-direction, but again allow for zero vorticity ion flow through the "open" boundary in the $\hat{y}$-direction. The open boundary also has the tangential ion flow set to zero, while the tangential components of magnetic field are set to be constant and uniform at the

value given by the initial condition. Natural boundary conditions are applied to the electron axial flow and vorticity variables, W_e and ω_e, respectively. The initial condition for these simulations is identical to those used in visco-resistive and electron MHD simulations: $\psi_0 = \lambda \ln[\cosh(y/\lambda)] + \delta\psi$, $\delta\psi = \epsilon \exp[-x^2/(2\lambda)^2] \exp[-y^2/(\lambda/2)^2])$, $\lambda = .5$, $\epsilon = 10^{-4}$, and all of the initial equilibrium out-of-plane plasma current has been assumed to be carried by the electron fluid $W_{e0} = -d_i/\left[\lambda \cosh^2(y/\lambda)\right]$.

It is important to note that the above system is reduced to the visco-resistive incompressible MHD system described in Section 3.2 in the limit of $d_i \to 0$, and approaches the inertia-less electron MHD limit described in Section 3.3, when $d_i \gg 1$.

3.4.2 Numerical results – three-state solution.

All of the simulations described below have been conducted with the ion inertial scale d_i much smaller than the system size $[L_x, L_y]$ or the initial equilibrium gradient scale λ, yet comparable to the resistive scale l_η which determines the width of a reconnection layer in an equivalent resistive MHD system. While all normalized coefficients are kept constant through each simulation run, systematic variation of d_i and η, with $\mu/\eta \leq 1$ and $\nu = \mu/100$, shows a variety of qualitatively and quantitatively different outcomes in a narrow parameter range.

Quasi-resistive evolution.

We first present results from a simulation with $d_i = 0.1$, $\eta = 4 * 10^{-4}$, and $\mu = 1 * 10^{-4}$ in a semi-periodic "open" box of half-width $L_y = 4$ and half-length $L_x = 24$. Figure 3.13 shows the time evolution and the near-final state of the simulation. By comparing the contour plots of poloidal magnetic flux, panel (a), and ion flow stream function, panel (b), to corresponding data from a visco-resistive simulation

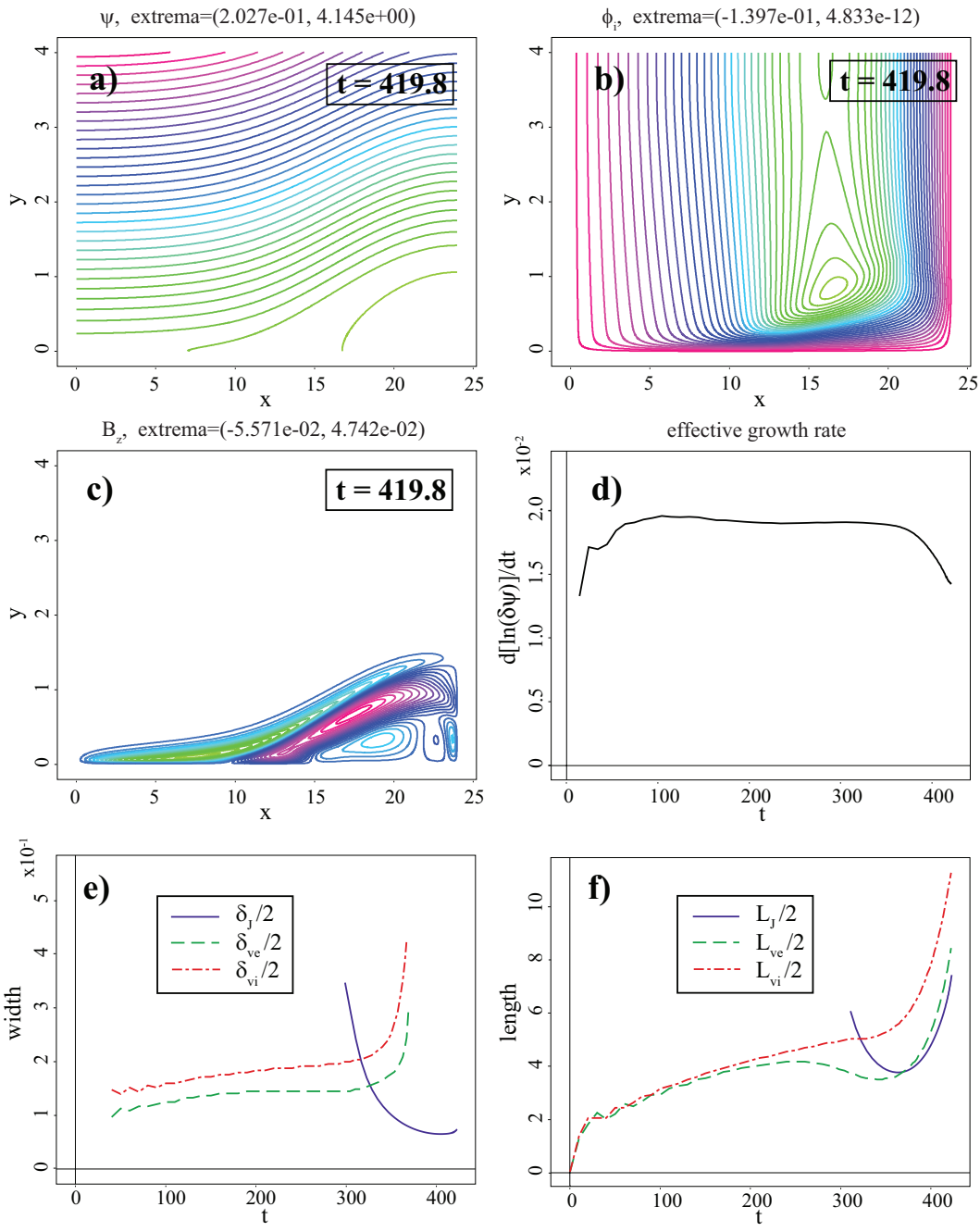

Figure 3.13: Contour plots of (a) ψ, (b) ϕ_i, and (c) B_z over the full computational domain at $t = 419.8$. Time-evolution of the effective growth rate $d\left[\ln(\delta\psi)\right]/dt$, and half-width $\delta/2$ and half-length $L/2$ of the RR are shown in panels (d),(e), and (f), respectively. Simulation has been conducted in a quarter-domain of size $[L_x, L_y] = [24, 4]$ with $d_i = 0.1$, $\eta = 4 * 10^{-4}$, $\mu = 1 * 10^{-4}$, and $\nu = 1 * 10^{-6}$.

presented in Fig. 3.5 above, it is apparent that for these parameters the two-fluid simulation closely reproduces the resistive current layer evolution. Though poloidal plasma currents are generated (see panel (c) of Fig. 3.13), nothing resembling an explosive onset of fast reconnection present in EMHD simulations, is observed here. As shown in panel (d), the effective growth rate of the MR process[7] is observed to drop following the linear and early non-linear tearing mode development phase, while panel (f) shows the length of the RR to grow on the ion Alfvén time scale as soon as a current layer stronger than the initial Harris current sheet equilibrium develops.

Due to the multiscale nature of two-fluid MR, in this Section we employ three separate measures of the width δ and length L of the RR: width and length of a plasma current layer at half-maximum value are denoted by δ_J and L_J, width and length of the electron inflow/outfow region from maximum inflow/outfow on one side of the RR to maximum on the other are denoted by δ_{ve} and L_{ve}, and similarly width and length of the ion inflow/outfow region are denoted by δ_{vi} and L_{vi}. Time evolution of all six scales is shown in panels (e-f) of Fig. 3.13. We note that, as expected, both δ_{ve} and δ_{vi} are well defined during the linear tearing mode evolution with $\delta_{vi} > \delta_{ve} \gtrsim d_i$. There, they define the width of the tearing layer. However, as soon as the quasi-resistive non-linear RR forms, both of these scales disappear and RR width is defined purely by the width of the current layer δ_J. This, once again, signifies that in resistive reconnection inflowing plasma is simply pulled into the RR by the outflowing plasma, which is itself accelerated by reconnected magnetic field lines.

[7] We define $\delta\psi \equiv (\psi_{max} - \psi_{min})|_{y=0}$, or equivalently the difference in poloidal magnetic flux between the X-point and O-point along the initial equilibrium current layer. Note that for a linear perturbation of a static equilibrium with growth rate γ, $d\left[\ln(\delta\psi)\right]/dt = (1/\delta\psi)[d(\delta\psi)/dt] = \gamma$.

Another interesting feature of the quasi-resistive two-fluid RR structure is noted by studying time-evolution of the RR outflow length scales. While the ions and electrons are shown to flow together during the linear phase, the outflows are observed to acquire somewhat different scales as soon as non-linear reconnection begins to take place. In fact, for a period of time, electron outflow layer appears to shorten, but is later dragged along by the ion outflow.

Panels (a-d) of Figure 3.14 show the ion and electron out-of-plane current layers, in-plane current stream function, and the contribution of the ideal $\mathbf{v}_e \times \mathbf{B}$ term to the reconnection electric field around the RR at $t = 419.8$. We observe that despite the single-fluid-like behavior of the system, most of the reconnection current is carried by electrons with $|W_e/W_i| > 5$. And while the current layer aspect ratio is $\delta_J/L_J \approx 100$, both the width and length of the electron current layer are distinctly smaller than the same for the ions. By comparing panels (a) and (e) for the ions and (b) and (f) for electrons, we also note that the length of ion/electron outflow layer corresponds almost exactly with the length of the ion/electron out-of-plane current layer, which is also confirmed by the time-traces in panel (f) of Fig. 3.13.

Studying the ion and electron in-plane flow patterns, we observe that despite somewhat different locations, the peak magnitudes of ion and electron outflows are nearly identical at all five times shown in panels (e-f) of Fig. 3.14 and are presumably determined by the magnitude of inflowing magnetic field B_{in}. On the other hand, the contour plot of difference in the flows throughout the quasi-resistive RR, *i.e.* the in-plane current stream function B_z, shows that the ion-electron inflow separation scale is determined by d_i and electrons are differentially rotated and accelerated through the RR only within the electron reconnection current layer.

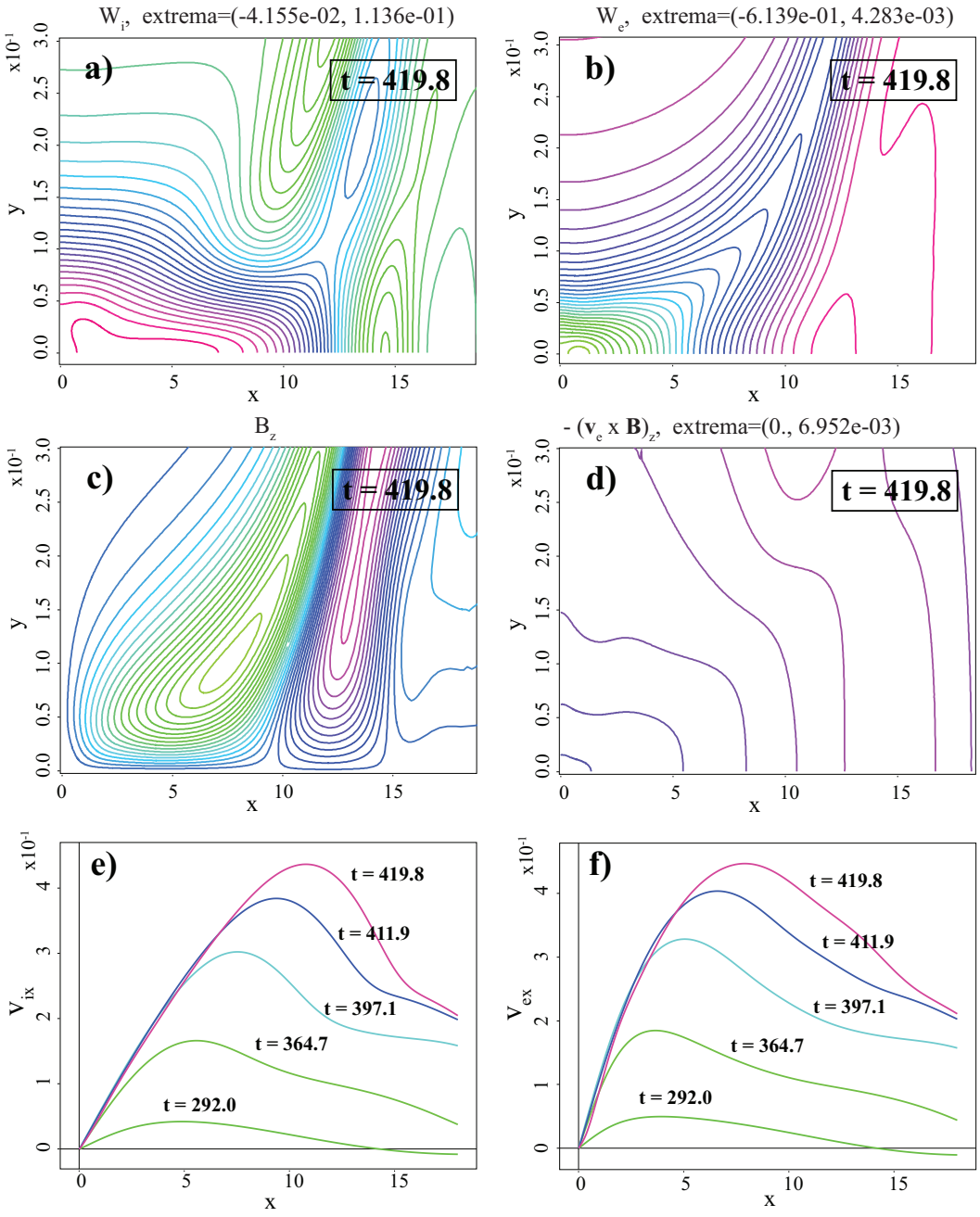

Figure 3.14: Contour plots of (a) W_i, (b) W_e, (c) B_z and (d) $-\hat{z}\cdot\mathbf{v}_e\times\mathbf{B}$ over the RR at $t = 419.8$. Profiles of (e) ion and (f) electron outflow velocities along the RR are shown at five different times during the non-linear evolution. Simulation has been conducted in a quarter-domain of size $[L_x, L_y] = [24, 4]$ with $d_i = 0.1$, $\eta = 4 * 10^{-4}$, $\mu = 1 * 10^{-4}$, and $\nu = 1 * 10^{-6}$.

Collapse to fast X-point reconnection.

We now present results from a calculation with $d_i = 0.1$, $\eta = 2.5 * 10^{-5}$, and $\mu = 2.5 * 10^{-5}$ in the same simulation domain. Note that resistivity has been reduced by a factor of eight with respect to the calculation described above. Figure 3.15 again shows the time evolution and the near-final state of the simulation and can be compared panel-by-panel with Fig. 3.13 above. We observe that the basic difference between the ψ contour plots is that between those achieved with visco-resistive and electron MHD reconnection simulations described previously: a very elongated current layer versus an open X-point like structure. Combining the data from in-plane ion flow and plasma current stream function contour plots, we observe that both fluids still elect to flow together into and out of the computational domain through the open boundary, while a completely new substructure has formed in the ion flow that well corresponds with the electron flow dominated in-plane current structure.

The direct evidence for explosive onset of fast reconnection precisely correlated with the RR collapse to an X-point is given in panels (d-f) of Figure 3.15. Instead of falling off, the reconnection growth rate is observed to dramatically increase by an order of magnitude in a time period $\Delta t \approx 50$, while a sharp drop in the RR length is observed.

Comparing the temporal evolution of the RR dimensions with the equivalent data for the more resistive simulation, we note that here even the linear tearing mode has a distinctly two-scale structure – with the ion tearing layer width determined by d_i and electron tearing layer width determined by the resistive scale l_η. (It is easy to show from the two-fluid Ohm's Law that kinematic electron viscosity begins to play a role only for current layer width $\delta < d_i(\nu/\eta)^{1/2}$. For the present parameters, that happens

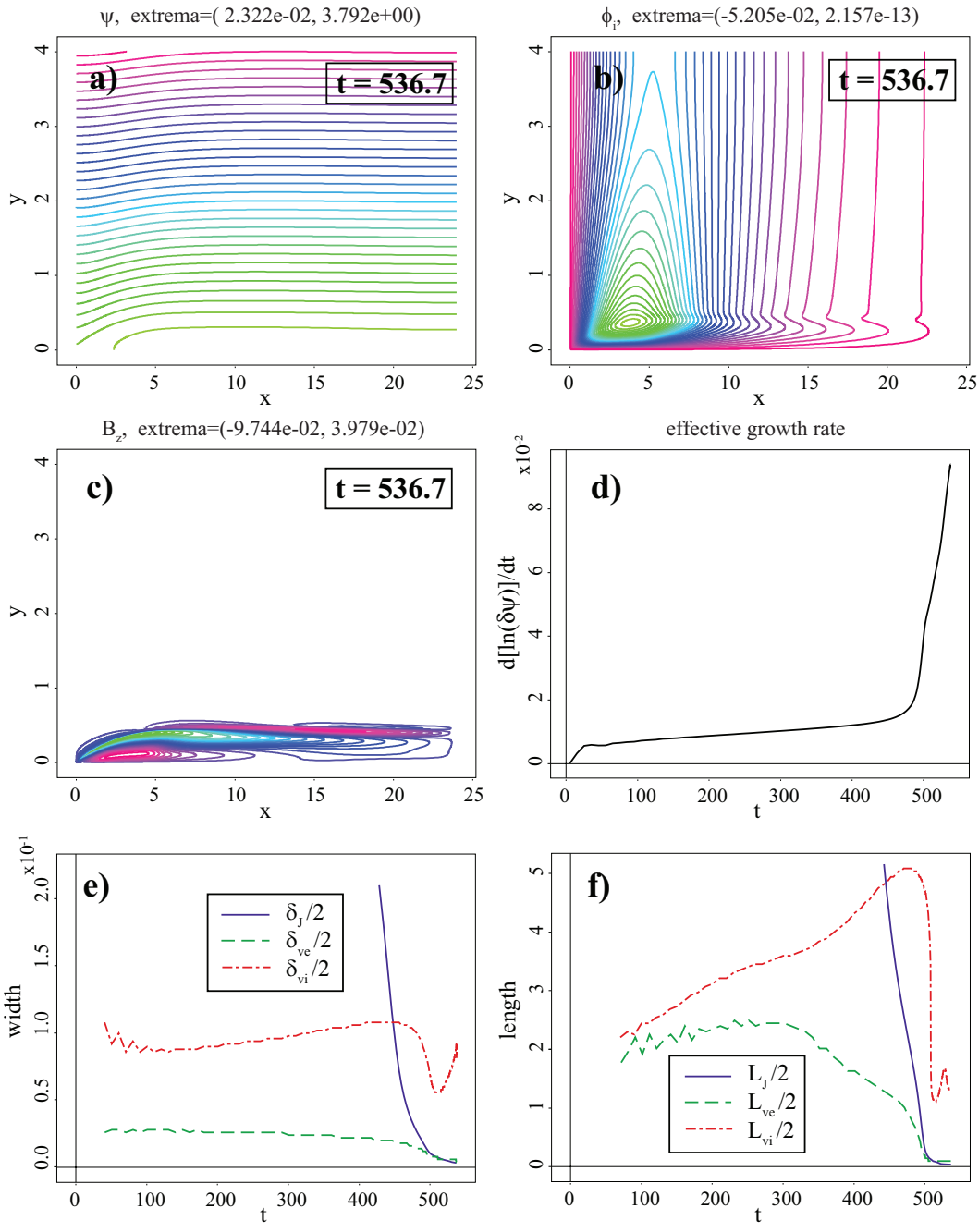

Figure 3.15: Contour plots of (a) ψ, (b) ϕ_i, and (c) B_z over the full computational domain at $t = 536.7$. Time-evolution of $d\left[\ln(\delta\psi)\right]/dt$, half-width $\delta/2$ and half-length $L/2$ of the RR are shown in panels (d),(e), and (f), respectively. Simulation has been conducted in a quarter-domain of size $[L_x, L_y] = [24, 4]$ with $d_i = 0.1$, $\eta = 2.5 * 10^{-5}$, $\mu = 2.5 * 10^{-5}$, and $\nu = 2.5 * 10^{-7}$.

when $\delta < 10^{-2}$, which is smaller than the width of the observed electron tearing layer $\delta \approx 2.5{*}10^{-2}$.) Similarly, the ion and electron tearing mode length scales are observed to diverge during the linear evolution with the electron scale L_{ve} reduced by factor of two during the early non-linear phase of the simulation $t \approx 300 - 450$.

In the fully developed non-linear phase, during the explosive onset of fast reconnection, it is primarily the outflow scales which appear to rapidly collapse. We note that immediately following the collapse, both dimensions of the ion inertial region also "recoil" in an apparent attempt to relax the magnetic field configuration outside of the RR. On the other hand, the electron inflow layer width δ_{ve} is shown to slowly decrease from the linear tearing mode width l_η to a new electron viscosity dominated scale l_ν. Figure 3.16 shows a close up of the ion inertial and electron diffusion regions following onset of fast reconnection at $t = 536.7$.

Observe that the sizes and aspect ratios of the respective regions are very different. The out-of-plane ion current layer, shown in panel (a), has an aspect ratio of ~ 40, sub-d_i width and $\sim 10 - 15 d_i$ length. The length of the ion current layer exactly corresponds to the length of the ion outflow layer, shown in panel (e). However, its width is significantly smaller than the width of the ion inflow layer, as seen in panel (e) of Fig. 3.15 at $t = 536.7$. (Recall that such relation between the in-plane and out-of-plane components of the flow has also been observed in the two-scale EMHD system when the out-of-plane current layer width was reduced below the electron inertial scale d_e.) On the other hand, the out-of-plane electron current layer, shown in panel (b) of Fig. 3.16, is approximately 10 times as strong as the ion reconnection current, has an aspect ratio of $\lesssim 10$, width on the electron viscous scale $l_\nu \lesssim 5 * 10^{-3} \ll l_\eta < d_i$ and sub-d_i length.[8] Panels (e) and (f) of Fig. 3.15, as well panels (c) and (f) of Fig. 3.16,

[8] For hydrogen plasma with $d_i = 0.1$, the corresponding electron inertial scale is $d_e = 2.33 * 10^{-3}$.

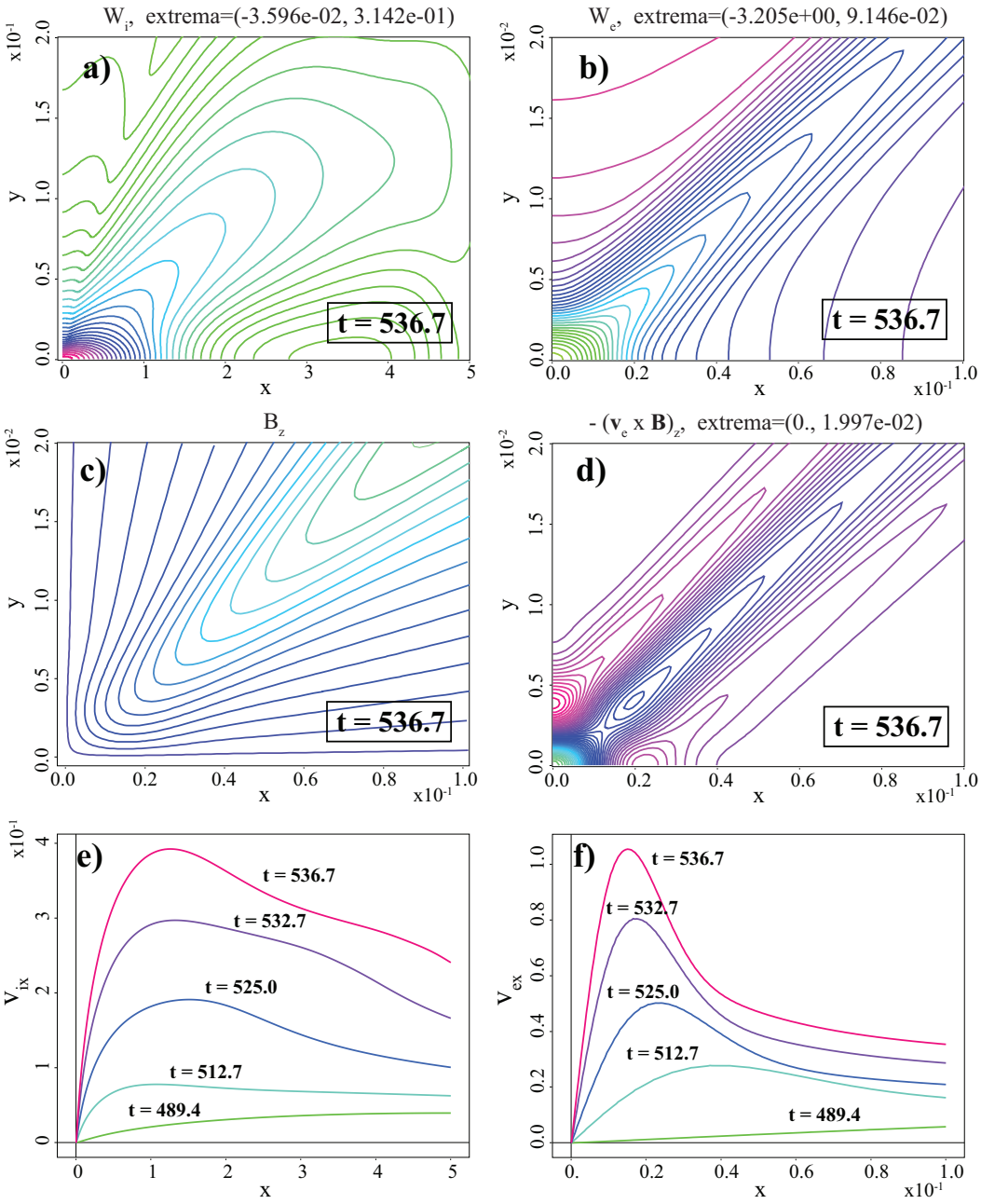

Figure 3.16: Contour plots of (a) W_i over the ion inertial region, and (b) W_e, (c) B_z and (d) $-\hat{z} \cdot \mathbf{v}_e \times \mathbf{B}$ over the current diffusion region at $t = 536.7$. Profiles of (e) ion and (f) electron outflow velocities along the RR are shown at five different times during the non-linear evolution. Simulation has been conducted in a quarter-domain of size $[L_x, L_y] = [24, 4]$ with $d_i = 0.1$, $\eta = 2.5{*}10^{-5}$, $\mu = 2.5{*}10^{-5}$, and $\nu = 2.5{*}10^{-7}$.

also show that the dimensions of the electron current channel exactly correspond to those of the electron inflow/outflow layer. We observe that here electron outflow velocity greatly exceeds the ion outflow velocity and therefore dominates the in-plane distribution of plasma currents.

Finally, we compare the contributions to the reconnection E-field made by the ideal $-\mathbf{v}_e \times \mathbf{B}$ term in the quasi-resistive and fast reconnection simulations, shown in panels (d) of Fig. 3.14 and Fig. 3.16, respectively. In the quasi-resistive case, weak variation is observed outside of the current layer and the resistive contribution inside the current layer approximately balances the ideal term outside. On the other hand, during fast reconnection, it is clear that the resistive term within the electron current layer is unable to balance the ideal contribution to the out-of-plane E-field outside of the layer and kinematic electron viscosity has to play a role. We note that the $-\hat{z} \cdot \mathbf{v}_e \times \mathbf{B}$ term has significant structure of enhanced electric field immediately surrounding the collapsed electron current layer, which also corresponds to the locations of maximum electron inflow and outflow velocity.

Intermediate regime with plasmoid generation.

As discussed above and previously shown by Cassak *et. al.*[32], a sufficiently resistive reconnecting two-fluid system has the macroscopic RR structure of a single-fluid resistive MHD, while sufficiently collisionless reconnecting two-fluid system generates an X-point-like microscopic electron current layer. In order to investigate the evolution of a reconnecting two-fluid system in the regime intermediate between the two

Therefore, since we have shown that electron inertia has no effect on a reconnecting system when $l_\nu \geq d_e$, we have not altered this two-fluid system's behavior by neglecting the electron inertial effects.

limiting configurations, a number of simulations with varying values of d_i, η and system size have been conducted. Table 3.1 summarizes the simulation parameters and the outcomes sorted by what we define to be the "two-fluid parameter" – $d_i/\eta^{1/2}$, where d_i determines the scale on which ion inflow separates from the magnetic field and electron fluid, and width of a resistive dissipation layer is proportional to $\eta^{1/2}$. As expected, for lowest values of the two-fluid parameter, formation of a system-length quasi-resistive current layer is consistently observed. However, as $d_i/\eta^{1/2}$ is increased and greater separation between the ion inertial scale and the current diffusion width becomes possible, the formation and elongation of the resistive current layer is observed to be interrupted by secondary instabilities of the electron current layer resulting in plasmoid generation. In fact, the electron current layer instabilities appear to have such high growth rates that simulations with the same plasma parameters and varied resolution are shown to become unstable at different times and produce secondary instabilities with different mode numbers. Figure 3.17 shows time-traces of the reconnection growth rate, panel (a), and half-width of the electron inflow layer, panel (b), from four simulations with identical plasma parameters and initial conditions on adaptive logical domains of varied size. It is immediately apparent that the four simulations produce identical results for $t \lessapprox 500$ with the system behaving in the quasi-resistive manner. However, as the system enters a strongly non-linear regime, its sensitivity to numerical noise becomes an important factor in the evolution. The three highest resolution runs are shown to successfully form a macroscopic resistive current layer, resulting in a slight drop of the reconnection growth rate and disappearance of the distinct electron inflow layer scale.

$d_i/\eta^{1/2}$	d_i	η	μ	L_x	n_x	n_y	outcome
3.16	0.10	$1.0 * 10^{-3}$	$1.0 * 10^{-4}$	24	20	20	layer
4	0.04	$1.0 * 10^{-4}$	$1.0 * 10^{-4}$	24	28	30	layer
4.74	0.15	$1.0 * 10^{-3}$	$1.0 * 10^{-4}$	24	20	20	layer
5	0.10	$4.0 * 10^{-4}$	$1.0 * 10^{-4}$	24	20	20	layer
5	0.05	$1.0 * 10^{-4}$	$1.0 * 10^{-4}$	24	20	20	electron $m = 2$, secondary electron $m = 1$
5	0.05	$1.0 * 10^{-4}$	$1.0 * 10^{-4}$	24	28	24	layer, secondary electron $m = 3$
6	0.06	$1.0 * 10^{-4}$	$1.0 * 10^{-4}$	24	20	20	electron $m = 1$
6	0.06	$1.0 * 10^{-4}$	$1.0 * 10^{-4}$	24	28	24	layer, secondary electron $m = 1$
6	0.06	$1.0 * 10^{-4}$	$1.0 * 10^{-4}$	24	28	30	layer, secondary electron $m = 2$
6	0.06	$1.0 * 10^{-4}$	$1.0 * 10^{-4}$	24	30	36	layer, secondary electron $m = 1$
7	0.07	$1.0 * 10^{-4}$	$1.0 * 10^{-4}$	24	20	20	electron $m = 1$
7.5	0.15	$4.0 * 10^{-4}$	$1.0 * 10^{-4}$	24	20	20	electron $m = 1$
8	0.08	$1.0 * 10^{-4}$	$1.0 * 10^{-4}$	24	20	20	electron $m = 1$
8	0.08	$1.0 * 10^{-4}$	$1.0 * 10^{-4}$	24	28	30	X-point
10	0.10	$1.0 * 10^{-4}$	$1.0 * 10^{-4}$	24	20	20	electron $m = 1$
10	0.10	$1.0 * 10^{-4}$	$2.5 * 10^{-5}$	24	20	20	electron $m = 1$
10	0.10	$1.0 * 10^{-4}$	$2.5 * 10^{-5}$	36	28	24	X-point
15	0.15	$1.0 * 10^{-4}$	$1.0 * 10^{-4}$	24	20	20	X-point
20	0.10	$2.5 * 10^{-5}$	$2.5 * 10^{-5}$	24	20	24	X-point
20	0.10	$2.5 * 10^{-5}$	$2.5 * 10^{-5}$	36	28	24	electron $m = 1$
20	0.10	$2.5 * 10^{-5}$	$2.5 * 10^{-5}$	36	36	30	X-point

Table 3.1: Results from a set of incompressible Hall MHD simulations with initial and boundary conditions as described in Section 3.4.1, sorted by the two-fluid parameter $d_i/\eta^{1/2}$, with normalized ion inertial scale d_i, resistivity η, kinematic ion viscosity μ, kinematic electron viscosity $\nu = \mu/100$, in the domain of length L_x and width $L_y = 4$, on an adaptive logical grid of size $[n_x, n_y, n_p]$, with $n_p = 8$.

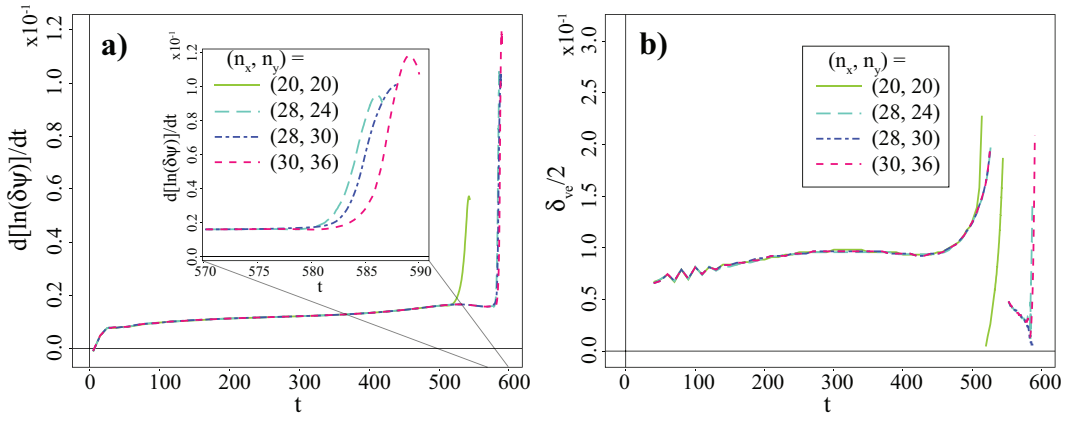

Figure 3.17: Time-traces of (a) reconnection growth rate $d\left[\ln(\delta\psi)\right]/dt$ and (b) electron inflow layer half-width $\delta_{ve}/2$ from four simulations with varied spatial resolution in a quarter-domain of size $(L_x, L_y) = (24, 4)$ with $d_i = 0.06$, $\eta = \mu = 10^{-4}$, and $\nu = 10^{-6}$.

We now recall from the analysis of visco-resistive RR evolution, shown in Figure 3.4 above, that the process of resistive current layer formation and elongation is accompanied by initial drop in the current layer width, as magnitude of the upstream B-field B_{in} is allowed to increase. It is during that intermediate phase that the current layer diffusion scale δ_J becomes smaller than d_i in these simulations. As a result, sub-d_i electron current layer is formed, marked by the reappearance of the δ_{ve} scale for $t \gtrsim 550$ in Fig. 3.17. Panels (a-b) of Figure 3.18 show the structure of the macroscopic two-scale RR at $t = 573.4$. We observe that the aspect ratio of the electron current layer is $\delta_{Je}/L_{Je} \approx 100$ and its width is determined by the resistive scale l_η. This electron current layer continues to grow narrower and eventually becomes unstable to secondary instabilities. Panels (c-d) and (e-f) of Fig. 3.18 show the structure of the RR a short time later from two simulations with different spatial resolutions. We observe that the two simulations produced different secondary instabilities: $m = 2$ for the lower resolution and $m = 1$ for the higher resolution run. (As

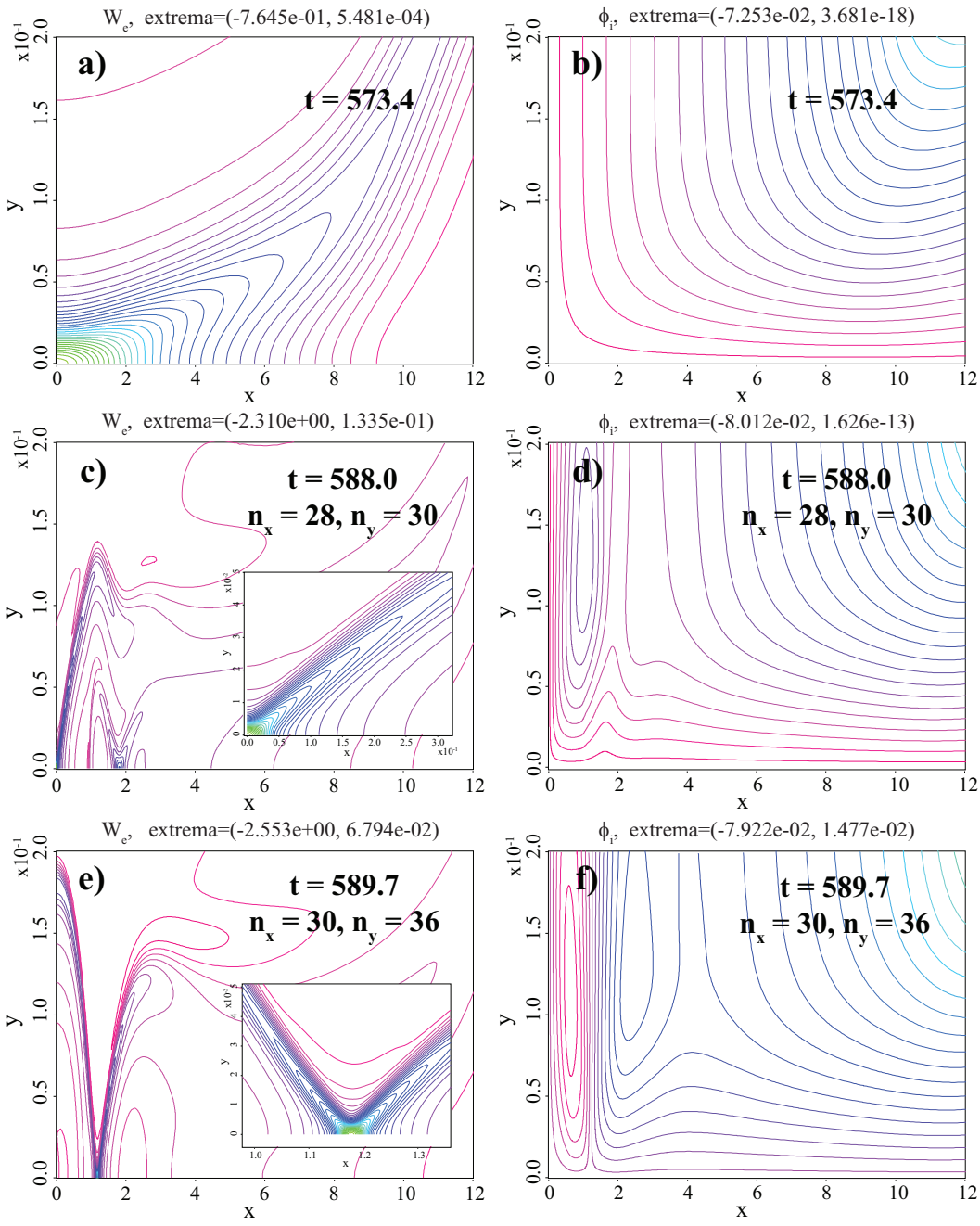

Figure 3.18: Contour plots of (a,c,e) W_e and (b,d,f) ϕ_i before the onset of secondary instabilities, panels (a-b), and after, panels (c-d) and (e-f), from two simulations with different logical grid sizes, $(nx, ny) = (28, 30)$ and $(nx, ny) = (30, 36)$, respectively. Both simulations used the adaptive temporal and spatial algorithms with the same spectral element polynomial order $n_p = 8$. The simulation were conducted in a quarter-domain of size $(L_x, L_y) = (24, 4)$ with $d_i = 0.06$, $\eta = \mu = 10^{-4}$, and $\nu = 10^{-6}$.

shown in Table 3.1, no general correlation is observed between the spatial resolution and m number of the secondary instabilities.) Yet, in both cases, the secondary instabilities have contracted the electron current layer to the microscopic l_ν scale, while the ion flow pattern demonstrates that the ion diffusion region has not collapsed and global length of the RR continues to be a large fraction of the simulation domain. Nevertheless, as shown in panel (a) of Fig. 3.17, onset of the secondary instabilities produces explosive growth of the reconnection rate, where all three highest resolution simulations show comparable magnitudes of the maximum growth rate.

We note that although there is a very definite correlation between the simulations' spatial resolutions and how long we are able to track the macroscopic current layer before it becomes unstable, the contour plots of Fig. 3.18 make it abundantly clear that in all of the simulations the spatial resolution of the solution is more than sufficient and by far exceeds that which can be expected in two-fluid MR simulations that rely on numerical diffusion for smoothness of the solution[73].[9] Thus, we must conclude that it is the explosive growth rate of the secondary electron instabilities which is responsible for the numerical non-reproducibility of the exact solution as the macroscopic electron current layer evolves in time.

Coming back to Table 3.1 to consider yet higher values of $d_i/\eta^{1/2}$, we observe that as the two-fluid parameter is increased, the system transitions from generating a macroscopic RR with embedded plasmoids, to producing a single localized plasmoid while the global RR opens into an X-point, to direct generation of an l_ν-scale electron current layer in an open global magnetic field configuration.

[9] As discussed in Section 2.2 above, the Crank-Nicholson time-advance together with the high order spectral element spatial representation combine to give virtually no numerical diffusion or dissipation of the solution in the SEL code.

3.4.3 Summary and discussion on two-fluid magnetic reconnection.

We now attempt to summarize the two-fluid results presented above and use them as well as results from other authors as a guide to form an overall framework for thinking about two-dimensional MR.

Fundamentally, MR acts to release energy stored in a global configuration of magnetic fields by changing its topology in a system where magnetic energy is generally assumed to dominate the kinetic energy of plasma flow. (MR in systems where energy of the plasma flow constitutes a large fraction of the total energy balance is the case of strongly driven MR, which has not been considered here.) In doing so, the system attempts to maximize the rate of energy release subject to the restrictions imposed by the mechanism allowing for the topological change. If and when such maximum energy release rate is achieved, the system enters a steady-state. On the other hand, a steady-state process can only happen in a global configuration which undergoes no changes in the shape and structure of the RR and magnetic fields immediately surrounding it. Therefore, a steady-state RR itself must be in the state of minimum energy, subject to matching conditions with the global B-field structure around it. In the simulations described above, we have not truly considered the asymptotic steady-states of two-fluid MR, but rather the various paths the system takes to get to those states and what those states might be for different values of plasma parameters.

Key observations.

One of the key observations made by combining all of the above results is what degrees of freedom are available to the full two-fluid system to achieve both the maximum reconnection rate and minimum energy configuration of the RR. Across the RR,

there are four: ion inertial scale (or the in-plane scale on which ions can become decoupled from the magnetic field), ion current layer width determined by the ion viscous effects, electron inertial scale, and electron current layer width determined either by the resistive diffusion or electron viscous effects. However, along the RR there appears to be only two: lengths of the ion and electron current layers which are equal to the lengths of the ion and electron outflow regions, respectively.

The other key observation is that magnetic energy contained in the B-fields immediately surrounding the RR plays an important role in determining the aspect ratio of the RR. The two main contributing factors are: (1) whether or not and on what scale plasma flows through the RR also carry current and therefore generate additional out-of-plane B-fields; and (2) the amount of energy in the reconnecting B-field as the aspect ratio of a RR is varied.

Minimum energy conjecture.

We recall that wherever a differential flow of two oppositely charged fluids exists, there is also a plasma current. And in the RR inflow-outflow configuration, where negatively charged electrons flow through the region faster than the positively charged ions, the resulting plasma currents also conspire to generate a quadrupolar structure of out-of-plane magnetic fields. Thus, a non-trivial configuration of magnetic fields and plasma currents that have non-zero components in all three directions is generated. We conjecture that in the collisionless limit, on the sub-d_i scale, it is the minimum energy state of this configuration around the X-point subject to matching the global magnetic field geometry constraint that determines the aspect ratio of a steady-state electron current layer and therefore the reconnection rate. Several observations made from the EMHD and X-point Hall MHD simulation results support the conjecture:

- Poloidal plasma currents are maximally aligned with poloidal magnetic field outside of the $B \approx 0$ region to minimize $\mathbf{J}_p \times \mathbf{B}_p$;

- Free energy available in a super-l_ν scale out-of-plane electron current layer, as evidenced by the existence of a current gradient instability described in Section 3.3.1 above, is always tapped to collapse the electron current layer to the l_ν scale;

- Enhanced reconnection E-field corresponding to a peaked profile of electron inflow and outflow velocities in the immediate neighborhood of the X-point signifies a self-driven system;

- The RR is consistently observed to relax following the explosive onset of fast reconnection, i.e. longer and wider RR than that which generates maximum R_{rec} appears to be consistent with the constraints of the steady-state solution.

Yet, even stronger evidence in favor of the conjecture comes from the moderately collisional regime, where resistivity is sufficiently high to form a macroscopic out-of-plane current layer of width $\delta_J/2 \geq d_i$, while it is low enough to only bind the poloidal electron flow to the poloidal ion flow on the super-d_i scale. It is remarkable that in that regime, despite the formation and apparent overall stability of a system-size RR, as soon as the half-width of the electron out-of-plane current layer is pulled in by the electron inflow to below the d_i scale, a secondary instability breaks up the macroscopic electron current layer to form a series of microscopic l_ν-scale electron current layers joint by one or more $\sim d_i$-width plasmoids within the global reconnection current layer. And the local structure of each of the inter-plasmoid current diffusion regions is identical to that observed in the EMHD and collisionless two-fluid regimes.

While not considered here so far, two-fluid MR in the presence of magnetic guide-field has been extensively studied elsewhere[53, 73, 122, 142, 77] and demonstrates further agreement with the proposed model. In particular, introduction of non-negligible magnetic guide-field has been shown to reduce the reconnection rate as a layer of enhanced out-of-plane B-field forms in the RR[73, 77]. In view of the conjecture, we believe that it is ultimately the gradient of the B_z-field within the RR which reduces R_{rec} by providing extra tension to an X-point configuration and forcing a more elongated current diffusion region. That conclusion is also consistent with the result of Section 3.3.1, where presence of a B_z-field gradient is shown to have a stabilizing effect on the electron current gradient layer instability.

As a side note, we have to point out that evidence of fast reconnection has recently been reported in two-dimensional particle simulations of collisionless electron-positron plasmas[11, 43]. There, due to equal mass of the species, no significant in-plane plasma currents are generated[11] and size of the current diffusion region is limited by a combination of kinematic viscosity and inertial effects[11, 43]. However, fast reconnection and very active plasmoid generation is still observed. While one could argue that these results contradict our conjecture, we believe that they only serve to further support it. We note that, on one hand, the Sweet-Parker-like derivation of R_{rec} and other RR parameters in the EMHD regime (see Section 3.1.2) does not make use of the in-plane plasma currents and still results in dissipation-independent fast reconnection, while on the other hand plasmoid generation by way of secondary tearing is in itself a form of local magnetic field relaxation and energy minimization.

Two-fluid RR structure.

Based on the simulation results and the discussion above, we suggest the following explanation for the structure of a two-fluid RR. Given a magnetic X-point which is somewhat longer than wider, the tension of the bent magnetic field lines accelerates them outward from the point of zero B-field through the smaller opening of the X-point. On distances beyond their inertial scale, charged particles are bound to the field lines and move together with them. Since electrons are $d_i^2/d_e^2 \gg 1$ times lighter than ions, it is the electrons which are accelerated in the interior of the RR. The region of acceleration is naturally the region of strongest current density, where most of the B-field curvature is accumulated, thus the corresponding lengths of the reconnection current and electron outflow layers.

As electron fluid is ejected from the X-point, it is kinematic viscosity and resistive drag plus electron inertia that counteract the acceleration. Whenever collisionality is sufficiently weak for the electron inertia to be the main counteracting force, the maximum electron outflow velocity, $v_{out}^e \leq v_A^e$, is determined by the magnitude of the reconnecting magnetic field. On the other hand, in the strong collisionality regime, it is the ion drag that counteracts electron outflow acceleration. Electrons are forced to drag ions along, while the resulting ion outflow is itself slowed down by the kinematic ion viscosity and ion inertia. It is the balance of the ion inertial and viscous forces against acceleration by the electron drag and the tension of reconnected magnetic field lines that determines the maximum ion outflow velocity, $v_{out}^i \leq v_A^i$, independently of plasma collisionality.

The length of the electron outflow region and therefore of the electron current layer is also limited by the forces acting to locally relax the B-field structure of

the RR. Since differential outflow generates in-plane currents perpendicular to the reconnected B-field and mainly carried by electrons, those electrons are deflected from the acceleration region to flow parallel to the magnetic field lines. They then can carry parallel poloidal current over large distances outside of the RR itself. (As has been recently shown in fully collisionless particle simulations by Karimabadi *et.al.*[81], the electron outflow has a two scale structure consisting of an acceleration region and a free outflow region. Here, we use "electron outflow region" to denote the acceleration region of Karimabadi *et.al.*.) On the other hand, the length of a steady-state ion outflow region beyond the d_i-scale is determined purely by a global configuration of B-fields which allows for maximum R_{rec}. As long as there is curvature in the reconnected magnetic field lines, *i.e.* out-of-plane plasma current, plasma continues to be accelerated from the X-point outwards.

Different factors determine the respective widths of the ion and electron inflow and dissipation regions. As plasma is ejected from the X-point, sufficient amount of plasma fluid must be "sucked in" to replace it. In a collisional regime, that is the only force acting to pull plasma in and therefore no peak in the plasma inflow velocity is observed. Nevertheless, the inflowing plasma carries with it oppositely directed poloidal magnetic field, thus generating further out-of-plane current with the width of the current layer determined by resistive diffusion.

In the collisionless limit, it is the electron fluid that is ejected and therefore must be replaced within the current layer. It is then mainly electrons that bring in further reconnecting B-field and are accelerated in the resulting out-of-plane current layer. Since the ion inflow velocity is also limited by its inertia within d_i of the X-point, EMHD approximation is generally applicable there and, as we have shown in

Section 3.3.1, electron inflow is not simply pulled towards the X-point, but is effectively pushed inwards by the out-of-plane current gradient. The width of the electron out-of-plane current layer is determined by the balance between the out-of-plane reconnection E-field and the forces acting to transport the electron momentum away from the electron current layer – electron viscous force and the resistive drag; and the width of the electron inflow layer is limited either by the width of that accelerating current layer or a mixed scale between l_ν and d_e, whenever $l_\nu < d_e$. Similarly, the width of the ion out-of-plane current layer is determined by the balance between the reconnection E-field on one hand and the ion viscous force and the resistive drag on the other; and the width of the ion inflow layer is limited by the ion inertial scale d_i. We note that fundamentally the same 4-scale structure of a collisionless RR has been observed by Ishizawa *et. al.*[74] in two-dimensional particle simulations, where the meandering orbits of ions and electrons played the roles of the effective ion and electron kinematic viscosities, respectively.

Conclusion.

We end this chapter on two-dimensional magnetic reconnection with the following proposition: A system that has free magnetic energy that can be released by way of magnetic reconnection will do so by whatever means are available to it and as fast as possible. Systems that allow for sufficiently fast magnetic reconnection by forming a steady-state RR which is itself in a local minimum energy state, such as a collisionless two-fluid system, do so. And systems that can find no such RR configuration maximize R_{rec} by producing "bursty" behavior, such as plasmoid formation and ejection, which results in the absence of a single steady-state RR.

Chapter 4

Incompressible internal kink mode simulations in helical geometry

Simulations of initially unstable, internally driven and externally driven $m = 1$ internal kink mode in a periodic cylinder are described in the Chapter below. Under the assumption of helical symmetry, both short-term and long-term evolution of two-dimensional incompressible visco-resistive and Hall MHD systems is studied in the regime of large axial guide-field. Aspects of the observed self-organization and magnetic reconnection phenomena, as well as sensitivity of the results to various plasma parameters are emphasized.

4.1 Helical symmetry.

Consider a periodic cylindrical geometry of radius r_0 and periodicity length $2\pi L$. Using the usual $\{r, \theta, z\}$ cylindrical coordinates, a helical angular coordinate τ is defined as:

$$\tau \equiv \theta + \epsilon z$$

where ϵ is the inverse-aspect-ratio parameter $\epsilon \equiv L^{-1}$ with all length normalized to r_0. We note that the helical coordinate τ has periodicity of 2π and $L \to \infty$ implies

$\epsilon \to 0$, thus reducing τ to the cylindrical angular coordinate θ. The unit vector corresponding to the helical coordinate is

$$\hat{\tau} = g(\hat{\theta} + \epsilon r \hat{z}),$$

where we have defined $g(r) \equiv (1 + \epsilon^2 r^2)^{-1/2}$. The third orthonormal vector $\hat{e}$ of the helical coordinate system is defined as

$$\hat{e} \equiv \hat{r} \times \hat{\tau} = g(\hat{z} - \epsilon r \hat{\theta}).$$

With the definitions above, the system is said to be helically symmetric if

$$\frac{\partial F}{\partial e} \propto \nabla F \cdot \hat{e} = 0,$$

for any scalar function $F(\mathbf{r})$. It follows that $F(\mathbf{r}) = F(r, \tau)$.

From here on, in this chapter, we consider only two-dimensional systems with helical symmetry, unless explicitly stated otherwise. A number of useful vector-differential identities in helical coordinates are given in Appendix A.1. We note that the assumption of helical symmetry, as defined above, excludes any perturbations with $m/n \neq 1$ from the system, where m and n are the angular and axial mode numbers that could, in principle, exist in a periodic cylinder. By the same token, all modes with $m/n = 1$ are included in the dynamics of the system being considered.

Using the helical coordinates, it is easy to show that any three-component divergence-less field can be expressed in terms of a potential function representing the field in the helical plane and an out-of-plane helical component. In particular any magnetic field $\mathbf{B}$ can be represented as

$$\mathbf{B} = g[\hat{e} \times \nabla\psi + B_e \hat{e}] = \hat{r}\left(-\frac{1}{r}\frac{\partial \psi}{\partial \tau}\right) + \hat{\tau}\left(g\frac{\partial \psi}{\partial r}\right) + \hat{e}\left(gB_e\right),$$

for some helical flux function $\psi(r,\tau)$ and helical B-field function $B_e(r,\tau)$. Using such representation, we readily find that the current density $\mathbf{J} = \nabla \times \mathbf{B}$ can be expressed as

$$\mathbf{J} = \hat{r}\left(\frac{1}{r}\frac{\partial B_e}{\partial \tau}\right) + \hat{\tau}\left(-g\frac{\partial B_e}{\partial r}\right) + \hat{e}\left(g\Delta^*\psi - 2\epsilon g^3 B_e\right) = g[\hat{e}\times\nabla(-B_e) + J_e\hat{e}],$$

where we have defined

$$\Delta^* F \equiv \frac{1}{g^2}\nabla\cdot(g^2\nabla F) = \frac{1}{rg^2}\left[\frac{\partial}{\partial r}\left(rg^2\frac{\partial F}{\partial r}\right) + \frac{1}{r}\frac{\partial^2 F}{\partial \tau^2}\right]$$

and

$$J_e \equiv \Delta^*\psi - 2\epsilon g^2 B_e.$$

Similarly, an incompressible velocity field $\mathbf{v}$ can be represented as

$$\mathbf{v} = g[\hat{e}\times\nabla\phi + V_e\hat{e}],$$

where $\phi(r,\tau)$ is the helical stream function and $gV_e(r,\tau)$ is the out-of-plane component of the plasma flow.

In this study, we use only the helical coordinates $\{r,\tau\}$ as the independent variables describing the two-dimensional physical space in which all simulations are performed. However, this is not the only possible set of independent spatial variables suitable for a system with helical symmetry. In fact, cylindrical (see Zhukov[161]) or Cartesian coordinate systems with appropriately expressed differential operators that account for the helical symmetry can also be used to represent the two-dimensional helical physical space. (See Appendix A.2 for the coordinate transformations of differential operators from helical to Cartesian coordinate systems preserving the helical symmetry.) We remark that the representation in the Cartesian coordinate system, in particular, can become very useful and/or necessary whenever a computational

grid does not itself have a polar $r = 0$ axis or adaptive evolution of the grid requires movement of the grid's polar axis or the $\tau = 0 = 2\pi$ equivalence line.

4.2 Linear study of the $n = 1$ internal kink mode.

We begin the numerical study with the linear growth rate calculations.

It was shown early on by Shafranov[132], Rosenbluth[129] and others that a periodic cylindrical plasma column surrounded by a fixed boundary and in magneto-hydrodynamic equilibrium with embedded axisymmetric magnetic fields can be linearly unstable to an $m = 1$ internal kink instability if the so-called "safety factor" $q(r) \equiv (rB_z/LB_\theta)$ of the magnetic field configuration equals unity for some $r = r_s$.

We use the SEL code described in Chapter 2 to conduct linear studies of the ideal and resistive $m = n = 1$ internal kink mode by advancing the full system of non-linear resistive MHD equations in time from a very small perturbation to a kink-unstable ideal equilibrium configuration through linear evolution to the early non-linear development stage. This linear study was done in order to verify the earlier numerical results by Park, *et.al.*[112] and the SEL code against each other and asymptotic analytic calculations of the instability growth rates made in the limit of $\epsilon \to 0$ and $\eta \to 0$.[129, 37]

4.2.1 Resistive incompressible MHD in helical symmetry.

In all of the calculations presented in this Chapter we make the assumption of exact incompressibility. Partial justification for the assumption is that here we only consider systems where energy contained in the out-of-plane helical magnetic fields $|\mathbf{B} \cdot \hat{e}|^2$ dominates that contained in in-plane magnetic fields or in-plane flows. Under such

conditions, in-plane plasma flows can be assumed to be largely incompressible, as they lack the energy necessary to compress the helical B-fields imbedded in the plasma fluid. Yet, as shown by Fitzpatrick[53], even in the presence of large magnetic guide-field the assumption of exact incompressibility is only strictly valid in the limit of large plasma pressure $(p/B^2) \gg 1$. Thus, while we conduct the simulations using the assumption in order to simplify both the calculations and their analysis, we must be conscious of the effects we are potentially neglecting.

We now consider the well known normalized resistive MHD equations in the limit of uniform density:

$$\begin{aligned} \frac{\partial \mathbf{v}}{\partial t} + \mathbf{v} \cdot \nabla \mathbf{v} &= \mathbf{J} \times \mathbf{B} - \nabla p \\ \mathbf{E} + \mathbf{v} \times \mathbf{B} &= \eta \mathbf{J}. \end{aligned} \tag{4.2.1}$$

By taking the $\hat{e}$-projection of Eqs. (4.2.1) and $\nabla\times$[Eqs. (4.2.1)], and using the above representation for the $\mathbf{B}$ and $\mathbf{v}$-fields, the incompressible resistive MHD system can be written in the following form:

$$\begin{aligned} \frac{\partial \psi}{\partial t} &+ \mathbf{v} \cdot \nabla \psi = \eta J_e \\ \frac{\partial (g^2 B_e - 2\epsilon g^4 \psi)}{\partial t} &+ \mathbf{v} \cdot \nabla (g^2 B_e) = \mathbf{B} \cdot \nabla (g^2 V_e) + \eta g^2 \Delta^* B_e \\ \frac{\partial \Omega}{\partial t} &+ \mathbf{v} \cdot \nabla \Omega = \mathbf{B} \cdot \nabla (g^2 J_e) \\ &+ \epsilon^2 g^4 \frac{\partial}{\partial \tau} \left(B_e^2 - V_e^2 \right) + 2\epsilon \mathbf{v} \cdot \nabla (g^4 V_e) \\ \frac{\partial V_e}{\partial t} &+ \mathbf{v} \cdot \nabla V_e = \mathbf{B} \cdot \nabla B_e, \end{aligned} \tag{4.2.2}$$

where we have defined $\Omega \equiv g^2 \Delta^* \phi$ to be the $\hat{e}$-component of flow vorticity and η is the uniform plasma resistivity.

4.2.2 Asymptotic linear growth rates.

The growth rates for both ideal and resistive internal kink modes in a periodic cylinder with given axisymmetric **B**-field configuration can be analytically computed in the asymptotic limit of $\epsilon r_s \ll 1$ and resistive layer thickness $\delta_\eta \ll r_s$, when $\eta \neq 0$[129, 37].

In that limit, the normalized ideal $m = 1$ internal kink growth rate given by Rosenbluth,*et.al.*[129] is

$$\gamma_I = -\frac{\pi}{|\partial(\mathbf{k}\cdot\mathbf{B})/\partial r|_{r=r_s} r_s^3} \int_0^{r_s} G(r)dr, \tag{4.2.3}$$

where $\mathbf{k}$ is the wave vector of the perturbation and function $G(r)$ is defined as:

$$G(r) \equiv \frac{k_z^2 r^2}{1+k_z^2 r^2}\left[2(J_\theta B_z - J_z B_\theta) + r(\mathbf{k}\cdot\mathbf{B})^2 + \frac{2}{r}\frac{k_z^2 r^2 B_z^2 - B_\theta^2}{1+k_z^2 r^2}\right].$$

The growth rate γ_R for the resistive internal kink instability is given by Coppi,*et.al.*[37] as a solution to the following equation:

$$\gamma_R = \gamma_I \frac{(\gamma_R\lambda)^{9/4}}{8} \frac{\Gamma\left(\frac{(\gamma_R\lambda)^{3/2}-1}{4}\right)}{\Gamma\left(\frac{(\gamma_R\lambda)^{3/2}+5}{4}\right)}, \tag{4.2.4}$$

where $\lambda \equiv \tau_A^{2/3}\tau_R^{1/3}$, τ_A is the poloidal Alfvén time and $\tau_R \equiv (1/\eta)$ is the resistive time at the singular surface $r = r_s$.

4.2.3 Initial ideal equilibrium.

Following Park,*et.al.*[112], we take the ideal incompressible equilibrium configuration of magnetic fields to be of the form:

$$\begin{aligned} g^2\Delta^*\psi_0 = 2r^2 - r_s^2 \quad &=> \quad \frac{\partial\psi_0}{\partial r} = \frac{r}{2g^2}(r^2 - r_s^2) \\ B_{e0} \quad &= \quad \epsilon^{-1}, \end{aligned} \tag{4.2.5}$$

where all spatial scales are normalized to the radius of the periodic cylinder r_0 and location of the singular surface r_s is chosen to be $r_s = .7$. There are no equilibrium flows.

For this equilibrium, we calculate $\int_0^{r_s} G(r)dr$ of Eq. (4.2.3) to the fourth order in ϵ to be

$$\int_0^{r_s} G(r)dr \approx -0.039817\epsilon^2 + 0.019805\epsilon^4$$

and the ideal $m = 1$ growth rate γ_I to be:

$$\frac{\gamma_I}{\epsilon^2} \approx 0.52097 - 0.51440\epsilon^2. \tag{4.2.6}$$

We note that due to symmetry inherent in the chosen equilibrium, the asymptotic polynomial expansion in ϵ for γ_I contains only even powers of ϵ.

The normalized λ factor of Eq. (4.2.4) is calculated for this equilibrium to be

$$\lambda = \eta^{-1/3} \left[r_s(1 + \epsilon^2 r_s^2) \right]^{-2/3}.$$

4.2.4 Numerical implementation.

Implementation of Eqs. (4.2.2) in the flux-source form required by the SEL code is straightforward and is not discussed here. The equations are advanced in time using the Crank-Nicholson scheme.

The equilibrium given by Eq. (4.2.5) is perturbed with a small perturbation in B_e:

$$\delta B_e = \alpha \sin(\tau) * e^{-w_0(r-r_s)^2}, \tag{4.2.7}$$

where $\alpha = 10^{-9}$ and $w_0 \approx 10 - 100$.

Perfectly conducting, perfect-slip wall boundary conditions are desired at $r = r_w$ for the linear study. These are implemented by satisfying the following set of boundary

PDEs:

$$\frac{\partial \psi}{\partial t}|_{r=r_w} = 0$$

$$\frac{\partial B_e}{\partial t}|_{r=r_w} = 0$$

$$\phi|_{r=r_w} = 0$$

$$\left(\frac{\partial V_e}{\partial r} - \epsilon r g^2 V_e\right)|_{r=r_w} = 0$$

$$\left(r\Omega + 2\epsilon g^2 V_e - g^2 \frac{\partial \phi}{\partial r}\right)|_{r=r_w} = 0.$$

Additionally, when studying the linear evolution of the resistive internal kink, resistive decay of the underlying ideal equilibrium has to be taken into account. The decay is prevented by introducing an effective current source throughout the domain to exactly cancel out the resistive decay of the ideal equilibrium, *i.e.* in Eqs. 4.2.2 the term $\eta\mathbf{J}$ is replaced by $\eta(\mathbf{J} - \mathbf{J}_0)$, where $\mathbf{J}_0$ is the plasma current density of the initial equilibrium.

As expected from the shape of the ideal eigenfunctions calculated by Rosenbluth[129] in the limit of $\epsilon \to 0$, it is found that the gradient scale of the ideal eigenfunction (*i.e.* width of the singular layer) tends to zero as $\epsilon \to 0$. Thus, in order to accurately resolve the eigenfunctions, strongly non-uniform computational grid is employed. Using the logical-to-physical space mapping described in Section 2.1.2, the physical radial coordinate r is designed to vary particularly slowly with the logical coordinate ξ around the singular layer radius r_s, while having much faster variation everywhere else. To satisfy this criteria, the following cubic function $r(\xi)$ that has the necessary values $r(0) = 0$ and $r(1) = 1$ at the boundaries of the logical and physical domains is chosen:

$$r(\xi) = \frac{(\xi - \xi_s)^3 + 5\alpha\xi + \xi_s^3}{1 + 5\alpha + 3\xi_s(\xi_s - 1)}.$$

ϵ	δt	α	γ_I	γ_I/ϵ^2
.245	8	.1	$1.556 * 10^{-2}$	.259
.18	15	.075	$1.027 * 10^{-2}$	.317
.1225	20	.075	$5.802 * 10^{-3}$	.387
.06125	50	.025	$1.775 * 10^{-3}$	.473
.04	75	.012	$7.974 * 10^{-4}$	.498
.03	150	$7 * 10^{-3}$	$4.571 * 10^{-4}$	.508
.02	250	$2.5 * 10^{-3}$	$2.058 * 10^{-4}$	.5145
.01	1000	$6.5 * 10^{-4}$	$5.19 * 10^{-5}$	.519

Table 4.1: Computed growth rates γ_I of the ideal $m = 1$ internal kink mode for various values of the inverse-aspect-ratio ϵ. Also shown are the time-step δt and computational grid non-uniformity parameter α used in each of the simulation runs.

Here, $\xi_s \equiv 1.5\alpha r_s + \frac{1-1.5\alpha}{1+((1-r_s)/r_s)^{1/3}}$ is defined by taking an approximate inverse of $r(\xi)$ to achieve high density grid at $r(\xi = \xi_s) = r_s$. The free parameter $\alpha \approx 6.5 * 10^{-4} - 0.1$ is an input parameter designed to determine the width of the highly resolved singular layer around $r = r_s$. An example of the resulting grid with $r_s = .7$ and $\alpha = 6.5 * 10^{-4}$ is shown in Fig. 4.1.

4.2.5 Computed ideal growth rates.

A set of ideal MHD simulations ($\eta = 0$) was conducted by varying the parameter ϵ to numerically determine the dependence of γ_I on ϵ for the equilibrium given by Eq. (4.2.5). Table 4.1 summarizes the input parameters and results of the simulations. Linear growth rates of the $m = 1$ eigenmode for different values of ϵ are determined by calculating $\gamma = \frac{\partial[ln(\Psi - \Psi_0)]}{\partial t}$ at some point on the (r, τ) plane and extracting the value from the prolonged flat part of the curve between the initial setting up of the eigenmode and time when the evolution becomes nonlinear.

Two separate quadratic fits to the data are attempted. (See Figure 4.2.) By fitting γ/ϵ^2 to $f = a + b\epsilon + c\epsilon^2$ for the set of five values of ϵ in the similar range

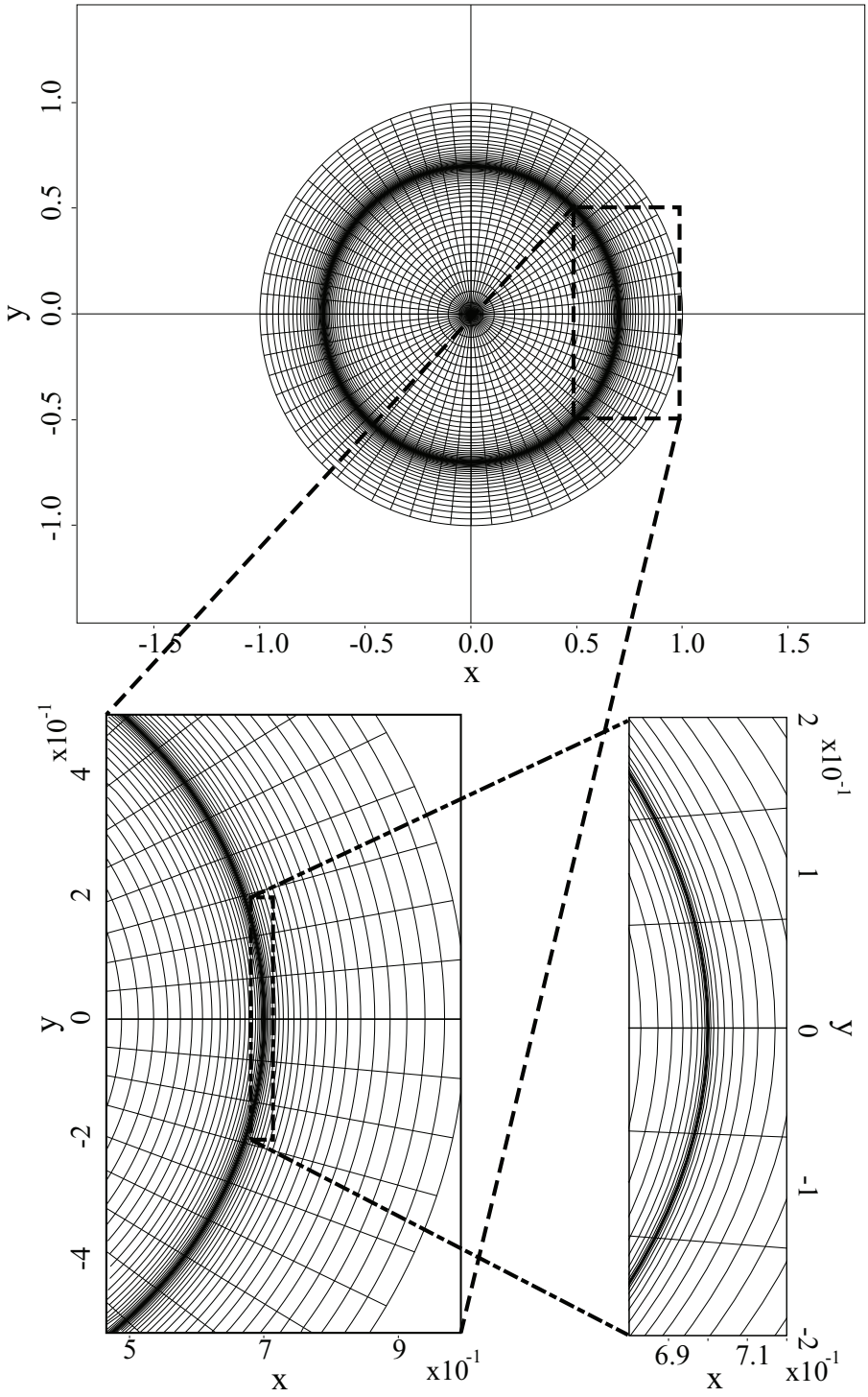

Figure 4.1: An example of a computational grid used for simulations of the ideal internal kink mode. Grid nodes shown represent the local density of the computational grid and not the actual locations of the grid points.

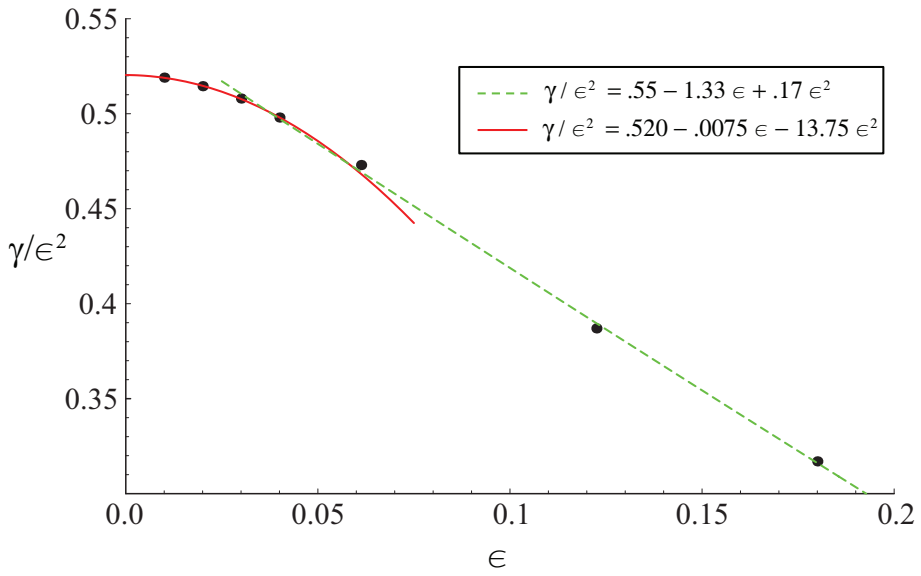

Figure 4.2: Two separate quadratic data fits for γ_I/ϵ^2 are presented for data points $\epsilon = \{.03, .04, .06125, .1225, .18\}$ and $\epsilon = \{.01, .02, .03, .04\}$. Quadratic behavior is shown to dominate for the set of data corresponding to smaller values of ϵ.

as those used to make a linear fit in Park,*et.al.*[112] linearized numerical calculations ($\epsilon = \{.03, .04, .06125, .1225, .18\}$) – a reasonably good fit of the form $\gamma/\epsilon^2 = .55 - 1.33\epsilon + .17\epsilon^2$ is achieved, which reproduces the previous result almost exactly.

However, by fitting γ/ϵ^2 to $f = a + b\epsilon + c\epsilon^2$ for the set of four smallest available values of $\epsilon = \{.01, .02, .03, .04\}$, we instead have functional dependence of the form $\gamma/\epsilon^2 = .520 - .0075\epsilon - 13.75\epsilon^2$, which is primarily a quadratic. That is consistent with the result in Eq. (4.2.6). Furthermore, in the limit of $\epsilon \to 0$, this quadratic fit produces a surprisingly good match to the asymptotic value of .5210 predicted by Eq. (4.2.6).

Since the above simulations were conducted by evolving the full non-linear set of ideal MHD equations with no diffusion on a non-uniform computational grid and near-perfect match to analytically computed asymptotic value of the internal kink growth

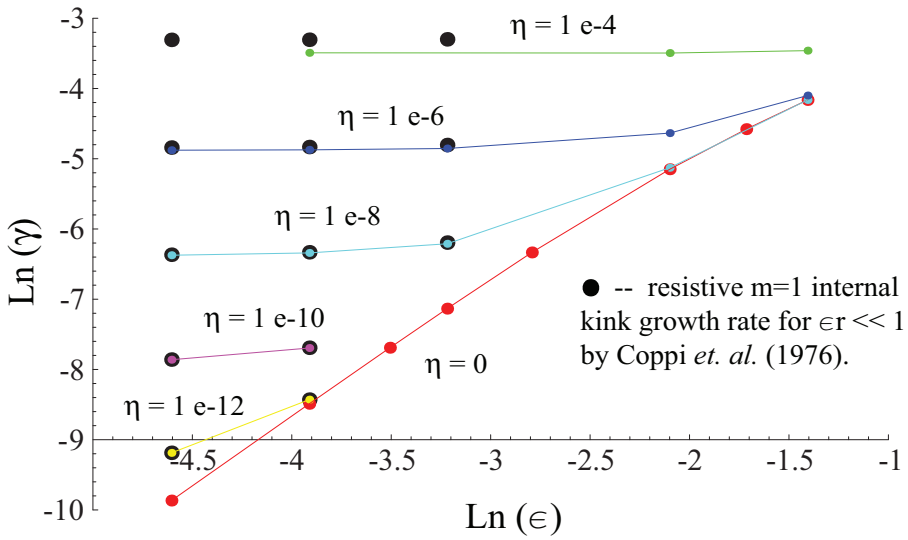

Figure 4.3: Linear growth rates of ideal and resistive internal kink modes observed in simulations (connected multi-colored circles) are shown against those computed from Eq. (4.2.4) by solving it numerically (black circles) for the corresponding **B**-field configuration, inverse aspect ratio ϵ, and resistivity η.

rate was achieved – we conclude that the SEL implementation of the Crank-Nicholson time-advance scheme can be taken to be entirely non-dissipative.

4.2.6 Computed resistive growth rates.

The code is further tested by conducting a systematic study of the resistive $m = 1$ internal kink growth rates. Results are compared against the growth rates predicted by Eq. (4.2.4). The same initial conditions as for the study of the ideal mode are employed. For the given **B**-field configuration, Eq. (4.2.4) is solved for γ_R by making use of the Mathematica 5.2 software package.

The results are presented in Fig. 4.3. (The presentation method was adopted from Tanaka,*et.al.*[145]). The analytical calculation is expected to be valid only in the limit of the resistive layer width δ_η being much smaller than the minor radius of

the equilibrium. That condition is satisfied only for sufficiently small values of both resistivity η and inverse aspect ratio ϵ. The numerical results in Fig. 4.3 are shown to appropriately converge to those calculated from the analytical model in that limit.

Having reproduced the linear analytic results for both ideal and resistive internal kink modes, we have the confidence to proceed to non-linear simulations of the phenomenon.

4.3 Visco-resistive non-linear internal kink simulations.

Below, we describe the results of multiple simulation runs, where incompressible visco-resistive MHD equation are evolved in time from some initial axisymmetric quasi-equilibrium perturbed to initialize an $m = 1$ internal kink instability. The evolution is followed through a single or multiple re-occurring internal reconnection events. The inverse-aspect-ratio ϵ, plasma resistivity η, ion viscosity μ, initial equilibrium configuration, and the drive applied to sustain and/or re-create a configuration of $\mathbf{B}$-fields with safety factor q below one on the magnetic axis, – are all systematically varied among the various simulation runs presented here.

4.3.1 Incompressible visco-resistive MHD equations in helical symmetry.

We begin the non-linear study of the internal kink mode by keeping the exact incompressibility condition and adding viscous terms to the resistive MHD system used for computing the linear growth rates. Once again, we assume plasma density to be initially uniform and therefore to stay constant and uniform due to the incompressibility condition. With those assumptions, the normalized system of visco-resistive

MHD equations is:

$$\frac{\partial \mathbf{v}}{\partial t} + \mathbf{v} \cdot \nabla \mathbf{v} = \mathbf{J} \times \mathbf{B} - \nabla p + \mu \nabla^2 \mathbf{v} \tag{4.3.1}$$

$$\mathbf{E} + \mathbf{v} \times \mathbf{B} = \eta \mathbf{J} \tag{4.3.2}$$

$$\mathbf{J} = \nabla \times \mathbf{B}, \quad \nabla \cdot \mathbf{v} = 0,$$

where μ is uniform ion viscosity and η is resistivity, which we now allow to have radial dependence $\eta = \eta(r)$.

As in Section 4.1, both **B**- and **v**-fields are expressed through the combination of in-plane helical flux/stream functions and out-of-plane field components:

$$\mathbf{B} = g[\hat{e} \times \nabla \psi + B_e \hat{e}], \quad \mathbf{v} = g[\hat{e} \times \nabla \phi + V_e \hat{e}].$$

Taking the $\hat{e}$-projection of Eqs. (4.3.1)-(4.3.2) and $\nabla\times$[Eqs. (4.3.1)-(4.3.2)], the visco-resistive MHD system can be written in the following form:

$$\frac{\partial \psi}{\partial t} + \mathbf{v} \cdot \nabla \psi = \eta J_e$$

$$\frac{\partial (g^2 B_e - 2\epsilon g^4 \psi)}{\partial t} + \mathbf{v} \cdot \nabla (g^2 B_e) = \mathbf{B} \cdot \nabla (g^2 V_e) + \eta g^2 \Delta^* B_e + g^2 \frac{\partial \eta}{\partial r} \frac{\partial B_e}{\partial r}$$

$$\begin{aligned} \frac{\partial (g^2 \Omega + 4\epsilon g^4 V_e)}{\partial t} &+ \mathbf{v} \cdot \nabla (g^2 \Omega + 2\epsilon g^4 V_e) = \mathbf{B} \cdot \nabla (g^2 J_e + 2\epsilon g^4 B_e) \\ &+ \epsilon^2 g^4 \frac{\partial}{\partial \tau} \left(B_e^2 - V_e^2 \right) - 8\epsilon^3 g^6 \left(B_e \frac{\partial \psi}{\partial \tau} - V_e \frac{\partial \phi}{\partial \tau} \right) + \mu g^2 \Delta^* \Omega \end{aligned}$$

$$\frac{\partial V_e}{\partial t} + \mathbf{v} \cdot \nabla V_e = \mathbf{B} \cdot \nabla B_e + \mu (\Delta^* V_e + 2\epsilon g^2 \Omega), \tag{4.3.3}$$

where $J_e \equiv \Delta^* \psi - 2\epsilon g^2 B_e$ and $\Omega \equiv \Delta^* \phi - 2\epsilon g^2 V_e$.

4.3.2 Internal kink evolution with direct current drive.

It is the goal of this work to not only observe and describe the evolution of a single internal reconnection (IR) event triggered by an internal kink instability in a prepared initial equilibrium, but also to describe how a periodic cycle of such events can be self-generated in a screw-pinch system with a given drive. In this Section, we describe the simulations conducted with direct current drive distributed across the simulation domain.

The ideal equilibrium given by Eqs. (4.2.5) with a perturbation given by Eq. (4.2.7) is taken as the initial condition. Resistivity η is taken to be spatially uniform and the same boundary conditions as in Section 4.2 are applied. The current source is chosen such that it exactly cancels the resistive decay of the initial ideal equilibrium, thus satisfying the boundary condition $\mathbf{E}|_{r=r_s} = 0$ and working to drive the system towards the initial $\mathbf{B}$-field configuration after an IR event takes place.

Direct current drive simulations have been conducted with two different values for the location of the $q|_{r=r_s} = 1$ surface at $r_s = 0.5$ and $r_s = 0.7$ with the aspect-ratio of the equilibrium at $1/\epsilon = 25$. (We note that here and in all of the simulation results presented below, initial axisymmetric equilibrium has axial magnetic field $B_z = 1/\epsilon$ on the magnetic axis and initial poloidal B-field $B_\theta \sim 1$. Thus, ϵ is also a measure of the effective out-of-plane magnetic guide-field present in the system.)

Time traces of the effective growth rate of the internal kink instability in the linear and non-linear phases of the simulations with $r_s = .7$ are shown in panel (a) of Figure 4.4. Following Aydemir[6], we measure the effective growth rate as $d[\ln(E_k)]/dt$, where E_k is the total integrated kinetic energy in the system. (Note that for an exponentially growing linear eigenmode $\propto \exp(\gamma t)$, this definition of a growth

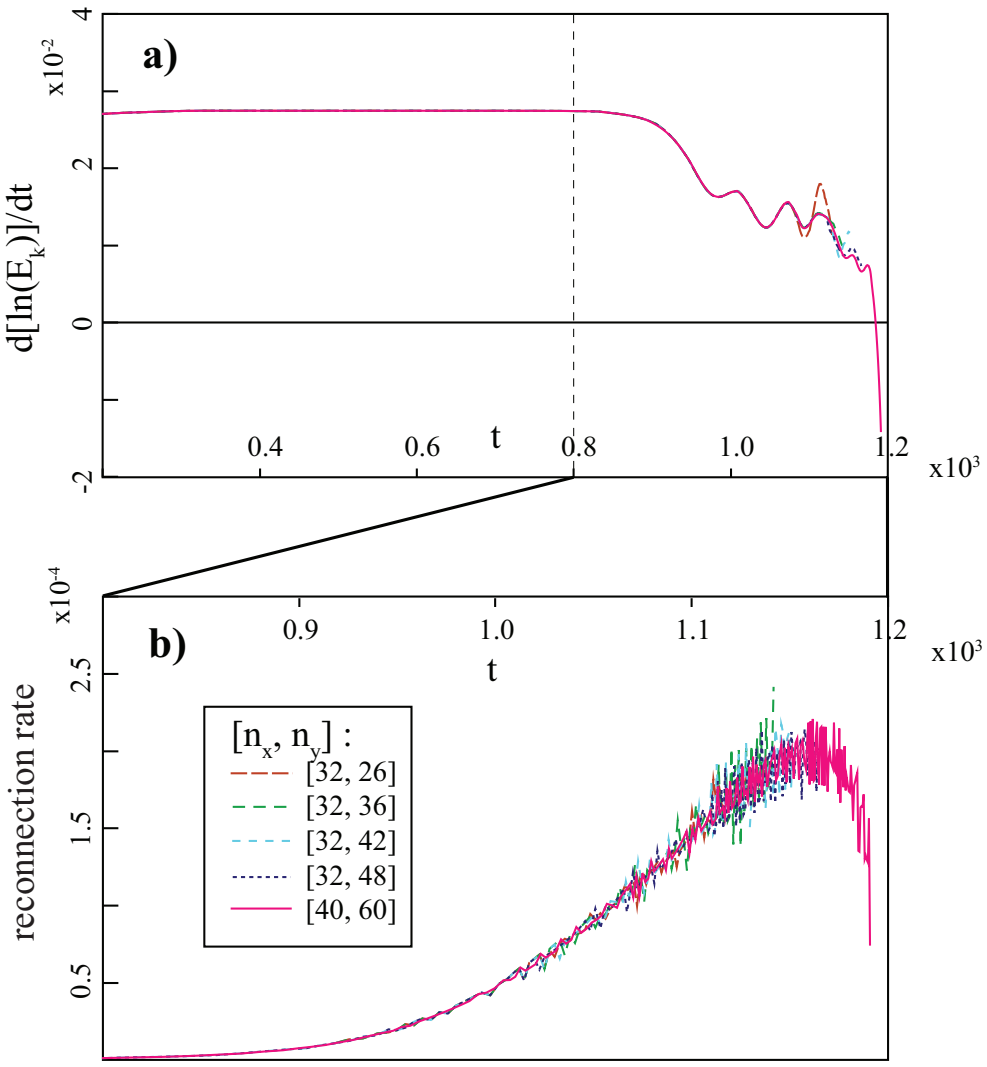

Figure 4.4: Time traces of (a) the effective growth rate of the linear and non-linear internal kink and (b) reconnection rate in the non-linear phase for several simulations with identical physical parameters but different sizes of the computational grid. The physical run parameters are: $\eta = \mu = 10^{-5}$, $r_s = 0.7$, $1/\epsilon = 25$ and $\delta B_e = 10^{-6}$ with direct current drive applied to support the initial equilibrium.

rate is equivalent to 2γ.) In these simulations, equilibrium was perturbed with a small $\delta B_e = 10^{-6}$ perturbation and after the initial set-up phase (not shown) exponential growth of the internal kink is apparent during the linear phase for $t \approx 200 - 800$. In the non-linear phase, during the time period $t \approx 900 - 1100$, another period of quasi-exponential growth appears to be present, thus reproducing a previous result that suggested fast reconnection of the central plasma core to be possible even within the single-fluid resistive MHD model[7]. In fact, panel (b) of Figure 4.4 shows the reconnection rate of the central core during the non-linear phase. Here, reconnection rate was measured by following the radially moving X-point in time(see Figures 4.5 and 4.6) and evaluating $d\psi/dt$ at the X-point. (The hash visible on the plot should be regarded as experimental noise due to inability to precisely pinpoint the exact location of the X-point at each time-step.) It is apparent that the reconnection rate does increase significantly during the non-linear phase, however no sign of explosive onset of fast reconnection observed in two-fluid simulations (see Section 3.4 above) is present here. We note that the numerical values presented in Figure 4.4 have to be re-normalized to estimate the true reconnection rate of the B-field in the system. As shown in panel (a) of Figure 4.6, the reconnecting helical B-field is only $\approx .1$ of the poloidal B_0 field all quantities are normalized to.

Finally, the five separate time-traces shown in each panel of Figure 4.4 come from five separate simulations of precisely the same system, but with different sizes of the computational spectral element grid. All five use the polynomial basis of order $n_p = 8$, but different numbers of cells in each of the two directions of the logical grid were used. It is clear that although simulations with smaller grid sizes fail to resolve all the structure present in the solution and therefore terminate prematurely, the data from

all five of the simulations falls on top of each other until right before those lacking sufficient resolution are terminated. This result confirms the accuracy of the adaptive re-gridding algorithm which was used heavily in these simulations.

Figure 4.5 shows snap-shots of the non-linear evolution of helical magnetic flux and helical stream function during the same internal kink simulations described in Figure 4.4. (Results from the highest resolution simulation are shown.) Complete Kadomtsev reconnection[79] of the central plasma core is observed. During the reconnection process, a long resistive current sheet accelerating plasma out of the layer is created. Furthermore, panels (b) and (c) of Figure 4.5 show that just prior to reaching the peak reconnection rate and immediately after the non-linear quasi-exponential growth of plasma kinetic energy is completed, the plasma core begins to be radially compressed with flux surfaces acquiring an elliptical shape. Such compression is a clear indication of inability of resistive diffusion to facilitate sufficiently fast reconnection of magnetic field lines and leads to further elongation of the current layer and resulting slow down of the reconnection rate, in agreement with the Sweet-Parker theory[115, 141] described in Section 3.1.1 above.

We note the remarkable up-down symmetry of the contour plots presented in Figure 4.5 to once again emphasize the accuracy of the algorithm used by the SEL code. Though no explicit symmetry requirements were enforced and the grid was adapted and the solution re-interpolated 27 times during the simulation, the exact lack of plasma rotation responsible for preserving the up-down symmetry introduced by the initial perturbation in single-fluid MHD was preserved throughout the simulation.

Figure 4.6 presents radial cuts at $\tau = \pi$ of the reconnecting component of B-field B_τ and out-of-plane reconnection plasma current J_e at several times during

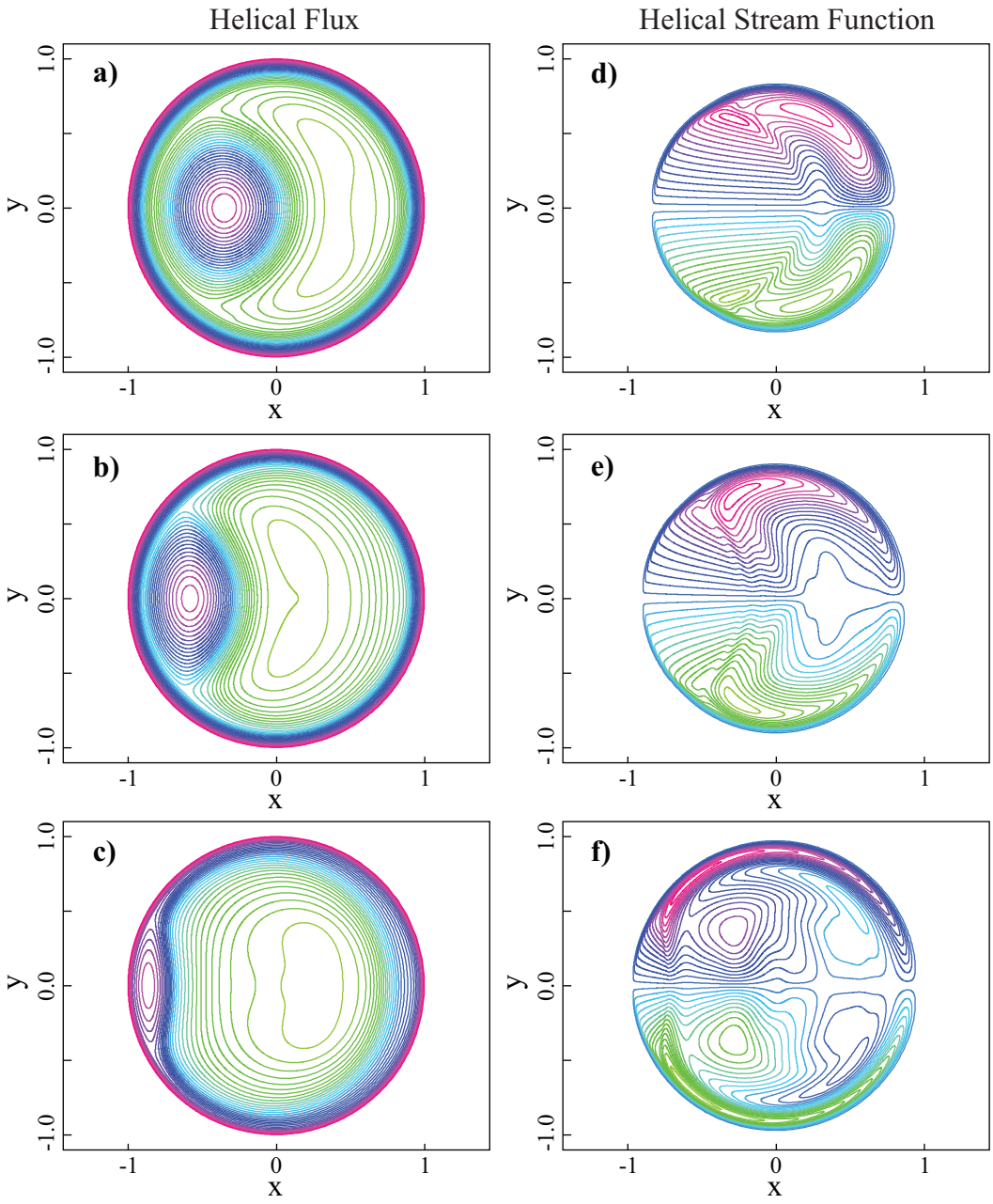

Figure 4.5: Contours of (a)-(c) helical magnetic flux ψ and (d)-(f) helical stream function ϕ at three different times $t_{a,d} = 1037$, $t_{b,e} = 1104$, and $t_{c,f} = 1170$. The results are from the $[n_x, n_y] = [40, 60]$ simulation run presented in Figure 4.4.

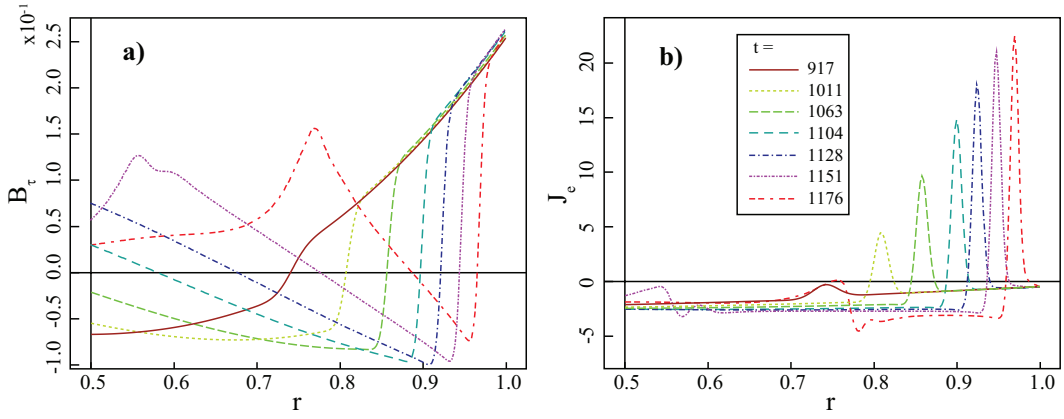

Figure 4.6: Radial cuts at $\tau = \pi$ of (a) reconnecting component of B-field, B_τ and (b) out-of-plane plasma current J_e at several times during the Kadomtsev reconnection cycle from the $[n_x, n_y] = [40, 60]$ simulation run presented in Figure 4.4.

the reconnection cycle. As reconnection progresses, the current sheet is observed to become narrower and magnitude of the reconnection current higher, corresponding to the higher reconnection rate. Radial cuts of B_τ at late times, $t = 1151$ and $t = 1176$, show that the radial compression of the core discussed above is also accompanied by a pile-up of B-field on the inner side of the plasma core (*i.e.* opposite to the reconnecting side). Such pile-up serves as further evidence of the core being driven outwards by re-circulating reconnection outflows, while slow Sweet-Parker reconnection cannot diffuse away magnetic fields fast enough.

Mixing radius r_M of an IR event is defined here as the outer most radius to which the plasma core reconnects before the reconnection process is either complete or is terminated by other intervening effects. It is easy to calculate from the initial equilibrium configuration given by Eq. (4.2.5), that in the case of complete Kadomtsev reconnection – the mixing radius for this equilibrium is given by:

$$r_M^2 = \frac{3}{4}\left[-(1/\epsilon^2 - r_s^2) + \sqrt{(1/\epsilon^2 - r_s^2)^2 + 16 r_s^2/3\epsilon^2}\right]. \tag{4.3.4}$$

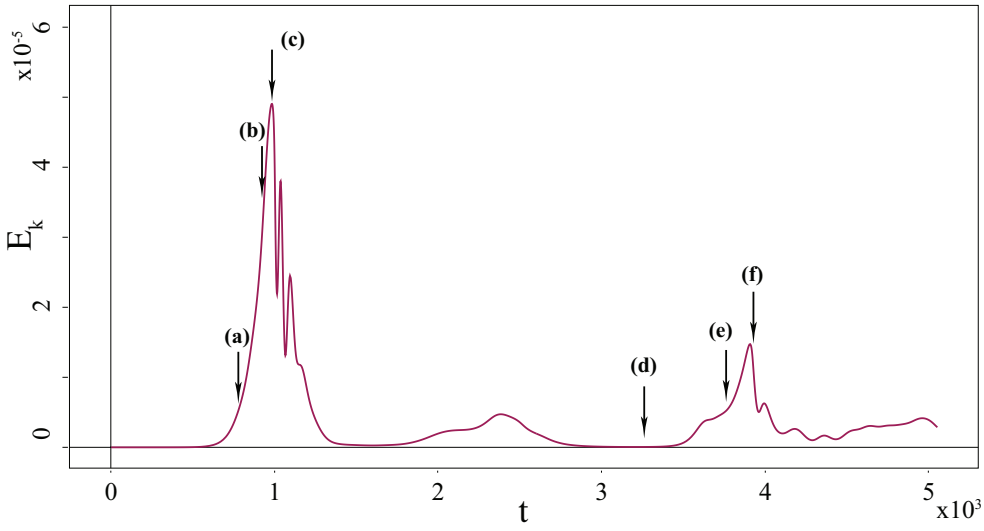

Figure 4.7: Time-trace of total kinetic energy in the system per unit length of the periodic cylinder for an internal kink simulation with $\eta = \mu = 10^{-5}$, $\epsilon = .04$, $r_s = 0.5$, perturbation $\delta B_e = 10^{-4}$ and direct current drive. Markers (a)-(f) note the approximate times at which corresponding panels of Figs 4.8-4.10 were taken.

For $r_s = .7$ and $1/\epsilon = 25$, Equation (4.3.4) gives for the mixing radius $r_M = 0.9898$. That is consistent with the results presented above and produces near-complete destruction of the initial equilibrium with the possibility of boundary effects having strong influence on the plasma dynamics.

Since we are also interested in observing the long-term evolution of the system following the initial internal kink reconnection event, we have attempted to remove the potential influence of the boundary by considering a B-field configuration whose Kadomtsev mixing radius is shifted inward and therefore moved away from the boundary of the computational domain. To do so, we have conducted simulations with the functional form of the initial B-field still given by Eq. (4.2.5), but with the initial $q = 1$ surface ar $r_s = .5$. For $1/\epsilon = 25$, Eq. (4.3.4) gives $r_M = .707$.

Results from a direct current drive simulation run with $\eta = \mu = 10^{-5}$, $\epsilon = .04$,

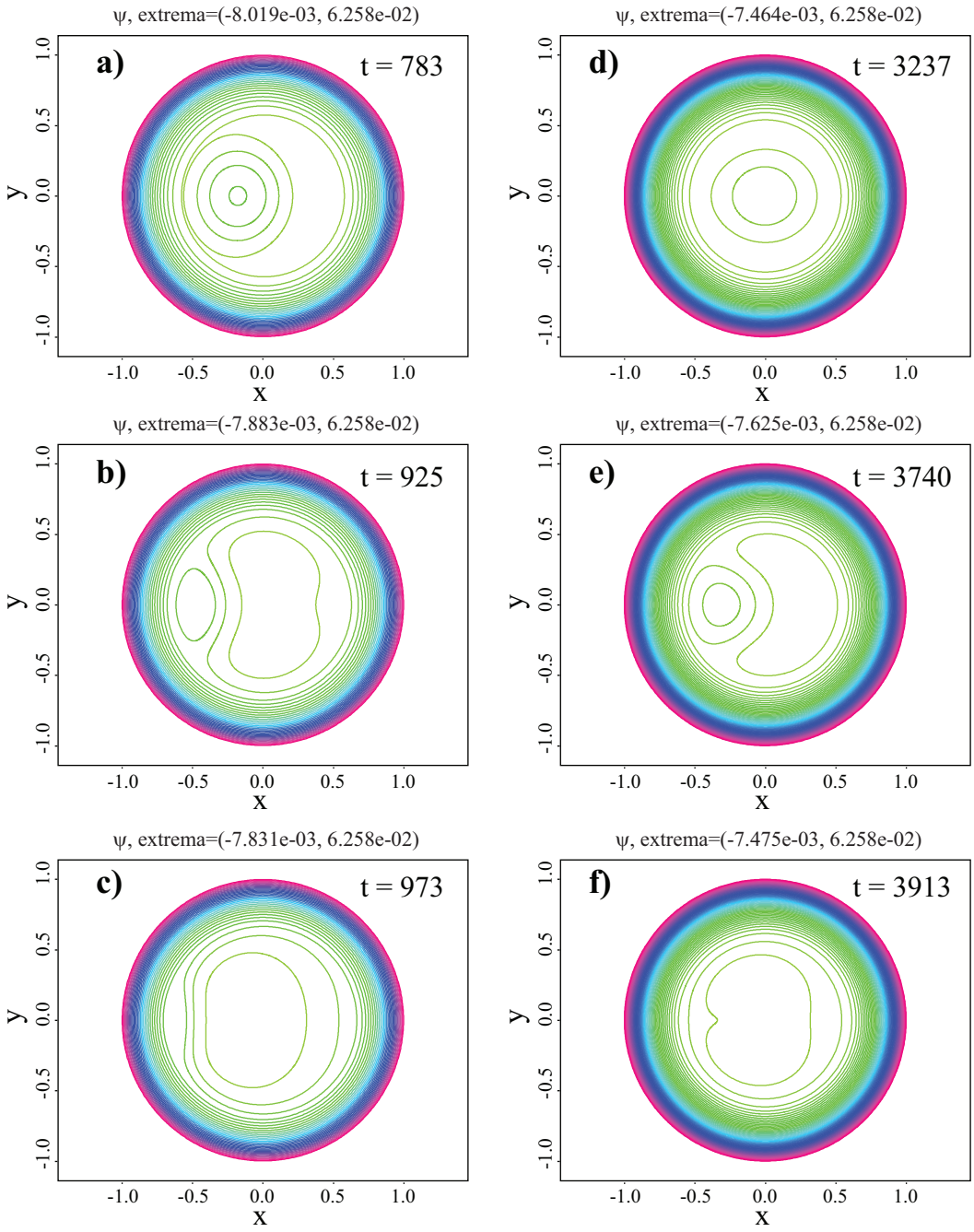

Figure 4.8: Contour plots of helical magnetic flux from the same simulation run and at six different times as noted in Figure 4.7. Min/max values associated with the color bar of the contours are shown at the top of each panel.

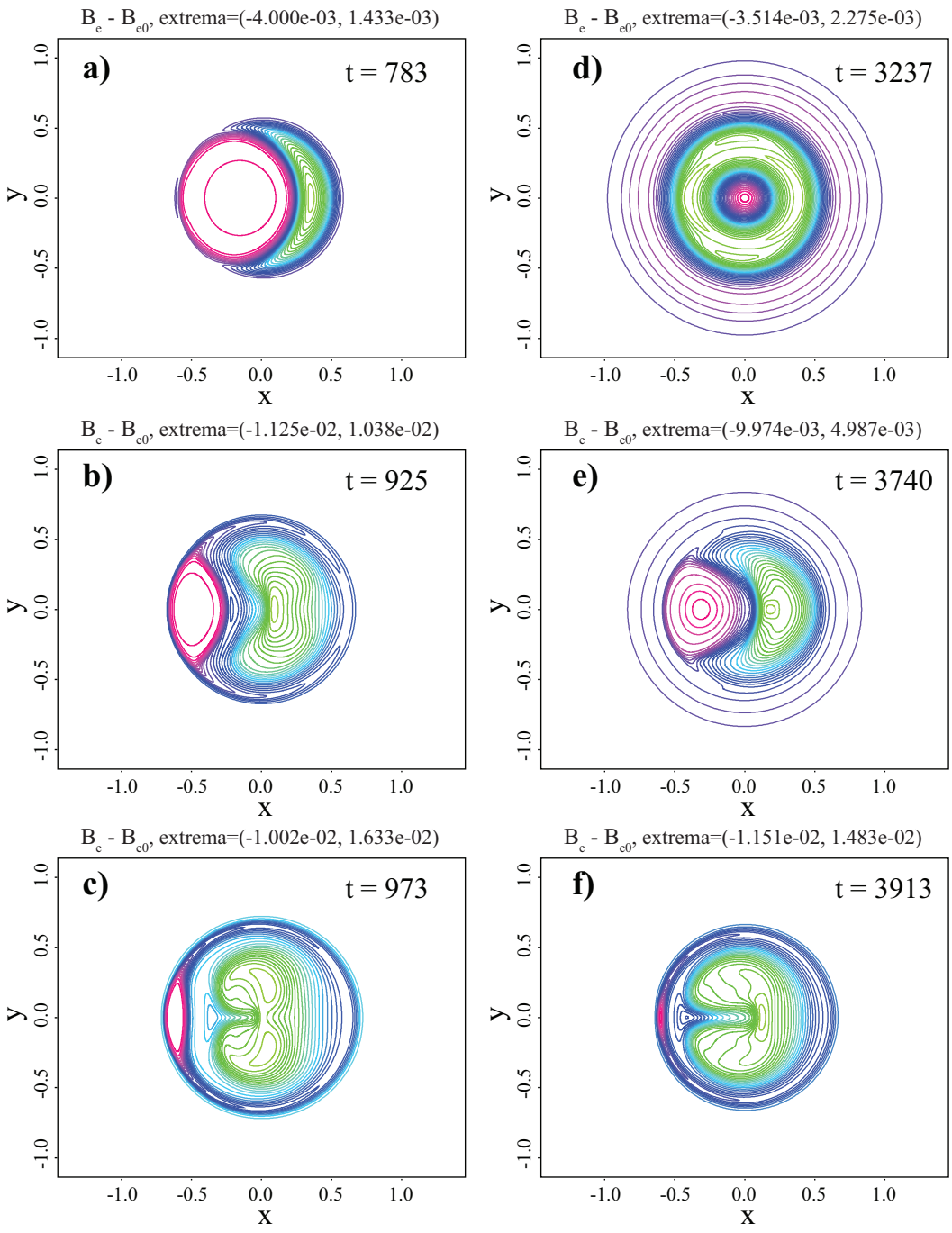

Figure 4.9: Contour plots of $B_e - 1/\epsilon^2$ from the same simulation run and at six different times as noted in Figure 4.7. Min/max values associated with the color bar of the contours are shown at the top of each panel.

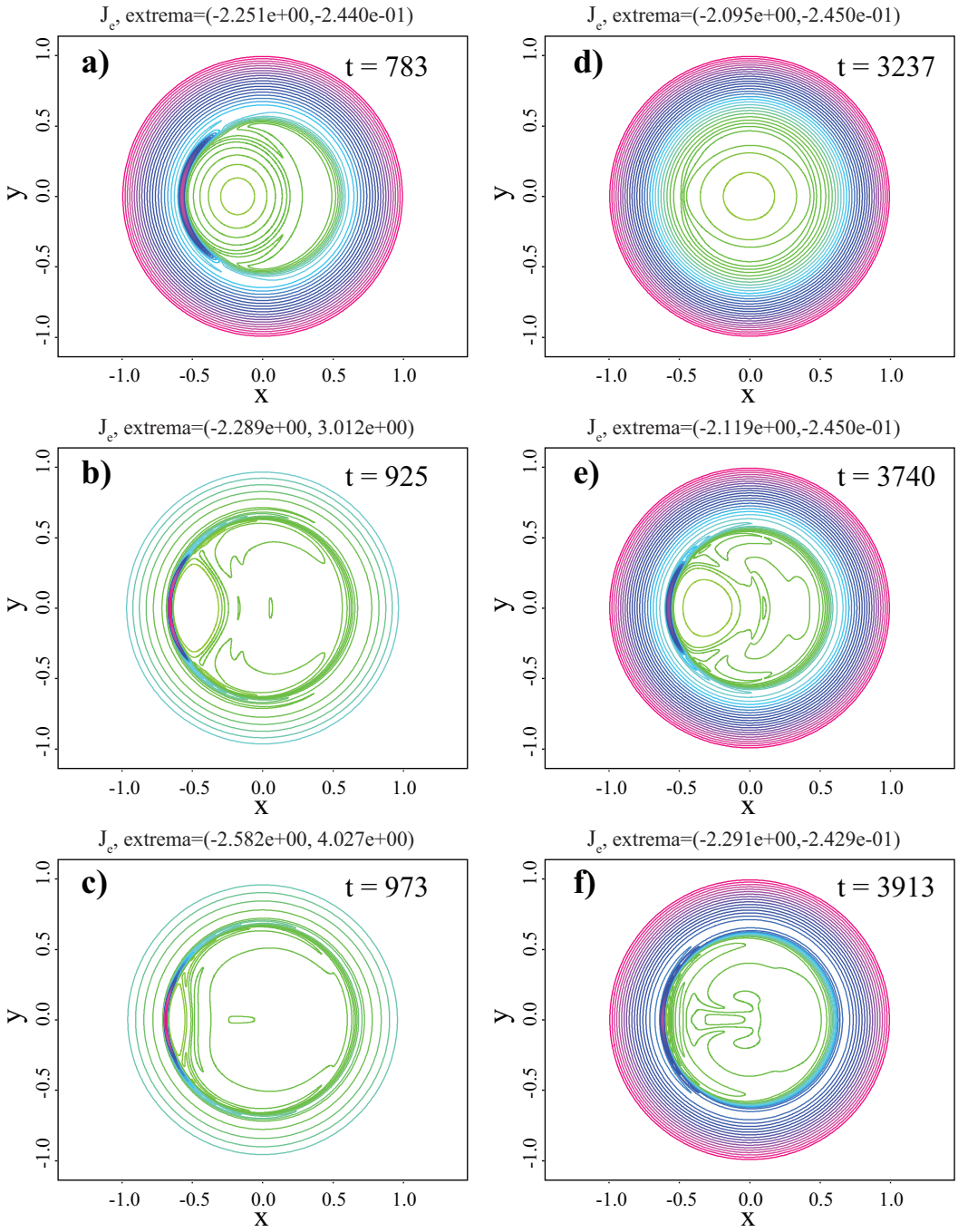

Figure 4.10: Contour plots of J_e from the same simulation run and at six different times as noted in Figure 4.7. Min/max values associated with the color bar of the contours are shown at the top of each panel.

$r_s = 0.5$ and perturbation $\delta B_e = 10^{-4}$ are shown in Figures 4.7-4.10. Figure 4.7 shows the time-trace of total kinetic energy in the system per unit length.[1] The large spike during $t \approx 700 - 1300$ corresponds to the first IR event, which is very similar in character to the one described above. As shown in panels (a-c) of Figures 4.8-4.10, outward motion of the plasma core is again accompanied by radial compression, with the main difference from the previous result being that the mixing radius of the complete Kadomtsev reconnection observed in this simulation run is further inwards at $r_M \approx .7$. Then, following a period of relatively quiet evolution with a minor IR event around $t \approx 2400$, a nearly axisymmetric state is achieved around $t \approx 3000$. Panel (d) of Figs. 4.8-4.10 demonstrates the quasi-equilibrium in which plasma is observed to stay for a prolonged period of time while the current source works to rebuild the initial equilibrium configuration of B-fields. However, unlike the initial equilibrium with B_e constant throughout the domain and $q = 1$ at $r_s = .5$, the singular surface of this new equilibrium appears to be located further inwards and out-of-plane B-field has a slightly paramagnetic profile within the new $q = 1$ surface[2]. The new equilibrium is then observed to also become unstable to the internal kink producing another spike in the system's kinetic energy. However, free magnetic energy deposited into the self-generated equilibrium before it becomes unstable appears to be significantly lower than that of the initial equilibrium, and both the flow energies and magnitude of the out-of-plane current in the reconnection current layer shown in Fig.4.10 are also much lower. Finally, we note that unlike the initial non-linear kink,

[1] Here and elsewhere in this Chapter, all integrals over the domain are taken over a two-dimensional computational plane and no account of the length of the periodic cylinder is taken. Thus, all energy measurements quoted below are those of energy per unit length of the cylinder.

[2] The shape of the self-generated equilibrium and its dependence on various physical parameters is discussed in detail in later Sections.

radial compression of the plasma core is not observed during the non-linear kinking of the new self-generated B-field configuration.

4.3.3 Comparing directly driven and boundary driven systems.

Having considered internal kink evolution with direct current drive, we now turn to a more realistic scenario of electric field being applied at the boundary of the domain and allowing it to diffuse radially inwards to drive the system. We begin by considering a problem set up as similar as possible to the one described above in order to compare the internally driven and boundary driven systems.

Since the equilibrium given by Eq. (4.2.5) contains no flows and purely $\hat{e}$-directed out-of-plane current, **E**-field initially present in the system is also purely $\hat{e}$-directed. Therefore, in order to consistently reproduce the current-driven system, $\hat{e}$-directed electric field $\mathbf{E} = E_b\hat{e}$ of magnitude $E_b = \eta_{r_s} J_0|_{r=1}$ is applied at the boundary and uniform resistivity is replaced by a radially dependent profile $\eta(r) \equiv E_b/J_0(r)$ with $\eta_{r_s} \equiv \eta(r = r_s)$ set to the same input value of $\eta_{r_s} = 10^{-5}$, as the previous direct current driven simulations.

Panel (a) of Figure 4.11 compares time histories of the total kinetic energy in the internally driven and boundary driven systems. Though some slight differences are apparent, qualitatively and, to a large degree, quantitatively, the two curves track each other. Both the initial and the self-generated IR events are observed to happen at about the same time and to produce similar magnitude spikes in kinetic energy in the two systems. Panel (b) of Figure 4.11 shows the time evolution of the local value of the safety factor $q_0 \equiv q(r = 0)$ (or equivalently – the local pitch of the magnetic field, which is generally the experimentally measured quantity[157, 138, 151, 108]) for

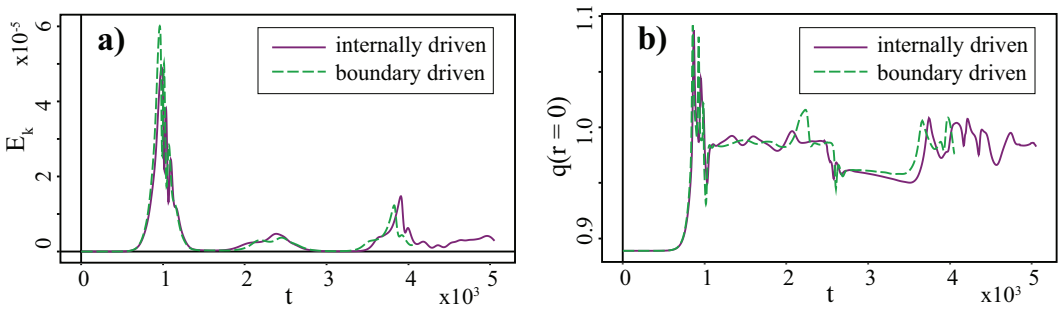

Figure 4.11: Time traces of (a) total kinetic energy and (b) local value of the safety factor q at $r = 0$, for two equivalent simulation runs – one with internally distributed current drive source and the other driven by corresponding E-field applied at the boundary of the domain.

the two systems.[3] These are also observed to be very similar both quantitatively and qualitatively. Following the initial IR event, q_0 is shown to sharply rise above 1.0 and then to fall back to about unity, where it stays until the self-generated equilibrium begins to form around $t \approx 2700$. After the self-generated IR event, q_0 is observed to again oscillate around unity until, presumably, a new self-generated equilibrium is formed at some later time.

[3]Here, we define $q(R) \equiv \left| d\bar{\Phi}/d\bar{\Psi} \right|$, where, in a toroidal system, $\bar{\Phi}$ is the toroidal magnetic flux defined as $\bar{\Phi} \equiv \int \mathbf{B} \cdot \nabla\phi \; dV$ and $\bar{\Psi}$ is the poloidal magnetic flux defined as $\bar{\Psi} \equiv \int \mathbf{B} \cdot \nabla\theta \; dV$. Replacing $\nabla\phi$ by $(\hat{z}/\epsilon)$ in the periodic cylindrical system, the following expressions for $\bar{\Phi}$ and $\bar{\Psi}$ in terms of the helical components of the magnetic field are derived:

$$\begin{aligned} \bar{\Phi}(R) &= \int_0^{2\pi} \int_0^R \epsilon r g^2 \left(\epsilon r \frac{\partial \Psi}{\partial r} + B_e \right) dr d\tau \\ \bar{\Psi}(R) &= \int_0^{2\pi} \int_0^R g^2 \left(\frac{\partial \Psi}{\partial r} - \epsilon r B_e \right) dr d\tau. \end{aligned}$$

Numerically, we evaluate $\lim_{r \to 0} q(r)$ as:

$$q_0 = \left| \frac{\bar{\Phi}(r + \Delta r) - \bar{\Phi}(r - \Delta r)}{\bar{\Psi}(r + \Delta r) - \bar{\Psi}(r - \Delta r)} \right|,$$

with $r \approx 10^{-2}$ and $\Delta r = r/4$.

This simple comparison study demonstrates that although not identical, the incompressible directly driven and boundary driven systems with time-independent resistivity are qualitatively and quantitatively similar. Thus, the conclusions drawn from the simulations of the boundary driven systems described below, are expected to also apply to similar directly driven systems.

4.3.4 Resistive axisymmetric equilibrium with axial electric field.

One of the more straightforward and widely used techniques for driving toroidal (axial) current in toroidal (straight cylinder) magnetic confinement devices is application of electric field in the corresponding direction at the boundary of the device, the so-called Ohmic current drive[156]. For the periodic cylinder system considered in this work, such axial electric field is a $\hat{z}$-directed E-field. With that in mind, we conduct the rest of the simulations with constant electric field $\mathbf{E}_b = E_b\hat{z}$ applied at the boundary of the domain. As an initial condition for these simulations, an axisymmetric resistive equilibrium with $\nabla \times \mathbf{E} = 0$ is desired.

Reduction of a helically symmetric system to axisymmetry implies that all non-zero quantities dependent only on radius r. Then, due to $\nabla \cdot \mathbf{B} = 0$, radial component of B-field is exactly zero and the condition of incompressibility in a circular domain also gives $v_r = 0$. Thus, in an incompressible time-independent system, the momentum equation is automatically satisfied and we only need to satisfy the Ohm's Law to derive a resistive equilibrium. (We return to the question of compressible equilibrium in later sections.)

Using $\hat{e} = g(\hat{z} - \epsilon r\hat{\theta})$ and $\hat{\tau} = g(\epsilon r\hat{z} + \hat{\theta})$, we have:

$$\mathbf{E}\cdot\hat{e} = g\frac{\partial\psi}{\partial t} = g\eta(r)\left[\Delta^*\psi - 2\epsilon g^2 B_e\right] = g(E_z - \epsilon r E_\theta) \tag{4.3.5}$$

$$\mathbf{E}\cdot\hat{\tau} = -g\eta(r)\frac{\partial B_e}{\partial r} = g(\epsilon r E_z + E_\theta). \tag{4.3.6}$$

On a circular domain, $\nabla\times\mathbf{E} = 0$ implies:

$$E_z = g(E_e + \epsilon r E_\tau) = E_b \tag{4.3.7}$$

$$E_\theta = g(E_\tau - \epsilon r E_e) = 0 \tag{4.3.8}$$

From Eq. (4.3.5) and Eq. (4.3.6), we have a system of equations:

$$\eta(r)g^2\left[\left(\Delta^*\psi - 2\epsilon g^2 B_e\right) - \epsilon r\frac{\partial B_e}{\partial r}\right] = E_b \tag{4.3.9}$$

$$\epsilon r\left(\Delta^*\psi - 2\epsilon g^2 B_e\right) + \frac{\partial B_e}{\partial r} = 0 \tag{4.3.10}$$

We now again assume the equilibrium profile of helical magnetic flux to be as in Park *et.al.*[112]:

$$\psi_0 = \frac{r^2}{4}\left(\frac{\epsilon^2 r^4}{3} + \frac{r^2}{2}(1-\epsilon^2 r_s^2) - r_s^2\right), \tag{4.3.11}$$

where r_s is the radial location of the singular surface. We also assume $B_{e0}(r=0) = 1/\epsilon$. Then, from Eq. (4.3.10):

$$B_{e0} = \frac{1}{g^2}\left[\frac{1}{\epsilon} - \frac{\epsilon r^2}{2}(r^2 - r_s^2)\right]. \tag{4.3.12}$$

Evaluating Eq. (4.3.9), we have:

$$\eta(r)\left[(1+2\epsilon^2 r^2)(r^2 - r_s^2) + \frac{r^2}{g^2} - 2\right] = E_b.$$

The constant E-field E_b is set by evaluating Eq. (4.3.7) at $r = r_s$ and setting $\eta(r = r_s) \equiv \eta_s$ to be an input parameter:

$$E_b = \eta_s\left[r_s^2(1+\epsilon^2 r_s^2) - 2\right].$$

It follows that:

$$\eta(r) = \frac{E_b}{(1+2\epsilon^2 r^2)(r^2 - r_s^2) + r^2/g^2 - 2}, \tag{4.3.13}$$

and J_e is evaluated to be:

$$J_{e0} = (1+2\epsilon^2 r^2)(r^2 - r_s^2) + r^2/g^2 - 2. \tag{4.3.14}$$

The q-profile corresponding to such axisymmetric configuration with concentric flux surfaces can also be easily evaluated as:

$$q(r) = \left| \frac{r\epsilon B_z}{B_\theta} \right| = \left| \frac{\epsilon r \frac{\partial \Psi}{\partial r} + B_e}{\frac{1}{\epsilon r}\frac{\partial \Psi}{\partial r} - B_e} \right| = \frac{1}{1 - (r^2 - r_s^2)/2g^2}. \tag{4.3.15}$$

4.3.5 Modified incompressible equilibrium.

As shown below, we have attempted to initialize our simulations of a self-reproducing Ohmic driven cycle of internal kink plasma relaxations with the resistive equilibrium derived above. We find that the amount of magnetic energy released during the relaxation event triggered by a small perturbation to the initial ideal kink-unstable equilibrium exceeds by more than an order of magnitude the magnetic energy released in the subsequent self-generated relaxation events. (See Fig 4.12 below.) Here, we derive a modified initial condition to have less magnetic energy available for release in the first reconnection event, while preserving the resistive equilibrium outside of the singular surface.

We modify the initial condition by finding a new helical flux function $\psi_1(r)$ for $0 \leq r \leq r_s$ and matching it to $\psi_0(r)$ for $r_s \leq r \leq 1$ at $r = r_s$ with the following

matching conditions:

$$\begin{aligned}
\psi_1|_{r_s} = \psi_0|_{r_s} &= -\frac{r_s^4}{8}\left(1+\frac{\epsilon^2 r_s^2}{3}\right) \\
\frac{\partial\psi_1}{\partial r}|_{r_s} &= \frac{\partial\psi_0}{\partial r}|_{r_s} = 0 \\
\frac{\partial}{\partial r}\left(rg^2\frac{\partial\psi_1}{\partial r}\right)|_{r_s} &= \frac{\partial}{\partial r}\left(rg^2\frac{\partial\psi_0}{\partial r}\right)|_{r_s} = r_s^3 \\
\frac{\partial}{\partial r}\left[\frac{1}{rg^2}\frac{\partial}{\partial r}\left(rg^2\frac{\partial\psi_1}{\partial r}\right)\right]|_{r_s} &= \frac{\partial}{\partial r}\left[\frac{1}{rg^2}\frac{\partial}{\partial r}\left(rg^2\frac{\partial\psi_0}{\partial r}\right)\right]|_{r_s} = 2r_s\left(2+3\epsilon^2 r_s^2\right),
\end{aligned}$$

where the matching conditions guarantee continuity of the helical magnetic flux, τ-component of magnetic field, helical plasma current density J_e, and radial derivative of J_e, respectively. The following form for ψ_1 is assumed:

$$\psi_1 = \frac{a_1}{8}r^8 + \frac{a_2}{6}r^6 + \frac{a_3}{4}r^4 + \frac{a_4}{2}r^2 + a_5.$$

By satisfying the matching conditions above, we derive ψ_1 to be:

$$\begin{aligned}
\psi_1 &= \frac{r^2}{4}\left(\frac{\epsilon^2 r^4}{3} + \frac{r^2}{2}(1-\epsilon^2 r_s^2) - r_s^2\right) - \frac{\bar{\psi}}{8r_s^4}\left(1+\frac{\epsilon^2 r_s^2}{3}\right)\left(r^2-r_s^2\right)^4 \\
&= \psi_0 - \frac{\bar{\psi}}{8r_s^4}\left(1+\frac{\epsilon^2 r_s^2}{3}\right)\left(r^2-r_s^2\right)^4, \qquad (4.3.16)
\end{aligned}$$

where $\bar{\psi}$ is an arbitrary constant such that for $\bar{\psi}=1$, $\psi_1(0)=\psi_1(r_s)$. It is easy to show that $\psi_1(r)$ has no local maxima or minima for $r\in(0,r_s)$ when $0\le\bar{\psi}\le\frac{1}{2\left(1+\frac{\epsilon^2 r_s^2}{3}\right)}$. Finally, we evaluate $J_e(r)$ for $0\le r\le r_s$ to be:

$$J_{e1} = J_{e0} - \frac{2\bar{\psi}}{r_s^4}\left(1+\frac{\epsilon^2 r_s^2}{3}\right)\left(r^2-r_s^2\right)^2\left[g^2\left(r^2-r_s^2\right)+3r^2\right].$$

Though the expressions derived above are valid for any $0<r_s<1$, we note that due to our desire to study long-term evolution of the system while limiting the influence of boundary effects on it, all simulations described below are conducted with $r_s=0.5$. As discussed in the previous sections, such choice guarantees that the

mixing radius of the IR events remains well within the boundaries of the domain, while allowing for the plasma core to occupy a large fraction of the domain.

4.3.6 Boundary conditions for Ohmic current drive simulations.

There are two separate boundary conditions that have to be enforced to simulate application of a purely axial electric field at the wall of a device. They are: $\mathbf{E}_b \cdot \hat{z} = g(E_e + \epsilon r E_\tau) = E_b$ and $\mathbf{E}_b \cdot \hat{\theta} = g(E_\tau - \epsilon r E_e) = 0$. Within the incompressible visco-resistive MHD model and with the representation of $\mathbf{B}$ and $\mathbf{v}$-fields described above, we implement them by enforcing the $\hat{z}$-projection of the Ohm's Law to guarantee $\mathbf{E}_b \cdot \hat{z} = E_b$ and $\hat{\theta}$-projection of the Ohm's Law to guarantee $\mathbf{E}_b \cdot \hat{\theta} = 0$, as follows:

$$\begin{aligned} g^2 \frac{\partial \psi}{\partial t} &= E_b + \epsilon g^2 r_w \left[\eta(r_w) \frac{\partial B_e}{\partial r} \right] \\ \epsilon r_w \frac{\partial \psi}{\partial t} &= -\eta(r_w) \frac{\partial B_e}{\partial r}, \end{aligned}$$

where r_w is the wall radius. The same as above boundary conditions on ion flow – no flow onto the wall and perfect slip flow tangential to the wall – are enforced.

4.3.7 Sensitivity to the initial conditions.

Before we proceed with detailed examination of the sawtoothing phenomena observed in the Ohmic driven incompressible resistive MHD simulations, we demonstrate the existence and apparent uniqueness of the limit cycle for given radial profiles of dissipation coefficients, magnitude of the applied E-field and conserved integral quantities, such as total axial magnetic flux in the domain.

Panel (a) of Figure 4.12 shows time-traces of total kinetic and poloidal magnetic energies integrated over the domain for two simulation runs identical except for the

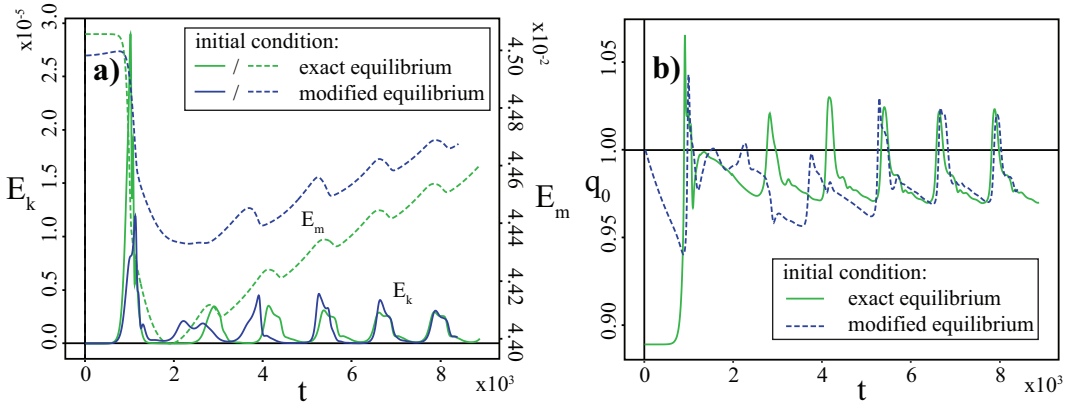

Figure 4.12: Comparison of two simulation runs identical except for the initial profile of helical magnetic flux ψ within the singular radius $r_s = .5$ given by Eq (4.3.11) for exact resistive equilibrium and by Eq (4.3.16) for modified equilibrium. Panel (a) shows time traces of total kinetic energy E_k and poloidal magnetic energy E_m; and panel (b) local value of safety factor q_0. Run parameters in both cases are: $\eta_s = 10^{-5}$, $\mu = 5 * 10^{-5}$, $1/\epsilon = 25$ and $\delta B_e = 10^{-3}$ with ohmic current drive.

initial profile of helical magnetic flux. It is immediately apparent that both the drop in poloidal magnetic energy and spike in kinetic energy are decreased by a large fraction when the exact resistive equilibrium is substituted by the modified initial condition described above. However, traces from the two runs are shown to converge to quantitatively the same quasi-periodic behavior we denote as the sawtoothing phenomena. The systematic rise in poloidal magnetic energy observed in both simulation runs is attributed to resistive rearranging of the magnetic fields outside of the mixing radius to match the value of B-fields at r_M of the internal reconnection events which constitute the sawteeth. Still, it is clear that magnetic energy released during the self-generated sawteeth is at least an order of magnitude less than that during the initial internal kink event. Panel (b) of Figure 4.12 shows that the local measure of the magnetic field configuration, q_0, also converges for the two simulation runs after

two distinctly different initial phases of evolution.

Thus, results shown in Figure 4.12 not only demonstrate the existence of quasi-periodic sawteeth, but also that their dynamics is independent of the exact initial conditions of the simulation. This justifies using modified resistive equilibrium as an initial condition for studying the sawteeth themselves, as the initial internal kink observed to develop with the modified equilibrium has less magnetic energy to release and is therefore less violent than that with the exact resistive equilibrium. Below, when studying the incompressible sawteeth, we do not distinguish between these two initial conditions.

4.3.8 Influence of the helical aspect ratio on the sawtoothing behavior.

We now consider how the aspect ratio of the periodic cylinder – and therefore the helical curvature of the assumed lines of symmetry and helicity of the initial equilibrium B-field – influence the plasma dynamics following the initial violent internal kink event.

Figure 4.13 compares evolution of total kinetic energy, panel (a), and q on the geometric axis, panel (b), for three values of the aspect ratio $1/\epsilon = 5$, 10, and 25. While qualitatively different, periodic behavior of the measured quantities is apparent for the two largest values of the aspect ratio. However, the simulation with $1/\epsilon = 5$ appears to settle into some stable state and no sawtoothing phenomena are observed. We note that although both the magnitude of the electric field applied at the wall and the exact resistivity profile depend on ϵ, the dependence is only second order in ϵr and is not expected to influence the results for the values of ϵ being considered. The details of the sawtooth dynamics for the two larger aspect ratios are described

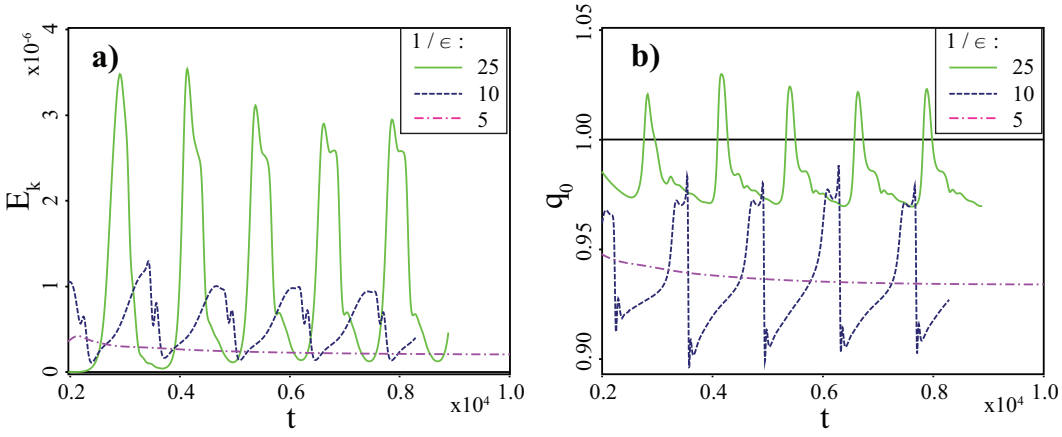

Figure 4.13: Time-traces from three simulation runs with varied helical aspect ratio $1/\epsilon$. Panel (a) shows evolution of total kinetic energy E_k and panel (b) local value of safety factor q_0 following the initial internal kink event. The dissipation parameters for all three runs are: $\eta_s = 10^{-5}$ and $\mu = 5 * 10^{-5}$.

in Figs. 4.14-4.19 below, while the stable state is discussed in the next section.

Large aspect ratio simulations – Kadomtsev sawteeth.

A single sawtooth of the largest aspect ratio simulation $1/\epsilon = 25$ is shown in Figure 4.14. The six different times at which the contour plots of helical magnetic flux and stream function are shown in Figs. 4.15-4.16 are marked with arrows in Figure 4.14.

Panel (a) of Figs. 4.15-4.16 show poloidal magnetic field configuration and flow pattern when minimum in kinetic energy and near-minimum in q_0 are achieved. We consider that to be the quasi-equilibrium state which then becomes unstable to an internal kink and produces a sawtooth. While mainly axisymmetric, contours of magnetic flux show a sign of a small $m = 1$ component even in that quasi-equilibrium state. A flow double-vortex is consistent with having an $m = 1$ B-field component. As the internal kink develops, panels (b)-(d) follow what appears to be complete Kadomtsev reconnection of the plasma core, with generated flows resulting in peaking

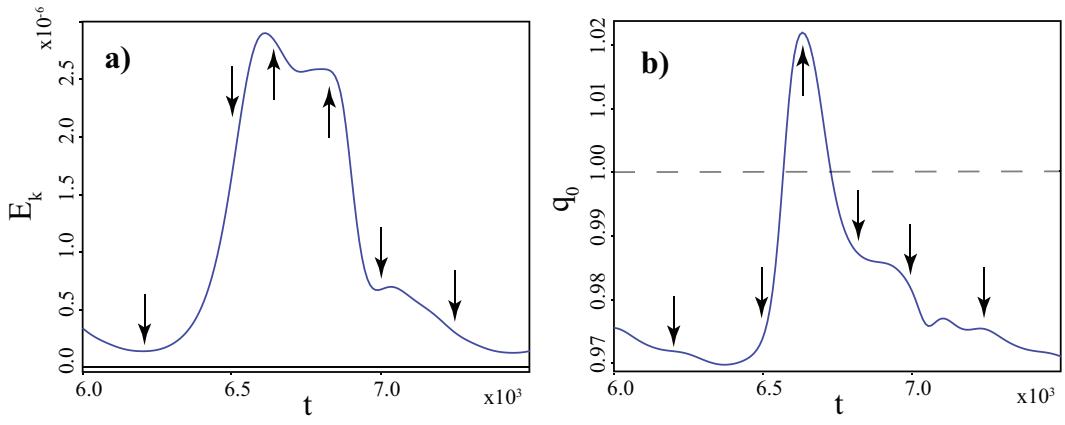

Figure 4.14: Time-traces of (a) total kinetic energy and (b) q_0 from a single sawtooth with helical aspect ratio of $1/\epsilon = 25$. Arrows denote the times at which contour plots of Figs. 4.15-4.16 are generated.

of kinetic energy and q_0 briefly rising above 1.0. During the sawtooth reconnection process, the shape of the core flux surfaces is observed to remain approximately circular, consistent with the previous observations of a directly driven system in Fig. 4.8.

Once the core has completely reconnected, panels (e) and (f) show how flux surfaces within $r < r_s$ begin to re-seal themselves and q_0 drops back to its lowest value. It is apparent that the new flux surfaces are initially formed by a pattern of return flows which force the flux surfaces to re-seal through a weak reconnection process, followed by further build up of the peaked current profile with Ohmic drive. This process of return flows is very similar to the "quasi-interchange" instability proposed by Wesson[153, 154] for the sawtooth crash mechanism and inferred to be observed experimentally on the JET Tokamak[67, 154, 155]. We note that consistent with the "quasi-interchange" mechanism proposed by Wesson, in these simulations, q within r_M is near unity following the complete Kadomtsev reconnection of the core.

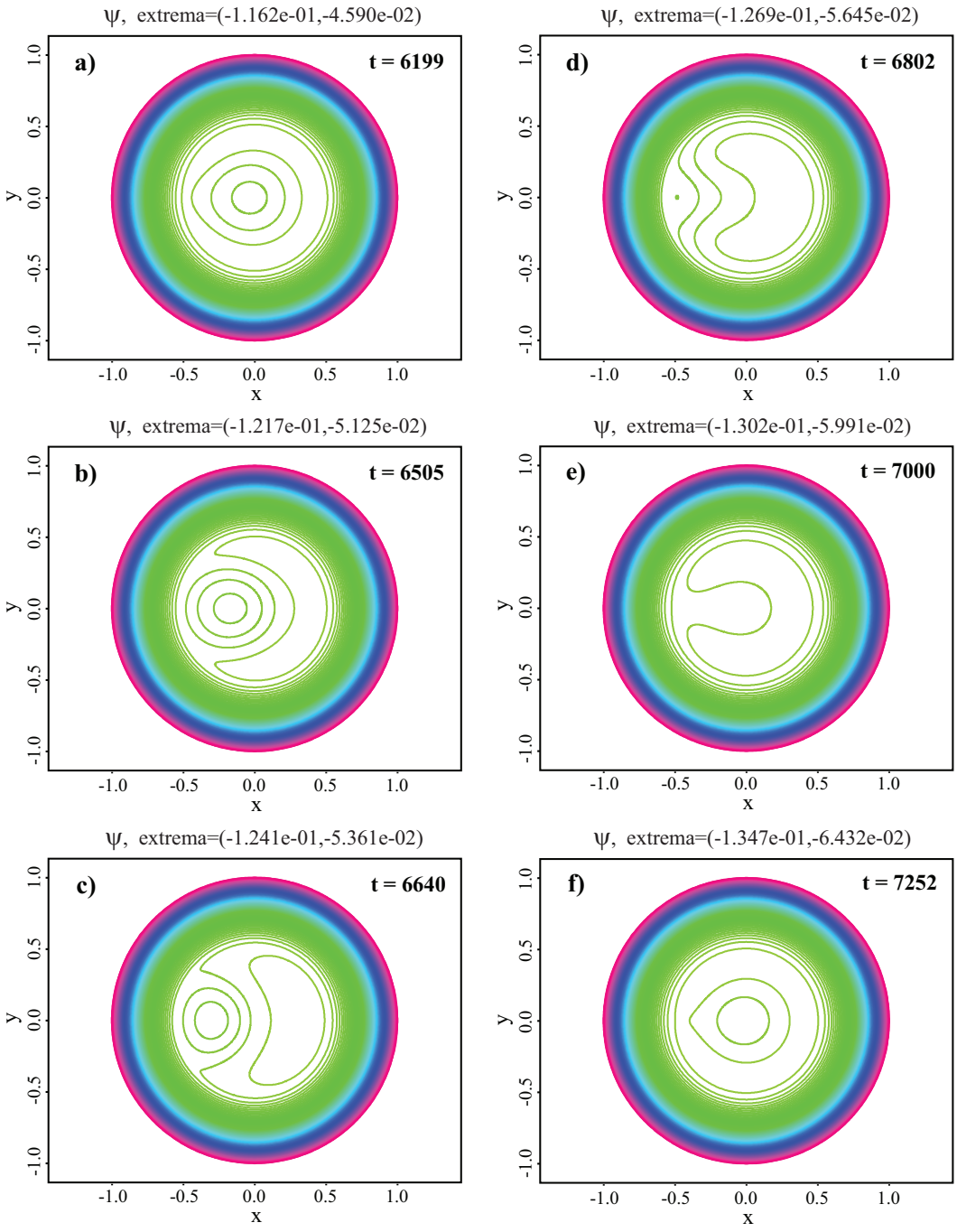

Figure 4.15: Contour plots of helical magnetic flux from the same simulation run and at six different times as noted in Figure 4.14 ($1/\epsilon = 25$). Min/max values associated with the color bar of the contours are shown at the top of each panel.

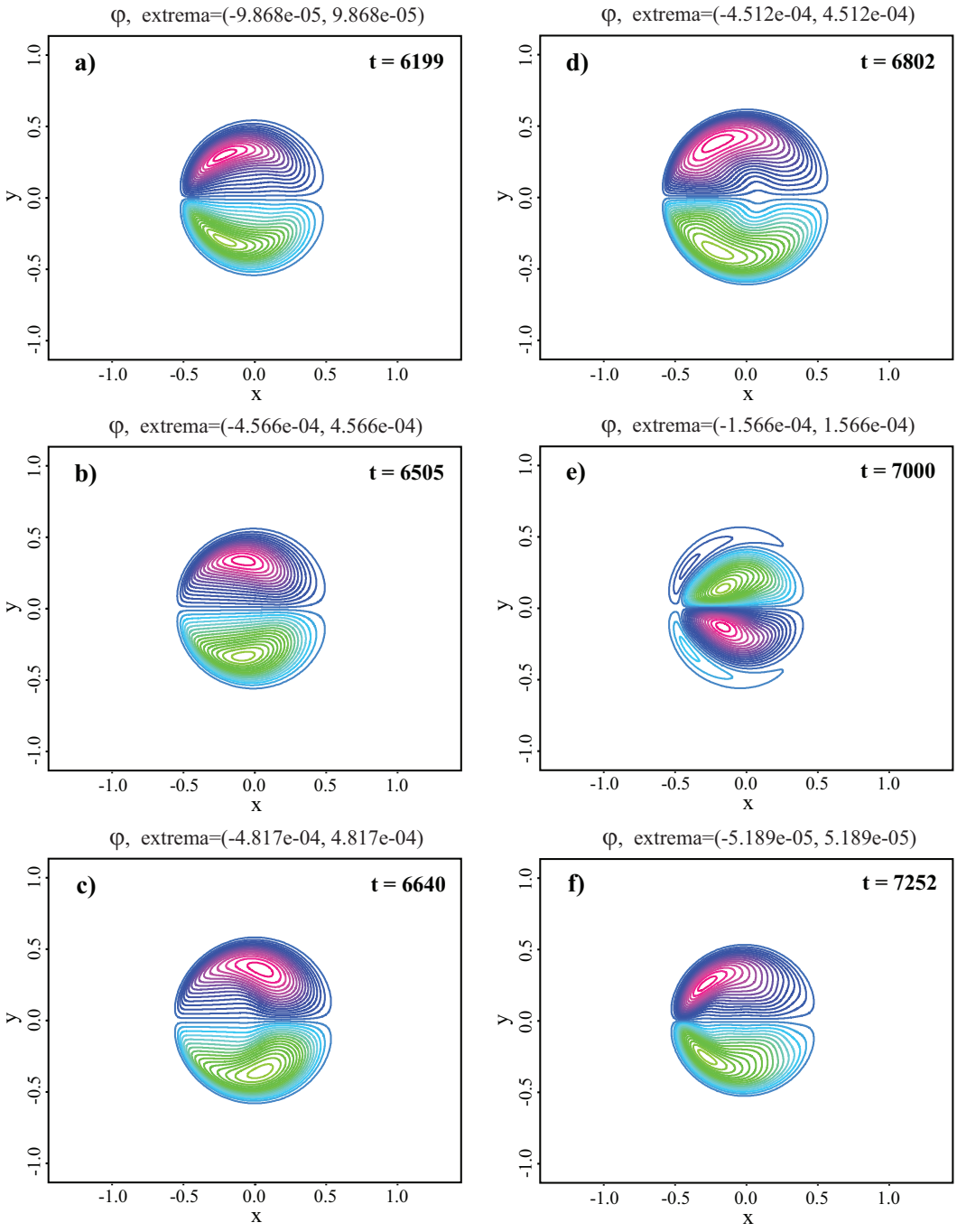

Figure 4.16: Contour plots of helical stream function from the same simulation run and at six different times as noted in Figure 4.14 ($1/\epsilon = 25$). Min/max values associated with the color bar of the contours are shown at the top of each panel.

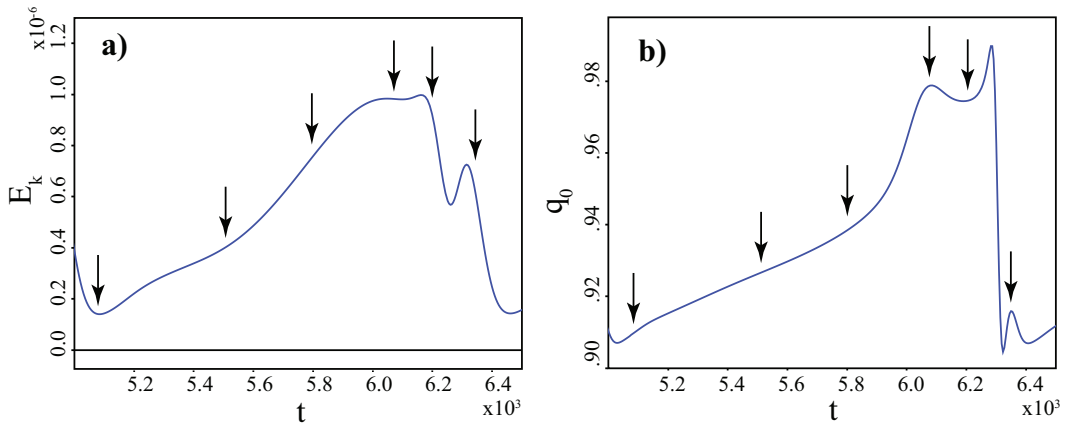

Figure 4.17: Time-traces of (a) total kinetic energy and (b) q_0 from a single sawtooth with helical aspect ratio of $1/\epsilon = 10$. Arrows denote the times at which contour plots of Figs. 4.18-4.19 are generated.

Moderate aspect ratio simulations – Porcelli sawteeth.

A similar set of figures (Figs. 4.17-4.19) describes dynamics of a single sawtooth for simulations with aspect ratio of $1/\epsilon = 10$. Comparing Fig. 4.17 to Fig. 4.14, it is immediately apparent that the smaller aspect ratio sawteeth acquire lower kinetic energy and take much longer for the internal kink to develop and raise q on the geometric axis, while q_0 never quite reaches unity. Panels (a)-(c) of Figs. 4.18-4.19 demonstrate evolution of poloidal magnetic field and plasma flow during this slow build up stage. With smaller aspect ratio, and therefore stronger effects of the helical curvature, magnetic axis of the quasi-equilibrium is shifted further from $r = 0$, thus exhibiting more of an $m = 1$ component and a prominent island structure which persists through the evolution. In the later stages of the sawtooth, unlike the $1/\epsilon = 25$ case, panels (d) and (e) show radial elongation of the plasma core with plasma flow beginning to reverse near the magnetic axis. This is immediately followed by a sharp drop in q_0 and secondary peak in the systems kinetic energy, when plasma core is

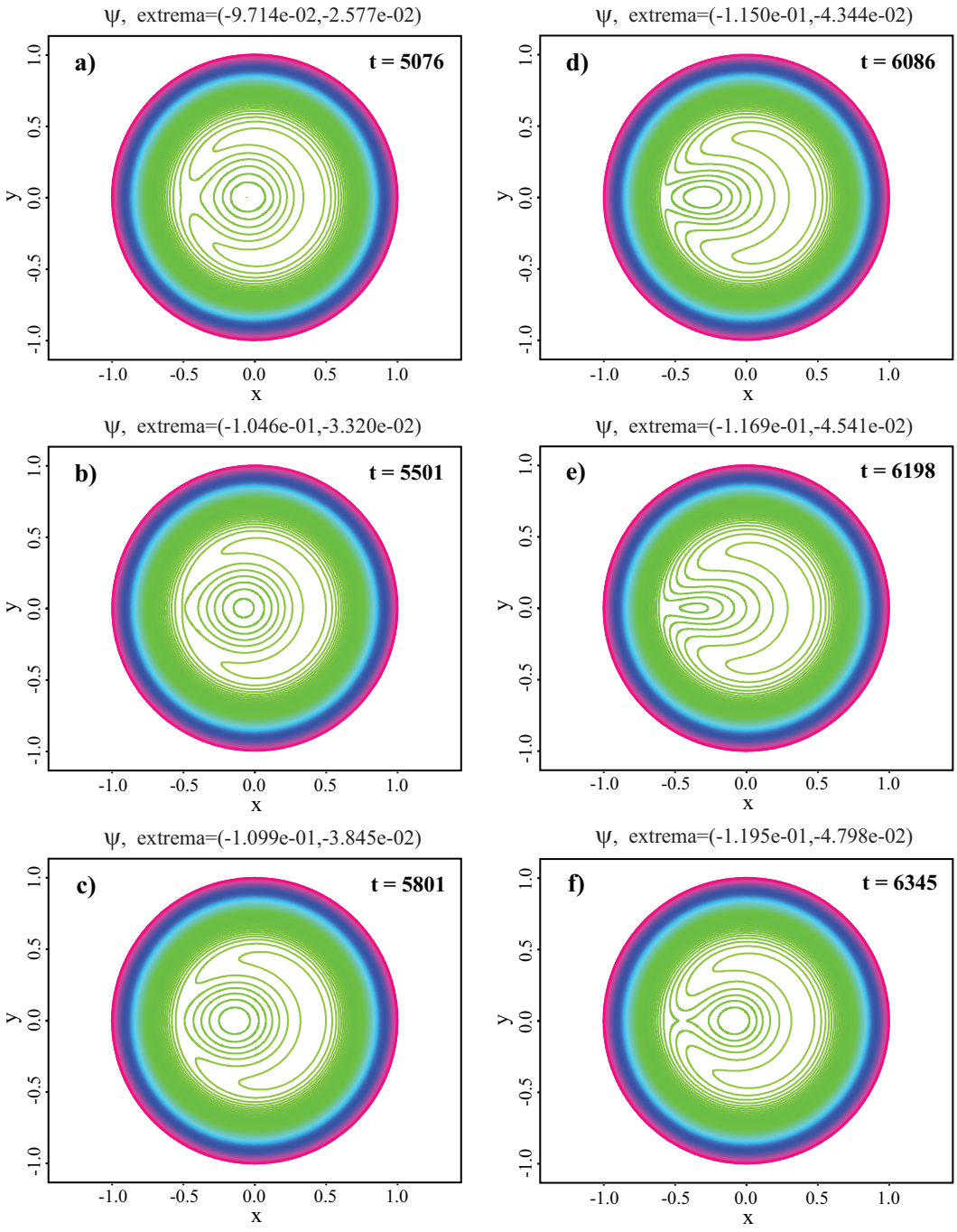

Figure 4.18: Contour plots of helical magnetic flux from the same simulation run and at six different times as noted in Figure 4.17 ($1/\epsilon = 10$). Min/max values associated with the color bar of the contours are shown at the top of each panel.

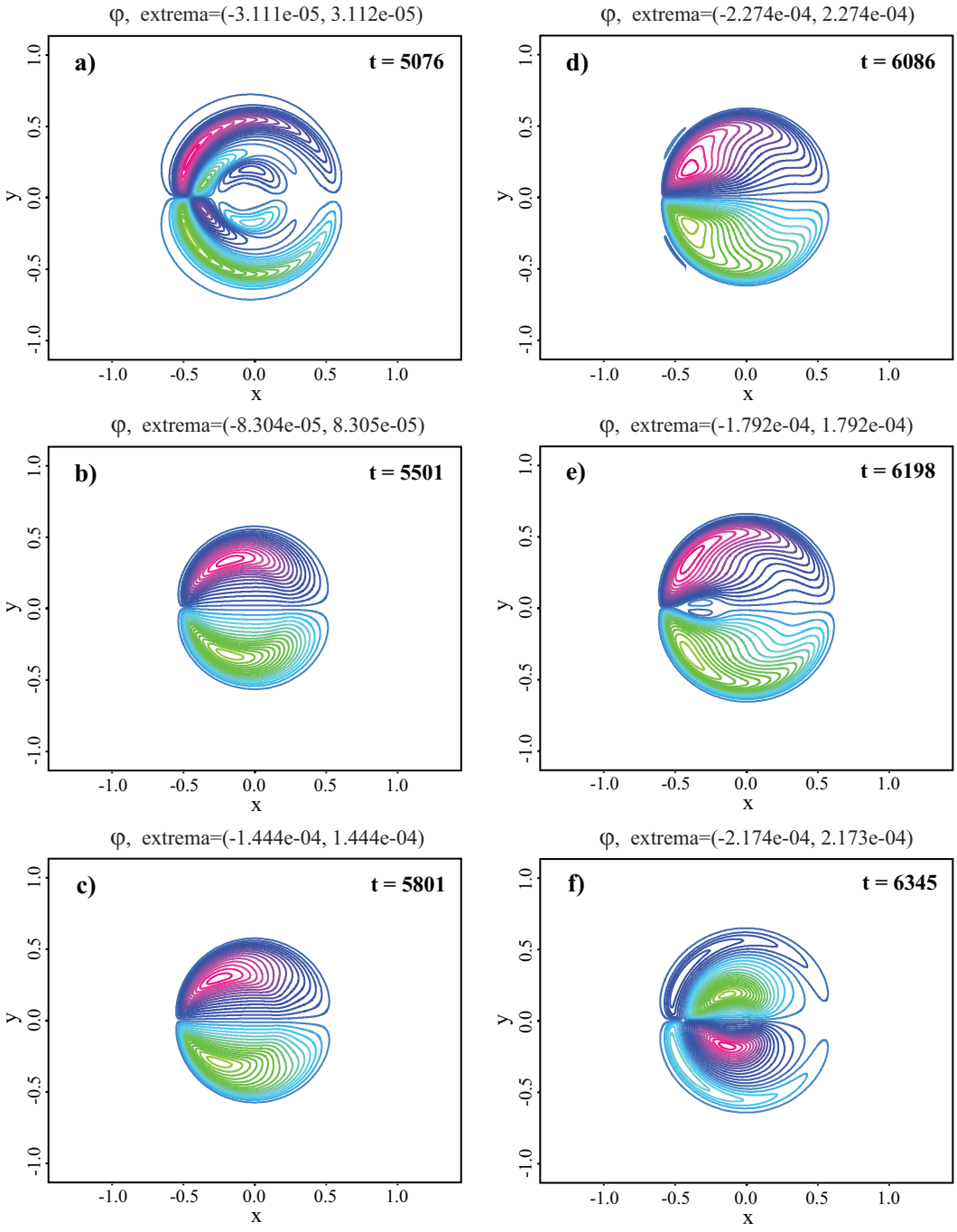

Figure 4.19: Contour plots of helical stream function from the same simulation run and at six different times as noted in Figure 4.17 ($1/\epsilon = 10$). Min/max values associated with the color bar of the contours are shown at the top of each panel.

observed to snap back towards the geometric axis before its reconnection is completed.

Once the magnetic axis is returned to near-center of the domain, as in the case of $1/\epsilon = 25$, return plasma flows again proceed to wrap additional flux surfaces around it in a manner similar to the quasi-interchange mode. In this case, however, q on the magnetic axis is ≈ 0.9, which appears to be inconsistent with the quasi-interchange theory[153, 154].

Thus, for $1/\epsilon = 10$, no complete Kadomtsev reconnection during the sawteeth is observed and only partial reconnection of the core, as in the Porcelli model[121], occurs. This result is in contradiction to the previous resistive MHD simulations of the internal kink[67]. Furthermore, incomplete reconnection of the internal kink is observed to be followed by a quasi-interchange-like behavior, which, nevertheless, is not easily describable by the existing theory of the quasi-interchange mode.

Compare and contrast.

We believe, the observed dynamics of a sawtooth for $1/\epsilon = 10$ can be qualitatively explained by studying and comparing its quasi-equilibrium configuration and kinking evolution with that of a sawtooth with very large aspect ratio case of $1/\epsilon = 25$. Panels (a) and (d) of Figure 4.20 demonstrate the feature of key importance: Unlike the axisymmetric resistive equilibrium the simulations are initialized with, where $B_{z0} = 1/\epsilon = const$, the self-generated quasi-equilibria have distinctly paramagnetic profiles of B_z. Since the model being considered is formulated as absolutely incompressible, the observed paramagnetism cannot be due to any transport related pinching effects, but has to be caused by plasma relaxing to a smaller energy state within the allowed helical symmetry. The largest aspect ratio case of $1/\epsilon = 25$ shows paramagnetic increase in B_z on axis to be $\delta B_z \approx 7.5 * 10^{-3}$, while simulation with $1/\epsilon = 10$

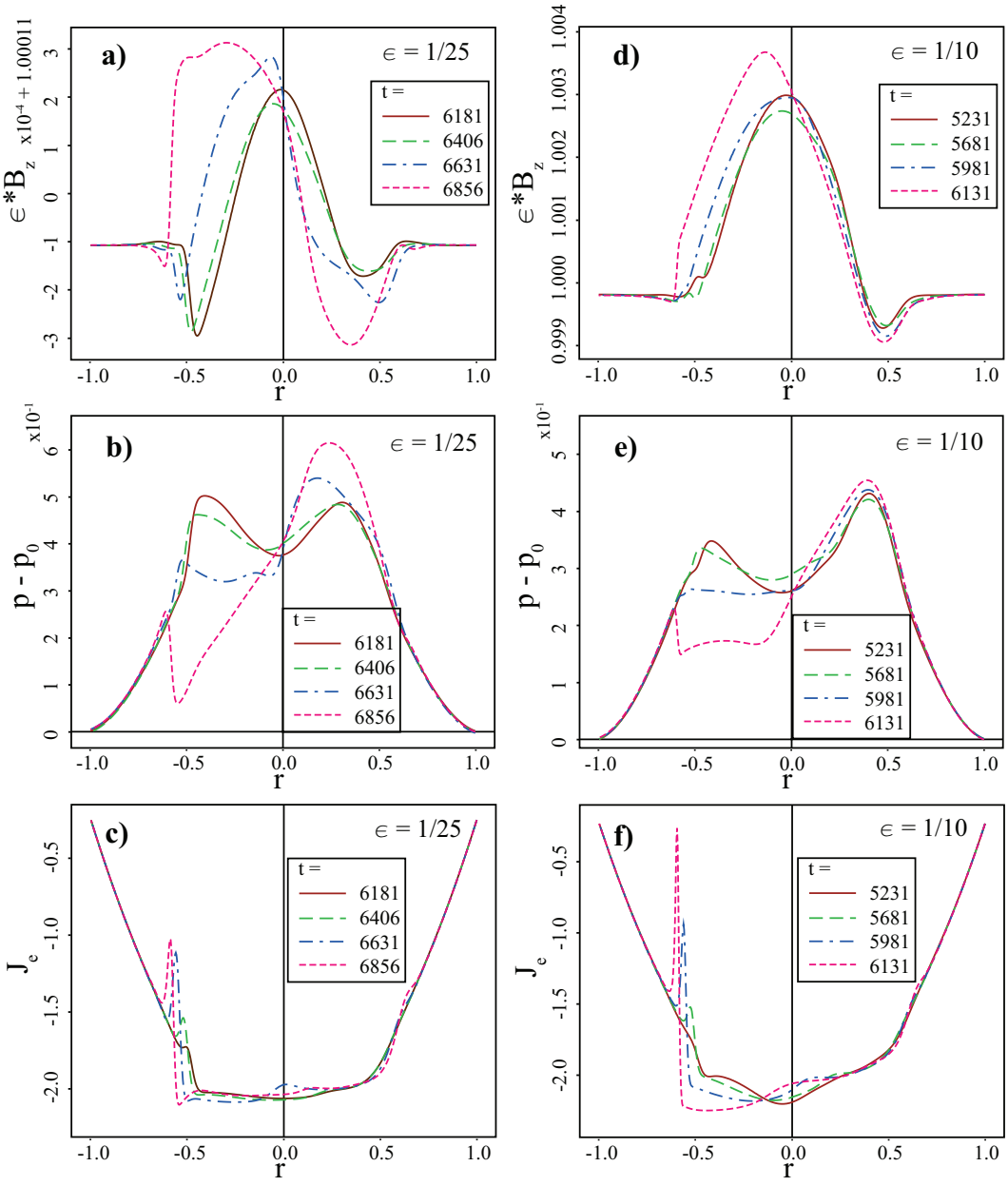

Figure 4.20: Profiles of axial component of magnetic field B_z normalized by the inverse aspect ratio [panels (a,d)], derived pressure [panels (b,e)], and helical component of plasma current J_e [panels (c,f)] through geometric and magnetic axes ($r = [-1, 1], \tau = 0$) are shown at several times during sawtooth cycles with helical aspect ratio $1/\epsilon = 25$, panels (a-c), and $1/\epsilon = 10$, panels (d-f). Profiles are taken from the same sawteeth as shown in Figs. 4.14-4.19 above.

produces $\delta B_z \approx 3 * 10^{-2}$. (We consider the structure of the helical quasi-equilibria in further detail in the next Section.) Though very small compared to the domain averaged values of B_z of 25 and 10, respectively, these perturbations are comparable to the magnitude of poloidal B-fields within r_s generated by the Ohmic current drive before each new IR event takes place.

The effects of the paramagnetic axial B-field on the sawtooth dynamics become apparent when one considers the resulting radial distribution and temporal evolution of plasma and magnetic pressure. Panels (b) and (e) of Figure 4.20 show the corresponding profiles of plasma pressure along the same cut across the domain: $r \in [-1, 1]$, $\tau = 0$ – where plasma pressure has been calculated by integrating the radial component of the momentum equation along the cut and making use of the up-down symmetry of the solution (as shown in Figs. 4.15-4.16 and Figs. 4.18-4.19). (In integrating the momentum equation, pressure has been assumed to have some value p_0 at the wall and contributions of the inertia, advection and viscous terms has been neglected as $|v_r| < 5 * 10^{-3}$ everywhere along the cut and $(\mathbf{J} \times \mathbf{B})_r$ is of order unity at the times shown.) Before the onset of kinking, a hollow profile of plasma pressure within the singular radius r_s with pressure peaking near $r = r_s$ is observed. Correlated with the magnitude of the paramagnetic δB_z, depression in pressure at $r = 0$ is stronger and peak pressure at $r = r_s$ is lower for the smaller aspect ratio quasi-equilibrium. During kinking, axial B-field in the core is shown to increase, resulting in further expulsion of plasma pressure from the core into the $m = 1$ island on the other side of the geometric axis.

It is also intuitively obvious that a kinking perturbation that radially displaces the plasma core together with the paramagnetic peak in B_z, as shown in Figure 4.20,

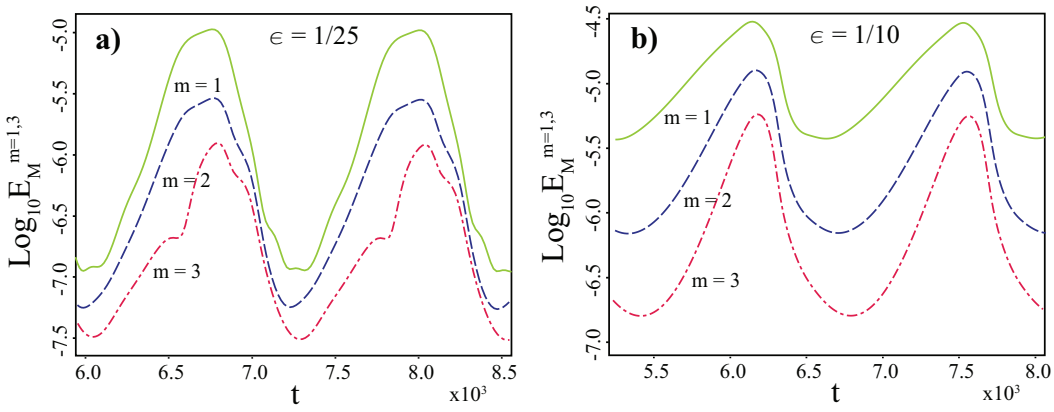

Figure 4.21: Time traces of magnetic energy in the three lowest non-axisymmetric m-modes $E_M^{m=1,3}$ during sawtooth oscillations in simulations with helical aspect ratios (a) $1/\epsilon = 25$; and (b) $1/\epsilon = 10$.

stretches magnetic field-lines by making the path of more magnetic field lines longer. Over a single period length of the cylinder $2\pi L$, to the leading order in ϵ, increase in the length of helical magnetic field lines due to such displacement to some radius r is $\delta l \approx \epsilon r L$. Then, increase in helical magnetic energy per unit length of the cylinder due to stretching is given by $\delta E_{Mz} \sim (B_z \delta B_z)(\epsilon r)$, and since $B_z \approx 1/\epsilon$, we have $\delta E_{Mz} \sim r \delta B_z$. Thus, as δB_z has been shown to increase with ϵ, paramagnetism of the helical quasi-equilibrium should be expected to produce greater increase in non-axisymmetric fraction of magnetic energy in the system during kinking for greater ϵ. Figure 4.21 shows temporal evolution of magnetic energy stored in the three lowest non-axisymmetric m-modes E_M^m during sawtooth oscillations in simulations with helical aspect ratios $1/\epsilon = 25$ [panel (a)] and $1/\epsilon = 10$ [panels (b)]. We note that the time periods shown in Figure 4.21 include those presented in Figure 4.14 and Figure 4.17 for the two helical aspect ratios. Not surprisingly, peak magnetic energy in the $m > 0$ modes is achieved at the time of maximum displacement (or

immediately prior to full reconnection) of the plasma core. The ratio of peak magnetic energy in the $m = 1$ mode for $1/\epsilon = 10$ to that for $1/\epsilon = 25$ is observed to be about $(10^{-4.6}/10^{-5.0}) \approx 2.51$, consistent with the estimate presented above. Furthermore, the minimum of magnetic energy stored in the $m = 1$ mode over an $1/\epsilon = 10$ sawtooth cycle is over an order of magnitude greater than that in an $1/\epsilon = 25$ sawtooth cycle, thus confirming the greater non-axisymmetry of the quasi-equilibria achieved with smaller helical aspect ratio.

Conclusions.

It follows from the observations above, that the paramagnetism of the helical quasi-equilibria has a stabilizing effect on the internal kink mode that develops in that quasi-equilibria due to continued Ohmic current drive imposed on the system. This appears to have several key consequences:

1. As evidenced by comparing magnetic flux contours in Fig. 4.15 and Fig. 4.18, more poloidal magnetic flux is generated by Ohmic current drive before the instability sets in when $1/\epsilon$ is smaller. Therefore, q on axis is lowered.

2. Given a plasma core with paramagnetic B_z, when radially displaced from $r = 0$, tear-drop shape radial elongation of the core minimizes δE_{Mz} (see panels (d,e) of Figure 4.18). As a result, magnetic reconnection proceeds through a short point-like layer, which greatly accelerates the process[7]. Greater peak reconnection currents for greater ϵ, shown in panels (c) and (f) of Figure 4.20, are the evidence of the accelerated magnetic reconnection.

3. As reconnection proceeds, the core has to move further and further outward

and increase δE_{Mz}. For large enough δB_z, the energy gain from continued reconnection of the poloidal B-field looses out to the the energy loss due to helical stretching of axial B-field before reconnection is complete. Thus, instability drive is exhausted and incomplete reconnection may result.

In simulations with $1/\epsilon = 10$, such incomplete reconnection is exactly what we have observed. Once reconnection ceases with a much smaller plasma core remaining, the stretched helical magnetic field lines act as a spring and quickly pull the remnants of the core back towards $r = 0$, as evidenced by a sudden drop in q_0 in Figure 4.17. Though q on the magnetic axis clearly stays significantly below unity, the large magnetic island shown on panel (e) of Figure 4.18 and occupying the region between the unreconnected core and mixing radius r_M, represents the region of $q \approx 1$ required by the Wesson's theory of the ideal quasi-interchange instability. We note that although local measurements of the pitch of magnetic field lines in and around the remaining core would yield $q < 1$, magnetic field lines immediately adjacent to the core also sample the plasma near r_M, where $q > 1$, with flux-surface averaged q being close to unity.

The results discussed above also provide a plausible explanation for the observations of density "snakes"[152, 60] and of central cold bubble in the tomographic soft x-ray emission reconstruction[155] during sawteeth in the JET Tokamak. The persistence of the large $m = 1$ island through multiple sawtooth cycles would allow for a density perturbation localized within such an island to survive through the sawteeth. Furthermore, while during the relatively slow resistive kinking the central core would become exposed to colder plasma by reconnecting with field lines lying outside of r_s,

the interior of the island would remain surrounded by plasma with the same average temperature. (Colder flux-surfaces on the outside of the island reconnect with hotter ones on the inside, thus approximately preserving the temperature around the island.) Then, during the fast quasi-interchange motion of the cooled down core back into the center of the domain, an effective cold bubble would be produced. We also note that the depression in plasma pressure in the center of plasma core shown in panels (b) and (e) of Fig. 4.20 could be interpreted as hollow plasma density profiles. Although plasma density was not evolved and, in fact, was assumed to be uniform in these simulations, such hollow density profiles would not be expected to significantly modify the sawtooth dynamics of an incompressible system.

Somewhat similar results of sawtooth oscillations around a helical quasi-equilibrium within a fully three-dimensional simulation with temperature dependent resistivity have been reported by Theobald, *et.al.*[146]. However, those simulation reported complete Kadomtsev reconnection, while they had very limited spatial resolution and high dissipation parameters.

4.3.9 Self-generated helical equilibrium.

We now study the structure of the helical quasi-equilibria in more detail, by turning to the apparently stable helical equilibrium self-generated in simulations with even lower helical aspect ratio $1/\epsilon = 5$.

Panels (a)-(c) of Figure 4.22 show contour plots of ψ, B_e, and ϕ at $t = 9940$ (see Fig. 4.13), when the plasma has settled into a stable steady-state configuration with $\nabla \times \mathbf{E} = 0$ and $\partial \mathbf{v}/\partial t = 0$ to a very good approximation.[4] A prominent $m = 1$ island,

[4]Note that the initial perturbation to an ideally unstable equilibrium is up-down symmetric and results in violent kinking during which a small plasmoid is produced and is eventually ejected to one side (upwards), thus breaking up-down symmetry otherwise preserved by the incompressible resistive

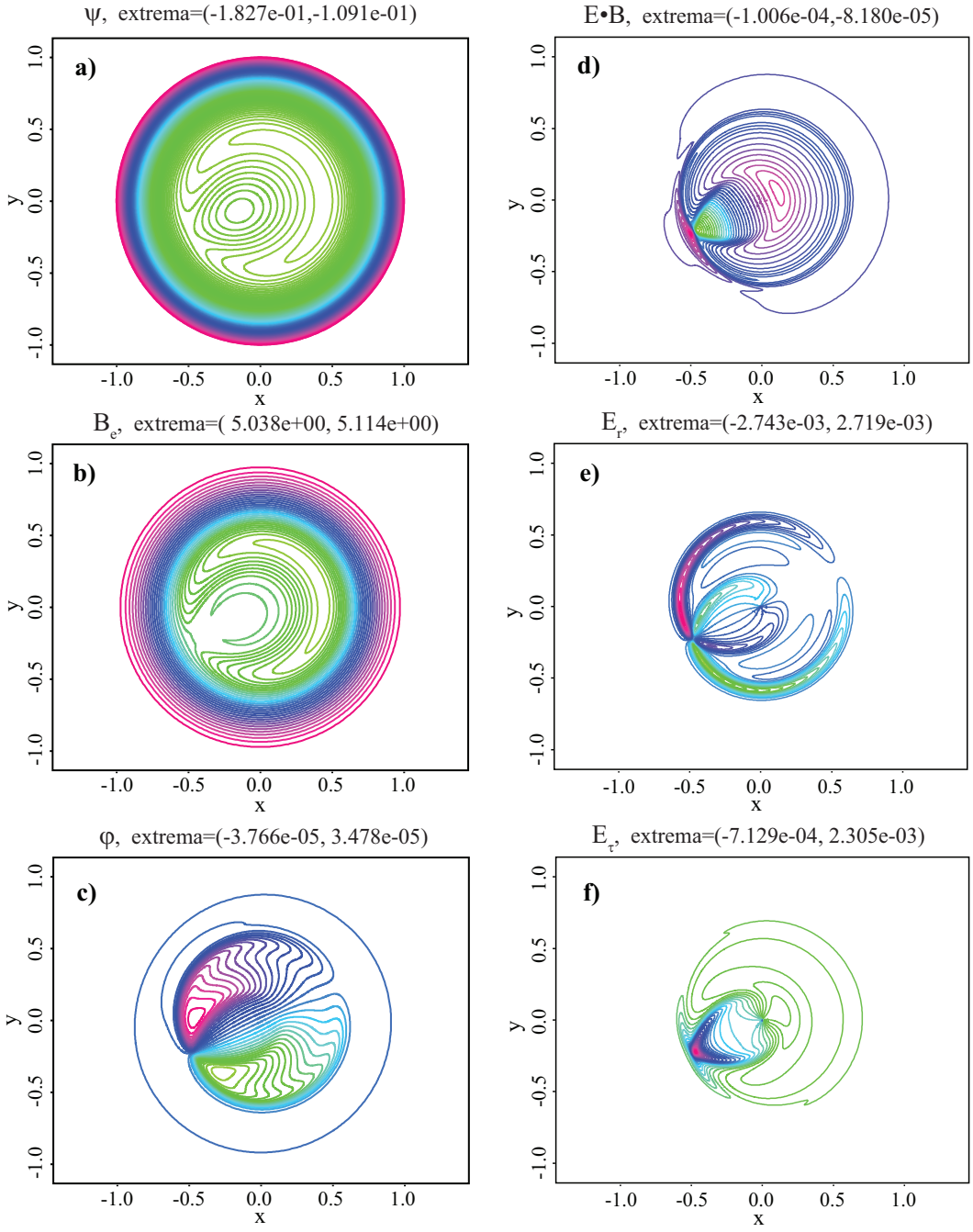

Figure 4.22: Contour plots of (a) ψ, (b) B_e, (c) ϕ, (d) $\mathbf{E} \cdot \mathbf{B}$, (e) radial component of E-field E_r, and (f) angular component of E-field E_τ of the stable helical resistive equilibrium self-generated in an Ohmic driven system with helical aspect ratio of $1/\epsilon = 5$.

paramagnetic peak in axial B-field in the core ($\delta B_z \approx 6.5 * 10^{-2}$), and a double-vortex of electrostatically driven flows are present in the equilibrium. The $m = 1$ signature of the helical equilibrium appears to extend to some critical radius r_c, beyond which complete axisymmetry is observed. In fact, the stable equilibrium configuration shown in Figure 4.22 greatly resembles that achieved in fully three-dimensional reversed field pinch (RFP) simulations[51, 21, 31] and identified as a resistive dynamo by Bonfiglio *et.al.*[21, 31]. Panel (d) of Fig. 4.22 shows $\mathbf{E} \cdot \mathbf{B}$ throughout the equilibrium. Depression in $\mathbf{E} \cdot \mathbf{B}$ within the core and peaking outside of the separatrix signify the rearrangement of B-field accomplished by the resistive dynamo action, as described by Blackman and Ji[20] for an equivalent RFP configuration. In effect, electrostatic dynamo flows work to convert the poloidal B-field generated by the Ohmic drive into a paramagnetic profile of axial B-field, which appears to make the configuration stable against kinking and would otherwise resistively decay. Radial and angular components of the electrostatic E-field responsible for the $\mathbf{E} \times \mathbf{B}$ dynamo flows are shown in panels (e) and (f) of Fig. 4.22 and well correspond to those computed in single helicity RFP configurations[21, 31].

Though more often discussed in the context of RFPs, where the q-profile generally decreases with radius, the self-organization observed in the simulations presented here should not be surprising. Even while reduced to a two-dimensional system, the helical terms in Eqs. (4.3.3) allow for the presence of the resistive dynamo effect described above[51]. Furthermore, the shape of the axisymmetric configuration of B-field outside of r_c does not appear to influence the helical part of the equilibrium

MHD equations. The symmetry breaking here is due purely to finite precision of computing. Several runs with slightly different resolution have been performed and the plasmoid ejection both upward and downward has been observed. No qualitative difference between such runs is noted. Integral measures of the results (such as total kinetic energy) remain quantitatively the same.

within r_c, thus diminishing the importance of the q-profile outside of r_c.

The dependence of the helical steady-state on magnitude of resistivity was studied by reducing the value of η_s, thus simultaneously reducing electric field applied at the wall and resistivity inside the domain. In this way, the shape of the resistivity profile and the axisymmetric part of the resistive equilibrium remained unchanged, while the helical part of the equilibrium was allowed to self-adjust. The steady state shown in Fig. 4.22 was taken as an initial condition at $t_0 = 9940$ and η_s was given temporal dependence of the form, $\eta_s(t) = (\eta_0 - \eta_1) \exp\left[-(t-t_0)^2/t_{decay}^2\right] + \eta_1$, where $\eta_s(t = t_0) = \eta_0 = 10^{-5}$, $t_{decay} = 200$ and several values for η_1 were taken. Ion viscosity was unchanged at $\mu = 5 * 10^{-5}$ and the simulations were continued until new steady-state was reached at some t_f, with $(t_f - t_0)/t_{decay} \approx 20 - 40$.

Panels (a) and (c) of Figure 4.23 unequivocally demonstrate the resistive nature of the flows present in the helical steady-state. Both maximum absolute velocity and $\sqrt{E_k}$ are shown to scale linearly with η_s, converging to zero as resistivity is reduced to zero. The helical plasma flow, which dominates the poloidal kinetic energy in this helical steady-state, is also shown to reduce by a factor of 10 as resistivity is reduced by a factor of 10. The cut through the plasma core, shown in panel (c), additionally demonstrates the nature of the sheared helical flow, acting to effectively rotate the poloidal B-field generated by Ohmic drive to maintain a paramagnetic profile of B_z against resistive decay. However, panels (b) and (d) of Fig. 4.23 show that an order of magnitude reduction in resistivity has very little influence on the magnetic configuration of the helical steady-state. As resistivity is reduced, the gradients in the current profile become sharper, but, unlike the saturated state of an ideal kink[129, 112], no singular current layers are generated. Instead, as $\eta \to 0$, the current profile

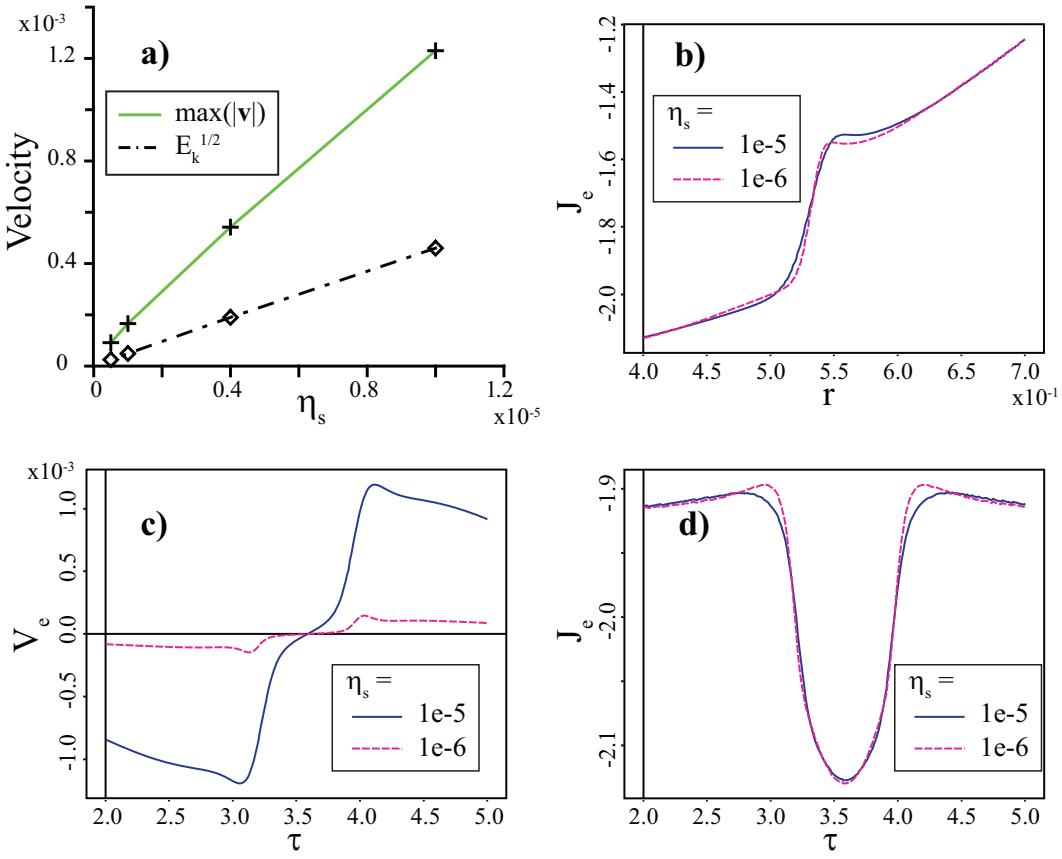

Figure 4.23: Sensitivity of the steady-state of Fig. 4.12 to variation in resistivity. Panel (a) shows maximum velocity and total kinetic energy of the steady state as a function of η_s; panel (b) radial cut of helical current J_e through the X-point of the steady-state ($\tau = 3.585$); and panels (c) and (d) show angular cuts of helical flow V_e and helical current J_e, respectively, through the plasma core at $r = .4$

tends to a step-function across r_c with some jump in helical current δJ_e.

For small but finite resistivity and viscosity, the width of the step function Δ can be easily estimated. As shown above, plasma flow within r_c is proportional to resistivity $\mathbf{v} \sim \eta$ in such a way that $v_p B_p \approx \eta \delta J_e$ to maintain resistive equilibrium and uniform axial E-field across r_c, with B_p and δJ_e independent of resistivity. Curl of the momentum equation gives:

$$\nabla \times [\mathbf{v} \cdot \nabla \mathbf{v}] = \nabla \times \left[\mathbf{J} \times \mathbf{B} + \mu \nabla^2 \mathbf{v} \right].$$

As shown in panel (c) of Fig. 4.22, the steady-state plasma flow is channeled through the X-point and then makes a 90 degree turn over width Δ. In such configuration, at the X-point, curl of the inertial term scales like $v_p^2/\Delta^2 \sim \eta^2/\Delta^2$, curl of the viscous term scales like $\mu v_p/\Delta^3 \sim \mu\eta/\Delta^3$ and curl of the $\mathbf{J} \times \mathbf{B}$ term, as $\delta J_e/\Delta \sim 1/\Delta$. Then, for sufficiently small η and non-zero μ, the inertial term can be neglected and $\Delta \sim \sqrt{\mu\eta}$. Therefore, as resistivity is reduced to zero, plasma relaxes to an ideal helical equilibrium with no singular current layers.

The importance of the helical equilibrium states in preference to the commonly considered axisymmetric configurations has been previously highlighted by Montgomery, *et.al.*[99, 100]. In fully three-dimensional periodic cylinder, Montgomery, *et.al.*[99] analytically derived and Theobald, *et.al.*[146] numerically observed a minimum energy-dissipation rate state with “antidynamo" electrostatic flows apparently acting to reduce helical plasma current in the core. It is important to note that the analytic derivation was conducted by assuming the helical perturbation to be a small perturbation to a uniform axisymmetric q-profile and the numerical quasi-equilibrium was observed following a complete reconnection event, which would also flatten the q-profile in the domain. As discussed above, such conditions are exactly

those assumed by Wesson[153, 154] for onset of an ideal quasi-interchange mode, whose final state (see Fig. 10 of Ref. [154]) strongly resembles that computed by Theobald, *et.al.*[146]. We therefore suggest that the helical quasi-equilibrium observed by Theobald, *et.al.*[146] can be equally well explained as a state of local minimum of magnetic energy, with plasma flows simply acting to maintain resistive equilibrium in that state.

The helical steady-state described by the present simulation results also appears to be a local minimum of magnetic energy stored in the system under the constraint of maintaining a resistive equilibrium. However, due to an assumed time-independent radial profile of resistivity given by Eq. (4.3.13) and designed to have axisymmetric $q > 1$ outside of $r = r_s$ while keeping it below unity at $r = 0$, a distinctly different steady-state is established. As shown in panel (d) of Fig. 4.23, the poloidal flows act to enhance the helical plasma current in the core and reduce it in the surrounding $m = 1$ island, thus serving as a direct resistive dynamo mechanism.

4.3.10 Sensitivity of sawtoothing dynamics to kinematic viscosity in large aspect ratio simulations.

The visco-resistive sawtooth simulations described so far have all been conducted with the same plasma resistivity profile given by Eq. (4.3.13) with $\eta_s = 10^{-5}$ and uniform kinematic viscosity $\mu = 5{*}10^{-5}$. With these parameters, the Prandtl number $P \equiv (\mu/\eta)$ within the mixing radius of the sawteeth has the value $P \approx 4 - 6$. We have conducted additional large aspect ratio ($1/\epsilon = 25$) simulations of ideally unstable internal kink mode followed by Ohmic driven sawteeth with lower values of kinematic viscosity, $\mu = 2 * 10^{-5}$ and $\mu = 10^{-5}$. (Note that the latter of the two has $P \approx 1$ within the mixing radius.)

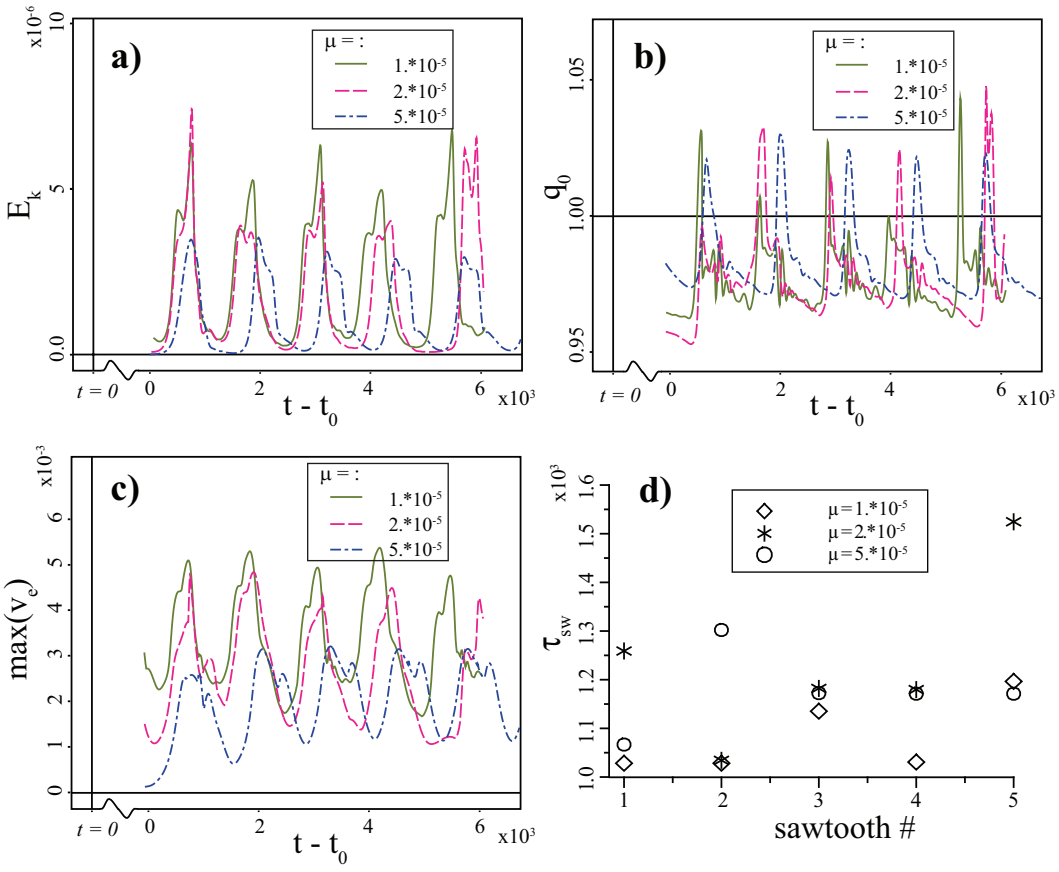

Figure 4.24: Panels (a-c) show time-traces of (a) E_k, (b) q_0, and (c) maximum over the domain of helical plasma velocity v_e for three sawtooth simulations with varied kinematic viscosity, resistivity profile given by Eq. (4.3.13) with $\eta_s = 10^{-5}$, and helical aspect ratio $1/\epsilon = 25$. The time scales on the horizontal axes in all three panels have been shifted by some t_0 for each of the simulation runs in order to focus on the sawtoothing phase of the evolution. Panel (d) shows sawtooth periods τ_{sw} for each of five sawteeth for each of the viscosity values using evolution of poloidal magnetic energy to measure the sawtooth timing.

Figure 4.24 compares time-traces of magnetic energy [panel (a)], pitch of the magnetic field on the geometric axis [panel (b)] and maximum magnitude of helical component of plasma velocity [panel (c)] for the three sawtooth simulations with varied kinematic viscosity. As could be expected, lower viscosity simulations show higher peaks in both E_k and maximum flow magnitudes during the sawteeth and have stronger flows in the quasi-equilibria that form between the sawteeth. While overall evolution of q_0 appears to be similar in the three simulations, we observe somewhat different pattern of periodicity in the higher and lower viscosity sawteeth: high viscosity sawteeth all have the same shape that is very well reproduced throughout, low viscosity sawteeth clearly show bi-periodic behavior, while the median viscosity run produces irregular sawteeth of varying shape and size. The sawtooth periods τ_{sw} for each of the sawteeth are shown in panel (d) of Figure 4.24 and also demonstrate the varied periodicity pattern of the simulations with different viscosities. The simulation with the Prantl number $P \approx 1$ appears to have two different sawtooth states it oscillates between: (1) shorter sawtooth period with stronger helical flows in the quasi-equilibrium preceding the sawtooth; (2) longer sawtooth period with weaker helical flows, yet greater peak kinetic energy during the internal reconnection event. The high viscosity sawtooth period settles to be approximately the same as that of the type (2) $P \approx 1$ sawteeth, and the simulation with $\mu = 2 * 10^{-5}$ produces widely scattered values of τ_{sw}.

Figure 4.25 further illuminates the differences between sawteeth obtained with different kinematic viscosity by showing time-traces of magnetic energy stored in the six lowest non-axisymmetric modes $E_M^{m=1,6}$ for each of the three viscosity values considered. We note that in all three cases, maximum magnetic energy put into the

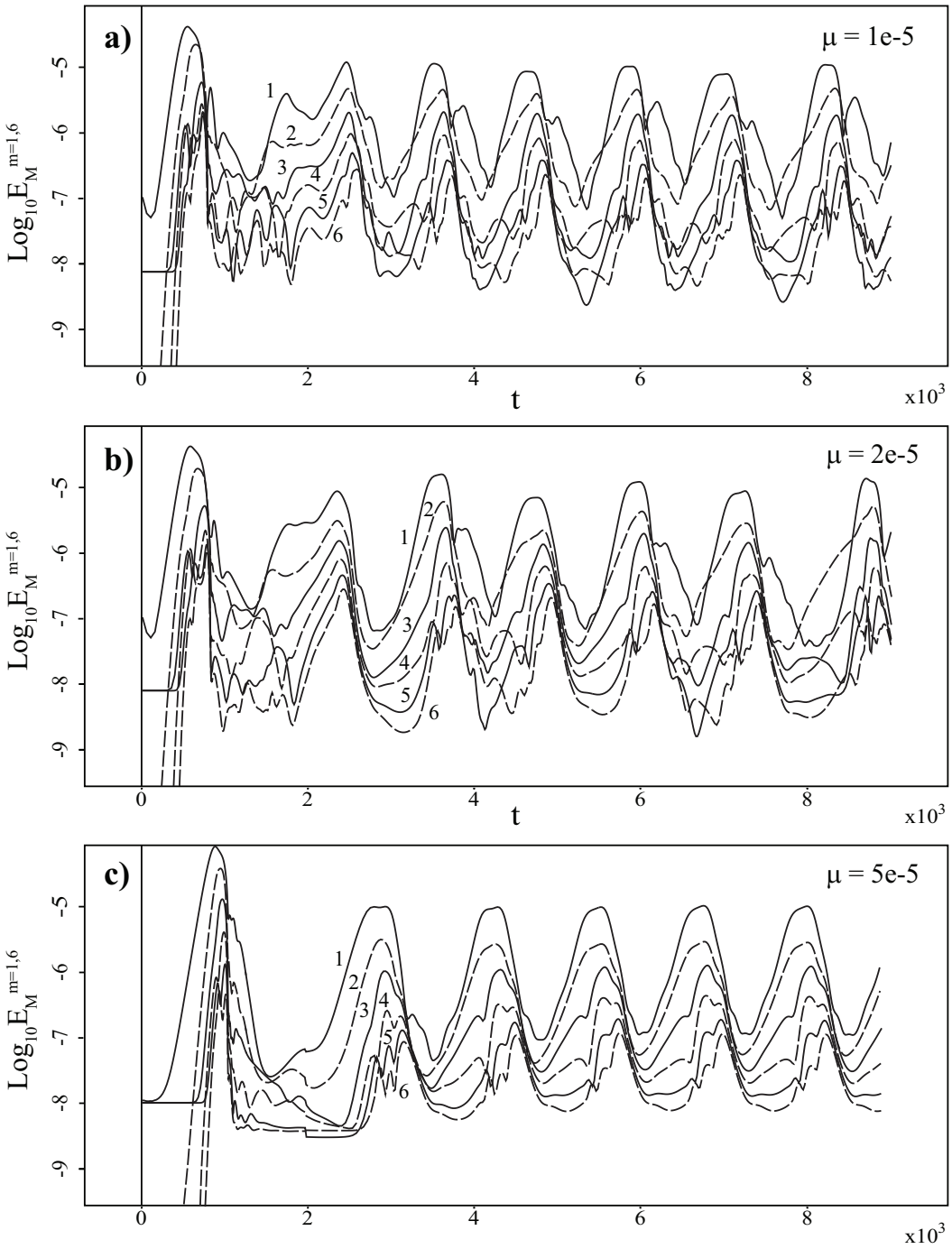

Figure 4.25: Time-traces of magnetic energy stored in the six lowest non-axisymmetric modes $E_M^{m=1,6}$ from three $1/\epsilon = 25$ simulations with different magnitudes of uniform kinematic viscosity: (a) $\mu = 10^{-5}$, (b) $\mu = 2 * 10^{-5}$, (c) $\mu = 5 * 10^{-5}$. All odd m modes are shown with solid lines and all even m modes are shown with dashed lines.

$m = 1$ mode during kinking of the plasma core is approximately the same. However, lower viscosity simulations are observed to have higher peak magnitudes of the higher m modes during those events. Furthermore, in panels (a) and (b) of Fig. 4.25, the magnetic energy in the $m = 2$ mode leads the $m = 1$ mode during build up of many of the sawteeth and a correlation between a sawtooth period shown in panel (c) of Fig. 4.24 and the distribution of magnetic energy among the modes in the quasi-equilibrium prior to a sawtooth can be observed: quasi-equilibria with less energy in the $m = 1$ mode have greater sawtooth periods and vice versa. Figure 4.25 also clearly demonstrates the existence of several different sawtooth types: $P \gg 1$ simulations produce laminar sawteeth, where there is always more magnetic energy in the lower m modes; $P \approx 2$ simulations generate both laminar and more chaotic sawteeth, where the even m modes sometimes overtake their odd $m-1$ counterparts; and $P \approx 1$ simulations show two types of "chaotic" sawteeth with different quasi-equilibria magnetic energy distributions.

The results described above are consistent with those from three-dimensional simulations and stability analysis in a periodic cylinder by Shan and Montgomery[135, 136, 100], where vastly different behavior of $m > 1$ modes in a magnetic field configuration with $q > 1$ everywhere was demonstrated for different values of viscosity. In particular, for given plasma resistivity, low values of viscosity resulted in destabilization of an axisymmetric Ohmic driven screw-pinch by high m modes, followed by characteristic "pulsation" behavior[136], while high viscosity simulations generated laminar time-independent solutions[135]. Similarly, three-dimensional numerical studies of RFP configurations in different visco-resistive regimes show that for given resistivity, a laminar single-helicity state that can be achieved with high kinematic

viscosity transitions to a turbulent multi-helicity state when viscosity is lowered past some critical value[51, 30].

In light of the previous results cited above and considering that the sawteeth presented in Figs. 4.24-4.25 were obtained in two-dimensional helical simulations with $q \approx 1$ within some radius $r_s \approx .5$, we attribute the difference in the observed sawtooth shapes and duration to different mechanisms responsible for triggering the internal kink instability. We suggest that in high viscosity simulations, it is primarily the resistive $m = 1$ kink that becomes linearly unstable and causes the ejection of the plasma core, while in low viscosity simulations $m > 1$ interchange-like instabilities of the same origin as that observed by Shan and Montgomery[135, 136] couple to the $m = 1$ mode and trigger the internal kink. Thus, from the large aspect ratio simulations described above, we conclude that the magnitude of kinematic viscosity influences the shape and duration of the sawteeth primarily through its affect on the stability of the quasi-equilibria achieved between the sawteeth, rather than the reconnection rate of the plasma core during kinking itself.

4.3.11 Sensitivity of sawtoothing dynamics to resistivity and kinematic viscosity in moderate aspect ratio simulations.

In Section 4.3.10, we have concluded that the strong variability of sawtoothing dynamics with kinematic viscosity in the large aspect ratio simulations was in part due to lack of magnetic field shear within the $q = 1$ radius r_s of the quasi-equilibria achieved between sawteeth (*i.e.* $q(r) \approx 1$ for $r < r_s$). Below, we describe results of several sawtooth simulations with "moderate" helical aspect ratio $1/\epsilon = 10$, where the magnitudes of both resistivity η_s and viscosity μ have been varied. We point out that,

as discussed in Section 4.3.8, the quasi-equilibria achieved between sawteeth in the $1/\epsilon = 10$ simulations have significant local shear and lower effective plasma pressure within $r < r_s$, both of which act to stabilize the interchange-like modes.

Since the focus of the present investigation is on the sawtooth dynamics as opposed to the evolution of the internal kink mode from an ideally unstable axisymmetric **B**-field configuration, we did not initialize all of these simulations from the axisymmetric initial condition given by Eqs. (4.3.11-4.3.12) or Eq. (4.3.16). Instead, a snap-shot of the simulation with $\eta_s = 10^{-5}$ and $\mu = 5 * 10^{-5}$ already described in Section 4.3.8 above was taken at $t_r = 3998.$, well after the the initial axisymmetric state has gone through the complete Kadomtsev reconnection cycle, and used as an initial condition for the other computations. Once restarted, resistivity, viscosity, or both have been smoothly transitioned to the new desired values in the same fashion as described in Section 4.3.9. Only results sufficiently removed in time from $t = t_r$ are analyzed below. As in Section 4.3.9, we note that any change in resistivity is accomplished by adjusting the scaling parameter η_s, while the shape of the resistivity profile remains unchanged and is given by Eq. (4.3.13).[5]

Figure 4.26 presents evolution of magnetic energy in the six lowest m-modes over a sawtooth cycle for two different combinations of kinematic viscosity and resistivity. These can also be compared to panel (b) of Fig. 4.21, where another set of viscosity and resistivity values ($\mu = 5 * 10^{-5}$, $\eta_s = 1.0 * 10^{-5}$) was considered with the same helical aspect ratio $1/\epsilon = 10$. Comparing the time-traces, it is apparent that a single mechanism for sawtooth instability is at work in the $1/\epsilon = 10$ simulations. Though

[5]Note that such resistivity adjustments also result in proportional changes of the axial electric field E_b applied at the $r = 1$ boundary of the domain, as well as the $\eta\mathbf{J}$ contribution to the **E**-field throughout the domain.

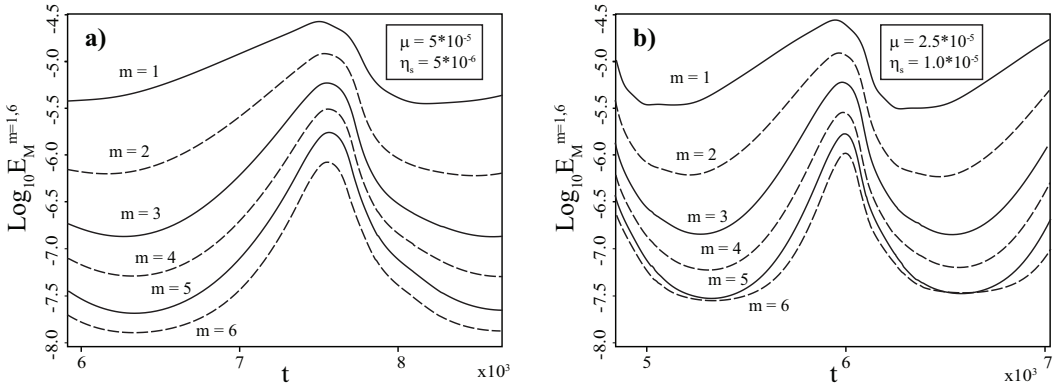

Figure 4.26: Time-traces of magnetic energy stored in the six lowest non-axisymmetric modes $E_M^{m=1,6}$ from two sawtooth simulations with different combinations of kinematic viscosity and resistivity: (a) $\mu = 5 * 10^{-5}$, $\eta_s = 5 * 10^{-6}$; and (b) $\mu = 2.5 * 10^{-5}$, $\eta_s = 1.0 * 10^{-5}$. All odd m modes are shown with solid lines and all even m modes are shown with dashed lines.

somewhat stronger high m-mode activity is observed in the lower Prandtl number quasi-equilibria, it is clear that in these cases only the $m = 1$ perturbation leads the instability. This points to the resistive kink as the sole trigger for the sawtooth onset.

Results from sawtooth simulations with four different combinations of kinematic viscosity and resistivity are shown in Figure 4.27. Two values of μ, each with two different values of η_s, have been considered. The set also includes two simulations with the same values of η_s, but different μ values. Time-traces of the reconnection rate R_{rec} during the IR events and the corresponding sawtooth periods τ_{sw} are shown. We observe that varying kinematic viscosity at constant resistivity and vice versa has a non-negligible effect on the "m=1" resistive kink reconnection rate. (This has also been previously shown by W. Park *et.al.*[113].) In particular, both the peak values of R_{rec} and the total duration of the IR events τ_{IR}[6] are observed to depend on the

[6]We define the duration of an internal reconnection event τ_{IR} as the period of time when R_{rec} remains positive in panel (a) of Figure 4.27.

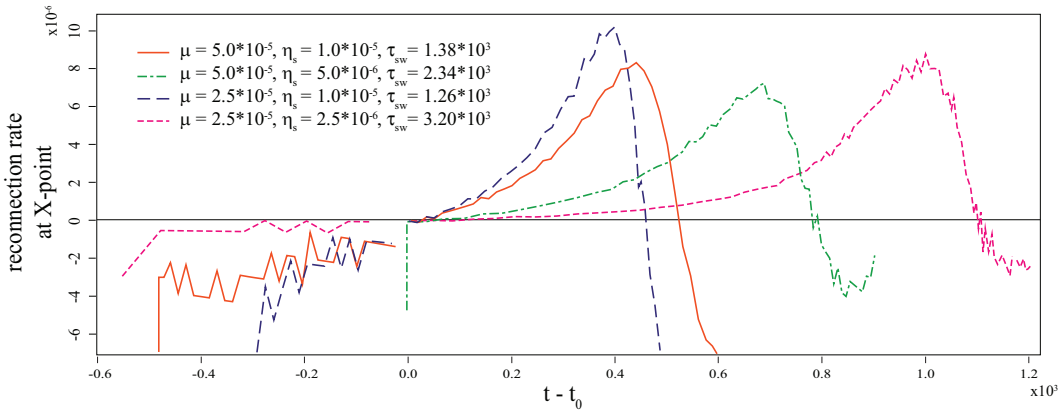

Figure 4.27: Time-traces of reconnection rate $[(\partial\psi(\mathbf{r}_X)/\partial t) - \dot{\psi}_0]$ calculated by tracking the location $\mathbf{r}_X$ of the X-point using the peak of helical current J_e during the IR event associated with resistive kinking during sawteeth with different combinations of kinematic viscosity and resistivity. The legend also shows the sawtooth periods τ_{sw} of the four μ, η_s combinations, while separate t_0 and $\dot{\psi}_0$ were found for each of the traces to adjust for the timing and background electric field of the sawteeth.

dissipation parameters: lower η results in lower peak R_{rec} and longer IR events, while lower μ results in higher peak R_{rec} and shorter IR events.

As in panel (b) of Fig. 4.4, where reconnection rate during evolution of the internal kink from an ideally unstable initial condition was shown, no period of constant R_{rec} is observed during the sawtooth internal reconnection events. Furthermore, the peak values of R_{rec} have a very weak scaling with resistivity (*i.e.* much weaker that the Sweet-Parker scaling $R_{rec}^{SP} \sim \eta^{1/2}$[115, 141]) and are at least as sensitive to μ at to η, while τ_{IR} appears to scale like $\eta^{1/2}$ when $\mu \approx \eta$ with even stronger dependence when $P \equiv (\mu/\eta) \gg 1$. We note that the latter is well explained by the modified visco-resistive Sweet-Parker scaling given by W. Park, *et.al.*[113] $R_{rec}^{Park} \sim \eta^{1/2}(1+\mu/\eta)^{-1/4}$. Similarly, the visco-resistive Sweet-Parker scaling reproduces the observed variation of the sawtooth period τ_{sw} with μ and η to within approximately 5%. On the other hand,

the former signifies that the magnitude of resistivity plays little role in determining the maximum R_{rec} in the late stages of an IR event. As follows from derivations by Petschek[116], Kulsrud[90] and W. Park, *et.al.*[113], in visco-resistive MHD, such situation is only possible when external forcing controls the reconnection rate and/or length of the current layer L is globally restricted to be of the same order as its width δ.

Structure of the reconnection region (RR) at the time of peak reconnection rate in a sawtooth with $\mu = 2.5 * 10^{-5}$ and $\eta_s = 2.5 * 10^{-6}$ is shown in Figure 4.28. Panel (a) presents contours of plasma flow stream function and helical plasma current around the RR, while panels (b) and (c) show details of the magnetic and velocity fields along the inflow and outflow directions. Two important observations about the nature of this RR can be made based on the data shown in Figure 4.28: (1) current layer length is $L \approx 0.1$ with the aspect ratio of $(L/\delta) \approx 10$, so that L is much smaller than the radius of the core, yet $(L/\delta) \gg 1$; (2) outflow velocity is significantly smaller than the Alfvén velocity based on the reconnecting B-field – outflow pressure balance is largely supported by the viscous effects (consistent with W. Park, *et.al.*[113] for $P \approx 10$). Comparing Figure 4.28 with the corresponding data from the other simulation runs (not shown), we also note that L at the time of peak R_{rec} is independent of μ or η, while width and magnitude of the reconnection current depend on the particular dissipation values.

Based on the evidence described above, we conclude that the observed visco-resistive IR process is generally well described by the modified Sweet-Parker theory by W. Park, *et.al.*[113]. The length of the reconnection layer during an IR event is controlled by the global magnetic field structure. The observed increase in the

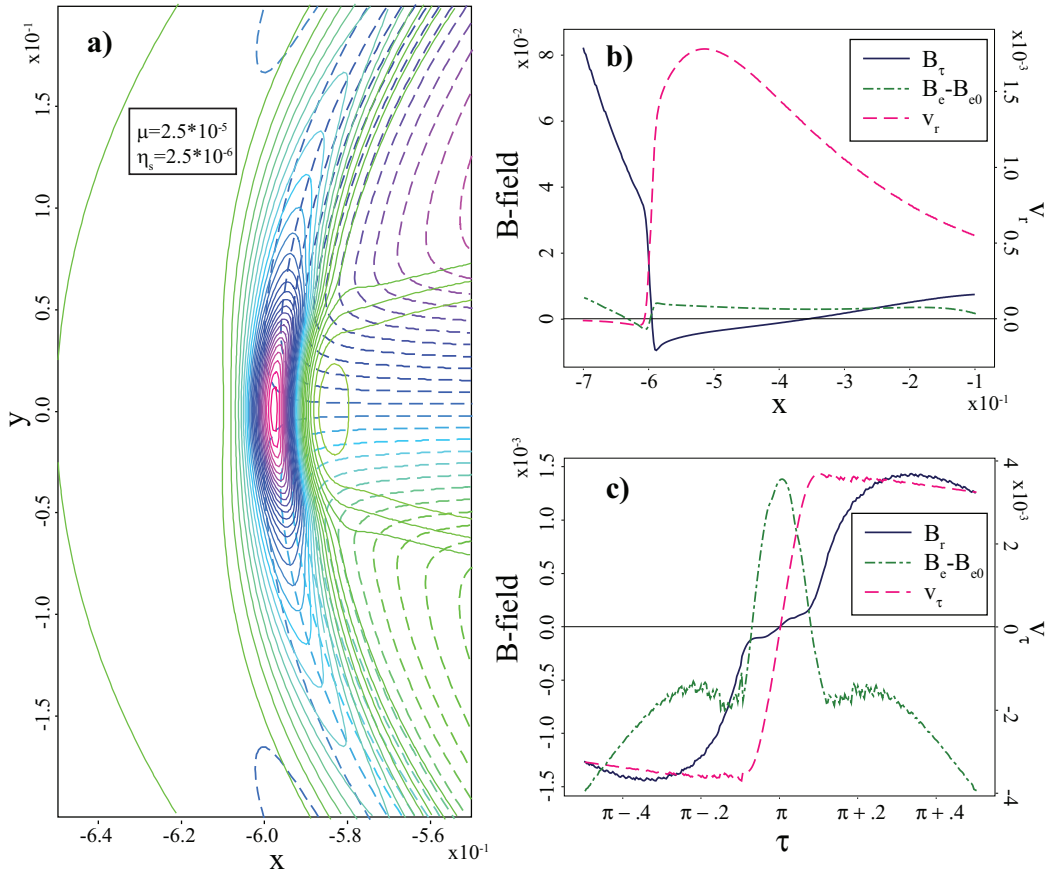

Figure 4.28: Structure of the reconnection region at the time of peak reconnection rate with $\mu = 2.5 * 10^{-5}$ and $\eta_s = 2.5 * 10^{-6}$. Shown are: (a) contours of plasma flow stream function ϕ (dashed lines) overlaid on top of J_e (solid lines) around the reconnection region; (b) profiles of reconnecting B-field B_τ, guide-field B_e, and inflow velocity v_r along a radial cut at $y = 0$ ($\tau = \pi$); (c) profiles of reconnected B-field B_r, guide-field B_e, and outflow velocity v_τ along an angular cut at $r = .597$. Background guide-field is $B_{e0} = 10.0345$.

reconnection rate with time is explained by, first, decrease in L due to decrease in the radius of the reconnecting plasma core[7], followed by accelerated shrinking of L due to transformation of the core from circular into a tear-drop shape, as described in Section 4.3.8. The time when the growth of the reconnection rate is stopped, then reversed, and the incompletely reconnected plasma core is pulled back towards $r = 0$ is determined by external forcing, as also described in Section 4.3.8. Thus, the maximum value of R_{rec} during an IR event is mainly determined by the global magnetic field structure and how much helical flux has reconnected prior to achieving that value.

We additionally note that the observed near-perfect visco-resistive Sweet-Parker scaling of $\tau_{sw} \propto \eta^{-1/2}(1+\mu/\eta)^{1/4}$ strongly suggests that magnetic reconnection plays the key role not only during an IR event itself, but also during the plasma core re-building process.

4.4 Hall MHD internal kink simulations.

Having thoroughly examined dynamics of a driven visco-resistive screw-pinch, we now consider what, if any, significant changes in the system's dynamics and time-scales of interest can be observed when weak two-fluid effects are introduced into the system. We note that large-scale tokamaks, such as JET, have minor radius $r_0 \approx 1$ meter and plasma number density $n_e \approx 10^{19} - 10^{20} m^{-3}$, which translates into normalized ion inertial scale $d_i \equiv (c/\omega_{pi})/r_0 \approx 2 - 3 * 10^{-2} \ll 1$[89]. We therefore do not expect the two-fluid effects to greatly modify the large scale properties of the system, such as the existence of a resistive dynamo described above. However, as shown in Section 3.4, any visco-resistive process that may occur on the sub-two-fluid scale, *e.g.*

magnetic reconnection, stands to undergo significant changes in both local dynamics and time-scales associated with the phenomenon.

4.4.1 Incompressible Hall MHD equations in helical symmetry.

In this study we maintain the condition of exact incompressibility and add the two-fluid Hall terms to the incompressible visco-resistive MHD system given by Eqs. 4.3.3. Additionally, kinematic electron viscosity is added to the system to define a diffusion scale for electron dynamics. And by assuming plasma density to be initially uniform, it is removed from the system.

With those assumptions, the normalized system of incompressible Hall MHD equations is:

$$\frac{\partial \mathbf{v}_i}{\partial t} + \mathbf{v}_i \cdot \nabla \mathbf{v}_i = \mathbf{J} \times \mathbf{B} - \nabla(p_i + p_e) + \mu \nabla^2 \mathbf{v}_i + \nu \nabla^2 \mathbf{v}_e \tag{4.4.1}$$

$$\mathbf{E} + \mathbf{v}_e \times \mathbf{B} = \eta \mathbf{J} - d_i \nabla p_e + d_i \nu \nabla^2 \mathbf{v}_e \tag{4.4.2}$$

$$d_i \mathbf{J} = \mathbf{v}_i - \mathbf{v}_e, \quad \nabla \cdot \mathbf{v}_i = \nabla \cdot \mathbf{v}_e = 0,$$

where μ is kinematic ion viscosity, ν is kinematic electron viscosity, and η is resistivity, which we again allow to have radial dependence $\eta = \eta(r)$.

Using the same representation for $\mathbf{B}$- and $\mathbf{v}_i$-fields as in Section 4.3.1 and taking the $\hat{e}$-projection of Eqs. (4.4.1)-(4.4.2) and $\nabla\times$[Eqs. (4.4.1)-(4.4.2)], the incompressible Hall MHD system can be written in the following form:

$$\begin{aligned} \frac{\partial \psi}{\partial t} &+ \mathbf{v} \cdot \nabla \psi = \eta J_e + d_i \mathbf{B} \cdot \nabla B_e \\ &- d_i \nu \left[\Delta^*(d_i J_e - V_e) - 4\epsilon^2 g^4 (d_i J_e - V_e) \right] \end{aligned}$$

$$
\begin{aligned}
\frac{\partial(g^2 B_e - 2\epsilon g^4 \psi)}{\partial t} &+ \mathbf{v}\cdot\nabla(g^2 B_e) = \mathbf{B}\cdot\nabla(g^2 V_e) + \eta g^2 \Delta^* B_e + g^2 \frac{\partial \eta}{\partial r}\frac{\partial B_e}{\partial r} \\
&+ d_i \left[\mathbf{J}\cdot\nabla(g^2 B_e) - \mathbf{B}\cdot\nabla(g^2 J_e)\right] \\
&- d_i \nu g^2 \Delta^* \left[2\epsilon g^2 (d_i J_e - V_e)\right]
\end{aligned}
$$

$$
\begin{aligned}
\frac{\partial(g^2\Omega + 4\epsilon g^4 V_e)}{\partial t} &+ \mathbf{v}\cdot\nabla(g^2\Omega + 2\epsilon g^4 V_e) = \mathbf{B}\cdot\nabla(g^2 J_e + 2\epsilon g^4 B_e) \\
&+ \epsilon^2 g^4 \frac{\partial}{\partial \tau}\left(B_e^2 - V_e^2\right) - 8\epsilon^3 g^6 \left(B_e \frac{\partial \psi}{\partial \tau} - V_e \frac{\partial \phi}{\partial \tau}\right) \\
&+ \mu g^2 \Delta^* \Omega + \nu g^2 \Delta^* \left[2\epsilon g^2 (d_i J_e - V_e)\right]
\end{aligned}
$$

$$
\begin{aligned}
\frac{\partial V_e}{\partial t} &+ \mathbf{v}\cdot\nabla V_e = \mathbf{B}\cdot\nabla B_e + \mu(\Delta^* V_e + 2\epsilon g^2 \Omega) \\
&- \nu\left[\Delta^*(d_i J_e - V_e) - 4\epsilon^2 g^4 (d_i J_e - V_e)\right], \qquad (4.4.3)
\end{aligned}
$$

where $J_e \equiv \Delta^*\psi - 2\epsilon g^2 B_e$, $\Omega \equiv \Delta^*\phi - 2\epsilon g^2 V_e$ and the in-plane components of the electron viscous tensor $\nabla^2 \mathbf{v}_e$ have been neglected[7].

Note that by assuming exact incompressibility and uniform density, the ∇p_α terms in the momentum equation, Eq. (4.4.1), and the Ohm's Law, Eq. (4.4.2), effectively play no role in the evolution, while the Hall term $d_i(\mathbf{J}\times\mathbf{B})$ in the Ohm's Law introduces some of the two-fluid effects into the model. We again point out that, as shown by Fitzpatrick[53], in a plasma with strong guide-field $B \gg B_p$ and small total plasma *beta*, $\beta_T \equiv p/B^2 \ll 1$, compressibility effects should not be completely discarded. Furthermore, as discussed in Section 3.4.1 above, in the regime of poloidal

[7] In all of the simulations described below, $\nu \ll \mu$ and $d_i \ll 1$. Thus, electron viscosity terms become non-negligible only whenever $|\mathbf{v}_i - \mathbf{v}_e| \gg |\mathbf{v}_i|$ and gradient scales become smaller than d_i. In systems we consider, where d_i is much smaller than any equilibrium gradient scale, the conditions above are only observed when fast Hall mediated reconnection takes place. As discussed elsewhere in this Dissertation, two-dimensional Hall reconnection produces very fast out-of-plane electron flows whose perpendicular scale is limited only by the electron viscosity, while the in-plane outflows are observed to be significantly slower. Thus, perpendicular viscosity of the out-of-plane electron flow has to be included in the model in order to define the scale of Hall mediated reconnection current layer, while viscosity of the in-plane electron flow can be neglected in favor of computational efficiency.

beta smaller than unity, $\beta_p \equiv p/B_p^2 \lesssim 1$, the dispersive nature of the kinetic Alfvén wave is lost altogether while the dispersive characteristic of the Whistler wave is only recovered when $d_i^2 k^2 > \beta_p/\beta_T \gg 1$. Similarly, when $\beta_p \gg 1 \gg \beta_T$, the dispersive coefficient of the kinetic Alfvén wave is reduced by $\approx \sqrt{\beta_T}$, thus reducing the effective two-fluid separation scale from d_i to the ion sound radius ρ_s[53, 68, 128]. Nevertheless, in the present study we enforce the condition of exact incompressibility, which in the presence of strong magnetic guide-field is equivalent to the assumption of $\beta_p \gg \beta_p/\beta_T \gg 1$.

4.4.2 Internal kink with direct current drive in Hall MHD regime.

We first present Hall MHD simulation results obtained from modeling an ideally unstable initial condition with uniform plasma resistivity and supported by a current source chosen such that it exactly cancels the visco-resistive decay of the initial ideal equilibrium. These simulations are exactly analogous to those described in Section 4.3.2 above, where the ideal equilibrium is given by Eqs. (4.2.5) with a perturbation given by Eq. (4.2.7). Again, same boundary conditions as in Section 4.2 are applied with an additional condition of $(\partial J_e/\partial t)|_{r=r_w} = 0$ necessary due to inclusion of the electron viscosity term in Eqs. (4.4.3).

Figure 4.29 presents time-traces of the effective internal kink growth rate, $d(\ln E_k)/dt = 2\gamma$, and the reconnection rate, $\partial\psi/\partial t = R_{rec}$ at the location of maximum current density, from three simulation runs, where $\eta = \mu = 100\nu = 10^{-5}$ and the magnitude of d_i has been varied between 0.00 and 0.02. It is apparent that all three cases have very similar linear growth rates. Furthermore, the $d_i = 0.01$ simulation run clearly demonstrates quasi-resistive behavior, where the two-fluid effects slightly enhance

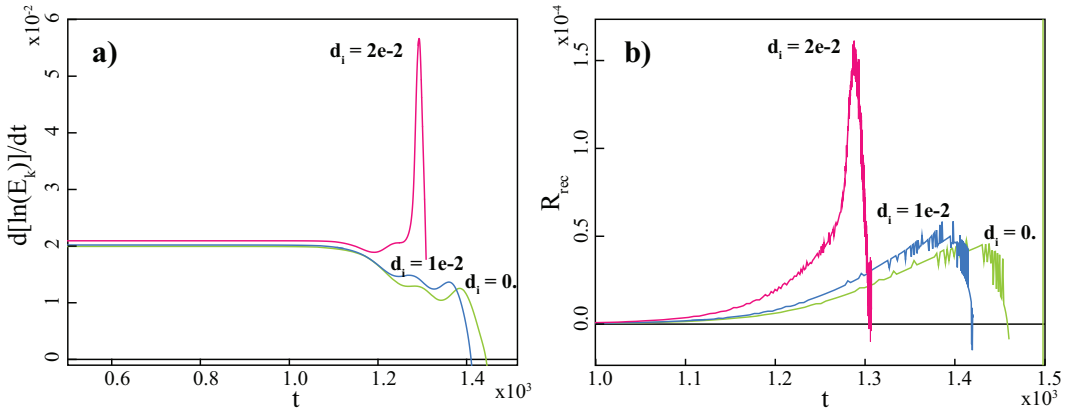

Figure 4.29: Time-traces of (a) effective internal kink growth rate and (b) core reconnection rate from three simulation runs with $d_i = \{0, 0.01, 0.02\}$ and $1/\epsilon = 25$, $r_s = 0.5$, $\eta = \mu = 100\nu = 10^{-5}$, $\delta B_e = 10^{-6}$.

the reconnection rate in the non-linear regime, yet no onset of fast reconnection is observed. On the other hand, in the simulation with $d_i = 0.02$, the transition to fast reconnection correlated with explosive growth of kinetic energy in the system is apparent. Note that similar transition to fast reconnection is also observed in a simulation with the dissipation coefficients halved, $\eta = \mu = 100\nu = 5 * 10^{-6}$, and $d_i = 10^{-2}$ (not shown).

It is easy to understand the system's divergent behavior by comparing the two-fluid scale to the expected Sweet-Parker width of the visco-resistive reconnection current layer for each simulation run. Recall from Section 3.1.1 that for a current layer of length L with reconnecting magnetic field of magnitude B_{in}, the visco-resistive Sweet-Parker reconnection current layer width is given by Eq. (3.1.1) as $\delta^{SP} = \eta^{1/2}(1 + \mu/\eta)^{1/4}\sqrt{2L/B_{in}}$.[8] Using $L \approx r_s$ and $B_{in} \approx 0.04$ (see Figures 4.30-4.31 below), for

[8] We note that the Sweet-Parker derivation assumed a symmetric RR, while the present configuration's plasma inflow is distinctly one-sided. This can introduce factors of order unity into the derivation, though those are not considered here.

simulations with $\eta = \mu = 10^{-5}$, we have $\delta^{SP} \approx 0.019$. Thus, for $d_i = \{0.01, 0.02\}$, $\delta^{SP}/2 \sim d_i$ with $d_i = 0.02$ sufficiently large to decouple ions from the magnetic field outside of the resistive current layer and allow for EMHD physics to determine the reconnection current layer evolution.

These results are in very good agreement with those discussed in Section 3.4 above, where incompressible two-fluid reconnection of a flat Harris sheet is studied. Similar explosive onset of fast $m = 1$ reconnection in the semi-collisional $\beta_p \gg 1 \gg \beta_T$ regime has been previously demonstrated by Aydemir[6] in the limit of $\delta^{SP} \ll \rho_s$.

Snap-shots of helical magnetic flux, magnetic field and plasma current immediately before and near saturation of fast reconnection transition are shown in Figure 4.30. Several important features of the solution should be highlighted. First, we note that introduction of two-fluid effects broke the symmetry of the solution and slow counter-clockwise rotation of the reconnecting core around the geometric axis is observed in the helical plane. This diamagnetic rotation is a quasi-linear effect fundamentally due to decoupling of the electron and ion flows[126]. Second, we observe that, as shown in panel (c), approximate symmetry of the quasi-resistive reconnection layer with respect to the plasma core prior to onset of fast reconnection is preserved. That is despite the presence of non-negligible poloidal currents $J_p \approx (\delta B_e/\delta) \approx 0.4$. Finally, after the onset of fast reconnection, we observe the expected collapse of the current layer; yet it occurs simultaneously with a rapid (relative to the diamagnetic rotation of the core plasma) clockwise rotation of the X-point. It should be emphasized that the rotation of the X-point is not only in the direction opposite to but is also much faster than the rotation of the core. The resulting displacement of the X-point relative to the core is, in part, what leads to saturation and damping of the reconnection rate shown in

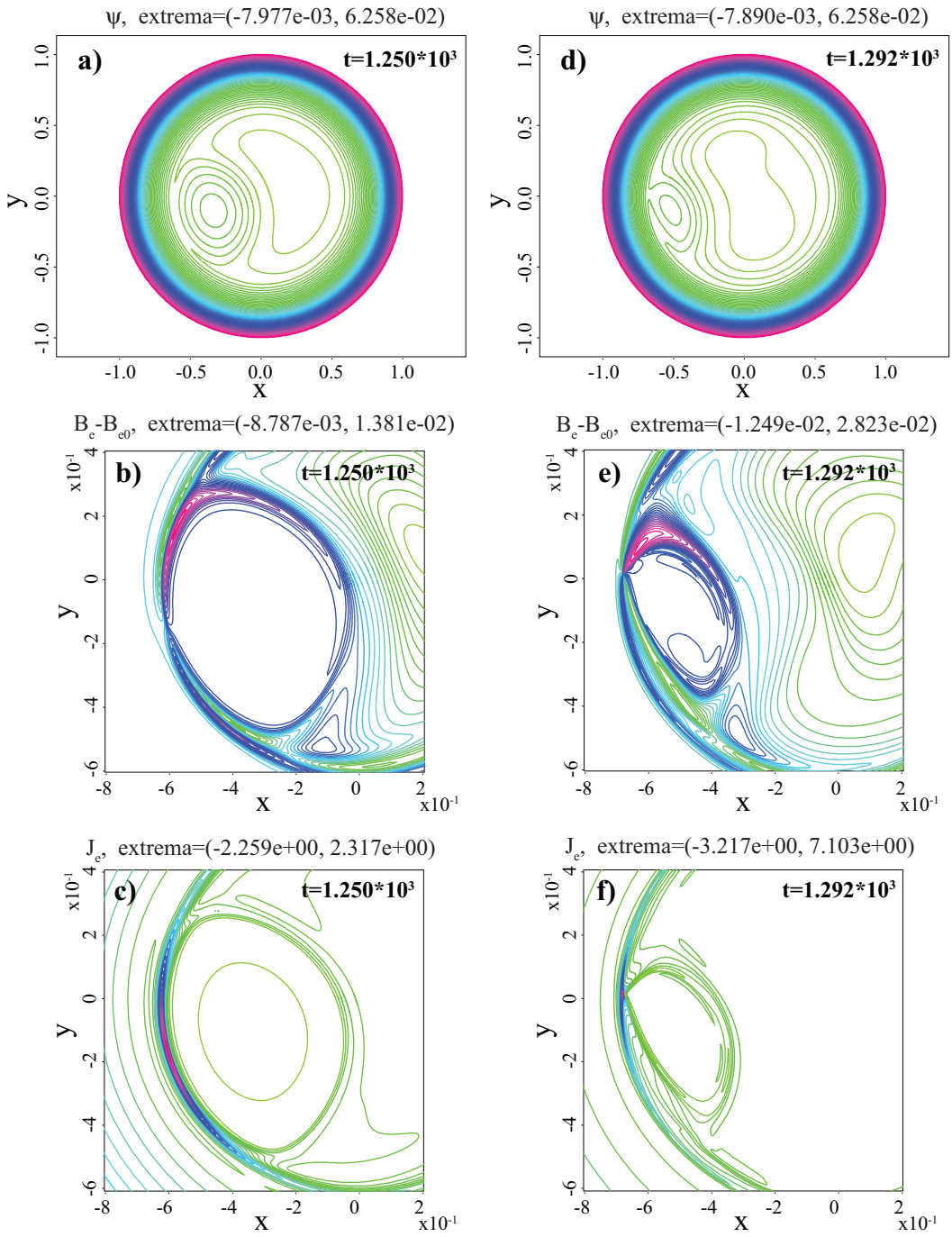

Figure 4.30: Contour plots of (a,d) helical magnetic flux ψ, (b,e) variation in helical magnetic field $B_e - B_{e0}$ ($B_{e0} = 1/\epsilon$), and (c,f) helical plasma current J_e immediately before onset of fast reconnection at $t = 1250$, panels (a-c), and near peak reconnection rate $t = 1292$, panels (d-f). Simulation parameters are $d_i = 0.02$, $1/\epsilon = 25$, $r_s = 0.5$, $\eta = \mu = 100\nu = 10^{-5}$ and $\delta B_e = 10^{-6}$.

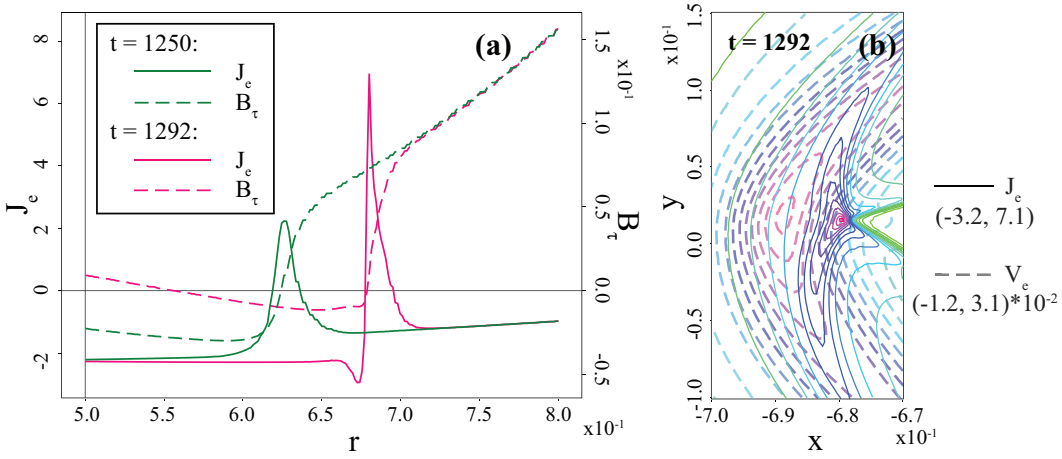

Figure 4.31: (a) radial profiles of J_e and B_τ through the X-point of the configuration immediately before onset of fast reconnection at $t = 1250$ ($\tau = 3.4120$) and near peak reconnection rate at $t = 1292$ ($\tau = 3.1195$); (b) contours of helical current density J_e (solid contours) overlaid onto the contours of helical ion flow V_e (dashed contours) near the X-point at $t = 1292$. Simulation parameters are $d_i = 0.02$, $1/\epsilon = 25$, $r_s = 0.5$, $\eta = \mu = 100\nu = 10^{-5}$ and $\delta B_e = 10^{-6}$.

panel (b) of Fig. 4.29. We note that the R_{rec} saturation mechanism observed here is distinctly different from that described by Biskamp and Sato[18], where rapid rotation of the plasma core itself was shown to be responsible for incomplete reconnection whenever equilibrium profile of plasma pressure is sufficiently steep.

The reason for the rapid X-point rotation appears to be the radially asymmetric profile of the reconnection current that forms during the current layer collapse. In panel (a) of Figure 4.31, we show two radial profiles of J_e and B_τ each, taken through the X-point (location of peak reconnection current density at r_X) at $t = 1250$ before and at $t = 1292$ after the collapse. It is apparent that accounting for the initial equilibrium J_{e0}, the quasi-resistive reconnection profile of J_e remains radially symmetric around the RR; and therefore the contributions of $d_i J_e B_\tau$ on the inner and outer sides of the X-point to the overall diamagnetic rotation of the RR approximately cancel.

However, in the fast reconnection phase, distinctly asymmetric radial profile of J_e with most reconnection current concentrated on the inner side of the RR leads to strong diamagnetic rotation of the X-point.

Panel (b) of Figure 4.31 shows the nature of the asymmetry with contour plots of the helical current density J_e (solid contours) and the helical ion flow V_e (dashed contours) in the immediate vicinity of the RR after the current layer collapse at $t = 1292$. Recalling that $\mathbf{v}_e = \mathbf{v}_i - d_i\mathbf{J}$, we note that ion current constitutes $\lesssim .25$ of the total reconnection current, electron reconnection current is localized to a small fraction of the d_i scale, and peaks in the ion and electron helical flows are radially displaced by $\approx d_i/2$.

The explanation for the observed structure of the two-fluid RR before and after the collapse lies in the mechanism responsible for driving reconnection and the primarily one-sided plasma inflow into the RR. During the early evolution of the ideally unstable internal kink, it is the ideal instability of the kinking plasma core that drives reconnection by forming a long current layer of length $L \sim r_s$, *i.e.* it is not the tension of the reconnected field lines but the inflow velocity drive that pushes plasma through the RR. As the core begins to reconnect out, the drive of the kinking core diminishes and is replaced by the drive provided by the pressure of the recirculating reconnection outflows on the core (see discussion in Section 4.3.2) and tension of the reconnected field lines, which pull plasma through the RR. In the presence of sufficiently high resistivity, the system proceeds to reconnect resistively, preserving a current layer of macroscopic length as it becomes narrower due to increase in upstream magnetic field and decrease in the RR length as the core's radius decreases. No significant ion/electron-fluid separation is observed and reconnection current layer

remains approximately symmetric as the one-sided inflow remains slow.

However, as discussed above, whenever the current layer half-width becomes smaller than the two-fluid separation scale, $\delta_J/2 \lesssim d_i$ (or $\delta_J/2 \lesssim \rho_s$, when finite compressibility is considered), EMHD effects may act to destabilize the electron current layer leading to its collapse to an X-point with magnetic field line curvature on the much smaller electron viscous scale. As a result, the magnetic field line tension becomes the dominant mechanism driving the reconnection and the one-sided plasma inflow is greatly accelerated. Furthermore, since during ideal and resistive kinking all reconnected field-line curvature is also located on the inner side of the current layer, $r \leq r_X$, it is energetically favorable for the two-fluid RR magnetic field configuration to adjust and shift the location of the greatest field-line tension, the X-point, radially inwards with respect to the outer un-reconnected region. That is where the electron reconnection current is localized. Yet, as ions decouple from the in-plane magnetic field on the two-fluid separation scale, ion reconnection current is distributed over a larger region around the X-point with the peak in helical ion current density corresponding to the point of zero poloidal ion flow – the location where the one-sided radial ion flow is stopped by the outer un-reconnected magnetic field. Thus, asymmetric reconnection current layer results.

4.4.3 Hall MHD simulations with Ohmic current drive.

Having considered directly driven Hall MHD internal kink simulations, we now return to the more realistic boundary driven configuration and study its evolution in the semi-collisional regime.

Problem setup.

The two E-field boundary conditions that have to be enforced to simulate application of a purely axial electric field at the wall of a device remain principally the same – $\mathbf{E}_b \cdot \hat{z} = g(E_e + \epsilon r E_\tau) = E_b$ and $\mathbf{E}_b \cdot \hat{\theta} = g(E_\tau - \epsilon r E_e) = 0$. However, with $d_i \neq 0$, the implementation presented in Section 4.3.6 is complicated by the addition of the Hall and kinematic electron viscosity terms to the Ohm's Law. The resulting E-field boundary condition equations take the following form:

$$\frac{\partial \psi}{\partial t} = E_b$$

$$\epsilon r_w E_b = -\eta(r_w)\frac{\partial B_e}{\partial r} - d_i \frac{B_e}{r_w}\frac{\partial B_e}{\partial \tau} - 2 d_i \nu \epsilon g^2 \left(d_i \frac{\partial J_e}{\partial r} - \frac{\partial V_e}{\partial r} - 2 r_w \epsilon^2 g^2 (d_i J_e - V_e) \right),$$

where a linear combination of the two E-field equations was used to simplify the above boundary condition expressions.

We again use the same boundary conditions on ion flow – no flow onto the wall and perfect slip flow tangential to the wall. We additionally note that the presence of kinematic electron viscosity in the Hall MHD equations requires specifying another boundary condition on electron flow (or current) along the boundary. We have set $[\partial(\mathbf{J} \cdot \hat{z})/\partial t]|_{r_w} = 0$, but other boundary conditions might be more appropriate.

The initial conditions used for all simulations presented in this Section are those described in Section 4.3.5 above.

Plasmoid generation by secondary current layer instabilities.

As we have shown in the self-driven Hall MHD reconnection simulations of the semi-open Harris equilibrium described in Section 3.4.1 above, the transitional regime between the slow quasi-resistive and fast virtually collisionless reconnection is occupied

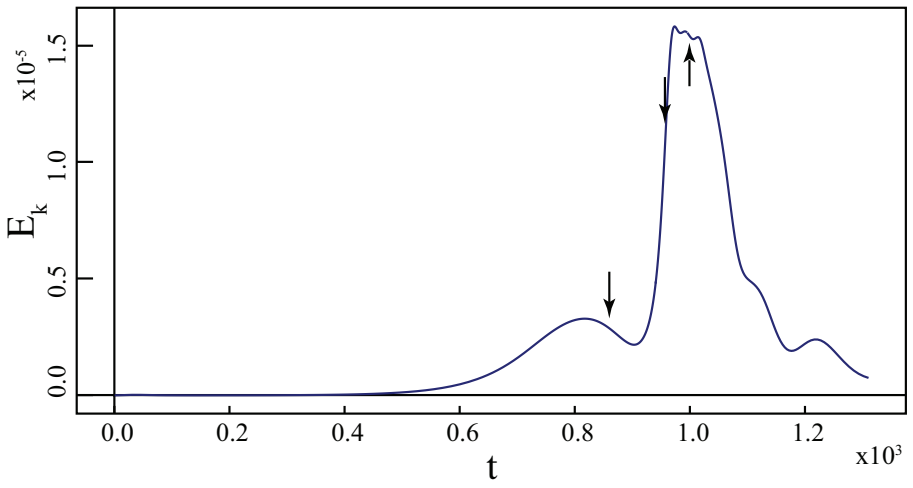

Figure 4.32: Time-trace of kinetic energy in a semi-collisional Hall MHD internal kink simulation with plasmoid formation. Arrows correspond to the snap-shots of the system shown in Figure 4.33. Simulation parameters are $d_i = 0.01$, $1/\epsilon = 25$, $r_s = 0.5$, $\eta_s = 5 * 10^{-6}$, $\mu = 5 * 10^{-5}$, $\nu = 10^{-8}$ and $\delta B_e = 10^{-3}$.

by an intermittent state of macroscopic quasi-resistive current sheets strongly unstable to secondary EMHD instabilities. Here, we describe the results of an equivalent simulation within the context of the internal kink mode.

Figure 4.32 shows a time-trace of the system's kinetic energy as the ideally unstable initial condition develops the non-linear internal kink mode. The first peak around $t \approx 800$ corresponds to the increase in the kinetic energy due to the kink itself. Panels (a,d) of Figure 4.33 show contour plots of ψ over the whole domain and J_e around the RR at $t = 845.3$ immediately after the peak in E_k is achieved and display a resistive current layer of length $L \approx 2r_s$. The high Prandtl number used in this simulation, $\mu/\eta \approx 5 * 10^{-5}/5 * 10^{-6} = 10$, is likely responsible for the observed decrease in the system's kinetic energy once such a long Sweet-Parker current layer has formed. However, after a period of quasi-resistive evolution, Fig. 4.32 shows a

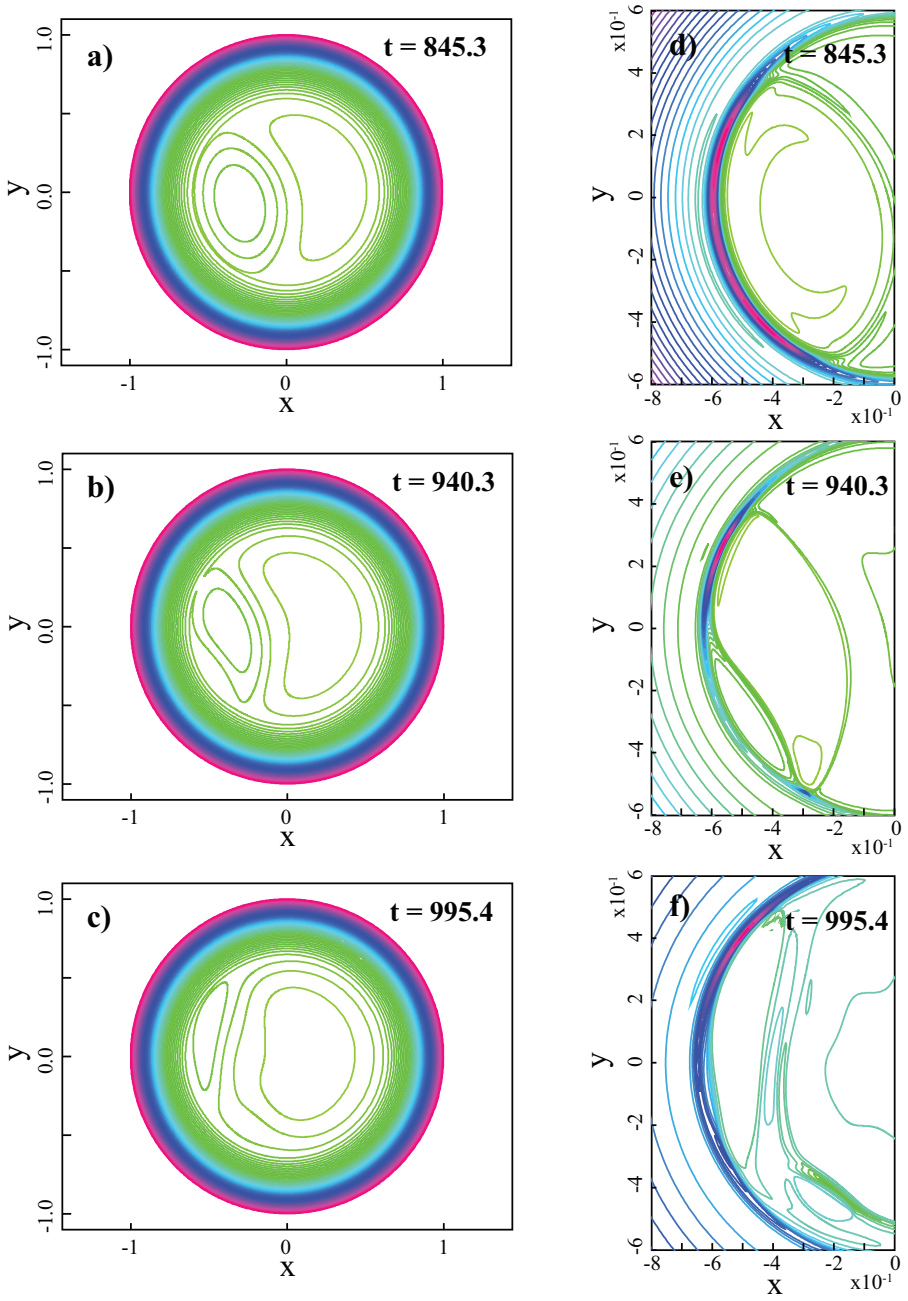

Figure 4.33: Contour plots of (a-c) ψ and (d-f) J_e from a semi-collisional Hall MHD internal kink simulation with plasmoid formation. Three times corresponding to those marked in Figure 4.32 are shown in panels (a,d) $t = 845.3$, (b,e) $t = 940.3$, and (c,f) $t = 995.4$. Simulation parameters are $d_i = 0.01$, $1/\epsilon = 25$, $r_s = 0.5$, $\eta_s = 5 * 10^{-6}$, $\mu = 5 * 10^{-5}$, $\nu = 10^{-8}$ and $\delta B_e = 10^{-3}$.

rapid increase in the system's kinetic energy, which is exactly correlated with the break up of the current layer and formation of a plasmoid, as shown in panels (b,e) of Fig. 4.33. By comparing panels (d) and (e) of Fig. 4.33, we observe that the two resulting shorter current layers are also significantly thinner than the macroscopic one and thus facilitate faster overall magnetic reconnection of the plasma core.

As the plasmoid grows by accumulating magnetic flux reconnected through the two X-points surrounding it, it is eventually ejected to one side of the core, as shown in panels (c,f) of Fig. 4.33. With the plasmoid ejected, the system is observed to convert back to a wider and weaker current layer with E_k rapidly falling off as magnetic reconnection is slowed down again.

We now note that at each stage of the evolution from generation through ejection of the plasmoid, the dimensions and dynamics of the observed current layers appear to be quasi-resistive. However, in the absence of two-fluid effects ($d_i = 0$), the only internal kink simulations in which we have ever observed resistive current layer break-up and plasmoid formation are those of the ideally unstable $1/\epsilon = 5$ configuration, where the ideal kink drive is sufficiently strong to compress the current layer to the point where it becomes unstable to a secondary resistive tearing mode. In the presently described $1/\epsilon = 25$ simulation, no such compression takes place.

We conclude that in the regime of $\delta_J/2 \approx d_i$, current layer break up, plasmoid formation and ejection is a likely outcome and results in higher overall reconnection rate than an equivalent purely visco-resistive Sweet-Parker reconnection.

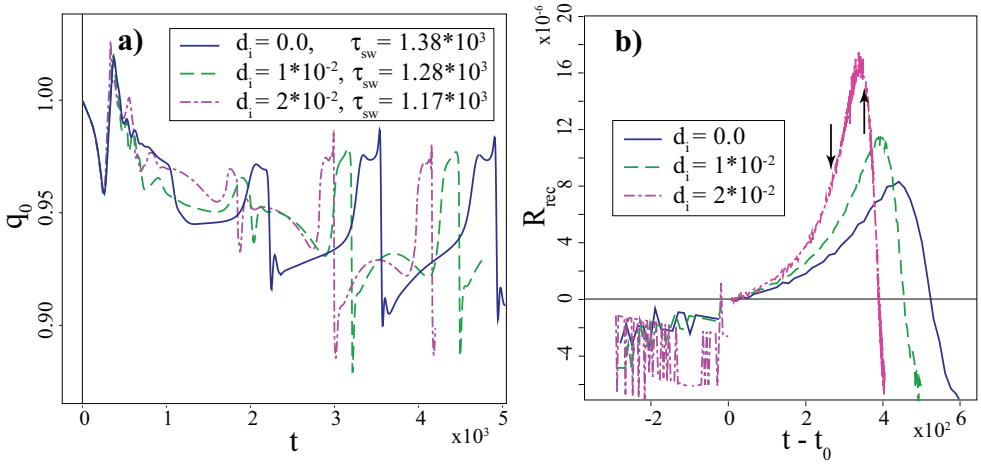

Figure 4.34: Time-traces of (a) q_0 and (b) R_{rec} in incomplete sawtooth simulations with $d_i = \{0, 0.01, 0.02\}$. Corresponding sawtooth periods are shown in the legend of panel (a). As in Fig. 4.27, traces of R_{rec} in panel (b) are adjusted for the timing and background electric field of the sawteeth. Arrows correspond to the snap-shots of the system shown in Fig. 4.35. Simulation parameters are $1/\epsilon = 10$, $r_s = 0.5$, $\eta_s = 10^{-5}$, $\mu = 5 * 10^{-5}$, $\nu = 2 * 10^{-8}$ and $\delta B_e = 10^{-3}$.

Incomplete sawteeth with two-fluid effects.

We now turn to consider if and how the sawtoothing behavior observed in the purely visco-resistive simulations is modified by the two-fluid effects. In particular, we conduct $1/\epsilon = 10$ aspect ratio simulations with $d_i \neq 0$ to evaluate whether or not the incomplete sawteeth persist in the presence of accelerated reconnection and diamagnetic rotation.

Figure 4.34 compares time-traces of q_0, panel (a), and R_{rec}, panel (b), from sawtooth simulations with $d_i = \{0, 0.01, 0.02\}$ holding all other parameters identical. It is apparent from evolution of the magnetic field-line pitch at the geometric axis that there is no qualitative difference between the three cases. Incomplete reconnection of the core is observed as clearly in the two-fluid simulations as in the single fluid

visco-resistive results presented above. However, it is just as clear that the two-fluid sawteeth have shorter period τ_{sw}, given in the legend of panel (a) of Fig. 4.34. Nearly all of the reduction in the sawtooth period is due to the shorter kink-driven IR events, as shown in panel (b) of Fig. 4.34. While the total amount of poloidal core flux reconnected during an incomplete sawtooth is approximately the same in all three simulations, the rate of reconnection increases significantly as d_i is increased. And the differences between the internal reconnection event durations account for nearly all of the differences in the measured τ_{sw}.

We note that unlike the equivalent comparison between the three ideally unstable internal kink simulations with $d_i = \{0, 0.01, 0.02\}$ and $\eta = 10^{-5}$ shown in Figure 4.29 above, the R_{rec} time-traces of $1/\epsilon = 10$ sawteeth are qualitatively not very different. An explosive increase in the reconnection rate when the two-fluid parameter exceeds some resistive current layer width does not take place in these sawtooth simulations. Instead, $R_{rec}(t)$ varies relatively gently with time for each value of d_i and its maximum over a sawtooth appears to also be a smooth function of d_i.

Nevertheless, the $d_i = 0.02$ incomplete sawteeth have a distinctly two-fluid character, as shown in the contour plots of J_e, in panels (c-d) of Figure 4.35. While the contour plots of ψ, shown in panels (a-b) of Figure 4.35, are very similar to the equivalent ones in purely visco-resistive simulations (see Fig. 4.18), the two-fluid reconnection current exhibits a clear signature of a localized and asymmetric current channel (see Fig. 4.28 for comparison), as discussed in Section 4.4.2 above.

The explanation for the lack of explosive onset of fast reconnection in the $1/\epsilon = 10$ sawteeth lies in the macroscopic configuration of the magnetic fields which are supposed to reconnect during the incomplete internal reconnection events. As we

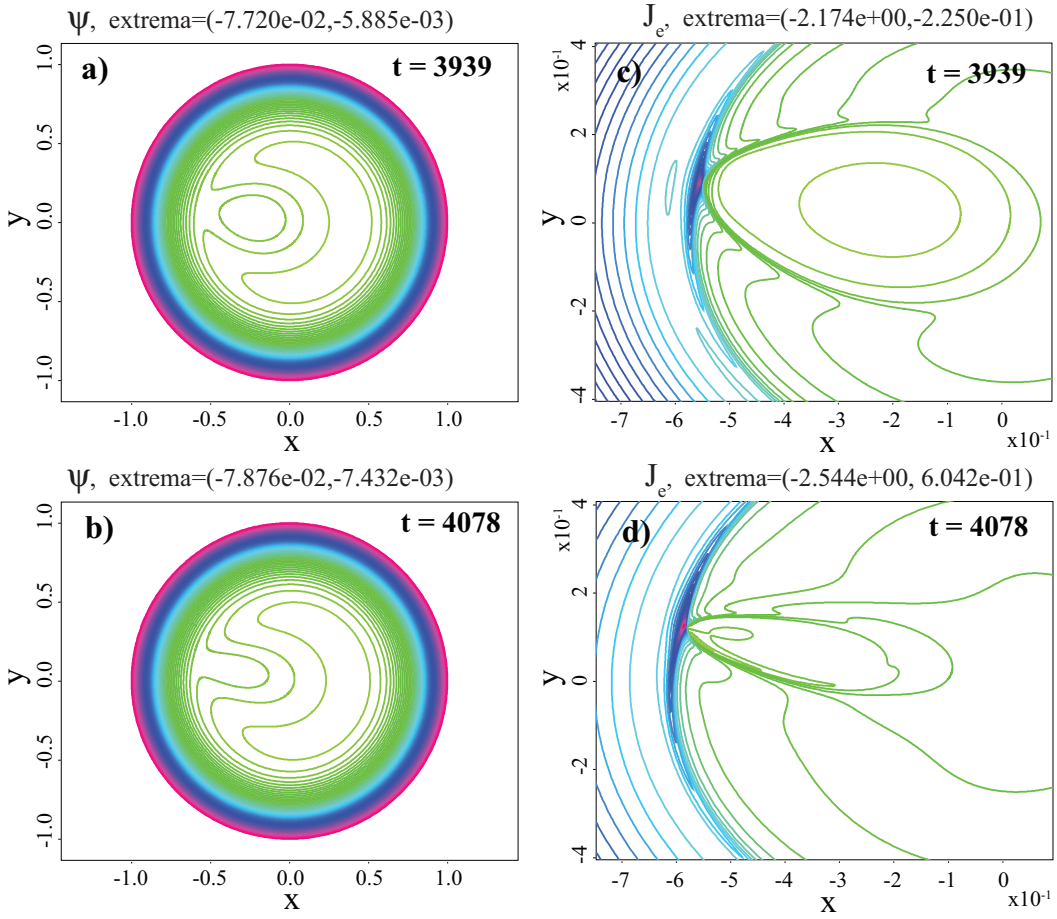

Figure 4.35: Contour plots of (a-b) ψ and (c-d) J_e from a Hall MHD incomplete sawtooth simulation. Two times corresponding to those marked in Fig. 4.34 are shown in panels (a,c) $t = 3939$ and (b,d) $t = 4078$. Simulation parameters are $d_i = 0.02$, $1/\epsilon = 10$, $r_s = 0.5$, $\eta_s = 10^{-5}$, $\mu = 5 * 10^{-5}$, $\nu = 2 * 10^{-8}$ and $\delta B_e = 10^{-3}$.

note in the previous sections, the reconnecting plasma core of these sawteeth takes a tear-drop shape preserving a relatively short current layer with $L \ll r_s$ and $L/\delta \approx 10$ even in a purely visco-resistive regime. Thus, no significant current layer collapse takes place when the two-fluid effects become important and no rapid change in the reconnection rate is observed.

We note that we have also conducted two-fluid long-term simulations of an Ohmic driven screw-pinch with the aspect ratio of $1/\epsilon = 25$ and $1/\epsilon = 5$ in order to compare them with the visco-resistive results described above. (See Appendix B for a summary table of all incompressible internal kink simulations conducted for the study described in this Dissertation.) However, no differences of significant interest with the single fluid simulations have been observed and therefore the data is not presented here.

4.4.4 Discussion of the two-fluid results.

The incompressible Hall MHD simulation results presented above demonstrate that while the two-fluid physics should not be ignored and may be important in explaining the time-scales observed in experiments, it does not qualitatively alter the underlying global self-organization properties of the system. The main features of the visco-resistive sawteeth – the dynamo-generated paramagnetism and the observed limit-cycle behavior of a relaxed weakly driven system, leading to a possibility of incomplete reconnection sawteeth, – are preserved.

At the same time, the characteristics of magnetic reconnection that takes place during the sawtooth IR events in the semi-collisional regime are in very good agreement with those observed and described in the reconnection focused simulations discussed in Chapter 3 above. The correspondence of the results in two very different configurations gives us confidence that the understanding achieved in the easiest to

analyze setups can be carried over to the more complex systems. This statement, however, has to be qualified by emphasizing that the temporal evolution and structure of a magnetic reconnection region can be strongly influenced by the global magnetic field structure and can, therefore, change depending on the exact problem being considered – that is an integral part of the understanding.

As we have already discussed, the exact incompressibility approximation made in these calculations is not appropriate for realistic tokamak plasmas with $\beta_T \ll 1$. Yet, based on the previously published results[53, 68, 128], we suggest that the character of the two-fluid internal kink will not change significantly aside from the reduction of the relevant two-fluid scale from d_i to ρ_s. We note that the presence of a strong magnetic guide-field, in and of itself, does not inhibit onset of fast reconnection and collapse of the reconnection current layer to the electron viscous scale.

4.5 Summary of the internal kink simulations.

In this study, we have accomplished several somewhat independent goals:

1. Further verify the SEL code, described in Chapter 2, against asymptotic analytical and other published numerical linear results in helical geometry. Reproduce known non-linear behavior of the ideally unstable visco-resistive and semi-collisional internal kink.

2. Demonstrate the importance of self-organization and relaxation phenomena in a tokamak-relevant magnetic field configuration and make connections with known results in the RFP community. For the first time, produce an $m = 1$ sawtooth simulation which exhibits incomplete reconnection of the plasma core and maintains $q < 1$ throughout the cycle.

3. Confirm the understanding of visco-resistive and two-fluid magnetic reconnection achieved in simulations of flat two-dimensional domains described in Chapter 3. Evaluate how the possibility of fast two-fluid reconnection affects the time-scales and dynamics of the sawteeth observed in the visco-resistive regime.

We now conclude this Dissertation with a discussion of overall results and future directions of the research described herein.

Chapter 5

Conclusions, discussion and future work.

5.1 SEL code

All of the simulation results presented in this Dissertation have been obtained with the 2D implicit adaptive parallel spectral element code SEL. The details of the code's core algorithm, its grid adaptation technique and both linear and non-linear verification studies conducted with the code are described in Chapter 2. As demonstrated with the verification studies and even more so with the results of the magnetic reconnection and internal kink simulations described above, the numerical approach chosen for implementation in the SEL code is highly accurate, robust and efficient, capable of long time-integration of strongly non-linear extended MHD systems. As discussed below, we believe that the accuracy of the code has been critical in obtaining the new results and understanding of the physics achieved in this Dissertation.

In conducting the non-linear simulations, we take advantage of the flexibility afforded by SEL's use of the PETSc library and, during the Newton iteration, try different parallel linear solvers, such as the iterative ILU preconditioned GMRES or the parallel direct solver SuperLU_dist, for different sets of PDEs and problem sizes.

Although we have not yet done a thorough scaling study, it appears that when using the direct SuperLU_dist solver, the code, employing all of its capabilities, scales slightly worse than weakly[1] to $\sim 100 - 150$ processors on the National Energy Research Scientific Computing (NERSC) IBM POWER 5 *Bassi* system[102]. In these preliminary scaling studies, all of the memory-per-processor available on the system is used and the biggest long time-integration problem solved so far is the Hall MHD Ohmic driven internal kink problem with 6 independent variables on an adaptive $[n_x, n_y, n_p] = [48, 72, 8]$ grid, run on 12 Bassi nodes of 8 processors and ≈ 19 GB of available memory each for ≈ 42 hours of wall-clock time. (Results of that simulation are presented in Section 4.4.3 and the description of the input parameters is given in Appendix B under "run #33".) It is well known that a direct solver intrinsically cannot scale to many more processors, and attempts to use the iterative GMRES solver on the same problem show a significantly worse scaling (to the same number of processors) and wall-clock run-time 3-4 times longer than the SuperLU_dist direct solver, though somewhat less memory is taken up by the iterative solver, as well.

We quote these numbers here to show the present limitations of the SEL code. While we see no good alternative to using the high order finite element (or, equivalently, spectral element) spatial representation and implicit temporal advance for future anisotropic extended MHD simulations in fully 3D systems[137], it is apparent that a new parallel linear solver for high order finite element based codes with better scaling properties is necessary to be able to accurately solve any problem of practical interest in reasonable time. Active research on that subject is now taking place, where the SEL code is used as a test-bed for the new algorithms recently developed in the

[1] Doubling problem size on a doubled number of processors results in $\approx 15 - 20\%$ increase in wall-clock run-time.

applied mathematics community[63, 84].

5.2 Magnetic reconnection

In this work, we consider only the two-dimensional aspects of magnetic reconnection. We qualitatively describe the structure of a 2D reconnection region and then proceed to analyze simulations of the same large scale semi-open tearing unstable magnetic field configuration with the visco-resistive, electron and two-fluid (Hall) MHD models in Chapter 3.

Well known visco-resistive result – slow Sweet-Parker reconnection through a macroscopic system-size current layer – is reproduced. In electron MHD (EMHD), observed structure and scalings of characteristic quantities of a microscopic EMHD reconnection region are shown to agree with the derived qualitative estimates. Width of the electron current layer is shown to be determined by electron viscosity, *not* electron inertia, and observed electron current layer instability is derived and numerically confirmed to be due to the interaction of electron inertia and frozen-in magnetic field effects, *not* Kelvin-Helmholtz instability of the sheared electron flow, as has been suggested previously[18].

In Hall MHD, in the semi-collisional regime, the reconnection region is shown to allow *three* different solutions: large aspect ratio system-size quasi-resistive reconnection region, localized X-point microscopic reconnection region, and an intermittent solution of a plasmoid formation unstable electron current layer embedded within a system-size reconnection region. The intermittent solution that we find to lie in between the quasi-resistive and X-point magnetic reconnection configurations is distinctly different than that recently reported in the literature[33]. We note that the

discrepancies between the previously obtained numerical results and those reported here are likely due to the lower physical dissipation coefficients and better numerics, particularly the improved spatial resolution and near-absence of numerical diffusion and dispersion, employed in this study.

Based on these and other reported two-fluid and collisionless particle simulation results, we propose an explanation for the numerically observed structure of a two-fluid reconnection region – 2-scale in the outflow direction and 4-scale in the inflow direction in the collisionless limit and single scale in both directions in the collisional limit. Based on the qualitative analysis which states that spontaneous magnetic reconnection is fundamentally driven by the tension of magnetic field lines in the outflow region, we propose that the velocity of the plasma outflow from a reconnection region will always be maximized subject to the inertial, collisional and kinetic effects present in any given plasma, *plus* the condition of local minimum energy state of the reconnection region itself. In our view, it is the combination of the two that determines the steady-state structure of a reconnection region in the various plasma parameter regimes. And in systems that can find no such reconnection region configuration, reconnection rate is effectively maximized by producing "bursty" behavior, such as plasmoid formation and ejection, which results in the absence of a single steady-state reconnection region.

Here, we fully recognize that our conclusions about the nature of two-dimensional magnetic reconnection are based solely on qualitative estimates and evidence obtained from multiple numerical experiments. While we believe that our explanation does not contradict any of the available numerical or experimental evidence, there still exists no precise analytical derivation determining the structure and reconnection rate of even

the simplest multi-scale reconnection region. We hope that the insights presented in this work might accelerate the arrival of such a theory.

5.3 Internal kink, sawtooth oscillations, and magnetic self-organization

We study a driven $m = n = 1$ internal kink unstable helical screw-pinch system in an incompressible cylindrical tokamak approximation in Chapter 4. Ideal and resistive linear and visco-resistive and Hall MHD non-linear simulations of the ideally unstable internal kink mode are shown to reproduce the known asymptotic analytical and previous numerical results. In particular, the observations by Aydemir[7] of the quasi-exponential non-linear growth of the visco-resistive kink mode in the limit of very small dissipation, and by Aydemir[6] and others of the explosive onset of fast reconnection during the semi-collisional and collisionless internal kink evolution, are confirmed.

Over a longer time-integration period, in systems driven towards a hollow q-profile with $q(r = 0) < 1$, regeneration of the plasma core followed by another smaller internal reconnection event is observed. Both the quantitative and qualitative long-term behavior of the system is shown to be independent of the nature of the drive – Ohmic boundary drive with assumed hollow resistivity profile or direct interior current-drive with uniform resistivity. Precise initial conditions are also observed to have little effect on the eventual limit-cycle of the resulting sawtooth oscillations and/or relaxation of the magnetic field configuration.

By varying the aspect ratio of the screw-pinch and relying on similar results in

simulations of reversed field pinches, clear evidence of self-organization of a tokamak-like magnetic field configuration is identified for the first time. Complete Kadomtsev reconnection sawteeth are observed in the very large aspect ratio $1/\epsilon = 25$ simulations, while stable helical resistive dynamo is demonstrated in the smallest aspect ratio $1/\epsilon = 5$ simulations. (Note that for these results, the physically relevant aspect ratio parameter is the ratio of the periodic length of the screw-pinch to the radius of the $q = 1$ surface, not to the radius of the domain.) However, for the first time, simulations of $m = 1$ sawteeth are also shown to exhibit incomplete reconnection of the plasma core and maintain $q < 1$ throughout the cycle in a screw-pinch system with $1/\epsilon = 10$. In all of the sawtooth simulations, "quasi-interchange"-like mechanism is observed to also be partially responsible for the restoration of the closed magnetic surfaces in the plasma core.

During both the ideally unstable internal kink and the following sawtooth oscillations, the coupling between the structure of the reconnection region and the global magnetic field configuration is emphasized and shown to play an important role in determining the observed reconnection rates. The results are well understood in the context of the visco-resistive and two-fluid magnetic reconnection simulations described in Chapter 3. In particular, during the sawtooth oscillations, presence of the Hall physics in shown to accelerate the non-linear development of the internal kink mode, while having little effect on the dynamics and time-scales observed during the remainder of a sawtooth cycle.

Finally, we note that the present study is only a first step towards improved understanding of the sawtooth phenomenon, universally observed in tokamaks and other toroidal confinement devices, by using high accuracy numerical methods. Even

within the cylindrical tokamak approximation, compressibility, non-uniform density, self-consistent and anisotropic heating and diffusion coefficients are bound to have non-negligible effects on the character of the time-asymptotic self-organized limit-cycle (or stable equilibrium) of the system. While preliminary simulations using such extended MHD model are presently under way (see Appendix C for the description of the extended MHD equations, their SEL implementation and employed initial and boundary conditions), we believe it is critical to maintain the accuracy level demonstrated in this study in order to continue to generate trustworthy results with the more complete systems.

Appendix A

Calculus in helical coordinates.

A.1 Useful vector-differential identities in helical coordinates with 2D helical symmetry.

Within helical symmetry, the usual differential operators in terms of the helical coordinates (r, τ) are as follows:

$$\nabla r = \hat{r}, \quad \nabla \tau = \frac{1}{rg}\hat{\tau}, \quad \nabla F = \frac{\partial F}{\partial r}\hat{r} + \frac{1}{rg}\frac{\partial F}{\partial \tau}\hat{\tau}$$

$$\nabla \cdot \mathbf{F} = \frac{1}{r}\frac{\partial (rF_r)}{\partial r} + \frac{1}{rg}\frac{\partial F_\tau}{\partial \tau}$$

$$\nabla \times \mathbf{F} = \frac{\hat{r}}{rg}\frac{\partial F_e}{\partial \tau} - \hat{\tau} g \frac{\partial}{\partial r}\left(\frac{F_e}{g}\right) + \hat{e}\left[\frac{1}{rg}\frac{\partial (rgF_\tau)}{\partial r} - \frac{1}{rg}\frac{\partial F_r}{\partial \tau} - 2\epsilon g^2 F_e\right]$$

Additional useful vector-differential identities are:

$$\nabla \times \hat{e} = \epsilon g^2(\epsilon r\hat{\tau} + 2\hat{e}), \quad \frac{\partial g}{\partial r} = -r\epsilon^2 g^3, \quad \frac{1}{rg}\frac{\partial (rgF)}{\partial r} = \frac{\partial F}{\partial r} + \frac{g^2}{r}F$$

$$\hat{r}\cdot\nabla\hat{r} = 0, \quad \hat{r}\cdot\nabla\hat{\tau} = \epsilon g^2\hat{e}, \quad \hat{r}\cdot\nabla\hat{e} = -\epsilon g^2\hat{\tau}$$

$$\hat{\tau}\cdot\nabla\hat{r} = \frac{g^2}{r}\left(\hat{\tau} - \epsilon r\hat{e}\right), \quad \hat{\tau}\cdot\nabla\hat{\tau} = -\frac{g^2}{r}\hat{r}, \quad \hat{\tau}\cdot\nabla\hat{e} = \epsilon g^2\hat{r}$$

$$\hat{e}\cdot\nabla\hat{r} = -\epsilon g^2\left(\hat{\tau} - \epsilon r\hat{e}\right), \quad \hat{e}\cdot\nabla\hat{\tau} = \epsilon g^2\hat{r}, \quad \hat{e}\cdot\nabla\hat{e} = -r\epsilon^2 g^2\hat{r}$$

$$
\begin{aligned}
\nabla\mathbf{A} &= \hat{r}\hat{r}\frac{\partial A_r}{\partial r} + \hat{\tau}\hat{r}\left[\frac{1}{rg}\frac{\partial A_r}{\partial \tau} - \frac{g^2}{r}\left(A_\tau - \epsilon r A_e\right)\right] + \hat{e}\hat{r}\left[\epsilon g^2\left(A_\tau - \epsilon r A_e\right)\right] \\
&+ \hat{r}\hat{\tau}\left[\frac{\partial A_\tau}{\partial r} - \epsilon g^2 A_e\right] + \hat{\tau}\hat{\tau}\left[\frac{1}{rg}\frac{\partial A_\tau}{\partial \tau} + \frac{g^2}{r}A_r\right] + \hat{e}\hat{\tau}\left[-\epsilon g^2 A_r\right] \\
&+ \hat{r}\hat{e}\left[\frac{\partial A_e}{\partial r} + \epsilon g^2 A_\tau\right] + \hat{\tau}\hat{e}\left[\frac{1}{rg}\frac{\partial A_e}{\partial \tau} - \epsilon g^2 A_r\right] + \hat{e}\hat{e}\left[r\epsilon^2 g^2 A_r\right]
\end{aligned}
$$

$$
\left[\left(\mathbf{A}\cdot\nabla\right)\mathbf{B}\right]\cdot\hat{r} = A_r\frac{\partial B_r}{\partial r} + \frac{A_\tau}{rg}\frac{\partial B_r}{\partial \tau} - \frac{g^2}{r}(A_\tau - \epsilon r A_e)(B_\tau - \epsilon r B_e)
$$

$$
\left[\left(\mathbf{A}\cdot\nabla\right)\mathbf{B}\right]\cdot\hat{\tau} = A_r\frac{\partial B_\tau}{\partial r} + \frac{A_\tau}{rg}\frac{\partial B_\tau}{\partial \tau} + \frac{g^2}{r}B_r A_\tau - \epsilon g^2(A_r B_e + A_e B_r)
$$

$$
\left[\left(\mathbf{A}\cdot\nabla\right)\mathbf{B}\right]\cdot\hat{e} = A_r\frac{\partial B_e}{\partial r} + \frac{A_\tau}{rg}\frac{\partial B_e}{\partial \tau} + \epsilon g^2(A_r B_\tau - A_\tau B_r) + r\epsilon^2 g^2 A_e B_r.
$$

A.2 Coordinate transformations from helical to cartesian coordinates for differential operators.

We note that $\partial F/\partial\tau = \partial F/\partial\theta$. Using that and the well known coordinate transformation between cylindrical and cartesian coordinate systems, we have the following relationships:

$$
\frac{\partial}{\partial r} = \frac{1}{r}\left(x\frac{\partial}{\partial x} + y\frac{\partial}{\partial y}\right), \qquad \frac{\partial}{\partial\theta} = \left(x\frac{\partial}{\partial y} - y\frac{\partial}{\partial x}\right)
$$

$$
\frac{\partial^2}{\partial r^2} = \frac{1}{r^2}\left(x^2\frac{\partial^2}{\partial x^2} + 2xy\frac{\partial^2}{\partial x\partial y} + y^2\frac{\partial^2}{\partial y^2}\right)
$$

$$
\frac{\partial^2}{\partial\theta^2} = x^2\frac{\partial^2}{\partial y^2} - 2xy\frac{\partial^2}{\partial x\partial y} + y^2\frac{\partial^2}{\partial x^2} - \left(x\frac{\partial}{\partial x} + y\frac{\partial}{\partial y}\right)
$$

$$
\frac{\partial^2}{\partial r\partial\theta} = \frac{1}{r}\left[(x^2 - y^2)\frac{\partial^2}{\partial x\partial y} - xy\left(\frac{\partial^2}{\partial x^2} - \frac{\partial^2}{\partial y^2}\right) + \left(x\frac{\partial}{\partial y} - y\frac{\partial}{\partial x}\right)\right]
$$

$$
\begin{aligned}
g^2\Delta^*[F] &= \frac{1}{r}\left[\frac{\partial}{\partial r}\left(rg^2\frac{\partial}{\partial r}\right) + \frac{1}{r}\frac{\partial^2}{\partial\theta^2}\right]F \\
&= \frac{\partial}{\partial x}\left[\left(1 - \frac{\epsilon^2 x^2}{1+\epsilon^2 r^2}\right)\frac{\partial}{\partial x} - \frac{xy\epsilon^2}{1+\epsilon^2 r^2}\frac{\partial}{\partial y}\right]F \\
&+ \frac{\partial}{\partial y}\left[\left(1 - \frac{\epsilon^2 y^2}{1+\epsilon^2 r^2}\right)\frac{\partial}{\partial y} - \frac{xy\epsilon^2}{1+\epsilon^2 r^2}\frac{\partial}{\partial x}\right]F
\end{aligned}
$$

$$\mathbf{B}\cdot\nabla F=\frac{\partial}{\partial y}\left(F\frac{\partial\psi}{\partial x}\right)-\frac{\partial}{\partial x}\left(F\frac{\partial\psi}{\partial y}\right),\quad \mathbf{J}\cdot\nabla F=\frac{\partial}{\partial x}\left(F\frac{\partial B_e}{\partial y}\right)-\frac{\partial}{\partial y}\left(F\frac{\partial B_e}{\partial x}\right),$$

where $r=\sqrt{x^2+y^2}$.

Appendix B

Summary table of all incompressible Hall MHD internal kink simulation runs.

All incompressible Hall MHD attempts at simulating the internal kink mode, either from an ideally unstable initial condition or in the sawtooth phase, are summarized in the table. Spectral elements of $n_p = 8$ order are used in all of the simulations. "Park" initial condition corresponds to the one given by Eqs. (4.2.5); resistive equilibrium ("resist. equil.") corresponds to that described in Section 4.3.4; and modified resistive equilibrium ("resist. equil.†") corresponds to that described in Section 4.3.5. Constant resistivity $\eta = \eta_s$ is used in directly driven simulations with the current source given by Eq. (4.3.14); and radial resistivity profile given by Eq. (4.3.13) with $\eta(r = r_s) = \eta_s$ is used in Ohmicly driven simulations. "*" mark next to the run number signifies that the simulation was conducted on the NIP parallel computer cluster of the Plasma Theory Group at the Los Alamos National Laboratory; otherwise, the simulations were conducted on the Bassi system of the NERSC Center.

#	$1/\epsilon$	r_s	d_i	η_s	μ/η_s	η_s/ν	n_x	n_y	δB_e	drive	init. cond.
03	25	.7	0	1e-5	1	100	32	26	1e-6	direct	Park
03b	25	.7	0	1e-5	1	100	32	36	1e-6	direct	Park
03c	25	.7	0	1e-5	1	100	32	42	1e-6	direct	Park
03d	25	.7	0	1e-5	1	100	32	48	1e-6	direct	Park
03e	25	.7	0	1e-5	1	100	40	60	1e-6	direct	Park
04a	25	.7	1e-2	1e-5	1	100	40	60	1e-6	direct	Park
06	10	.7	0	1e-5	1	100	32	26	1e-6	direct	Park
05*	10	.7	1e-2	1e-5	1	100	36	28	1e-6	direct	Park
07*	10	.7	2e-2	1e-5	1	100	36	28	1e-6	direct	Park
16*	25	.5	0	1e-5	0.2	100	36	42	1e-4	Ohmic	Park
08	25	.5	0	1e-5	1	100	40	60	1e-6	direct	Park
08*	25	.5	0	1e-5	1	100	36	42	1e-4	direct	Park
14*	25	.5	0	1e-5	1	100	36	42	1e-4	Ohmic	Park
29	25	.5	0	1e-5	1	500	32	48	1e-3	Ohmic	resist. equil.†
20	25	.5	0	1e-5	2	100	32	40	1e-3	Ohmic	resist. equil.†
15*	25	.5	0	1e-5	5	100	28	33	1e-4	Ohmic	resist. equil.
19*	25	.5	0	1e-5	5	100	28	30	1e-4	Ohmic	resist. equil.†
12	25	.5	1e-2	5e-6	1	100	40	60	1e-4	direct	Park
13*	25	.5	1e-2	5e-6	10	100	36	42	1e-4	direct	Park
24	25	.5	1e-2	5e-6	1	500	40	60	1e-3	Ohmic	resist. equil.†
09	25	.5	1e-2	1e-5	1	100	40	60	1e-6	direct	Park
23*	25	.5	1e-2	1e-5	5	500	28	36	1e-3	Ohmic	resist. equil.†
10	25	.5	2e-2	1e-5	1	100	40	60	1e-6	direct	Park
10b	25	.5	2e-2	1e-5	1	100	48	72	1e-6	direct	Park
21*	25	.5	2e-2	1e-5	5	20	28	36	1e-3	Ohmic	resist. equil.†
25*	10	.5	0	1e-5	5	500	28	30	1e-3	Ohmic	resist. equil.†
25b*	10	.5	0	5e-6	10	500	28	30	1e-3	Ohmic	from #25*
25c*	10	.5	0	1e-5	2.5	500	28	30	1e-3	Ohmic	from #25*
25d*	10	.5	0	2.5e-6	10	500	28	30	1e-3	Ohmic	from #25*
26	10	.5	1e-2	1e-5	5	500	40	60	1e-3	Ohmic	resist. equil.†
26b	10	.5	1e-2	5e-6	10	500	40	60	1e-3	Ohmic	from #26
26e	10	.5	1e-2	5e-6	10	100	40	60	1e-3	Ohmic	from #26
26c	10	.5	1e-2	1e-5	1	500	40	60	1e-3	Ohmic	from #26
26d	10	.5	1e-2	2.5e-6	20	250	40	60	1e-3	Ohmic	from #26
33	10	.5	2e-2	1e-5	5	500	48	72	1e-3	Ohmic	resist. equil.†
27*	5	.5	0	1e-5	5	500	28	34	1e-3	Ohmic	resist. equil.†
30*	5	.5	0	1e-6	50	500	28	34	1e-3	Ohmic	from #27*
31*	5	.5	0	5e-7	100	500	28	34	1e-3	Ohmic	from #30*
32*	5	.5	0	4e-6	12.5	500	28	34	1e-3	Ohmic	from #27*
28	5	.5	1e-2	1e-5	5	500	32	48	1e-3	Ohmic	resist. equil.†

Appendix C

Preliminary two-fluid extended MHD simulations in helical symmetry.

The formulation of the two-fluid extended MHD system of equation in helical symmetry, the implementation in the SEL code, and initial and boundary conditions for the preliminary simulations of the internal kink mode with a fully compressible two-fluid model are described below.

C.1 Extended MHD equations in helical coordinates.

We formulate two-fluid extended MHD equations in helical coordinates with the following primary variables:

1. n – plasma density;
2. $v_r \equiv n\mathbf{v}_i \cdot \hat{r}$ – $\hat{r}$-component of ion momentum;
3. $v_\tau \equiv n\mathbf{v}_i \cdot \hat{\tau}$ – $\hat{\tau}$-component of ion momentum;
4. $v_e \equiv n\mathbf{v}_i \cdot \hat{e}$ – $\hat{e}$-component of ion momentum;
5. ψ – helical magnetic flux;

6. $B_e \equiv \frac{1}{g}\mathbf{B}\cdot\hat{e}$ – modified $\hat{e}$-component of magnetic field;

7. $j_e \equiv \mathbf{v}_e\cdot\hat{e}$ – $\hat{e}$-component of electron velocity;

8. p_i – ion pressure;

9. p_e – electron pressure.

Magnetic field is expressed as

$$\mathbf{B} = g[\hat{e}\times\nabla\psi + B_e\hat{e}] = \hat{r}\left(-\frac{1}{r}\frac{\partial\psi}{\partial\tau}\right) + \hat{\tau}\left(g\frac{\partial\psi}{\partial r}\right) + \hat{e}\left(gB_e\right),$$

plasma current is

$$\mathbf{J} = \hat{r}\left(\frac{1}{r}\frac{\partial B_e}{\partial\tau}\right) + \hat{\tau}\left(-g\frac{\partial B_e}{\partial r}\right) + \hat{e}\left(g\Delta^*\psi - 2\epsilon g^3 B_e\right),$$

and components of electron momentum are

$$\begin{aligned} n\mathbf{v}_e\cdot\hat{r} &= v_r - \frac{d_i}{r}\frac{\partial B_e}{\partial\tau} \\ n\mathbf{v}_e\cdot\hat{\tau} &= v_\tau + d_i g\frac{\partial B_e}{\partial r} \\ n\mathbf{v}_e\cdot\hat{e} &= nj_e = v_e - d_i g\left(\Delta^*\psi - 2\epsilon g^2 B_e\right). \end{aligned}$$

The following diffusion/dissipation parameters are taken to be non-negligible:

$\eta_\perp = d_i/(n\tau_e\omega_{ce})$ – perpendicular resistivity, where $\tau_e(n,p_e)$ is the electron collision time and ω_{ce} is the electron cyclotron frequency assumed to be uniform and evaluated at the value of the main axial field;

$\eta_\parallel = \eta_\perp/1.96$ – parallel resistivity;

$q_{ie} = 3/(d_i\tau_e\omega_{ce})$ – heat exchange coefficient;

$\mu_0 = 0.96 d_i p_i \tau_i \omega_{ci}$ – compressional ion viscosity, where $\tau_i(n, p_i)$ is the ion collision time, $\omega_{ci} = \epsilon_m \omega_{ce}$ is the ion cyclotron frequency, and $\epsilon_m = (m_e/m_i)$ is the electron-to-ion mass ratio;

$\mu_i = 6 d_i p_i / (5 \tau_i \omega_{ci})$ – collisional ion viscosity;

$\nu_e = 2 \epsilon_m d_i p_e / (\tau_e \omega_{ce})$ – collisional electron viscosity;

$\kappa^i_{\parallel} = 3.9 d_i p_i \tau_i \omega_{ci}$ – parallel ion heat conduction;

$\kappa^i_{\wedge} = 5 d_i p_i / 2$ – cross-field ion heat conduction;

$\kappa^i_{\perp} = 2 d_i p_i / (\tau_i \omega_{ci})$ – perpendicular ion heat conduction;

$\kappa^e_{\parallel} = 3.2 d_i p_e \tau_e \omega_{ce}$ – parallel electron heat conduction;

$\kappa^e_{\wedge} = 5 d_i p_e / 2$ – cross-field electron heat conduction;

$\kappa^e_{\perp} = 4.7 d_i p_e / (\tau_e \omega_{ce})$ – perpendicular electron heat conduction;

under the assumption of large B-field, $\tau_e \omega_{ce} \gg \tau_i \omega_{ci} \gg 1$, and the ion skin depth $d_i \equiv \langle c/\omega_{pi} \rangle / r_0 \ll 1$, yet non-negligible.

Using two-fluid MHD formulation by Braginskii[24], we solve the following set of equations:

$$\frac{\partial n}{\partial t} + \nabla \cdot (n \mathbf{v}_i) = 0 \tag{C.1.1}$$

$$\begin{aligned} m_i \frac{\partial (n \mathbf{v}_i)}{\partial t} \quad &+ \quad \nabla \cdot \left(m_i n \mathbf{v}_i \mathbf{v}_i + \Pi^i \right) = -\nabla p_i + e \left(n \mathbf{E} + \frac{n \mathbf{v}_i \times \mathbf{B}}{c} \right) \\ &- \quad n \left[\eta_{\perp} \mathbf{J} + (\eta_{\parallel} - \eta_{\perp}) (\mathbf{J} \cdot \hat{b}) \hat{b} \right] \end{aligned} \tag{C.1.2}$$

$$en\mathbf{E} + \nabla \cdot \Pi^e = -\nabla p_e - e \frac{n \mathbf{v}_e \times \mathbf{B}}{c} + n \left[\eta_{\perp} \mathbf{J} + (\eta_{\parallel} - \eta_{\perp}) (\mathbf{J} \cdot \hat{b}) \hat{b} \right] \tag{C.1.3}$$

$$\begin{aligned}\frac{3}{2}\frac{\partial p_i}{\partial t} &+ \nabla\cdot\left\{\frac{3}{2}p_i\mathbf{v}_i-(\kappa_\parallel^i-\kappa_\perp^i)\left[\nabla\left(\frac{p_i}{n}\right)\cdot\hat{b}\right]\hat{b}+\kappa_\wedge^i\hat{b}\times\nabla\left(\frac{p_i}{n}\right)-\kappa_\perp^i\nabla\left(\frac{p_i}{n}\right)\right\}\\ &= -p_i\nabla\cdot\mathbf{v}_i-\Pi^i:\nabla\mathbf{v}_i+q_{ie}(p_e-p_i) \qquad \text{(C.1.4)}\end{aligned}$$

$$\begin{aligned}\frac{3}{2}\frac{\partial p_e}{\partial t} &+ \nabla\cdot\left\{\frac{3}{2}p_e\mathbf{v}_e-(\kappa_\parallel^e-\kappa_\perp^e)\left[\nabla\left(\frac{p_e}{n}\right)\cdot\hat{b}\right]\hat{b}-\kappa_\wedge^e\hat{b}\times\nabla\left(\frac{p_e}{n}\right)-\kappa_\perp^e\nabla\left(\frac{p_e}{n}\right)\right\}\\ &= -p_e\nabla\cdot\mathbf{v}_e-\Pi^e:\nabla\mathbf{v}_e+q_{ie}(p_i-p_e)\\ &- \left[\eta_\perp\mathbf{J}+(\eta_\parallel-\eta_\perp)(\mathbf{J}\cdot\hat{b})\hat{b}\right]\cdot(n\mathbf{v}_e-n\mathbf{v}_i) \qquad \text{(C.1.5)}\end{aligned}$$

$$\mathbf{J}=en(\mathbf{v}_i-\mathbf{v}_e) \qquad \text{(C.1.6)}$$

$$\begin{aligned}\Pi^i &= -\mu_0\left(\nabla\cdot\mathbf{v}_i\right)\left[\mathrm{I}-2\hat{e}\hat{e}\right]-\mu_i\left[\nabla\mathbf{v}_{i\parallel}+\left(\nabla\mathbf{v}_{i\parallel}\right)^T\right]\\ &- \frac{\mu_i}{4}\left[\nabla\mathbf{v}_{i\perp}+(\nabla\mathbf{v}_{i\perp})^T-(\nabla\cdot\mathbf{v}_{i\perp})(\mathrm{I}-\hat{e}\hat{e})\right]\\ \Pi^e &= -\nu_e\left[\nabla\mathbf{v}_{e\parallel}+\left(\nabla\mathbf{v}_{e\parallel}\right)^T\right],\end{aligned}$$

where, in accordance with the ordering introduced above, we neglect electron inertia, cross-field thermal force and corresponding frictional heat flux, perpendicular heat conductivities for both species, and parts of the pressure tensors, as described below.

The system is normalized by setting $\mathbf{B}=B_0\hat{\mathbf{B}}$, $n=n_0\hat{n}$, $\mathbf{v}_\alpha=v_0\hat{\mathbf{v}}_\alpha$ ($v_0\equiv B_0/\sqrt{4\pi m_i n_0}$), $\nabla=(1/r_0)\hat{\nabla}$, $\partial/\partial t=(1/t_0)\partial/\partial\hat{t}$ ($t_0\equiv r_0/v_0$), $\mathbf{E}=(B_0v_0/c)\hat{\mathbf{E}}$, and $p_\alpha=m_in_0v_0^2\hat{p_\alpha}$. It is clear that by specifying background B-field B_0, background density n_0 and system scale r_0, we uniquely determine normalizations of all other physical quantities. We now use appropriate expressions[24] for ion and electron collision times with reference tokamak-like plasma parameters of minor radius $r_0=100cm$, B-field $B_0=10^3Gauss$, and plasma density $n_0=10^{14}cm^{-3}$ to estimate $\tau_e\omega_{ce}$,

$\tau_i\omega_{ci}$, and d_i. We have

$$\begin{aligned}
\tau_e\omega_{ce} &= 4.47 * 10^{27}\frac{B_0^4}{n_0^{5/2}}\left(\frac{\hat{p_e}^{3/2}}{\hat{n}^{5/2}}\right) = 4.47 * 10^4\frac{\hat{p_e}^{3/2}}{\hat{n}^{5/2}} \\
\tau_i\omega_{ci} &= 1.48 * 10^{26}\frac{B_0^4}{n_0^{5/2}}\left(\frac{\hat{p_i}^{3/2}}{\hat{n}^{5/2}}\right) = 1.48 * 10^3\frac{\hat{p_i}^{3/2}}{\hat{n}^{5/2}} \\
d_i &= 2.28 * 10^{-2},
\end{aligned}$$

which easily satisfies the ordering specified above. We also note that $T_0 = p_0/n_0 = 4.97 * 10^2 eV$ follows from the normalization relations.

We combine ion momentum Equation (C.1.2) and electron momentum (Ohm's Law) Equation (C.1.3) to form a vector equation on total plasma momentum and drop hats over normalized quantities to arrive at the set of normalized equations evolved by the SEL code:

$$\frac{\partial n}{\partial t} + \nabla \cdot (n\mathbf{v}_i) = 0 \tag{C.1.7}$$

$$\frac{\partial (n\mathbf{v}_i)}{\partial t} + \nabla \cdot \left[n\mathbf{v}_i\mathbf{v}_i + \left(p_i + p_e + \frac{B^2}{2}\right)\mathrm{I} - \mathbf{BB} + \Pi^i + \Pi^e \right] = 0 \tag{C.1.8}$$

$$\begin{aligned}
\mathbf{E} &+ \frac{d_i}{n}\nabla \cdot \Pi^e = -\frac{d_i}{n}\nabla p_e - \mathbf{v}_e \times \mathbf{B} \\
&+ \frac{\eta_\perp}{d_i}(n\mathbf{v}_i - n\mathbf{v}_e) + (\eta_\parallel - \eta_\perp)J_\parallel \hat{b}
\end{aligned} \tag{C.1.9}$$

$$\begin{aligned}
\frac{3}{2}\frac{\partial p_i}{\partial t} &+ \nabla \cdot \left\{ \frac{3}{2}p_i\mathbf{v}_i - (\kappa_\parallel^i - \kappa_\perp^i)\nabla_\parallel\left(\frac{p_i}{n}\right) + \kappa_\wedge^i \hat{b} \times \nabla\left(\frac{p_i}{n}\right) - \kappa_\perp^i \nabla\left(\frac{p_i}{n}\right) \right\} \\
&= -p_i\nabla \cdot \mathbf{v}_i - \Pi^i : \nabla\mathbf{v}_i + q_{ie}(p_e - p_i)
\end{aligned} \tag{C.1.10}$$

$$\begin{aligned}
\frac{3}{2}\frac{\partial p_e}{\partial t} &+ \nabla \cdot \left\{ \frac{3}{2}p_e\mathbf{v_e} - (\kappa_\parallel^e - \kappa_\perp^e)\nabla_\parallel\left(\frac{p_e}{n}\right) - \kappa_\wedge^e \hat{b} \times \nabla\left(\frac{p_e}{n}\right) - \kappa_\perp^e \nabla\left(\frac{p_e}{n}\right) \right\} \\
&= -p_e\nabla \cdot \mathbf{v}_e - \Pi^e : \nabla\mathbf{v}_e + q_{ie}(p_i - p_e) + \eta_\perp\frac{|n\mathbf{v}_e - n\mathbf{v}_i|^2}{d_i^2} \\
&+ (\eta_\parallel - \eta_\perp)J_\parallel^2
\end{aligned} \tag{C.1.11}$$

$$d_i \nabla \times \mathbf{B} = (n\mathbf{v}_i - n\mathbf{v}_e) \tag{C.1.12}$$

$$\begin{aligned}
\Pi^i &= -\mu_0 \left(\nabla \cdot \mathbf{v}_i\right) \left[\mathrm{I} - 2\hat{e}\hat{e}\right] - \mu_i \left[\nabla \mathbf{v}_{i\|} + \left(\nabla \mathbf{v}_{i\|}\right)^T\right] \\
&- \frac{\mu_i}{4} \left[\nabla \mathbf{v}_{i\perp} + \left(\nabla \mathbf{v}_{i\perp}\right)^T - (\nabla \cdot \mathbf{v}_{i\perp})(\mathrm{I} - \hat{e}\hat{e})\right] \\
\Pi^e &= -\nu_e \left[\nabla \mathbf{v}_{e\|} + \left(\nabla \mathbf{v}_{e\|}\right)^T\right],
\end{aligned}$$

where $\nabla_\| F \equiv (\hat{b} \cdot \nabla F)\hat{b}$ and $J_\| \equiv (\nabla \times \mathbf{B}) \cdot \hat{b}$.

The full Braginskii ion and electron pressure tensors[24] are approximated according to the ordering of the characteristic ion/electron collision and cyclotron frequencies discussed above and magnitude and direction of flow gradients expected in the system. The ion pressure tensor is approximated by including the full compressional and collisional parts of the tensor and assuming the helical magnetic field to dominate the total **B**-field:

$$\begin{aligned}
\Pi^i &= -\mu_0 (\nabla \cdot \mathbf{v}_i)(\mathrm{I} - 2\hat{e}\hat{e}) - \mu_i \left\{\nabla \left(\frac{v_e}{n}\hat{e}\right) + \left[\nabla \left(\frac{v_e}{n}\hat{e}\right)\right]^T\right\} \\
&- \frac{\mu_i}{4} \left\{\nabla \left(\frac{v_r \hat{r} + v_\tau \hat{\tau}}{n}\right) + \left[\nabla \left(\frac{v_r \hat{r} + v_\tau \hat{\tau}}{n}\right)\right]^T - (\nabla \cdot \mathbf{v}_i)(\mathrm{I} - \hat{e}\hat{e})\right\},
\end{aligned}$$

Only parallel collisional component of the electron pressure tensor is included in our model:

$$\Pi^e = -\nu_e \left\{\nabla \left(j_e \hat{e}\right) + \left[\nabla \left(j_e \hat{e}\right)\right]^T\right\}.$$

C.2 SEL implementation of the extended MHD equations in helical coordinates.

Below, we expand out each of the normalized two-fluid extended MHD equations (Eqs. (C.1.7-C.1.12)) evolved by the SEL code in primary variables, helical coordinates, and in the flux-source form required by the code.

There are following $M = 9$ equations written in the flux-source form solved by SEL:

Density equation:

$$r\frac{\partial n}{\partial t} + \frac{\partial (rv_r)}{\partial r} + \frac{\partial}{\partial \tau}\left(\frac{v_\tau}{g}\right) = 0 \tag{C.2.1}$$

r-momentum equation:

$$\begin{aligned} r^2 g\frac{\partial v_r}{\partial t} &+ \frac{\partial}{\partial r}\left[r^2 g\frac{v_r^2}{n}\right] + \frac{\partial}{\partial \tau}\left[r\frac{v_r v_\tau}{n}\right] + r^2 g\hat{r}\cdot\left[\nabla\cdot\left(\Pi^i + \Pi^e\right)\right] \\ &= -r^2 g^3 B_e\frac{\partial B_e}{\partial r} - (rg)^2\frac{(v_e - nj_e)}{d_i}\frac{\partial \psi}{\partial r} - r^2 g\frac{\partial (p_i + p_e)}{\partial r} \\ &+ rg^3\left[\frac{v_r^2}{n} + (v_\tau - \epsilon r v_e)\left(\frac{v_\tau}{n} - \epsilon r\frac{v_e}{n}\right)\right] \end{aligned} \tag{C.2.2}$$

τ-momentum equation:

$$\begin{aligned} r^2 g\frac{\partial v_\tau}{\partial t} &+ \frac{\partial}{\partial r}\left[r^2 g\frac{v_r v_\tau}{n}\right] + \frac{\partial}{\partial \tau}\left[r\frac{v_\tau^2}{n} + r\left(p_i + p_e + \frac{(gB_e)^2}{2}\right)\right] \\ &+ r^2 g\hat{\tau}\cdot\left[\nabla\cdot\left(\Pi^i + \Pi^e\right)\right] = -rg\frac{\partial \psi}{\partial \tau}\frac{(v_e - nj_e)}{d_i} + 2\epsilon r^2 g^3 v_r\frac{v_e}{n} \end{aligned} \tag{C.2.3}$$

e-momentum equation:

$$\begin{aligned} \frac{r}{g}\frac{\partial v_e}{\partial t} &+ \frac{\partial}{\partial r}\left[\frac{r}{g}\frac{v_r v_e}{n} + B_e\frac{\partial \psi}{\partial \tau}\right] + \frac{\partial}{\partial \tau}\left[\frac{1}{g^2}\frac{v_\tau v_e}{n} - B_e\frac{\partial \psi}{\partial r}\right] \\ &+ \frac{r}{g}\hat{e}\cdot\left[\nabla\cdot\left(\Pi^i + \Pi^e\right)\right] = 0 \end{aligned} \tag{C.2.4}$$

e-component of Ohm's Law:

$$\begin{aligned} r\frac{\partial \psi}{\partial t} &+ \frac{r}{g}\frac{d_i}{n}\hat{e}\cdot[\nabla\cdot\Pi^e] = \frac{1}{n}\frac{\partial \psi}{\partial r}\left(d_i\frac{\partial B_e}{\partial \tau} - rv_r\right) - \frac{1}{n}\frac{\partial \psi}{\partial \tau}\left(d_i\frac{\partial B_e}{\partial r} + \frac{1}{g}v_\tau\right) \\ &+ \frac{r}{g}\left[\eta_\perp\frac{(v_e - nj_e)}{d_i} + (\eta_\parallel - \eta_\perp)J_\parallel b_e\right], \end{aligned} \tag{C.2.5}$$

$-rg\hat{e}\cdot\{\nabla\times[\text{Ohm's Law}]+2\epsilon g^2[\text{Ohm's Law}]\}$:

$$\begin{aligned} rg^2\frac{\partial(B_e-2\epsilon g^2\psi)}{\partial t} &- rg\hat{e}\cdot\left\{\nabla\times\left[\frac{d_i}{n}\nabla\cdot\Pi^e\right]+2\epsilon g^2\left[\frac{d_i}{n}\nabla\cdot\Pi^e\right]\right\} \\ &+ \frac{\partial}{\partial r}\left\{g^2\frac{B_e}{n}\left(rv_r-d_i\frac{\partial B_e}{\partial\tau}\right)+gj_e\frac{\partial\psi}{\partial\tau}\right. \\ &- \left. rg\left[\eta_\perp g\frac{\partial B_e}{\partial r}-(\eta_\parallel-\eta_\perp)J_\parallel b_\tau\right]\right\} \\ &+ \frac{\partial}{\partial\tau}\left\{g\frac{B_e}{n}\left(v_\tau+d_ig\frac{\partial B_e}{\partial r}\right)-gj_e\frac{\partial\psi}{\partial r}\right. \\ &- \left.\left[\eta_\perp\frac{1}{r}\frac{\partial B_e}{\partial\tau}+(\eta_\parallel-\eta_\perp)J_\parallel b_r\right]\right\} \\ &= \frac{d_i}{n^2}\left(\frac{\partial p_e}{\partial r}\frac{\partial n}{\partial\tau}-\frac{\partial p_e}{\partial\tau}\frac{\partial n}{\partial r}\right) \end{aligned} \tag{C.2.6}$$

e-component of Ampere's Law:

$$\frac{\partial}{\partial r}\left[d_irg^2\frac{\partial\psi}{\partial r}\right]+\frac{\partial}{\partial\tau}\left[\frac{d_i}{r}\frac{\partial\psi}{\partial\tau}\right]=2d_i\epsilon rg^4B_e+rg(v_e-nj_e) \tag{C.2.7}$$

ion pressure equation:

$$\begin{aligned} \frac{3}{2}r\frac{\partial p_i}{\partial t} &+ \frac{\partial}{\partial r}\left\{\frac{3}{2}rv_r\frac{p_i}{n}-(\kappa_\parallel^i-\kappa_\perp)b_r\left[rb_r\frac{\partial}{\partial r}\left(\frac{p_i}{n}\right)+\frac{b_\tau}{g}\frac{\partial}{\partial\tau}\left(\frac{p_i}{n}\right)\right]\right. \\ &- \left.\kappa_\wedge^i\frac{b_e}{g}\frac{\partial}{\partial\tau}\left(\frac{p_i}{n}\right)-\kappa_\perp^ir\frac{\partial}{\partial r}\left(\frac{p_i}{n}\right)\right\} \\ &+ \frac{\partial}{\partial\tau}\left\{\frac{3}{2}\frac{v_\tau}{g}\frac{p_i}{n}-(\kappa_\parallel^i-\kappa_\perp)\frac{b_\tau}{g}\left[b_r\frac{\partial}{\partial r}\left(\frac{p_i}{n}\right)+\frac{b_\tau}{rg}\frac{\partial}{\partial\tau}\left(\frac{p_i}{n}\right)\right]\right. \\ &+ \left.\kappa_\wedge^i\frac{b_e}{g}\frac{\partial}{\partial r}\left(\frac{p_i}{n}\right)-\kappa_\perp^i\frac{1}{rg^2}\frac{\partial}{\partial\tau}\left(\frac{p_i}{n}\right)\right\} \\ &= -p_i\left[\frac{\partial}{\partial r}\left(\frac{rv_r}{n}\right)+\frac{1}{g}\frac{\partial}{\partial\tau}\left(\frac{v_\tau}{n}\right)\right]-r\Pi^i:\nabla\mathbf{v}_i+rq_{ie}(p_e-p_i) \end{aligned} \tag{C.2.8}$$

and electron pressure equation:

$$\begin{aligned}
\frac{3}{2}r\frac{\partial p_e}{\partial t} &+ \frac{\partial}{\partial r}\left\{\frac{3}{2}r\frac{p_e}{n}\left(v_r - \frac{d_i}{r}\frac{\partial B_e}{\partial \tau}\right) - (\kappa_\parallel^e - \kappa_\perp^e)b_r\left[b_r r\frac{\partial}{\partial r}\left(\frac{p_e}{n}\right) + b_\tau\frac{1}{g}\frac{\partial}{\partial \tau}\left(\frac{p_e}{n}\right)\right]\right. \\
&+ \left.\kappa_\wedge^e\frac{b_e}{g}\frac{\partial}{\partial \tau}\left(\frac{p_e}{n}\right) - \kappa_\perp^e r\frac{\partial}{\partial r}\left(\frac{p_e}{n}\right)\right\} \\
&+ \frac{\partial}{\partial \tau}\left\{\frac{3}{2}\frac{1}{g}\frac{p_e}{n}\left(v_\tau + d_i g\frac{\partial B_e}{\partial r}\right) - (\kappa_\parallel^e - \kappa_\perp^e)\frac{b_\tau}{g}\left[b_r\frac{\partial}{\partial r}\left(\frac{p_e}{n}\right) + b_\tau\frac{1}{rg}\frac{\partial}{\partial \tau}\left(\frac{p_e}{n}\right)\right]\right. \\
&- \left.\kappa_\wedge^e\frac{b_e}{g}\frac{\partial}{\partial r}\left(\frac{p_e}{n}\right) - \kappa_\perp^e\frac{1}{rg^2}\frac{\partial}{\partial \tau}\left(\frac{p_e}{n}\right)\right\} \\
&= -p_e\left[\frac{\partial}{\partial r}\left(\frac{rv_r}{n}\right) + \frac{1}{g}\frac{\partial}{\partial \tau}\left(\frac{v_\tau}{n}\right) + \frac{d_i}{n^2}\left(\frac{\partial B_e}{\partial \tau}\frac{\partial n}{\partial r} - \frac{\partial B_e}{\partial r}\frac{\partial n}{\partial \tau}\right)\right] - r\Pi^e : \nabla\mathbf{v}_e \\
&+ r\left\{\eta_\perp\left[\frac{1}{r^2}\left(\frac{\partial B_e}{\partial \tau}\right)^2 + g^2\left(\frac{\partial B_e}{\partial r}\right)^2 + \frac{1}{d_i^2}(nj_e - v_e)^2\right] + (\eta_\parallel - \eta_\perp)J_\parallel^2\right\} \\
&+ rq_{ie}(p_i - p_e). \qquad \text{(C.2.9)}
\end{aligned}$$

Components of the ion pressure tensor are as follows:

$$\begin{aligned}
\Pi_{rr}^i &= -\mu_0\nabla\cdot\mathbf{v}_i - \frac{\mu_i}{4}\left[\frac{\partial}{\partial r}\left(\frac{v_r}{n}\right) - \frac{1}{rg}\frac{\partial}{\partial \tau}\left(\frac{v_\tau}{n}\right) - \frac{1}{r}\frac{v_r}{n}\right], \\
\Pi_{r\tau}^i &= \Pi_{\tau r}^i = -\frac{\mu_i}{4}\left[\frac{\partial}{\partial r}\left(\frac{v_\tau}{n}\right) + \frac{1}{rg}\frac{\partial}{\partial \tau}\left(\frac{v_r}{n}\right) - \frac{g^2}{r}\frac{v_\tau}{n}\right], \\
\Pi_{re}^i &= \Pi_{er}^i = -\mu_i\frac{1}{g}\frac{\partial}{\partial r}\left(g\frac{v_e}{n}\right) - \frac{\mu_i}{2}\epsilon g^2\frac{v_\tau}{n}, \\
\Pi_{\tau\tau}^i &= -\mu_0\nabla\cdot\mathbf{v}_i - \frac{\mu_i}{4}\left[-\frac{\partial}{\partial r}\left(\frac{v_r}{n}\right) + \frac{1}{rg}\frac{\partial}{\partial \tau}\left(\frac{v_\tau}{n}\right) + \frac{g^2}{r}(1-\epsilon^2r^2)\frac{v_r}{n}\right], \\
\Pi_{\tau e}^i &= \Pi_{e\tau}^i = -\mu_i\frac{1}{rg}\frac{\partial}{\partial \tau}\left(\frac{v_e}{n}\right) + \frac{\mu_i}{2}\epsilon g^2\frac{v_r}{n} \\
\Pi_{ee}^i &= \mu_0\nabla\cdot\mathbf{v}_i - \frac{\mu_i}{2}r\epsilon^2 g^2\frac{v_r}{n}
\end{aligned}$$

and its divergence can be expressed as

$$
\begin{aligned}
\nabla\cdot\Pi^i &= \hat{r}\frac{1}{r^2 g}\left\{\frac{\partial}{\partial r}\left[-\mu_0 r^2 g(\nabla\cdot\mathbf{v}_i)-\frac{\mu_i}{4}\left(r^2 g\frac{\partial}{\partial r}\left(\frac{v_r}{n}\right)-r\frac{\partial}{\partial\tau}\left(\frac{v_\tau}{n}\right)-rg\frac{v_r}{n}\right)\right]\right.\\
&+ \frac{\partial}{\partial\tau}\left[-\frac{\mu_i}{4}\left(r\frac{\partial}{\partial r}\left(\frac{v_\tau}{n}\right)+\frac{1}{g}\frac{\partial}{\partial\tau}\left(\frac{v_r}{n}\right)-g^2\frac{v_\tau}{n}\right)\right]\\
&+ \left.\mu_0 r g^3(2.-\epsilon^2 r^2)(\nabla\cdot\mathbf{v}_i)-\mu_i 2\epsilon r g^2\frac{\partial}{\partial\tau}\left(\frac{v_e}{n}\right)+\frac{\mu_i}{2}\epsilon^2 r^2 g^3\frac{v_r}{n}\right\}\\
&+ \hat{\tau}\frac{1}{r^2 g}\left\{\frac{\partial}{\partial r}\left[-\frac{\mu_i}{4}\left(r^2 g\frac{\partial}{\partial r}\left(\frac{v_\tau}{n}\right)+r\frac{\partial}{\partial\tau}\left(\frac{v_r}{n}\right)-rg^3\frac{v_\tau}{n}\right)\right]\right.\\
&+ \frac{\partial}{\partial\tau}\left[-\mu_0 r(\nabla\cdot\mathbf{v}_i)-\frac{\mu_i}{4}\left(-r\frac{\partial}{\partial r}\left(\frac{v_r}{n}\right)+\frac{1}{g}\frac{\partial}{\partial\tau}\left(\frac{v_\tau}{n}\right)+g^2(1-\epsilon^2 r^2)\frac{v_r}{n}\right)\right]\\
&+ \left.\mu_i 2\epsilon r^2 g^2\frac{\partial}{\partial r}\left(g\frac{v_e}{n}\right)+\mu_i\epsilon^2 r^2 g^5\frac{v_\tau}{n}\right\}\\
&+ \hat{e}\frac{g}{r}\left\{\frac{\partial}{\partial r}\left[-\mu_i\frac{r}{g^2}\frac{\partial}{\partial r}\left(g\frac{v_e}{n}\right)-\frac{\mu_i}{2}\epsilon r g\frac{v_\tau}{n}\right]+\frac{\partial}{\partial\tau}\left[-\mu_i\frac{1}{rg^3}\frac{\partial}{\partial\tau}\left(\frac{v_e}{n}\right)+\frac{\mu_i}{2}\epsilon\frac{v_r}{n}\right]\right\}.
\end{aligned}
$$

Accordingly, ion viscous heating can be written as:

$$
\begin{aligned}
\Pi^i:\nabla\mathbf{v}_i &= -\mu_0(\nabla\cdot\mathbf{v}_i)^2-\frac{\mu_i}{4}\left[\frac{\partial}{\partial r}\left(\frac{v_\tau}{n}\right)+\frac{1}{rg}\frac{\partial}{\partial\tau}\left(\frac{v_r}{n}\right)-\frac{g^2}{r}\frac{v_\tau}{n}\right]^2\\
&- \frac{\mu_i}{4}\left[\frac{\partial}{\partial r}\left(\frac{v_r}{n}\right)-\frac{1}{rg}\frac{\partial}{\partial\tau}\left(\frac{v_\tau}{n}\right)-\frac{g^2}{r}\frac{v_r}{n}\right]^2+\frac{\mu_i}{4}r\epsilon^2 g^2\frac{v_r}{n}\left(\nabla\cdot\mathbf{v}_i+r\epsilon^2 g^2\frac{v_r}{n}\right)\\
&- \mu_i\left[\left(\frac{\partial}{\partial r}\left(\frac{v_e}{n}\right)+\epsilon g^2\left(\frac{v_\tau}{n}-\epsilon r\frac{v_e}{n}\right)\right)^2+\left(\frac{1}{rg}\frac{\partial}{\partial\tau}\left(\frac{v_e}{n}\right)-\epsilon g^2\frac{v_r}{n}\right)^2\right.\\
&+ \left.\frac{\epsilon g^2}{2}\left(\frac{v_\tau}{n}\frac{\partial}{\partial r}\left(\frac{v_e}{n}\right)-\frac{1}{rg}\frac{v_r}{n}\frac{\partial}{\partial\tau}\left(\frac{v_e}{n}\right)-r\epsilon^2 g^2\frac{v_\tau}{n}\frac{v_e}{n}\right)\right].
\end{aligned}
$$

Components of the electron pressure tensor, its divergence, and electron viscous heating are given by:

$$\begin{aligned}
\Pi^e_{re} &= \Pi^e_{er} = -\nu_e \frac{1}{g}\frac{\partial (g j_e)}{\partial r}, \quad \Pi^e_{\tau e} = \Pi^e_{e\tau} = -\nu_e \frac{1}{rg}\frac{\partial j_e}{\partial \tau} \\
\nabla \cdot \Pi^e &= \hat{r}\left[-\nu_e \frac{2\epsilon g}{r}\frac{\partial j_e}{\partial \tau}\right] + \hat{\tau}\left[\nu_e 2\epsilon g \frac{\partial (g j_e)}{\partial r}\right] \\
&+ \hat{e}\frac{g}{r}\left[-\frac{\partial}{\partial r}\left(\frac{r}{g^2}\nu_e \frac{\partial (g j_e)}{\partial r}\right) - \frac{\partial}{\partial \tau}\left(\nu_e \frac{1}{rg^3}\frac{\partial j_e}{\partial \tau}\right)\right] \\
-rg\hat{e} &\cdot \left[\nabla \times \left(\frac{d_i}{n}\nabla \cdot \Pi^e\right) + 2\epsilon g^2 \left(\frac{d_i}{n}\nabla \cdot \Pi^e\right)\right] = \\
&- \frac{\partial}{\partial r}\left[\frac{d_i}{n}\nu_e 2\epsilon r g^3 \left(\frac{\partial j_e}{\partial r} - r\epsilon^2 g^2 j_e\right)\right] - \frac{\partial}{\partial \tau}\left[\frac{d_i}{n}\nu_e \frac{2\epsilon g}{r}\frac{\partial j_e}{\partial \tau}\right] \\
\Pi^e : \nabla \mathbf{v}_e &= -\nu_e \left(\frac{\partial j_e}{\partial r} - r\epsilon^2 g^2 j_e\right)\left[\frac{\partial j_e}{\partial r} - r\epsilon^2 g^2 j_e + 2\epsilon g^2 \left(\frac{v_\tau}{n} + g\frac{d_i}{n}\frac{\partial B_e}{\partial r}\right)\right] \\
&- \nu_e \frac{1}{r^2 g^2}\frac{\partial j_e}{\partial \tau}\left[\frac{\partial j_e}{\partial \tau} - 2\epsilon g^3 \left(r\frac{v_r}{n} - \frac{d_i}{n}\frac{\partial B_e}{\partial \tau}\right)\right].
\end{aligned}$$

Finally, for completeness, we specify parallel component of current $J_\parallel$ as:

$$J_\parallel = \frac{b_r}{r}\frac{\partial B_e}{\partial \tau} - g b_\tau \frac{\partial B_e}{\partial r} + b_e \frac{v_i - n j_e}{d_i}.$$

C.3 Simulating internal kink mode with two-fluid extended MHD.

We have conducted two-fluid extended MHD simulations of the internal kink from two distinctly different initial conditions:

1. Magnetic field configuration given by Eq. (4.3.11) and Eq. (4.3.12), which is *a priori* unstable to ideal kink, with all current carried by electrons and with no regard to resistive equilibrium conditions outside of enforcing radial pressure balance;

2. Configuration of B-field, derived below, which is initially stable to kinking and takes account of anisotropic resistivity and two-fluid effects to initialize the system with only $\hat{z}$-directed electric fields.

The first of the two was conducted to compare the results of a compressible extended MHD simulation with anisotropic temperature-dependent coefficients and non-uniform density to previously described analogous simulations with incompressible resistive and Hall MHD models. The second, to simulate self-generation of a kink-unstable configuration and following instability dynamics from an initially stable configuration. Below, we describe each set of initial and boundary conditions.

C.3.1 Initial and boundary conditions for simulating ideally unstable internal kink.

In a system with finite compressibility, the most important initial condition (IC) to be satisfied is the pressure balance. In the absence of Alfvénic flows, that is accomplished by balancing magnetic tension and pressure gradient forces. For an axisymmetric IC, the following equation has to be satisfied:

$$-g^2 B_{e0}\frac{\partial B_{e0}}{\partial r} - g^2 J_e \frac{\partial \psi_0}{\partial r} = \frac{\partial p_0}{\partial r}, \tag{C.3.1}$$

where $p_0 = p_{i0}+p_{e0}$ is the total plasma pressure. With the magnetic field configuration given by Eq. (4.3.11) and Eq. (4.3.12), radial profile of total pressure with peak axial pressure of β_0 is:

$$\begin{aligned} p_0(r) = \beta_0 \;&-\; r^2\left[\frac{3}{20}\epsilon^4 r^8 + \frac{5}{16}\epsilon^2 r^6(1-\epsilon^2 r_s^2) + \frac{1}{6}r^4\left((1-\epsilon^2 r_s^2)^2 - 2\epsilon^2(2+r_s^2)\right)\right. \\ &-\; \left.\frac{3}{8}r^2(1-\epsilon^2 r_s^2)(2+r_s^2) + \frac{1}{4}(2+r_s^2)^2\right]. \end{aligned}$$

We assume a uniform electron-to-total pressure ratio $\beta_e \equiv p_{e0}/p_0$, so that $p_{e0} = \beta_e p_0$ and $p_{i0} = (1-\beta_e)p_0$. In order to be able to assign an initial value for electron temperature dependent plasma resistivity at the singular surface, initial electron temperature profile is taken as $T_{e0}(r) = 1+T_c(r_s^2-r^2)$, where T_c is a positive constant determining the temperature drop between the center and edge of the simulation domain. Then, plasma density profile is calculated as:

$$n_0(r) = \beta_e \frac{p_0(r)}{T_{e0}(r)}.$$

For given values of r_s and β_0, we have chosen T_c to be such that $|\partial n_0/\partial r|_{r=r_w} = 0$. We note that this condition results in non-zero gradient of plasma pressure (and therefore temperature) at the outer wall radius $r = r_w$. All axisymmetric ion flows are zeroed out and initial current is carried by electrons.

A small ($\delta v_i \approx 10^{-3}$) $m = 1$ incompressible perturbation to the poloidal ion velocity field is added to this axisymmetric IC to trigger the $m = 1$ mode. We specifically choose the perturbation to be incompressible, as otherwise we observe a fast compressional mode become excited, resulting in very high frequency slowly decaying oscillations in the solution, which are in no way related to the dynamics of interest. Stream function ϕ corresponding to such an incompressible perturbation is taken to be:

$$\phi = \delta v_i \frac{r^2}{2} \exp\left[-\left(\frac{\alpha r}{r_s}\right)^{2n}\right] \sin(\tau),$$

where $\alpha \approx 1. - 1.5$ and $n \approx 2 - 4$.

The desired boundary conditions (BC) for simulations of a single ideally unstable internal kink event with mixing radius $r_M < r_w$ are those that would avoid creating thin boundary layers at $r = r_w$, while providing a buffer zone $r_M < r < r_w$ in between the reconnecting plasma core and the boundary of the domain. Since reconnection

time of a single ideally unstable kink is much smaller than the resistive diffusion time of the plasma column, here, we assume the influence of BC on the evolution of a single internal kink event to be negligible.

In order to enable comparisons with previously described incompressible simulations, electric field at the wall $\mathbf{E}_b$ is again taken to be purely axial by enforcing the following BC:

$$\begin{aligned} \mathbf{E}_b \cdot \hat{z} &= E_b = g(E_e + \epsilon r E_\tau) \\ \mathbf{E}_b \cdot \hat{\theta} &= 0 = g(E_\tau - \epsilon r E_e). \end{aligned}$$

These are combined to give

$$\begin{aligned} gE_b &= E_e \Rightarrow \frac{\partial \psi}{\partial t} = E_b \\ g\epsilon r E_b &= E_\tau \Rightarrow \\ \Rightarrow \epsilon r E_b &= \frac{d_i}{n}\left[\frac{1}{rg^2}\frac{\partial p_e}{\partial \tau} + \frac{1}{r}B_e\frac{\partial B_e}{\partial \tau} + \nu_e 2\epsilon g\left(\frac{\partial j_e}{\partial r} - r\epsilon^2 g^2 j_e\right)\right] \\ &- B_e\frac{v_r}{n} + \eta_\perp \frac{\partial B_e}{\partial r} - \frac{1}{g}(\eta_\parallel - \eta_\perp)J_\parallel b_\tau, \end{aligned} \tag{C.3.2}$$

and evaluated at $r = r_w$. The following BC on plasma density, pressures and flow components at $r = r_w$ are also enforced:

$$\begin{aligned} \frac{\partial n}{\partial r} &= 0, \quad \frac{\partial}{\partial t}\left[\frac{\partial}{\partial r}\left(\frac{p_i}{n}\right)\right] = 0, \quad \frac{\partial}{\partial t}\left[\frac{\partial}{\partial r}\left(\frac{p_e}{n}\right)\right] = 0 \\ \frac{v_r}{n} &= 0, \quad \frac{\partial}{\partial r}\left(\frac{v_\tau}{n}\right) = 0, \quad \frac{\partial}{\partial r}\left(\frac{v_e}{n}\right) = 0. \end{aligned}$$

Another boundary condition on electron flow (or current) along the boundary is necessary for the system's time evolution to be uniquely determined, but no such physically meaningful BC is presently known to the authors. For these simulations, we have set $[\frac{\partial j_e}{\partial t}]|_{r_w} = 0$.

C.3.2 Initial and boundary conditions for simulating internal kink dynamics resulting from a self-generated kink-unstable equilibria.

Unlike initial and boundary conditions used to simulate a single ideally unstable internal kink event, much greater care is taken in formulating IC and BC for producing boundary-driven self-generated internal reconnection events on the longer resistive time-scale.

We first construct an axisymmetric configuration of helical B-fields such that tangential electric field generated by the finite anisotropic conductivity of the plasma at the domain boundary has only an axial $\hat{z}$-component. We recall that $\eta_\perp = 1.96\eta_\parallel \approx 2\eta_\parallel$ and use this approximation in the derivation below.[1] In order to enforce $\mathbf{E}\cdot\hat{\theta} = 0$, a solution to the following equation has to be found:

$$\eta_\perp \mathbf{J}\cdot\hat{\theta} + (\eta_\parallel - \eta_\perp) J_\parallel \hat{b}\cdot\hat{\theta} \approx \eta_\parallel (2\mathbf{J}\cdot\hat{\theta} - J_\parallel \hat{b}\cdot\hat{\theta}) = 0. \tag{C.3.3}$$

It is easy to see that one such solution is given by $\psi = 0$ and $B_e = 1/(\epsilon g)$, so that $\mathbf{B} = \hat{e}(1/\epsilon) = (g/\epsilon)\left[-\epsilon r\hat{\theta} + \hat{z}\right]$ and $\mathbf{J} = -g^2\left[\epsilon r\hat{\tau} + 2\hat{e}\right] = g^3\left[\epsilon r\hat{\theta} - (2+\epsilon^2 r^2)\hat{z}\right]$. In a periodic cylinder with aspect ratio of $1/\epsilon$, such configuration corresponds to a uniform q-profile of $q(r) = 1$. However, since it is an axisymmetric configuration where all quantities are purely r-dependent, a configuration with $\alpha\epsilon$ substituted for ϵ, where α is an arbitrary constant, is also a solution to Eq. (C.3.3) and has $q(r) = 1/\alpha$. Thus, we derive a family of B-field configurations with uniform q-profiles and satisfying

[1] The small deviation of the resulting E-field from being purely axial is self-corrected in the first few time-steps of the simulation by slightly adjusting the magnetic fields and non-resistive terms of the Ohm's Law at the domain boundary.

Eq. (C.3.3), given by:

$$\psi_0(r) = \frac{1-\alpha}{\alpha}\frac{\sqrt{1+\alpha^2\epsilon^2 r^2}-1}{\alpha^2\epsilon^2} \tag{C.3.4}$$

$$B_{e0}(r) = \frac{1+\alpha\epsilon^2 r^2}{\alpha\epsilon\sqrt{1+\alpha^2\epsilon^2 r^2}}. \tag{C.3.5}$$

Since we are interested in modeling the core of a tokamak and would like the initial condition to be stable to ideal MHD modes, α is generally taken to be slightly below unity to provide $q > 1$ at the boundary of the domain, while suppressing any pressure-driven modes observed to arise when $q \approx 1$.

Using Eqs. (C.3.4-C.3.5) and assuming the system to be in pressure balance, radial profile of total pressure is derived from Eq. (C.3.1) to be:

$$p_0(r) = \beta_0 - \frac{1}{2\alpha^2\epsilon^2}\ln(1+\alpha^2\epsilon^2 r^2), \tag{C.3.6}$$

where β_0 is again the plasma pressure at $r = 0$, $p_{e0}(r) = \beta_e p_0(r)$, and $p_{i0}(r) = (1-\beta_e)p_0(r)$. As in the previous section, initial electron temperature profile is taken as $T_{e0}(r) = 1+T_c(r_s^2-r^2)$, plasma density profile is calculated as $n_0(r) = \beta_e[p_0(r)/T_{e0}(r)]$, and T_c is chosen such that $|\partial n_0/\partial r|_{r=r_w} = 0$.

We now observe that, as follows from Eq. (C.1.9), perpendicular electric field is induced in a two-fluid system with non-uniform pressures unless each species is allowed to drift perpendicular to the magnetic field with its own diamagnetic drift velocity. As we prefer to avoid imposing *a priory* charge separation, for the case of $p_{e0}/p_0 = \beta_e = const$, this results in perpendicular plasma current $\mathbf{J}_\perp = (n\mathbf{v}_{i\perp} - n\mathbf{v}_{e\perp})/d_i$ being divided between the ion and electron flows according to $\mathbf{v}_{e\perp}/\mathbf{v}_{i\perp} = \beta_e/(\beta_e - 1)$. However, we also note that non-zero ion flows may produce non-zero contribution of the ion flow stress tensor to the radial projection of the momentum equation Eq. (C.1.8), which has been assumed to be zero in enforcing Eq. (C.3.1). Therefore,

the condition $d_i \mathbf{J}_\perp = n\mathbf{v}_{i\perp}/(1-\beta_e)$ is supplemented with $\hat{r}\cdot\nabla\left[n\mathbf{v}_i\mathbf{v}_i\right] = 0$ to determine the initial ion flow profile. Due to assumed axisymmetry of the initial condition and near-incompressibility of the plasma with large axial B-field, we take radial component of the flow to be zero, $v_{r0} = 0$, resulting in the following profiles of the other two ion flow components:

$$v_{\tau 0} = -d_i(1-\beta_e)\frac{\epsilon r g}{\sqrt{1+\alpha^2\epsilon^2 r^2}} \tag{C.3.7}$$

$$v_{e0} = -d_i(1-\beta_e)\frac{g}{\sqrt{1+\alpha^2\epsilon^2 r^2}}. \tag{C.3.8}$$

This completely determines the axisymmetric initial conditions. An $m = 1$ incompressible perturbation of the ion flow field, as described in the previous section, can also be added to introduce small degree of asymmetry to the simulation at $t = 0$.

Boundary conditions imposed for these long time integration simulations are also modified from those used in the previous section. Since we continue to apply axial Ohmic drive at the boundary of the domain, we retain the electric field BC expressed in Eqs. (C.3.2). However, we modify the radial inflow/outflow BC by allowing for plasma to drift in and out of the domain and fixing the normal gradient of radial ion velocity to zero. We also modify the pressure BC by assuming existence of an infinite heat bath at the initial temperature at the boundary of the domain. Finally, we change the boundary condition on helical electron velocity to Neumann BC. Perfect slip BC are retained on tangential components of ion velocity and Neumann BC is again assumed for plasma density. These are summarized as follows:

$$\begin{aligned}
\frac{\partial n}{\partial r} &= 0, \quad \frac{\partial}{\partial t}\left(\frac{p_i}{n}\right) = 0, \quad \frac{\partial}{\partial t}\left(\frac{p_e}{n}\right) = 0, \\
\frac{\partial j_e}{\partial r} &= 0, \quad \frac{\partial}{\partial r}\left(\frac{v_r}{n}\right) = 0, \quad \frac{\partial}{\partial r}\left(\frac{v_\tau}{n}\right) = 0, \quad \frac{\partial}{\partial r}\left(\frac{v_e}{n}\right) = 0.
\end{aligned}$$

BC outlined above appear to allow for time-integration over multiple resistive times

without formation of particularly problematic boundary layers and are generally consistent with conditions in the plasma core.

Bibliography

[1] M. Abramowitz and I.A. Stegun, *Handbook of Mathematical Functions with Formulas, Graphs, and Mathematical Tables*, p. 793, (Dover, New York, 1964).

[2] R.W. Anderson, N.S. Elliott, R.B. Pember, J. Comput. Phys. **199**, 598 (2004).

[3] W.R. Ashby, in *Principles of Self-organization* edited by H. von Foerster and G.W. Zopf, Jr (Pergamon Press 1962).

[4] A.Y. Aydemir, J.C. Wiley, and D.W. Ross, Phys. Fluids B **1**, 774 (1989).

[5] A.Y. Aydemir, Phys. Fluids B **2**, 2135 (1990).

[6] A.Y. Aydemir, Phys. Fluids B **4**, 3469 (1992).

[7] A.Y. Aydemir, Phys. Rev. Lett. **78**, 4406 (1997).

[8] R.E. Bank, *et. al.*, IEEE Transactions on Electron Devices **32**, 1992 (1985).

[9] M. Berger and J. Oliger, J. Comput. Phys. **53**, 484 (1984).

[10] M.J. Berger and P. Collela, J. Comput. Phys. **82**, 64 (1989).

[11] N. Bessho, A. Bhattacharjee, Phys. Plasmas **14**, 56503 (2007).

[12] A. Bhattacharjee, K. Germaschewski, and C.S. Ng, Phys. Plasmas **12**, 42305 (2005).

[13] J. Birn, J.F. Drake, M.A. Shay, B.N. Rogers, R.E. Denton, M. Hesse, M. Kuznetsova, Z.W. Ma, A. Bhattacharjee, A. Otto, P.L. Pritchett, J. Geophys. Res. **106**, 3715 (2001).

[14] D. Biskamp, Phys. Rev. Lett. **46**, 1522 (1981).

[15] D. Biskamp, Phys. Fluids **29**, 1520 (1986).

[16] D. Biskamp, Phys. Fluids B **3**, 3353 (1991).

[17] D. Biskamp and J.F. Drake, Phys. Rec. Lett. **73**, 971 (1994).

[18] D. Biskamp and T. Sato, Phys. Plasmas **4**, 1326 (1997).

[19] D. Biskamp, D. Schwarz and J.F. Drake, Phys. Plasmas **4**, 1002 (1997).

[20] E.G. Blackman, H. Ji, Mon. Not. R. Astron. Soc. **369**, 1837 (2006).

[21] D. Bonfiglio, S. Cappello, D.F. Escande, Phys. Rev. Lett. **94**, 145001 (2005).

[22] J.U. Brackbill and H.M. Ruppel, J. Comput. Phys. **65**, 314 (1986).

[23] J.U. Brackbill, J. Comput. Phys. **108**, 38 (1993).

[24] S.I. Braginskii, Reviews of Plasma Physics (Consultants Bureau, New York, 1965), Vol.1, p.205.

[25] J.A. Breslau and S.C. Jardin, Phys. Plasmas **10**, 1291 (2003).

[26] J.A. Breslau, S.C. Jardin, W. Park, Phys. Plasmas **10**, 1665 (2003).

[27] M.R. Brown, Phys. Plasmas **6**, 1717 (1999).

[28] M.N. Bussac, R. Pellat, D. Edery, and J.L. Soule, Phys. Rev. Lett. **35**, 1638 (1975).

[29] E. Cafaro, D. Grasso, F. Pegoraro, F. Porcelli, A. Saluzzi, Phys. Rev. Lett. **80**, 4430 (1998).

[30] S. Cappello, D.F. Escande, Phys. Rev. Lett. **85**, 3838 (2000).

[31] S. Cappello, D. Bonfiglio, D.F. Escande, Phys. Plasmas **13**, 56102 (2006).

[32] P.A. Cassak, M.A. Shay, J.F. Drake, Phys. Rev. Lett. **95**, 235002 (2005).

[33] P.A. Cassak, J.F. Drake, M.A. Shay, B. Eckhardt, Phys. Rev. Lett. **98**, 215001 (2007).

[34] L. Chacon, G. Lapenta, J. Comput. Phys. **212**, 703 (2006).

[35] S. Chapman, P.C. Kendall, Proc. Ry. Soc. London A **271**, 435 (1963).

[36] S.A. Colgate, H. Li, V. Pariev, Phys. Plasmas **8**, 2425 (2001).

[37] B. Coppi, R. Galvão, R. Pellat, M. Rosenbluth, and P. Rutherford, Fiz. Plazmy **2**, 961 (1976).

[38] C.D. Cothran, A. Falk, A. Fefferman, M. Landerman, M.R. Brown, M.J. Schaffer, Phys. Plasmas **10**, 1748 (2003).

[39] C.D. Cothran, M. Landerman, M.R. Brown, W.H. Matthaeus, Geophys. Res. Lett. **32**, 3105 (2005).

[40] I.J.D. Craig, J. Heerikhuisen, P.G. Watson, Phys. Plasmas **10**, 3120 (2003).

[41] N.A. Crocker, G. Fiksel, S.C. Prager, J.S. Sarff, Phys. Rev. Lett. **90**, 035003 (2003).

[42] W. Daughton, J. Scudder, and H. Karimabadi, Phys. Plasmas **13**, 72101 (2006).

[43] W. Daughton, H. Karimabadi, Phys. Plasmas **14**, 72303 (2006).

[44] R.E. Denton, J.F Drake, R.G. Kleva, and D.A. Boyd, Phys. Rev. Lett. **56**, 2477 (1986).

[45] M.A. Dubois, A. Samain, Nucl. Fusion **20**, 1101 (1980).

[46] M.A. Dubois, A.L. Pecquet, C. Reverdin, Nucl. Fusion **23**, 147 (1983).

[47] P.A. Duperrex, A. Pochelon, A.W. Edwards, J.A. Snipes, Nucl. Fusion **32**, 1161 (1992).

[48] J. Egedal, W. Fox, M. Porkolab, A. Fasoli, Phys. Plasmas **12**, 52107 (2005).

[49] F.V. Coroniti, "Magnetosphere," in *Encyclopedia of Physics, 2nd ed.*, edited by R.G. Lerner and G.L. Trigg (VCH Publishers, New York, 1991).

[50] D.A. Falconer, R.L. Moore, J.G. Porter, G.A. Gary, T. Shimizu, Ap. J. **482**, 519 (1997).

[51] J.M. Finn, R. Nebel, C. Bathke, Phys. Fluids B **4**, 1262 (1992).

[52] R. Fitzpatrick, Phys. Plasmas **11**, 937 (2004).

[53] R. Fitzpatrick, Phys. Plasmas **11**, 3961 (2004).

[54] H.U. Frey, T.D. Phan, S.A Fuselier and S.B. Mende, Nature. **426**, 533 (2003).

[55] Keizo Fujimoto, Phys. Plasmas **13**, 72904 (2006).

[56] I. Furno, *et.al.*, Phys. Plasmas. **12**, 55702 (2005).

[57] H.P. Furth, J. Killeen, M.N. Rosenbluth, Phys. Fluids **6**, 459 (1963).

[58] S.P. Gary, Phys. Plasmas **9**, 2437 (2002).

[59] K.W. Gentle, M.E. Austin, P.E. Phillips, Phys. Rev. Lett. **91**, 255001 (2003).

[60] R.D. Gill, A.W. Edwards, D. Pasini, A. Weller, Nucl. Fusion **32**, 723 (1992).

[61] A.H. Glasser and X.Z. Tang, Comp. Phys. Comm. **164**, 237 (2004).

[62] A.H. Glasser, V.S. Lukin, V.D. Liseikin, I.A. Kitaeva, *"Adaptive Grid Generation for Magnetically Confined Plasmas"*, 17th IMACS World Congress on Scientific Computation, Applied Mathematics and Simulation: Conf. Proceedings, (2005).

[63] A.H. Glasser, *Preconditioning and Scalability of Implicit Extended MHD Plasma Simulation by FETI-DP Domain Substructuring*, 2007 International Conference on Numerical Simulations of Plasmas, Austin, TX.

[64] S. von Goeler, W. Stodiek, and N. Sauthoff, Phys. Rev. Lett. **33**, 1201 (1974).

[65] D. Grasso, F. Califano, F. Pegoraro, F. Porcelli, Plasma Phys. Rep. **26**, 512 (2000).

[66] E.G. Harris, Nuovo Cimento **23**, 115 (1962).

[67] R.J. Hastie, Astrophysics and Space Science **256**, 177 (1998).

[68] R.D. Hazeltine, M. Kotschenreuther, and P.J. Morrison, Phys. Fluids **28**, 2466 (1985).

[69] R.D. Hazeltine, J.D. Meiss, and P.J. Morrison, Phys. Fluids **29**, 1633 (1986).

[70] R.D. Henderson, in *High-Order Methods for Computational Physics*, edited by T.J. Barth and H. Deconinck (Springer, New York, 1999).

[71] F. Heylighen, to be published in *Encyclopedia of Library and Information Sciences*, edited by M.J. Bates and M.N. Maack (Taylor and Francis, 2008).

[72] C.W. Hirt, A.A. Amsden, J.L. Cook, J. Comput. Phys. **14**, 227 (1974).

[73] J.D. Huba, Phys. Plasmas **12**, 12322 (2005).

[74] A. Ishizawa and R. Horiuchi, Phys. Rev. Lett. **95**, 45003 (2005).

[75] S.C. Jardin, J.L. Johnson, J.M. Greene, R.C. Grimm J. Comp. Phys. **29**, 101 (1978).

[76] S.C. Jardin and J.A. Breslau, Phys. Plasmas **12**, 56101 (2005).

[77] S.C. Jardin, N. Ferraro, J.A. Breslau, *et. al.*, *Two-fluid Extended-MHD Calculations of Collisionless Reconnection in Magnetized Plasmas with a Strong Guide Field*, 2007 International Sherwood Fusion Theory Conference, Annapolis, MD.

[78] H. Ji, S. Terry, M. Yamada, R, Kulsrud, A. Kuritsyn, and Y. Ren, Phys. Rev. Lett **92**, 115001 (2004).

[79] B.B. Kadomtsev, Fiz. Plazmy **1**, 710 (1975).

[80] B.B. Kadomtsev, in *Plasma Physics and Controlled Nuclear Fusion Research 1976* (International Atomic Energy Agency, Vienna, 1977), Vol 1, p. 555.

[81] H. Karimabadi, W. Daughton, J. Scudder, Geophys. Res. Lett. **34**, L13104 (2007).

[82] G.E. Karniadakis and S.J. Sherwin, *Spectral/hp Element Methods for CFD* (Oxford University Press, New York, 1999).

[83] D.S. Kershaw, M.K. Prasad, M.J. Shaw, and J.L. Milovich, Comput. Methods Appl. Engrg. **158**, 81 (1998).

[84] A. Klawonn and O.D. Widlund, Comm. Pure Appl. Math. **59**, 1523 (2006).

[85] R.G. Kleva, J.F. Drake, and R.E. Denton, Phys. Fluids **30**, 2119 (1987).

[86] D.A. Knoll and L. Chacón, Phys. Plasmas **13**, 32307 (2006).

[87] P. Knupp, J. Comput. Phys. **119**, 142 (1995).

[88] Ya.I. Kolesnichenko, Yu.V. Yakovenko, D. Anderson, M. Lisak, F. Wising, Phys. Rev. Lett. **68**, 3883 (1992).

[89] M. Kubič, I. Ďuran, *Review of plasma parameters of the JET tokamak in various regimes of its operation*, Bachelor Thesis (Czech Technical University, 2007).

[90] R.M. Kulsrud, Earth, Planets Space **53**, 417 (2001).

[91] J.A. Linker, Z. Mikic, R. Lionello, P. Riley, T. Amari, D. Odstrcil, Phys. Plasmas **10**, 1971 (2003).

[92] M.G. Linton and E.R. Priest, Ap. J. **595**, 1259 (2003).

[93] V.D. Liseikin, *A Computational Differential Geometry Approach to Grid Generation* (Springer Verlag, October 2003).

[94] N.F. Loureiro, S.C. Cowley, W.D. Dorland, M.G. Haines, A.A. Schekochihin, Phys. Rev. Lett. **95**, 235003 (2005); N.F. Loureiro, *Studies of Nonlinear Tearing Mode Reconnection*, PhD Dissertation (Imperial College London, 2005).

[95] L.M. Malyshkin, T. Linde, R.M. Kulsrud, Phys. Plasmas **12**, 102902 (2005).

[96] M.E. Mandt, R.E. Denton and J.F. Drake, Geophys. Res. Lett. **21**, 73 (1994).

[97] W.H. Matthaeus, C.D. Cothran, M. Landerman, and M.R. Brown, Geophys. Res. Lett. **32**, 23104 (2005).

[98] S. Migliuolo, Nucl. Fusion **33**, 1721 (1993).

[99] D. Montgomery, L. Phillips, M.L. Theobald, Phys. Rev. A **40**, 1515 (1989).

[100] D. Montgomery, Plasma Phys. Control. Fusion **35**, B105 (1993).

[101] D. Nandy, M. Hahn, R.C. Canfield and D.W. Longcope, Ap. J. **597**, L73 (2003).

[102] National Energy Research Scientific Computing (NERSC) Center. URL: http://www.nersc.gov .

[103] G. Nicolis and I. Prigogine, *Self-organization in Nonequilibrium Systems: From Dissipative Structures to Order through Fluctuations* (John Wiley and Sons, 1977).

[104] *NRL Plasma Formulary, 2000 Revised*, edited by J.D. Huba (Naval Research Laboratory, Washington, 2000).

[105] M. Oieroset, R.P. Lin, T.D. Phan, D.E. Larson, and S.D. Bale, Phys. Rev. Lett. **89**, 195001 (2002).

[106] Y. Ono, M. Katsurai, M. Yamada, AIP Conf. Proc. **311**, 186 (1994).

[107] Y. Ono, M. Inomoto, T. Okazaki, Y. Ueda, Phys. Plasmas **4**, 1953 (1997).

[108] J. O'Rourke, Plasma Phys. Control. Fusion **33**, 289 (1991).

[109] M. Ottaviani and F. Porcelli, Phys. Rev. Lett. **71**, 3802 (1993).

[110] M. Ottaviani and F. Porcelli, Phys. Plasmas. **2**, 4104 (1995).

[111] H.K. Park, *et. al.*, Phys. Rev. Lett. **96**, 195004 (2006).

[112] W. Park, D.A. Monticello, R.B. White, S.C. Jardin, Nucl. Fusion **20**, 1181 (1980).

[113] W. Park, D.A. Monticello, R.B. White, Phys. Fluids **27**, 137 (1984).

[114] W. Park, D.A. Monticello, Nucl. Fusion **30**, 2413 (1990).

[115] E.N. Parker, J. Geophys. Res. **62**, 509 (1957).

[116] H.E. Petschek, in *AAS/NASA Symposium on the Physics of Solar Flares*, edited by W.N. Hess (NASA, Washington DC, 1964), p. 425.

[117] Portable, Extensible Toolkit for Scientific computation (PETSc). URL: http://www.mcs.anl.gov/petsc .

[118] T.D. Phan, *et. al.*, Nature. **439**, 175 (2006).

[119] F. Porcelli, Phys. Fluids **30**, 1734 (1987).

[120] F. Porcelli, Phys. Rev. Lett. **66**, 425 (1991).

[121] F. Porcelli, D. Boucher, and M.N. Rosenbluth, Plasma Phys. Control. Fusion **38**, 2163 (1996).

[122] P.L. Pritchett, Phys. Plasmas **12**, 62301 (2005).

[123] A.J. Redd, B.A. Nelson, T.R. Jarboe, P. Gu, R. Raman, R.J. Smith, K.J. McCollam, Phys. Plasmas **9**, 2006 (2002).

[124] Y. Ren, M. Yamada, S. Gerhardt, H. Ji, R, Kulsrud, and A. Kuritsyn, Phys. Rev. Lett **95**, 055003 (2005).

[125] D.R. Reynolds, R. Samtaney, C.S. Woodward, J. Comput. Phys. **219**, 144 (2006).

[126] B. Rogers and L. Zakharov, Phys. Plasmas **2**, 3420 (1995).

[127] B. Rogers and L. Zakharov, Phys. Plasmas **3**, 2411 (1996).

[128] B.N. Rogers, R.E. Denton, J.F. Drake, M.A. Shay, Phys. Rev. Lett. **87**, 195004 (2001).

[129] M.N. Rosenbluth, R.Y. Dagazian, and P.H. Rutherford, Phys. Fluids **16**, 1894 (1973).

[130] T. Sato and the Complexity Simulation Group, Phys. Plasmas **3**, 2135 (1996).

[131] I. Semenov, S. Mirnov, D. Darrow, L. Roquemore, E.D. Fredrickson, J. Menard, D. Stutman, A. Belov, Phys. Plasmas **10**, 664 (2003).

[132] V.D. Shafranov, Zh. Tekh. Fiz. **40**, 241 (1970) [Sov. Phys. Tech. Phys. **15**, 175 (1970)].

[133] I.F. Shaikhislamov, Plasma Phys. Control. Fusion **47**, 645 (2005).

[134] M.A. Shay, J.F. Drake, M. Swisdak, B.N. Rogers, Phys. Plasmas **11**, 2199 (2004).

[135] X. Shan and D. Montgomery, Plasma Phys. Control. Fusion **35**, 619 (1993).

[136] X. Shan and D. Montgomery, Plasma Phys. Control. Fusion **35**, 1019 (1993).

[137] M. Sipics, *Taking on the ITER challenge, scientists look to innovative algorithms, petascale computers*, SIAM News **39**, (September, 2006).

[138] H. Soltwisch, Rev. Sci. Instrum. **59**, 1599 (1988).

[139] C.R. Sovinec, A.H. Glasser, T.A. Gianakon, D.C. Barnes, R.A. Nebel, S.E. Kruger, D.D. Schnack, S.J. Plimpton, A. Tarditi and the NIMROD Team, J. Comput. Phys. **195**, 355 (2004).

[140] R.L. Stenzel, J.M. Urrutia, M. Griskey, and K. Strohmaier, Phys. Plasmas **9**, 1925 (2002).

[141] P.A. Sweet, in *Electromagnetic Phenomena in Cosmical Physics*, edited by B. Lehnert (Cambridge U.P., New York, 1958), p. 123.

[142] M. Swisdak, J.F. Drake, M.A. Shay, and J.G. McIlhargey, J. Geophys. Res. **110**, 5210 (2005).

[143] A. Sykes and J.A. Wesson, Phys. Rev. Lett. **37**, 140 (1976).

[144] S.I. Syrovatsky, Sov. Phys. JETP **33**, 933 (1971).

[145] Y. Tanaka, M. Azumi, G. Kurita, and T. Takeda, Plasma Phys. Control. Fusion **27**, 579 (1985).

[146] M.L. Theobald, D. Montgomery, G.D. Doolen, J.P. Dahlburg, Phys. Fluids B **1**, 766 (1989).

[147] D.A. Uzdensky and R.M. Kulsrud, Phys. Plasmas **7**, 4018 (2000).

[148] A. Vaivads, *et. al.*, Phys. Rev. Lett. **93**, 105001 (2004).

[149] F.L. Waelbroeck, Phys. Fluids B **1**, 2372 (1989).

[150] X. Wang and A. Bhattacharjee, Phys. Rev. Lett. **70**, 1627 (1993).

[151] H. Weisen, G. Borg, B. Joye, A.J. Knight, J.B. Lister, Phys. Rev. Lett. **62**, 434 (1989).

[152] A. Weller, *et. al.*, Phys. Rev. Lett. **59**, 2303 (1987).

[153] J.A. Wesson, Plasma Phys. Control. Fusion **28**, 243 (1986).

[154] J.A. Wesson, in A. Bondeson, E. Sindoni and F. Troyon (eds.), *Theory of Fusion Plasmas* (Proc. Varenna Workshop, Editrice Compositori Bologna, 1987), p. 253.

[155] J.A. Wesson, B. Alper, A.W. Edwards, and R.D. Gill, Phys. Rev. Lett. **79**, 5018 (1997).

[156] J.A. Wesson, *Tokamaks* (Clarendon Press, Oxford, 2004).

[157] W.P. West, D.M. Thomas, J.S. deGrassie, S.B. Zheng, Phys. Rev. Lett. **58**, 2758 (1987).

[158] M. Yamada, *et. al.*, Phys. Plasmas **13**, 052119 (2006).

[159] L. Zakharov and B. Rogers, Phys. Fluids B **4**, 3285 (1992).

[160] V.P. Zhukov and G. Fuchs, Fiz. Plazmy **24**, 996 (1998) [Plasma Phys. Rep. **24**, 929 (1998)].

[161] V.P. Zhukov, Fiz. Plazmy **31**, 721 (2005) [Plasma Phys. Rep. **31**, 665 (2005)].